The Oxidation of Individually Levitated Char Particles

Thesis by

Brian Alan Wong

In Partial Fulfillment of the Requirements
for the Degree of
Doctor of Philosophy

California Institute of Technology
Pasadena, California

1991

(Defended May 22, 1991)

Acknowledgements

I would like to thank my advisor, Dr. Richard C. Flagan, and co-advisor, Dr. George R. Gavalas, for their patience, advice and helpful discussions. I also thank them for their inspiration and encouragement when things looked bleak.

I appreciate the assistance I received from all of the EES staff. Gunilla Hastrup and Rayma Harrison were always extraordinarily helpful and friendly. The secretaries always provided lots of assistance, especially Evelina Cui and Fran Matzen. I especially thank Joe Fontana and Rich Eastvedt, who allowed me to use all the tools and equipment in the shops, and provided instructions, too.

I saw many fellow graduate students come and go during my stay here (far too many), but I especially want to thank Yiannis Levendis, Teri Olson, David James, Ranajit Sahu, Chak Chan, Xiao-Ming Li and Steven Rogak for their assistance, helpful discussions and overall companionship. I offer my thanks to the many others that I neglected to mention.

My mother and father and their generation worked extraordinarily hard and sacrificed much so that their children might enjoy a better life. I hope that I will be able to follow their examples.

I thank my two boys, Andy and Tony, for being ideal children (nearly).

Finally, I thank my wife, Vickie, for her love, patience, and whole-hearted support.

Abstract

An electrodynamic balance was constructed for use as a single particle thermogravimetric analyzer. The electrodynamic balance uses a vertical DC field to levitate an electrically charged particle. An AC voltage is applied to a ring electrode surrounding the particle between the DC electrodes. This AC field provides a restoring force if the particle is displaced from the center of the balance. A carbon dioxide laser was used to heat the particle. The temperature of the particle was measured by a dual-wavelength optical pyrometer. Two materials were the subject of oxidation studies, a porous synthetic carbon, Spherocarb and char made from PSOC 1451 bituminous coal. Two studies were performed, an ignition study, and a low temperature oxidation study. In the ignition study, a suspended particle was heated by a series of 500 millisecond pulses from the laser, at increasing oxygen concentrations. The particle temperature trace shows the ignition delay as predicted by Semenov's thermal explosion theory. A simple isothermal sphere model was applied with literature values for the physical parameters. A reasonably good match of the data to the model was found. In the low temperature experiments char particles were heated in air to a temperature of about 600°C. Some of the particles did not react at constant diameter, as expected. In particular, Spherocarb shrank or densified, as noted by others. The char particles formed from a narrow size cut of PSOC 1451 bituminous coal devolatilized at 1200K also shrank in size as it reacted. However the char formed at 1600K did not shrink, but oxidized at constant diameter. The densification phenomenon, then, is dependent on the devolatilization process and charring temperature. Simple char oxidation models will not accurately predict the size changes of these shrinking chars.

Table of Contents

List of Figures

List of Tables

Chapter 1

Introduction

Coal combustion is a major source of energy to produce electricity. In the United States, 56% of the electricity production comes from coal, 19% from nuclear power and the remainder from hydroelectric, oil- and gas-fired, and miscellaneous solar and wind power stations (Corcoran, 1991). The large majority of the United States fossil fuel reserves are in coal. Future technologies, such as fusion power, are not anticipated to be a significant factor in energy production for some decades. Other technologies, such as solar, wind and geothermal energy production are not cost effective compared with electricity production by more conventional means. Nuclear power development has been stalled because of popular fears of the hazards of waste disposal and radiation exposure and a lack of confidence in the engineering technocracy and regulatory agencies. Thus, for the foreseeable future, coal remains the fuel of lowest cost, greatest abundance, and proven technology for electricity production.

From an environmental viewpoint, coal combustion has major drawbacks, however. The burning of coal, along with the use of petroleum fuel in vehicles, are major contributors to anthropogenic carbon dioxide emission to the atmosphere. The increase in the global atmospheric concentration of carbon dioxide is postulated to contribute to the greenhouse effect, a gradual warming of the earth (Schneider, 1989). The mineral matter in coal also causes problems. As a coal particle burns, the mineral matter fragments and disperses, and evaporates

and recondenses to form flyash, a nuisance dust at best, and a potentially toxic material at worst. Toxic metals tend to concentrate on the surface of flyash particles (Davison et al., 1974 and Helble and Sarofim, 1989). The mineral matter can also coalesce and collect on heat transfer tubes in the combustor, degrading heat transfer and reducing power generation efficiency. Sulfur and nitrogen in the coal, and nitrogen in the combustion air are converted to sulfur and nitrogen oxides. These gases are subsequently released from the stacks into the atmosphere, where they react to form secondary pollutants that contribute to acid deposition and atmospheric oxidants (Schwartz, 1989). Research is being conducted to develop technologies to reduce these emissions, i. e., to develop techniques to scrub acid gases, or capture flyash more efficiently. Understanding coal combustion on the fundamental level will also provide information that can be used to solve some of the problems of coal combustion.

Coal Combustion

Coal is the remains of thick layers of prehistoric vegetative matter that was buried and subjected to heat and pressure. Because of differences in the starting material and in the coalification process, coal, as we find it now, has a wide range of properties. One of the most important is the carbon content, which defines a coal's rank. The anthracites have the highest rank and heating value, at 86 to 98% carbon. The bituminous coals have a lower carbon content. The subbituminous and lignites have the lowest carbon contents and heating values. Other properties that are important in classifying coals include mineral, sulfur and nitrogen content, but these will not be addressed in the present work.

In pulverized coal combustion, the coal is ground to small particles,

typically 50 μm in diameter, entrained in an air stream and blown into the combustor (Field, 1967). A coal particle burns in two steps. First, as it heats up, the coal dries and then devolatilizes as low vapor pressure organic compounds are driven off. The char residue that remains after devolatilization is mostly carbon and ash. The char is very porous; the nature and extent of the porosity depending on the initial coal structure and on the rate of heating and ultimate temperature attained during the devolatilization process. After most of the low vapor pressure materials have outgassed, oxygen diffuses into the pores and oxidizes the carbon matrix. The heat release from the exothermic carbon-oxygen reaction increases the particle temperature and accelerates the rate of reaction of the carbon with oxygen. When the heat generation due to the carbon oxidation exceeds the heat loss due to conduction and radiation, ignition occurs, and oxidation of the particle proceeds rapidly.

Many reviews of coal combustion mechanisms and kinetics have been written. Field et al. (1967) provides an overview of all aspects of coal combustion. He reviews the practical aspects of large-scale combustion such as flow patterns and heat transfer in combustors. The reaction rate of an individual coal particle is also modeled. Smoot and Smith (1985) also review the coal combustion field, with additional information on fluidized bed combustion and the effects of turbulence on combustion. Essenhigh's (1981) review of coal combustion focuses more on the kinetics of char reactions.

A recent issue of the journal *Energy and Fuels* was devoted to coal pyrolysis and devolatilization (Serio, et al., 1988), including discussion of the mechanisms of pyrolysis, kinetics of devolatilization, and models of the devolatilization process. Though devolatilization is outside of the scope of this thesis, it

will be shown in Chapter 3 that the conditions of devolatilization may have an effect on subsequent char oxidation behavior.

Char oxidation studies have been extensively reviewed by Laurendreau (1978) and Smith (1978; 1982). Smith compiled the existing data on the reactivity of chars and other carbons and inferred an Arrhenius rate expression for the intrinsic rate of the carbon/oxygen reaction. However, the many measurements were widely scattered. This was attributed to differences in atomic structure of the carbons and effects of impurities in the chars. Research in char oxidation continues in order to sort out these differences. One study pertinent to this thesis examined physical properties such as surface area, and the oxidation rates of three bituminous coals (Sahu et al., 1988).

The ignition process in coal combustion was reviewed by Essenhigh et al. (1989). The motivation for studying ignition initially began with safety concerns and the attempts to identify the reasons for the spontaneous combustion of coal dust. Recently, efforts have been geared towards a more quantitative understanding of the ignition process for a single particle and eventually relating single particle work to clouds of particles. The thermal explosion theory of Semenov was presented with a summary of experimental results from ignition studies on single particles (Essenhigh et al., 1989). The results from the experiments showed the predicted decrease of ignition temperature with increasing particle size.

Experimental Techniques for Studying Char Oxidation

Most studies of char oxidation have used a thermogravimetric analyzer (TGA) or an entrained flow furnace. The thermogravimetric analyzer uses

milligram quantities of the material being studied. The sample is placed on a microbalance pan that is suspended inside a heated tube. Gas flows through the tube to provide a constant gas reactant concentration and composition. The tube is heated at known rates to a preset temperature. The mass of the sample is monitored to provide a rate of mass change (Essenhigh, 1981; Floess et al., 1991). Disadvantages of the TGA technique include possible diffusion limitations of the reactant through the bed of sample, and heat transfer and heating rate limitations (Essenhigh, 1981; Bar-Ziv et al., 1989).

In entrained flow experiments, pulverized coal or char is entrained in a gas flow and injected into a furnace. This kind of system can simulate the temperature, gas composition and radiant environment of coal combustion in an industrial boiler. Mitchell and coworkers (1982; Waters et al. 1988ab; Niksa et al., 1984) injected fuel particles into a burner that was heated by many small diffusion flames. The gas temperature and composition were controlled through the inlet gas composition. Particle sizes and temperatures are determined by an optical pyrometric method. To achieve very high gas temperatures, Field (1969) and Leslie et al. (1989) used thermal plasmas for high temperature reactivity studies. Sarofim and coworkers (1982; 1989) and Levendis et al. (1987; 1989) used electrically heated furnace reactors. Particle temperature was measured with an optical pyrometer. Linak and Peterson (1984) used a self-sustaining laboratory combustor which maintained combustion without external sources of heat. In these experiments, the temperature of the particle may exceed the ambient temperature by several hundred degrees. Particle temperature was inferred from operating conditions for the systems in which the particle temperature was not directly measured. Relatively large quantities of material must be used in these systems, so differences on a particle to particle basis cannot be determined.

In an effort to eliminate the variability associated with coal char and the effects of mineral matter and other heterogeneities, in studies of char oxidation mechanism and rates, Levendis et al. (1989a,b) developed mono-sized synthetic char particles with a range of porous microstructures. These experiments revealed oxygen-catalyzed rearrangements of the carbon microstructure, and provided a rigorous test for char combustion models. In other studies, several groups have used Spherocarb, a commercially available, porous synthetic carbon, as a surrogate for coal char because of its high purity, large specific surface area, spherical shape and ready availability. Floess et al. (1988) and Waters et al. (1988b) determined the activation energy for Spherocarb oxidation in different temperature ranges. Hurt et al. (1988; 1991) and Dudek et al. (1989) studied surface area related effects in Spherocarb.

The Electrodynamic Balance

The electrodynamic balance (EDB) is a tool that has been used to study individual droplets and particles. The EDB consists of three electrodes. Two electrodes support a DC field that levitates a charged particle against gravity, as in the Millikan oil-drop experiment (Davis, 1987). The particle, while suspended vertically, is subject to horizontal motion by brownian forces. A ring, supporting an AC voltage, was added to the mid plane between the two endcap electrodes, to provide a restoring force to keep the particle centered. This improvement to the Millikan apparatus was first described by Paul and Raether (1955) and employed in studies of micron-sized particles by Straubel (1956) and Wuerker et al. (1959). Interest in the electrodynamic balance has grown, with much of the work focussing on the physics and optical properties of small particles of atmospheric

interest. The electrodynamic balance has been used in optical studies of small particles, including light scattering and absorption measurements (Davis and Periasamy, 1985). Considerable work in condensation and evaporation and the thermodynamics of supersaturated solutions has been performed in the electrodynamic balance (Davis, 1983; Sageev et al., 1986; Cohen et al., 1987ab). Grader et al. (1987) described the use of the electrodynamic balance for Fourier transform infrared spectroscopy of a single particle, while Folan and Arnold (1986) measured the fluorescence emission from a single particle. Mass and size measurements are readily performed in the electrodynamic balance (Philip et al., 1983; Davis and Ray, 1980.)

Recently, the electrodynamic balance has been adapted to perform as a thermogravimetric analyzer by heating the suspended particle with a carbon dioxide laser (Spjut et al., 1985; Monazam et al., 1988; Bar-Ziv et al., 1989). Dudek et al. (1988) presented theoretical and experimental studies of natural convection of a heated particle. Dudek et al. (1989) and Bar-Ziv et al (1991) determined the surface area of a Spherocarb particle in the electrodynamic balance by measuring the mass increase as carbon dioxide was adsorbed. Spherocarb and other particles were oxidized in the electrodynamic balance and found to shrink, unexpectedly (Hurt et al., 1988). Monazam et al. (1989) measured the heat capacities and absorptivities of Spherocarb particles at elevated temperatures. Thus, the electrodynamic balance is increasingly being used for high temperature studies on single particles. One reason for the development of the electrodynamic balance as a thermogravimetric analyzer is to perform char oxidation studies, free of the disadvantages mentioned for the bulk TGA studies. The total mass is reduced to that of a single particle, so there is no bed of material to cause bed diffusion limitations. High heating rates are possible with

the carbon dioxide laser, with no heat transfer limitations other than the particle thermal conductivity. Thus, the electrodynamic balance is potentially an excellent instrument for studying char oxidation.

The electrodynamic balance is not, however, without limitations. At high temperatures, in excess of 1200-1300K, particles lose charge. Dudek et al. (1990) found thermionic emission to be the most likely explanation for the charge loss. They proposed an equation that included the effect of the particle excess surface charge, surface irregularities and surface contamination with the Richardson-Dushman thermionic emission equation. This charge loss limits the maximum temperature of the suspended particle to temperatures considerably below those normally encountered in pulverized coal combustion (2000K and higher).

The objective of this study was to gain a better understanding of char oxidation focussing on structural transformations experienced by the char during oxidation. The experimental work was performed using an electrodynamic balance that I constructed to levitate a single particle that could be heated with a carbon dioxide laser. The electrodynamic balance was designed, constructed, and calibrated along with the supporting instrumentation. This thesis presents the results from oxidation experiments performed with a Spherocarb char and a coal char in the electrodynamic balance. Chapter 2 describes ignition experiments in which a particle was suspended and heated with short pulses of laser radiation. After each pulse, the oxygen content of the surrounding gas was increased until the particle ignited. The temperature traces of particles that underwent ignition are compared with the thermal explosion theory. Chapter 3 examines the phenomenon of gasification-induced densification of char, first noted by Hurt et al. (1988). Low temperature oxidation studies were carried out on char made at

different charring temperatures from PSOC 1451 bituminous coal. Details of the construction and operation of the balance, and supporting instrumentation are presented in the Appendices.

References

Bar-Ziv, E., Jones, D. B., Spjut, R. E., Dudek, D. R., Sarofim, A. F. and Longwell, J. P. (1989). *Comb. Flame.* 75:81-106.

Bar-Ziv, E., Longwell, J. P. and Sarofim, A. F. (1991). *Energy and Fuels.* 5:227-228.

Cohen, M. D., Flagan, R. C. and Seinfeld, J. H. (1987a). *J. Phys. Chem.* 91:4563-4574.

Cohen, M. D., Flagan, R. C. and Seinfeld, J. H. (1987b). *J. Phys Chem.* 91:4575-4582.

Corcoran, E. (1991). *Sci. Am.* 264(5):107-116.

Davis, E. J. (1983). *Aerosol Sci. Technol.* 2:121-144.

Davis, E. J. (1987). In *Surface and Colloid Science.* (E. Matijevic, ed.). Vol. 14, Plenum Press, New York.

Davis, E. J. and Periasamy, R. (1985). *Langmuir.* 1:373-379.

Davis, E. J. and Ray, A. K. (1980). *J. Colloid Interface Sci.* 75:566-576.

Davison, R. L., Natusch, D. F. S., Wallace, J. R. and Evans, C. A. (1974). *Env. Sci. Tech.* 8:1107-1113.

Dudek, D. R., Longwell, J. P. and Sarofim, A. F. (1989). *Energy and Fuels.* 3:24-28.

Dudek, D. R., Wright, D. A., Longwell, J. P. and Sarofim, A. F. (1990). *Combust. Sci. and Tech.* 73:447-461.

Essenhigh, R. H. (1981). In *Chemistry of Coal Utilization* (M. A. Elliot, ed.). John Wiley and Sons, New York.

Essenhigh, R. H., Misra, M. K. and Shaw, D. W. (1989). *Comb. Flame.* 77:3-30.

Field, M. A. (1969). *Comb. Flame.* 13:237-252.

Field, M. A., Gill, D. W., Morgan, B. B. and Hawksley, P. G. W. (1967). *The Combustion of Pulverized Coal.* The British Coal Utilization Research Association, Leatherhead.

Floess, J. K., Chomiak, J., Sarofim, A. F. and Longwell, J. P. (1991). *Energy and Fuels.* 5:138-140

Floess, J. K., Longwell, J. P. and Sarofim, A. F. (1988). *Energy and Fuels.* 2:18-26.

Folan, L. M. and Arnold, S. (1986). *Rev. Sci. Instrum.* 57:2250-2253.

Grader, G. S., Flagan, R. C., Seinfeld, J. H. and Arnold, S. (1987). *Rev. Sci. Instrum.* 58:584-587.

Helble, J. J. and Sarofim, A. F. (1989). *J. Colloid Interface Sci.* 128:348-362.

Hurt, R. H., Dudek, D. R., Longwell, J. P. and Sarofim, A. F. (1988). *Carbon.* 26:433-439.

Hurt, R. H., Sarofim, A. F. and Longwell, J. P. (1991). *Energy and Fuels.* 5:290-299.

Laurendreau, N. M. (1978). *Prog. Energy Combust. Sci.* 4:221-270.

Leslie, I. H., Jost, M. and Kruger, C. H. *Comb. Flame.* 78:195-203.

Levendis, Y. A. and Flagan, R. C. (1987). *Combust. Sci. and Tech.* 53:117-136.

Levendis, Y. A., Flagan, R. C. and Gavalas, G. R. (1989). *Comb. Flame* 76:221-241.

Levendis, Y. A., Sahu, R., Flagan, R. C. and Gavalas G. R. (1989). *Fuel.* 68:849-855.

Monazam, E. R., Maloney, D. J. and Lawson, L. O. (1989). *Rev. Sci. Instrum.* 60:3460-3465.

Niksa, S., Mitchell, R. E., Hencken, K. R. and Tichenor, D. A. (1984). *Comb. Flame.* 60:183-193.

Philip, M. A., Gelbard, F. and Arnold, S. (1983). *J. Colloid Interface Sci.* 91:507-515.

Quann, R. J. and Sarofim, A. F. (1982). *Nineteenth Symp. (Int.) Comb.* The Combustion Institute, p.1429-1440.

Sageev, G., Flagan, R. C., Seinfeld, J. H. and Arnold, S. (1986). *J. Colloid Interface Sci.* 113:421-429.

Sahu, R., Levendis, Y. A., Flagan, R. C. and Gavalas, G. R. (1988). *Fuel.* 67:275-282.

Schneider, S. H. (1989). *Science.* 243:771-781.

Schwartz, S. E. (1989). *Science.* 243:753-763.

Serio, M. A., Gavalas, G. R., Maloney, D. J. and Suuberg, E. M. (1988). *Energy and Fuels.* 2:361, and following.

Smith, I. W. (1978). *Fuel.* 57:409-414.

Smith, I. W. (1982). In *Nineteenth Symp. (Int.) Comb.* The Combustion Institute, p. 1045-1065.

Smoot, L. D. and Smith, P. J. (1985). *Coal Combustion and Gasification.* Plenum Press, New York.

Spjut, R. E., Sarofim, A. F. and Longwell, J. P. (1985). *Langmuir.* 1:355-360.

Straubel, H. (1956). *Z. Elektrochem.* 60:1033-1036.

Waters, B. J., Mitchell, R. E., Squires, R. G. and Laurendreau, N. M. (1988a). In *Twenty-Second Symp. (Int.) Comb.* The Combustion Institute, p. 17-27.

Waters, B. J., Squires, R. G., Laurendreau, N. M. and Mitchell, R. E. (1988b). *Comb. Flame.* 74:91-106.

Wuerker, R. F., Shelton, H. and Langmuir, R. V. (1959). *J. Appl. Phys.* 30:342-349.

Chapter 2

Laser Ignition of Levitated Char Particles

by

B. A. Wong, G. R. Gavalas and R. C. Flagan

Abstract

The temperature history of a char particle heated by a carbon dioxide laser to ignition was studied in the electrodynamic balance. The experiments were conducted using Spherocarb particles, 140 to 240 μm in diameter, and char particles from a bituminous coal, 150 to 300 μm in diameter. In a typical experiment, a charged char particle was suspended in the electrodynamic balance and heated by a 500 ms pulse of radiation from a CO_2 laser. The temperature of the particle was measured with an optical pyrometer. The oxygen concentration in the ambient gas, initially only nitrogen, was slowly increased as successive laser pulses were given, until the particle ignited. Once ignition occurred, the particle lost charge and dropped from the center of the balance. The particle temperature profile at ignition shows the ignition delay predicted by Semenov's thermal explosion theory. The measured temperature traces could be described well by calculations treating the particle as a sphere and using rate parameters given in the literature.

Introduction

In pulverized coal combustion, small particles, typically 50 μm in size are burned while entrained in the combustion gases. As a coal particle heats up, it devolatilizes and pyrolyzes. The remaining material, char, is a porous, primarily carbonaceous material. The carbon reacts with the oxygen in the surrounding atmosphere, generating heat. Ignition occurs when the heat produced by the exothermic oxidation reaction exceeds the heat loss from the system due to conduction, convection and radiation. This concept of ignition applies to an entire system, e.g., a cloud of coal particles in a furnace, as well as to an individual particle (Field et al., 1967; Essenhigh et al., 1989). Two mechanisms of ignition have been identified for coal particles, homogeneous and heterogeneous (Essenhigh et al., 1989). Homogeneous ignition occurs when the devolatilizing gases react with oxygen to ignite first, producing a flame front that initially stands off from the particle but eventually reaches the char surface as the devolatilization ceases. Heterogeneous ignition occurs directly on the particle surface as oxygen reacts with the char particle. Experimental (Howard and Essenhigh, 1967) and theoretical (Annamalai and Durbetaki, 1977) results have demonstrated that the heterogeneous ignition mechanism dominates for smaller (<350μm diameter) coal particles. The ignition characteristics of coal or char are important to the fundamental understanding of the coal combustion process. Historically, ignition was studied, not only for application in furnaces and combustors, but also because of safety concerns. Coal piles, coal dust, and dust of other materials such as grain have been known to occasionally explode and burn. Research was initiated to determine the cause of, and prevent such unplanned explosions (Essenhigh et al., 1989). Research into the ignition process continues as part of the broad area of research in coal combustion fundamentals in efforts to improve efficiency and

minimize fouling, waste products and pollution in current combustor technology. The development of new technologies, such as coal-fired diesel engines, coal gasification and liquefaction and magneto-hydrodynamics will also benefit from a better understanding of coal combustion fundamentals.

The criteria used to define ignition is based on Semenov's thermal explosion theory (Essenhigh et al., 1989; Chen et al., 1984; Thomas et al., 1973). The classical conditions for ignition state that the heat loss from the particle, Q_l must be equal to the heat generated, Q_g

$$Q_g = Q_l \tag{1}$$

and that the heat loss curve must be tangent to the heat generation curve

$$\frac{dQ_g}{dT} = \frac{dQ_l}{dT} . \tag{2}$$

More generally, ignition occurs when the heat generation equals or exceeds the heat loss (Essenhigh et al., 1989, Chen et al., 1984)

$$Q_g \geq Q_l . \tag{3}$$

The ignition limit defined by equations 1, 2 and 3 is illustrated in Figure 1 which shows the heat loss and gain for a 50 μm diameter coal particle in a hot gas as a function of particle temperature (Field et al., 1967). The dotted lines show the heat loss and heat generation for the particle in a hot gas with 10% oxygen at 900K. At point A the curves intersect, i.e., $Q_g = Q_l$, but the tangency requirement is not met, so the particle reaches an equilibrium temperature

without igniting. If the particle temperature increases, the heat loss is greater than the heat gain, and the particle will cool back to the equilibrium temperature. If the particle temperature undergoes a slight decrease, the heat gain becomes greater than the heat loss, and the particle warms back to the equilibrium temperature. The solid curves show the heat loss and heat generation for the particle in 10% oxygen at 1235K. Under these conditions, the reaction with oxygen causes the particle temperature to increase to about 1360K, at which point (B), the heat loss and heat gain curves are equal and, also, tangent, indicating the ignition limit. Any perturbation in temperature above this value will cause the particle temperature to increase further since the heat generation rate is greater than the heat loss rate. The final steady-state temperature of the ignited particle is attained at the point C at which the two curves again intersect. The dashed curves show the heat loss and heat generation for the particle in 10% oxygen at 1400K. The heat generation is significantly greater than the heat loss, until the boundary layer diffusion of oxygen becomes the limiting factor to any further temperature rise, and the curves intersect at point D. Mass loss has not been considered explicitly in this simple model. Instead, we have determined the steady-state temperature that would result if the particle temperature rise occurred very rapidly compared to its loss of mass by oxidation.

A detailed examination of char ignition requires solving the unsteady energy balance

$$m\, C_p \frac{dT}{dt} = Q_g - Q_l \tag{4}$$

in conjunction with a model of the oxidation process. Here, m is the mass of the particle, C_p is the heat capacity, T is the temperature, and t is the time. In Figure 2, the dotted curve shows the temperature of a 50μm particle immersed in

a gas at 900K. The particle temperature increases and then levels out at the temperature corresponding to the intersection of the heat loss and heat gain curve (point A) in Figure 1. For the same particle immersed in a gas at 1235K, the curve (solid line) plateaus at the ignition temperature, and then rapidly increases. The inflection point in this curve corresponds to point B in Figure 1. The length of time spent in the plateau is known as the ignition delay or induction time (Essenhigh et al., 1989; Bandyopadhyay and Bhaduri, 1972; Thomas et al., 1973). The temperature rises until it plateaus at point C. The dashed curve shows the rapid temperature rise of a particle at a surrounding temperature of 1400K. At this high temperature, the particle ignites without the ignition delay (Thomas et al., 1973) and the temperature rises to a new steady–state in which oxidation is limited by the external diffusion of oxygen to the particle.

There have been many studies of the ignition process, with special interest in the ignition temperatures of coal or char particles and the relationship to particle diameter. Different techniques were devised to accomplish the three major steps in these experiments; holding or isolating the particle, heating the particle, and monitoring the transient particle temperature and identifying ignition. Bandyopadhyay and Bhaduri (1972) placed a coal particle onto a fine platinum wire and inserted the wire into a furnace. The insertion step was repeated after increasing the temperature of the furnace until an ignition flash was observed. Karcz et al. (1980) placed a single coal particle on the tip of a quartz needle and inserted the needle into a heated furnace. As in the experiments of Bandyopadhyay. and Bhaduri, the insertion was repeated with the furnace temperature increased stepwise until ignition was observed. Ubhayakar and Williams (1976) mounted a small carbon particle on the end of a glass fiber and heated the particle with a ruby laser pulse. The particle was monitored by a high-

speed camera that recorded the igniting particle as a bright spot on the film. The temperature of the particle was also monitored by dual-wavelength optical pyrometry. Cassel and Liebman (1959), Chen et al. (1984) and Seixas and Essenhigh (1986) injected particles into a heated drop-tube furnace, and observed them with a photomultiplier tube. The temperature of the furnace was gradually increased until a flash was seen, indicating ignition. Gomez and Vastola (1985) injected particles into a heated gas stream, and analyzed the resultant gases for CO and CO_2. The ratio of the two gas concentrations was used to distinguish between heterogeneous and homogeneous ignition. Ignition was also confirmed by light emission measurements. Tognotti, et al. (1985) placed milligram quantities of coal or char in a thermogravimetric analyzer (TGA) in an inert (N_2) or oxidizing atmosphere, and slowly ramped the temperature. The ignition temperature was defined as the point at which the weight vs. temperature curve for the coal or char in the oxidizing atmosphere deviated from that in the inert atmosphere. In all of the above experiments, the ignition temperature was found to decrease with increasing particle size, in agreement with the thermal explosion theory. The activation energies determined from these experiments encompass a wide range of values (11 to 50 kcal/mole) because of the variety of coals and chars tested, and probably because of other differences from experiment to experiment. Essenhigh et al. (1989) have reviewed early theories as well as more recent theoretical and experimental work on ignition.

These approaches have a number of drawbacks. In the experiments where a single coal particle is mounted on a thin wire (Bandyopadhyay and Bhaduri, 1972; Karcz et al., 1980; Ubhayakar and Williams, 1976) the effects of the physical contact on the energy balance have been assumed negligible. In the experiments which detect ignition by visual or optical detection (Chen et al., 1984;

Bandyopadhyay and Bhaduri, 1972; Karcz et al., 1980; Cassel and Leibman, 1959; Seixas and Essenhigh, 1986; Gomez and Vastola, 1985) the determination of ignition is dependent on the spectral sensitivity of the selected detector. Only Ubhayakar and Williams (1976) measured the actual particle temperature. Most investigators inferred particle temperature from the ambient value.

Ideally, one would like to isolate a single particle free of physical contact, rapidly heat the particle, and measure its temperature directly. In this paper we present an experimental investigation of ignition that more closely approaches this ideal. In our experiments, electrically charged char particles were levitated in an electrodynamic balance and heated with laser radiation. This type of electrodynamic thermogravimetric analyzer has been previously used in studies of char particle oxidation (Spjut et al., 1985; Bar-Ziv et al., 1989). The balance is an improved version of Millikan's oil-drop apparatus. In the electrodynamic balance, a charged particle is suspended in a DC field between two end-cap electrodes, as in the Millikan cell. In the midplane between the electrodes, a ring electrode surrounds the particle. When the particle is at the center of the cell it is not affected by the alternating field. If, however, it is displaced from that null point in any direction, the particle experiences an alternating force that increases with displacement. The particle then oscillates but lags the AC field in phase due to inertia and aerodynamic drag. The time-average force experienced by the particle drives it back toward the center of the cell. With the addition of this dynamic focussing, a particle that is levitated electrostatically can be subjected to rather strong forces without being lost. The electrodynamic balance has a long history (Davis, 1987), and has been used in previous studies of ignition processes. Nelson et al. (1968) used a form of the electrodynamic balance to suspend metal particles, which were ignited by a pulsed Nd-doped glass laser. Liebman et al.

(1972) also used a quadrupole levitator to suspend magnesium particles for ignition by a Nd-doped glass laser. Bar-Ziv (1989) reports on some ignition studies in the electrodynamic thermogravimetric analyzer in his review article on single particle char combustion kinetics. We report here on the use of an electrodynamic balance to study laser-induced ignition of a freely levitated char particle.

Experimental

The use of the electrodynamic balance for single particle studies is well documented (Spjut et al., 1985; Davis, 1987; and Monazam et al., 1989; Bar-Ziv et al., 1989). The electrode configuration in the electrodynamic balances most commonly used has a hyperboloidal geometry. The electric field in the hyperboloidal geometry balance is well-characterized (Davis, 1987), but this understanding is not critical to its use. Many other electrode geometries have been used in previous applications of the electrodynamic balance (Davis, 1987; Arnold and Folan, 1987; Davis et al., 1990). Sloane and Elmoursi (1989) have theoretically examined the characteristics of a number of electrode arrangements. We used hemispherical endcap electrodes and a right cylinder ring as illustrated in Figure 3. The electric field near the center of this balance, and therefore its operating characteristics, very closely approximates that of the hyperboloidal geometry (Sloane and Elmoursi, 1989; Wong, 1991). The electrode cell was housed in an evacuable stainless steel chamber with total volume of 250 cm^3. The atmosphere in the chamber was controlled by introduction of gases with the desired composition.

A 20-Watt Carbon Dioxide laser (Advanced Kinetics MIRL-20) was used

to heat the particle. The laser was modified to produce a TEM-01* beam. In this mode, the cross-section of the beam appears to be doughnut-shaped rather than Gaussian shaped as in more common TEM-00 mode. The TEM-01* mode was selected because when the particle is heated, thermophoretic and photophoretic forces tend to push the particle away from the area of highest intensity (Greene, 1985). In a Gaussian beam, then, the particle tends to be pushed out of the laser beam. The particle will remain trapped in a doughnut mode beam. The laser beam is directed by mirrors into the top of the chamber through a KCl window, and the beam is focused onto the particle with a ZnSe lens. The lens can be moved vertically to focus or defocus the beam with respect to the particle, changing the intensity of the beam incident on the particle.

The TEM-01* mode of the laser was very sensitive to laser temperature and power variations, therefore laser pulsing could not be controlled by pulsing the power supply. An external shutter was constructed from refractory and attached to a pneumatic piston. The laser beam was uncovered or covered in 3 to 4 milliseconds by the shutter. The length of time that the shutter was opened was controlled electronically.

A 5-mW HeNe laser (Melles Griot) was directed through the bottom of the chamber onto the particle for illumination. The particle was observed with a microscope and with a catadioptric microscope (Questar) and video camera combination. The images from the video camera were recorded on a video cassette recorder. The particle image was also focused onto a position-sensitive-detector (PSD). The outputs from the PSD were connected to a proportional-integral- derivative (PID) controller which fed back to the DC voltage control. Thus, any force causing the particle to deviate vertically from the center in the

vertical plane would cause the PID controller to adjust the DC voltage restoring the particle back to the center of the chamber.

The temperature of the particle was monitored by a two-color optical pyrometer, pictured schematically in Figure 4. Radiation from the particle was collimated by a CsF_2 lens, and then split by a coarse grating beam splitter. The two beams then passed through CsF_2 focusing lenses and interference filters at 1.48 and 3.42 μm and onto an InGaAs and an InSb detector. The output from the detectors was processed with a log-ratio amplifier, and monitored with a PC-based data acquisition system. The optical pyrometer was calibrated by inserting a type R thermocouple into the chamber with the bead placed at the center of the cell in place of the particle. The thermocouple was heated by the CO_2 laser while the thermocouple output and the pyrometer output were recorded. The pyrometer output is plotted against the thermocouple temperature in Figure 5.

The gas composition in the chamber was varied by using a 3-liter glass vessel as a continuous flow stirred tank reactor (CSTR). Nitrogen was passed through the vessel and through the chamber. At the onset of the experiment, oxygen was admitted into the CSTR. The output from the CSTR was then a N_2–O_2 mixture that was slowly increasing in oxygen. This mixture flowed through the chamber and into an oxygen analyzer (Beckman, Model 755). The TGA chamber also acted as a CSTR, but with a much shorter residence time so that concentration of oxygen was very close to that of the larger vessel.

Two materials were used in this study. The first was Spherocarb, a highly porous synthetic carbon intended for use as a gas chromatograph column packing. (Alltech purchases this material from Analabs and markets it as "Carbosphere." Because Spherocarb is the trade name more commonly found in literature

references, we shall call the material Spherocarb). Because of its high pososity, relative freedom from impurities, and highly spherical shape, this material has been used in many carbon oxidation studies (Waters et al., 1988; Floess, 1988; Bar-Ziv et al., 1989). The second material studied was char from PSOC 1451 bituminous coal previously characterized by Sahu et al. (1988a).

Procedure

An experiment was started by presetting the AC and DC voltages of the electrodynamic balance to previously determined values. A small amount of char was placed on a small electrode and pushed under the bottom end-cap electrode. A Zerostat (Discwasher, Inc.) anti-static device was used to generate a short high voltage pulse to the electrode. Char particles on the electrode acquired charge and were repelled from the electrode through the opening in the bottom electrode into the electrodynamic cell, where some were captured by the AC field. The AC and DC voltages were manipulated to isolate a single particle. Following the suspension of an isolated particle the chamber was flushed with nitrogen. The dimensions of the particle were then measured with an eyepiece micrometer. After these preliminaries, the CO_2 laser was pulsed by opening the shutter for 500 milliseconds. During this pulse, the output from the pyrometer, the balancing voltage, and the position were recorded on a PC–based data acquisition system. The temperature rise observed in the absence of oxygen provides the data needed to calculate the laser energy absorbed by the particle. Oxygen was then admitted into the CSTR and as the N_2–O_2 mixture of increasing O_2 concentration was passed through the chamber, additional laser pulses were administered until the particle ignited.

Results

The time-temperature history of a Spherocarb particle undergoing a laser pulse in nitrogen is shown in Figure 6a. The solid line connects experimental data points. It can be seen that the particle temperature increases, reaches a steady state level and then drops when the laser pulse ends. Figure 6b shows the same particle heated in 20% oxygen. The steady state temperature is now higher, due to increased rate of carbon oxidation. At each laser pulse the oxygen concentration was about 5% higher than that present at the previous pulse. This particular Spherocarb particle ignited when the oxygen concentration reached 40%, as illustrated in Figure 6c. The temperature trace shows an ignition delay time of approximately 300 milliseconds.

The vertical position trace of a Spherocarb particle in nitrogen is shown in Figure 7a, where 0 denotes the center of the chamber. Prior to the laser pulse, the particle is oscillating with an amplitude of the order of $\pm 15\mu$m. When the particle is pulsed, the oscillation changes, but the particle does not deviate from the center of the chamber. This pattern was generally observed for subsequent pulses as shown in Figure 7b. Figure 7c shows that for a particle suspended in 40% oxygen, the amplitude of the oscillations, initially very small, greatly increases during heating. Finally, when the particle reaches a temperature of 1200 to 1300K, it begins to lose charge (Dudek et al., 1990), and the particle eventually drops from the center of the chamber, as shown by the position trace.

Figure 8 shows the heat loss and heat generation curves for a Spherocarb particle exposed to different oxygen concentrations. The curves are analogous to those in Figure 1. The heat loss curve is the labeled solid line. The horizontal solid line represents the heat generation curve in nitrogen. Since the only source

of heat is the laser, the particle temperature is constant, and the line is horizontal. The short-dashed line is the heat generation in 20% oxygen. This curve intersects the heat loss curve, indicating a stable temperature, without ignition. The long-dashed line shows the heat generation curve at 40% oxygen. This curve is above the heat loss curve, satisfying equations (2) and (3), so the particle ignites. The region in Figure 6c where the particle temperature rises slowly corresponds to the area where the heat generation and heat loss curves are close to each other.

The temperature trace of a 300 μm bituminous char particle laser-heated in nitrogen is shown in Figure 9a. The steady-state temperature trace fluctuates somewhat due to the more irregular shape and uneven heating of the char particle. In 10% oxygen, Figure 9b shows that the particle temperature dips slightly, then returns to a steady state level, until the laser pulse is off. The video recording shows that the dip in the temperature is due to movement and rotation of the unevenly heated particle. When the oxygen pressure reaches 15%, the particle ignites. Figure 9c shows that ignition was attained after a short induction time.

The vertical position trace of the bituminous char particle is shown in Figures 10a,b and c. When the laser is pulsed on, the particle undergoes a larger displacement from that of a Spherocarb particle, and rises in the chamber. This is evidently because of the greater buoyancy effect on the lower density char. As with the Spherocarb particles, as it ignites, the char particle drops out of the center because of charge loss.

Discussion

In a simple analysis of particle ignition, a spherical and isothermal particle

is assumed to be at rest relative to the surrounding gas. The heat loss to the gas may be written in the form of Newton's law of cooling. The heat transfer coefficient determined from the Nusselt number, which equals 2 for spheres at low Reynolds numbers, as in this case. The contribution of radiation to the particle heat loss is small but increases as the temperature of the particle increases. The heat loss due to conduction and radiation for a sphere are:

$$H_c = \frac{k\,(T_p - T_g)}{r} \tag{5}$$

$$H_r = \varepsilon\,\sigma\,(T_p^4 - T_g^4) \tag{6}$$

where k is the thermal conductivity of air, T_p is the particle temperature, T_g is the gas temperature, r is the particle radius, ε is the particle emissivity, and σ is the Stefan-Boltzman constant.

The rate of carbon oxidation, R_C, is generally expressed in the simple form

$$R_C = Ae^{(-E_a/RT_p)}P_{O_2}^n \tag{8}$$

where E_a is the activation energy, R is the gas constant, A is the pre-exponential factor, P_{O_2} is the pressure of oxygen, and n is the reaction order. The heat generation term is then given by:

$$H_g = R_C Q_{\text{eff}} \tag{9}$$

where Q_{eff} is the heat released by carbon oxidation. The time dependent equation (3) can therefore be written as

$$mC_p\frac{dT}{dt} = 4\pi a^2(H_g + H_l - H_c - H_r) \tag{10}$$

The term H_l is the heat gain from absorption of the laser energy.

The value of the heat capacity, C_p, for Spherocarb was taken from Monazam et al. (1989). An apparent activation energy, E_a, of 20 kcal/mole and a reaction order with respect to oxygen, n, of one-half was assumed, as determined by Waters et al. (1988) in their study of Spherocarb oxidation in the temperature range of 1400 to 2200K. The diffusion of oxygen through the porous char matrix becomes the limiting factor in the carbon oxidation rate at these temperatures. The particle temperatures being measured were approaching this range, hence the apparent rate parameters were selected. Also in the experiment by Waters et al., it was determined that the oxidation products were CO and CO_2 in a 65% to 35% ratio, and Q_{eff} was calculated accordingly. Table I gives the values used for each parameter and the literature source.

The value of H_l was determined from the particle temperature trace when heated in nitrogen. In the absence of oxygen, H_g is zero, and at steady state, $H_l = H_c + H_r$. After H_l was determined, the time dependent equation (10) was solved using a fourth-order Runge-Kutta routine. The pre-exponential factor was varied until a reasonable fit of the curve to the experimental data from the ignition event was obtained.

The calculated temperature traces are shown by the dashed lines in Figures 6a to 6c and 9a to 9c. The good agreement between calculated traces and measured traces for the nitrogen atmosphere (Figures 6a and 9a) simply reflects the choice of the parameter, H_l, which was adjusted to match those two traces.

The calculated laser intensity is listed in Table 2. The density parameter was adjusted to match the initial slope of the calculated trace to the measured trace in a nitrogen atmosphere. The density values are larger than the density of 600 kg/m^3 found for Spherocarb particles by D'Amore et al. (1988), but they cluster around the value of 1050 kg/m^3 used by Monazam et al. (1989) when he measured the heat capacity of Spherocarb.

Table 2 shows the fitted parameters for several particles. The fitted pre-exponential factors ranged from 3.6 to 6.1. The preexponential factor that was determined by Waters et al. (1988) was 10.6 Kg m^{-2} s^{-1}(mole O_2 cm^{-3})$^{-n}$. Although the pre-exponential factor is the nominal fitting parameter, Q_{eff} and $P^n_{O_2}$ can also be lumped in with the exponential factor. Therefore, the uncertainty in the fitted exponential value is also indicative of uncertainties in Q_{eff} and $P^n_{O_2}$.

The calculated trace in Figure 6b was determined using the fitted parameters from Figures 6a and 6c. It appears to over-predict the measured temperature. This discrepancy may be due to experimental error such as fluctuations in the laser power, or it may be due to the uncertainties in the Q_{eff} and $P^n_{O_2}$ as mentioned previously. A general trend of increasing steady state temperature with increasing oxygen concentration could be detected, however, the scatter in the data was substantial, and the relationship could not be quantified.

Sahu et al. (1988b) determined an apparent activation energy of 17 kcal/mole for char made from PSOC 1451 bituminous coal with a pre-exponential factor of 107.1 g cm^{-2} s^{-1} atm^{-1}. When the apparent activation energy is used, and the pre-exponential factor varied to achieve a reasonable fit, Figure 9c results.

There are an number of problems with this experiment which are not apparent from the results presented. The first is related to the laser stability. The laser power, as measured on a power meter, was subject to fluctuations and occasionally drifted over a long period of time. To minimize the effect of drift, the experiments were performed only when it appeared that the laser was operating stably and the power was not drifting. However, the fluctuations were always present. Another difficulty was that the laser heated the particle from the top only. Video recordings of a Spherocarb particle during heating clearly show a thermal gradient across the particle. Thus, the model used to describe the experiments is an oversimplification. Bar-Ziv et al. (1989), and Monazam et al., (1989) addressed this problem for a particle heated on opposite sides and concluded that the maximum temperature difference between the surface and center of the particle was about 8K for a particle 1000°C above ambient. They concluded that this difference may be disregarded for most combustion studies. For one sided heating, however, the temperature difference is greater, although the magnitude of the temperature gradient is not known.

A particle heated on one side might lead to ignition at a point, or a very small area, as discussed by Levendis et al. (1989). Those authors used two–color pyrometry to measure the temperature of a char particle burning in a drop-tube furnace. They observed signal intensities which increased in the individual detectors while the ratio of the signal intensities remained relatively constant, indicating a relatively uniform temperature. They attributed the increase in signal intensity to localized ignition on the particle surface which gradually spread over the surface of the particle. In the present experiments we did not measure the individual signal intensities but only their ratios therefore, it is unknown whether the detector signal levels are changing while their ratio remains constant.

Observations from the video recording of the particle ignition do not show localized ignition on a Spherocarb particle. The particle appears to glow uniformly as the temperature nears the ignition point (although saturation of the video camera precludes quantitative interpretation of these images). As the particle ignites, it appears to expand to about twice its original diameter. This expansion may be due to an oscillation of the particle that is too rapid to be resolved by the video camera, or it may result from camera saturation. At this point, the particle loses a significant amount of charge, and drops from the center of the chamber. No hot spots are visible, no jetting is observed, and Spherocarb particles always move in the downwards direction. Hence, it is believed that the Spherocarb particles are igniting uniformly across the surface of the particle. In contrast, there is clear evidence of localized ignition on char particles. Video recordings show that, when a coal char particle is heated, small areas glow considerably more intensely than other areas. Since the char is irregularly shaped, this is not unexpected. Even when a char particle ignites, hot spots often are visible.

Conclusions

This experiment has shown that ignition experiments are feasible in the electrodynamic balance With the particle suspended without physical contact, heat transfer other than by conduction and radiation is avoided. The particle temperature is measured by the optical pyrometer and does not need to be calculated from the ambient temperature. There are some difficulties which need to be addressed in order to increase the utility of this experiment. The first is the temperature gradient along the particle due to heating from the top side only. When we attempted to heat from both sides, the particle bounced around

excessively. The solution might be using a more powerful laser, such as used by Monazam et al. (1989), in the Gaussian mode. The problem of charge loss at high temperatures also limits the usefulness of the electrodynamic balance somewhat in that the particle is lost once it reaches ignition temperatures. There are other techniques that can levitate an uncharged particle which are as yet untested for char oxidation studies.

The temperature traces of particles that ignited clearly show an induction time, or ignition time lag, as predicted by the solution of the time dependent equation for a heated particle. The effect of increasing the oxygen concentration is also seen in the increasing equilibrium temperature at sub-ignition conditions, though it was not quantifiable in this study. A simple isothermal sphere model was used with parameters obtained from the literature which adequately predicted the experimentally obtained time-temperature histories of igniting Spherocarb particles. A reasonable fit to the bituminous char data was achieved using rate parameters determined by Sahu et al. (1988b). These experiments provide the first examples in which the oxidation of char during ignition is rigorously modeled and compared with existing literature data. The electrodynamic balance can be used in ignition experiments to measure the apparent char oxidation rate parameters, and probe particle–to–particle variations in the apparent kinetics.

Acknowledgements

This research was supported by the U.S. Department of Energy University Coal Research Program under grant number DE-FG22-89PC89765.

References

Annamalai, K. and Durbetaki, P. (1977). *Comb. Flame.* 29: 193-208.

Arnold, S. and Folan, L. M. (1987). *Rev. Sci. Instrum.* 58:1732-1735.

Bandyopadhyay, S. and Bhaduri, D. (1972). *Comb. Flame.* 18:411-415.

Bar-Ziv, E., Jones, D. B., Spjut, R. E., Dudek, D. R. and Sarofim, A. F. (1989). *Comb. Flame.* 75:81-106.

Cassel, H. M. and Leibman, I. (1959). *Comb. and Flame.* 3:467-475.

Chen, M.-R., Fan, L.-S. and Essenhigh, R. H., *Proc. Twentieth Symp. (Int.) Comb.* 1513, (1984).

D'Amore, M., Dudek, D. R., Sarofim, A. F. and Longwell, J. P. (1988). *Powder Technol.* 56:129-134.

Davis, E. J. (1965). In *Surface and Colloid Sci.* (E. Matijevic, ed.). Plenum Press, New York. Vol. 14.

Davis, E. J., Buehler, M. F., Ward, T. L. (1990). *Rev. Sci. Instrum.* 61:1281-1288.

Dudek, D. R., Wright, D. A., Longwell, J. P., Sarofim, A. F. and Yeheskel, J. (1990). *Combust. Sci. and Tech.* 73:447-461.

Essenhigh, R. H., Misra, M. K. and Shaw, D. W. (1989). *Comb. and Flame.* 77:3-30.

Field, M. A., Gill, D. W., Morgan, B. B. and Hawksley, P. G. W. (1967). *Combustion of Pulverized Coal*, The British Coal Utilisation Research Association, Leatherhead.

Floess, J. K., J. P. Longwell and Sarofim, A. F. (1988). *Energy and Fuels.* 2: 18-26.

Greene, W. M., Spjut, R. E., Bar-Ziv, E., Longwell, J. P. and Sarofim, A. F. (1985). *Langmuir.* 1:361-365.

Gomez, C. O. and Vastola, F. J. (1985). *Fuel.* 64:558-563.

Howard, J. B. and Essenhigh, R. H. (1967). *Eleventh Symp. (Int.) Comb.*, The Combustion Institute, Pittsburgh, p.399-408.

Karcz, H., Kordylewski, W. and Rybak, W. (1980). *Fuel.* 59:799-802.

Levendis, Y. A., Sahu, R., Flagan, R. C. and Gavalas, G. R. (1989). *Fuel.* 68:849-855.

Liebman, I., Corry, J. and Perlee, H. E. (1972). *Comb. Sci. and Tech.* 5:21-30.

Monazam, E. R., Maloney, D. J. and Lawson, L. O. (1989). *Rev. Sci. Instrum.* 60: 3460-3465.

Nelson, L. S., Richardson N. L. and Prentice, J. L., *Rev. Sci. Instrum.* 39, 744 (1968).

Sahu, R., Levendis, Y. A., Flagan, R. C. and Gavalas, G. R. (1988a). *Fuel.* 67: 275-283.

Sahu, R., Northrop, P. S., Flagan, R. C. and Gavalas, G. R. (1988b). *Comb. Sci. Tech.* 60:215-230.

Seixas, J. P. S. and Essenhigh, R. H. (1986). *Comb. and Flame.* 66:215-218.

Sloane, C. S. and Elmoursi, A. A. (1989). *IEEE Trans. Ind. Appl.* 25:711-719.

Spjut, R. E., Sarofim, A. F. and Longwell, J. P. (1985). *Langmuir.* 1:355-360.

Thomas, G. R., Stevenson A. J. and Evans, D. G. (1973). *Comb. and Flame.* 21:133-136.

Tognotti, L., Malotti, A., Petarca, L. and Zanelli, S. (1985). *Comb. Sci. and Tech.* 44:15-28.

Ubhayakar, S. K. and Williams, F. A. (1976). *J. Electrochem. Soc.* 123, 747 (1976).

Waters, B. J., Squires, R. G., Laurendreau, N. M and Mitchell, R. E. (1988). *Comb. and Flame.* 74:91-106.

Wong, B. A. (1991). *The Oxidation of Individually Levitated Char Particles*, Ph.D. Thesis, California Institute of Technology.

Table 1

Parameters Used in Model

Parameter	Value	Source
Heat Capacity, C_p	$0.4\ \frac{cal}{g\ degK}$	Monazam et al., 1989
Thermal Conductivity, k	$k_0\left(\frac{T_p+T_g}{2T_0}\right)^{0.75}\ \frac{cal}{cm\ s\ degK}$	Field et al., 1967
Emissivity	0.8	Monazam et al., 1989
Activation Energy, E_a	$20\ \frac{kcal}{mole}$	Waters et al., 1988
Reaction order, n	0.5	Waters et al., 1988
Heat Release, Q_{eff}	$0.35\ Q_{CO_2} + 0.65\ Q_{CO}$ $(40.82\ kcal/mole)$	Waters et al., 1988
Particle Density	Fitted	
Laser Intensity	Fitted	
Pre–exponential, A	Fitted	
Activation Energy, E_a for Char	$17\ \frac{kcal}{mole}$	Sahu et al., 1988b
Pre–exponential, A for Char	Fitted	

Table 2

Spherocarb Experiments

Series	Size μm	Laser Intensity W/m^2	Density kg/m^3	A $kg/m^2s(KPa)^{.5}$	P_{O_2} %
1	100	3.13×10^6	1100	3.6	50
2	98	4.65×10^6	1200	4.2	13
3	75	4.11×10^6	1000	6.1	25
4	99	3.04×10^6	800	3.73	40
5	99	3.45×10^6	1100	5.0	35
6	105	3.46×10^6	1000	3.6	35
7	82	4.54×10^6	1000	3.6	25
8	79	3.85×10^6	1000	5.2	30
9	95	3.54×10^6	1100	4.0	25

Figure Captions

Figure 1. Rate of heat loss or gain for a 50 μm diameter particle at 900K (small-dashed lines), 1235K (solid lines) and 1400K (large-dashed lines). Physical parameters are from Field et al (1967). The lettered points are described in the text.

Figure 2. Curve showing ignition induction time for a 50 μm particle (solid line). The curves and the lettered points correspond to the same conditions as in figure 1.

Figure 3. Schematic of the electrodynamic balance electrodes, heating system, and position monitoring system.

Figure 4. Schematic of the optical pyrometer

Figure 5. Calibration Curve for the optical pyrometer

Figure 6. Temperature trace for a 198 μm diameter spherocarb particle. Experimental data are shown in open circles. a. Laser pulse in nitrogen gas. b. Laser pulse in 20% oxygen. c. Laser pulse in 40% oxygen.

Figure 7. Vertical position of the Spherocarb particle. a. Spherocarb pulsed in nitrogen. b. Spherocarb pulsed in 20% oxygen. c. Spherocarb pulsed in 40% oxygen.

Figure 8. Rate of heat generation and heat loss for a 198 μm diameter spherocarb particle. The solid line shows the heat gain in nitrogen. The dash-dotted line shows the heat gain in 20% oxygen. The dashed line shows the heat gain in 40% oxygen. The dash-dot-dot line shows the heat loss curve.

Figure 9. Temperature traces for a 300 μm diameter char particle produced from PSOC 1451 bituminous coal. Experimental data are shown in open circles. a. Laser pulse in nitrogen gas. b. Laser pulse in 10% oxygen. c. Laser pulse in 15% oxygen.

Figure 10. Vertical position of the bituminous char particle. a. Char pulsed in nitrogen. b. Char pulsed in 10% oxygen. c. Char pulsed in 15% oxygen.

Figure 1

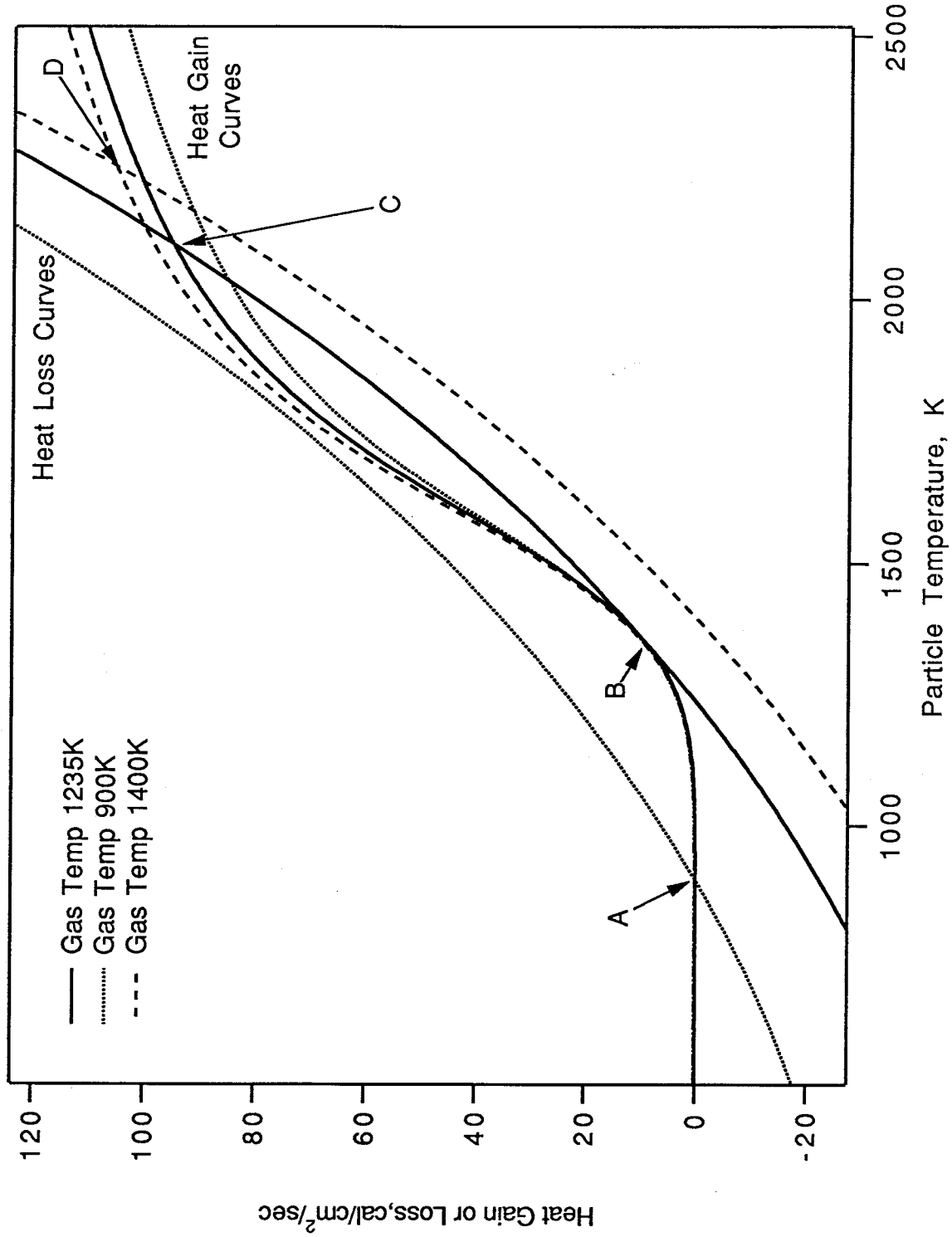
Heat Gain or Loss,cal/cm²/sec
120
100
80
60
40
20
0
-20
1000
1500
2000
2500
Particle Temperature, K
Heat Loss Curves
Heat Gain Curves
Gas Temp 1235K
Gas Temp 900K
Gas Temp 1400K
A
B
C
D

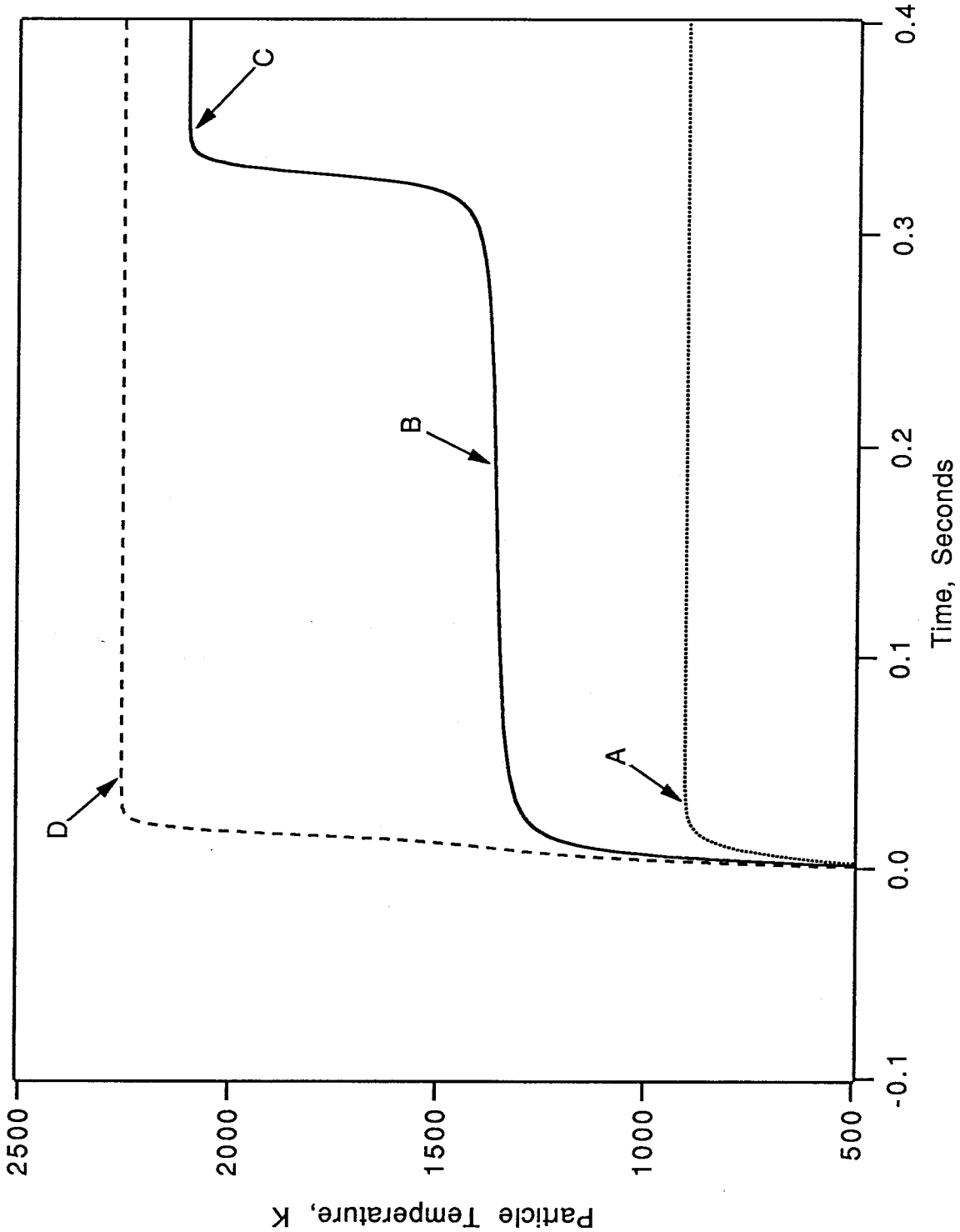
Particle Temperature, K
2500
2000
1500
1000
500
-0.1
0.0
0.1
0.2
0.3
0.4
Time, Seconds
A
B
C
D

Figure 2

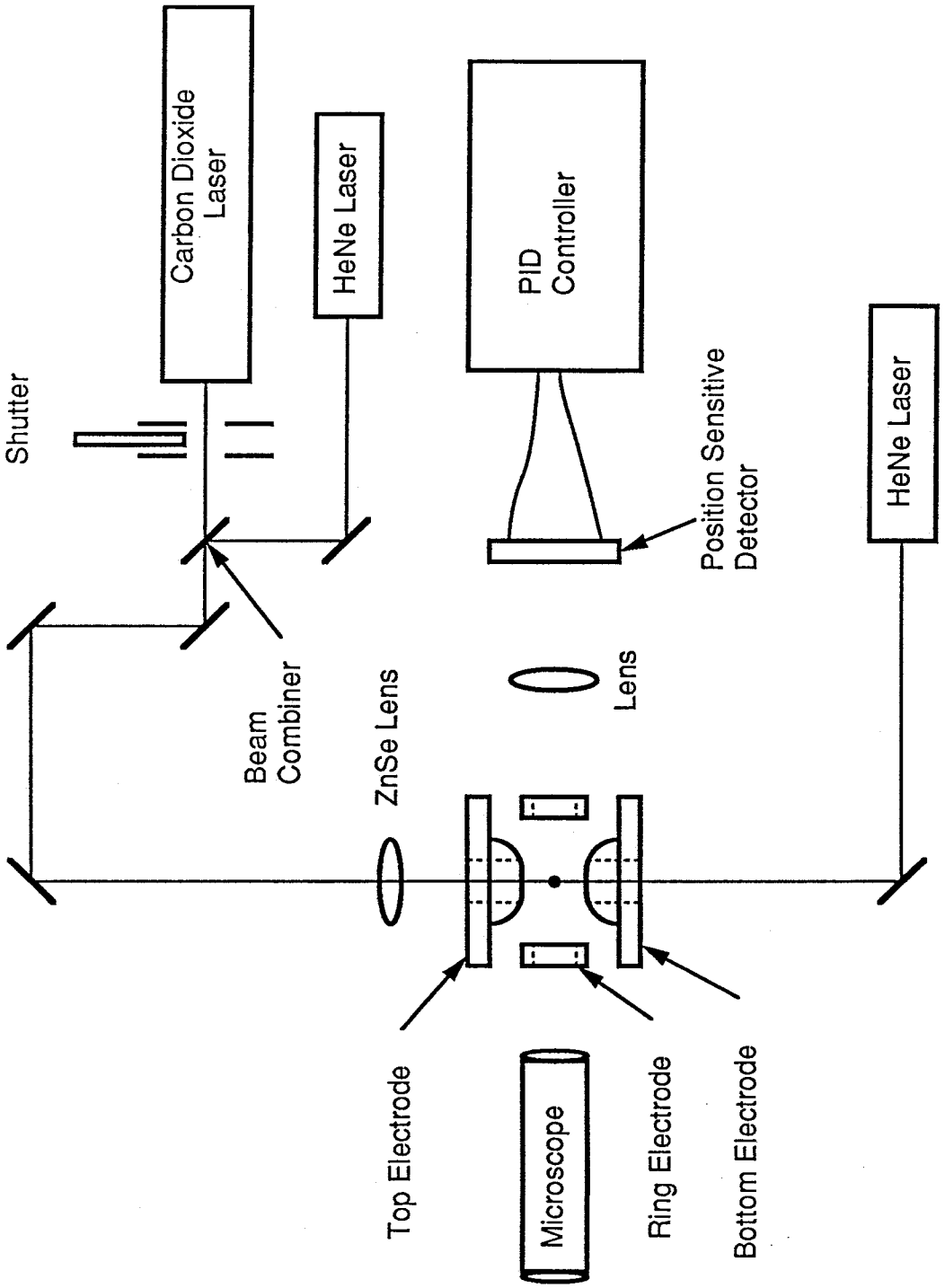

Figure 3. Schematic of the EDTGA

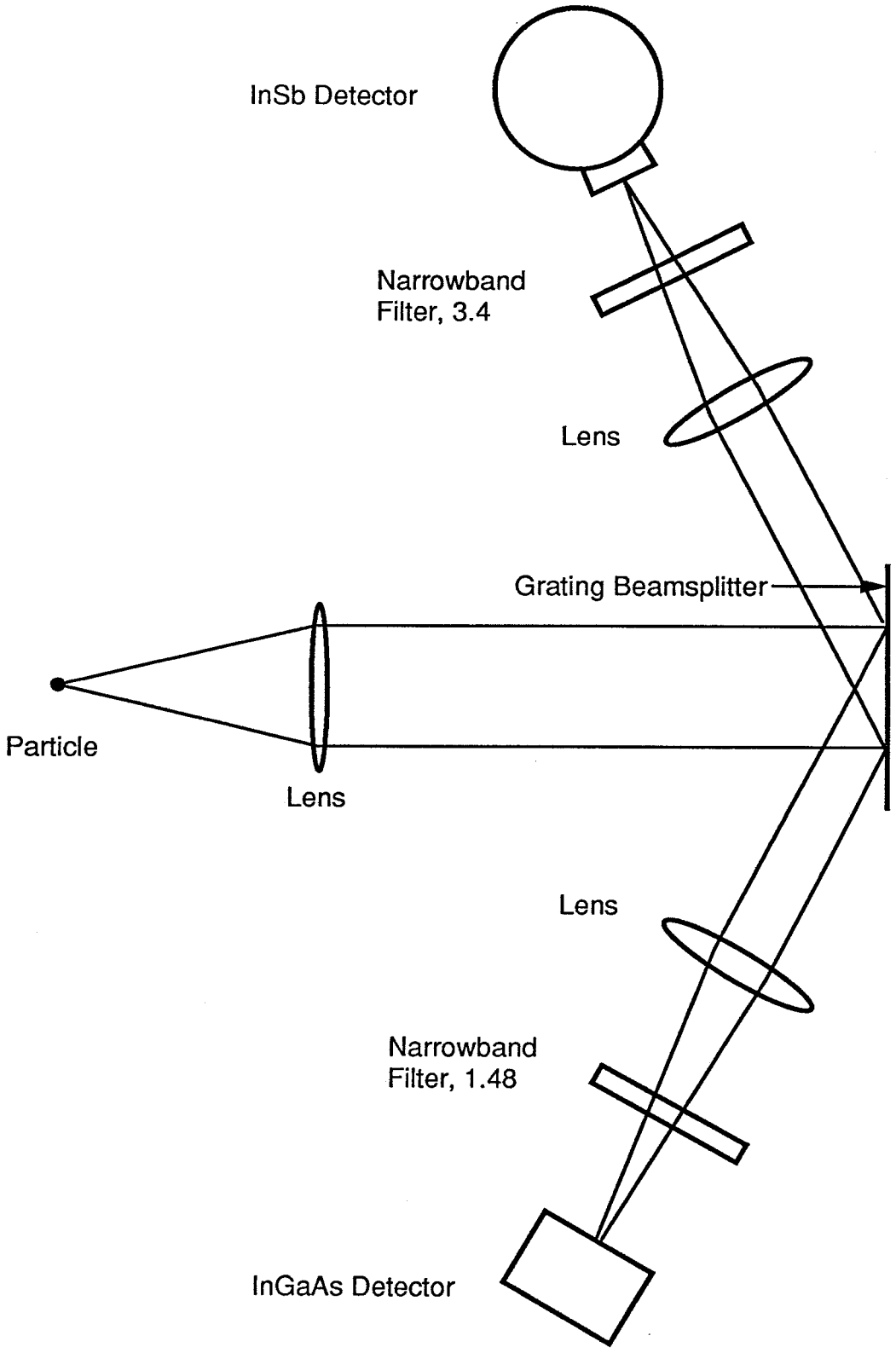

Figure 4. Pyrometer Schematic

Figure 5

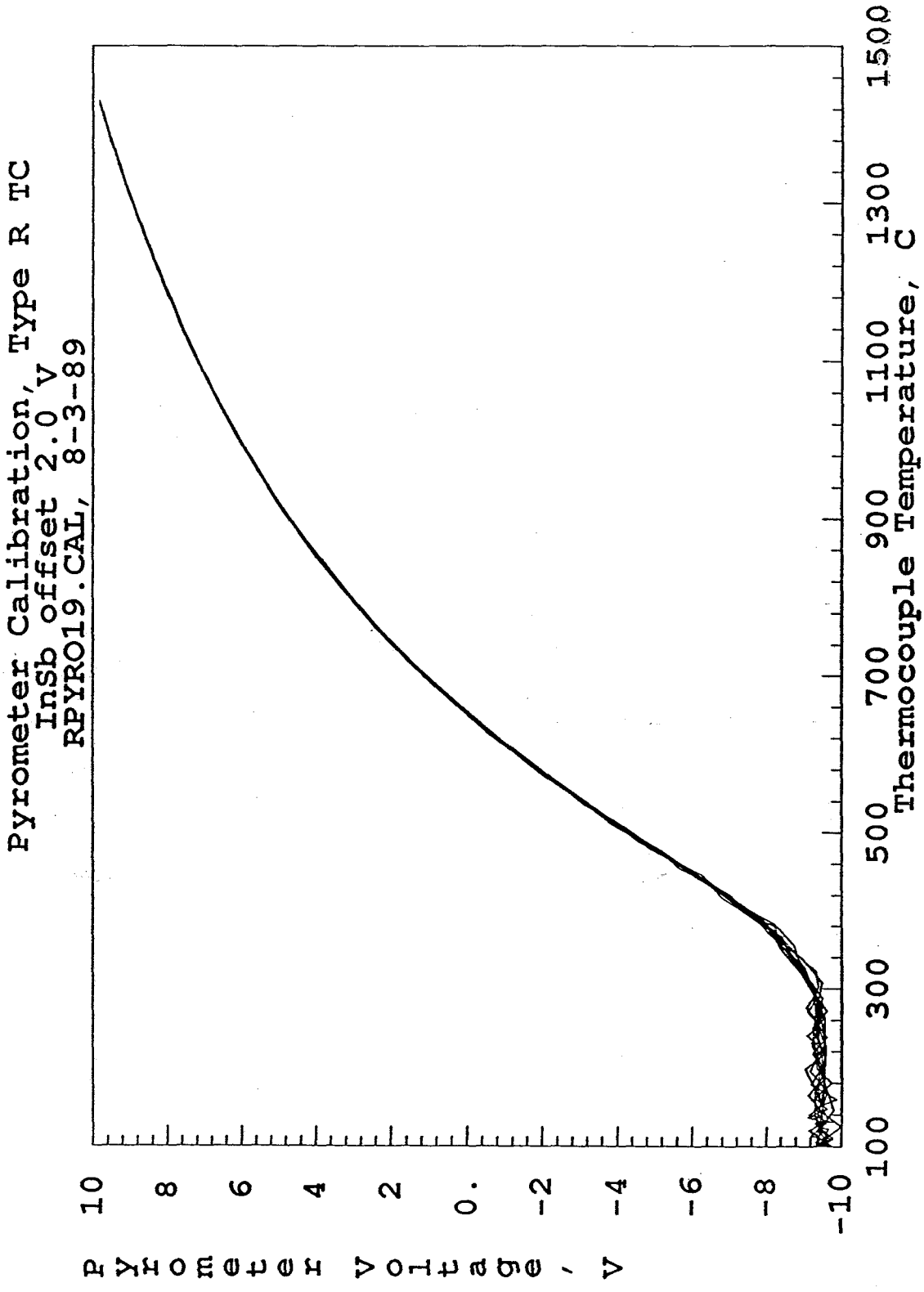
Pyrometer Calibration, Type R TC
InSb offset 2.0 V
RPYRO19.CAL, 8-3-89
Pyrometer Voltage, V
10
8
6
4
2
0.
-2
-4
-6
-8
-10
100
300
500
700
900
1100
1300
1500
Thermocouple Temperature, C

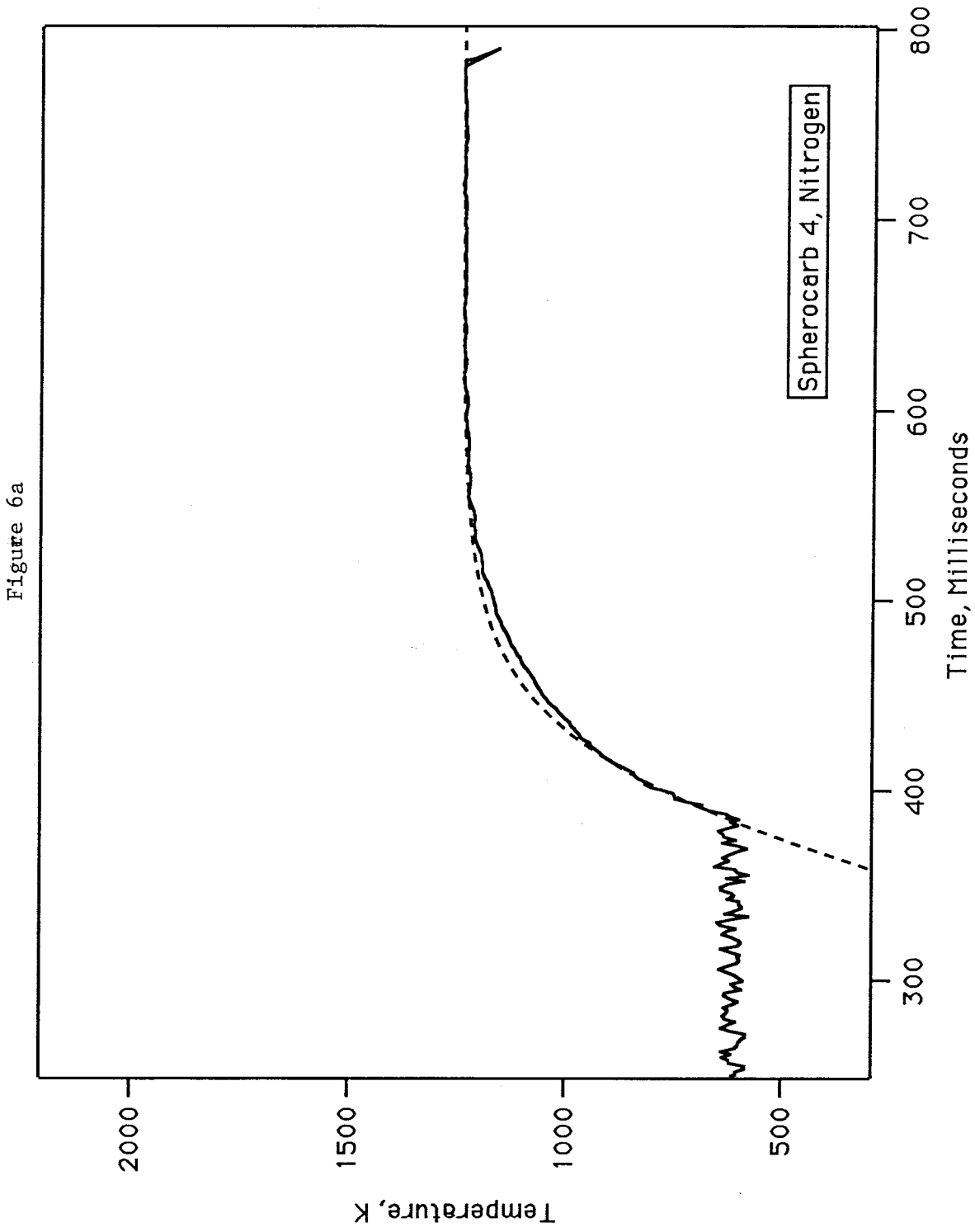
Temperature, K
2000
1500
1000
500
300
400
500
600
700
800
Time, Milliseconds
Spherocarb 4, Nitrogen

Figure 6a

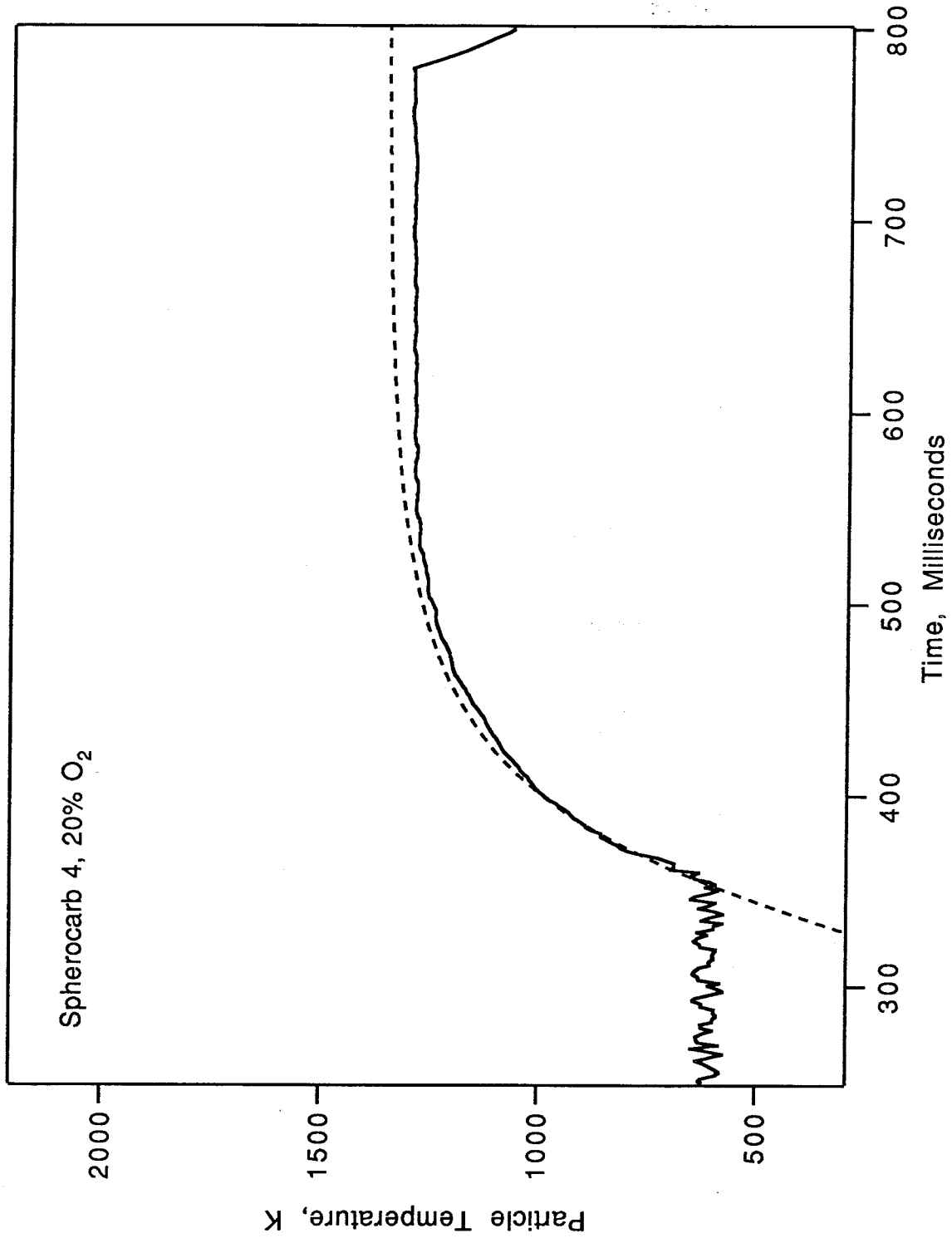
Spherocarb 4, 20% O_2
Particle Temperature, K
2000
1500
1000
500
300
400
500
600
700
800
Time, Milliseconds

Figure 6b

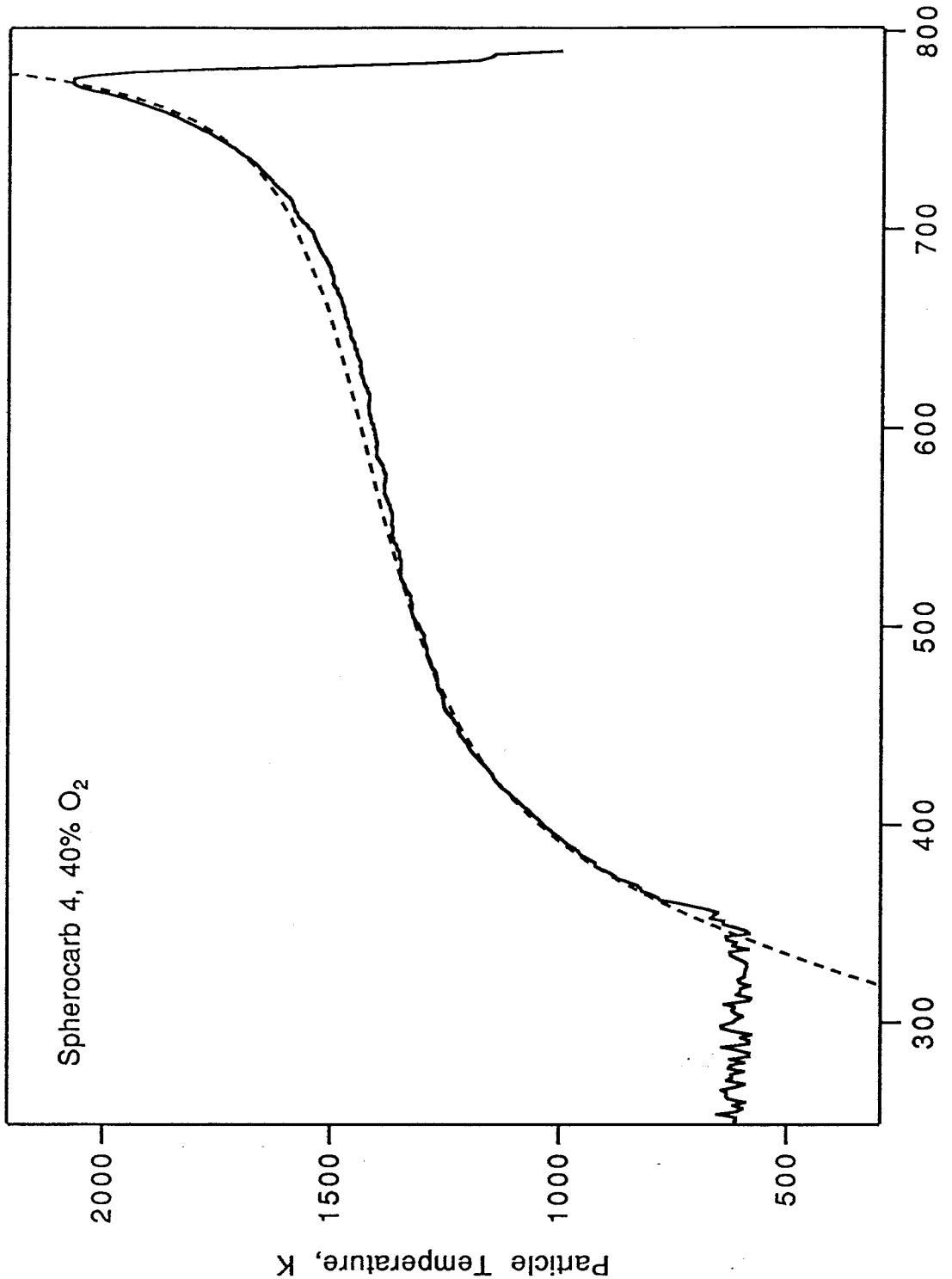
Spherocarb 4, 40% O_2
Particle Temperature, K
2000
1500
1000
500
300
400
500
600
700
800
Time, Milliseconds

Figure 6c

Figure 7a

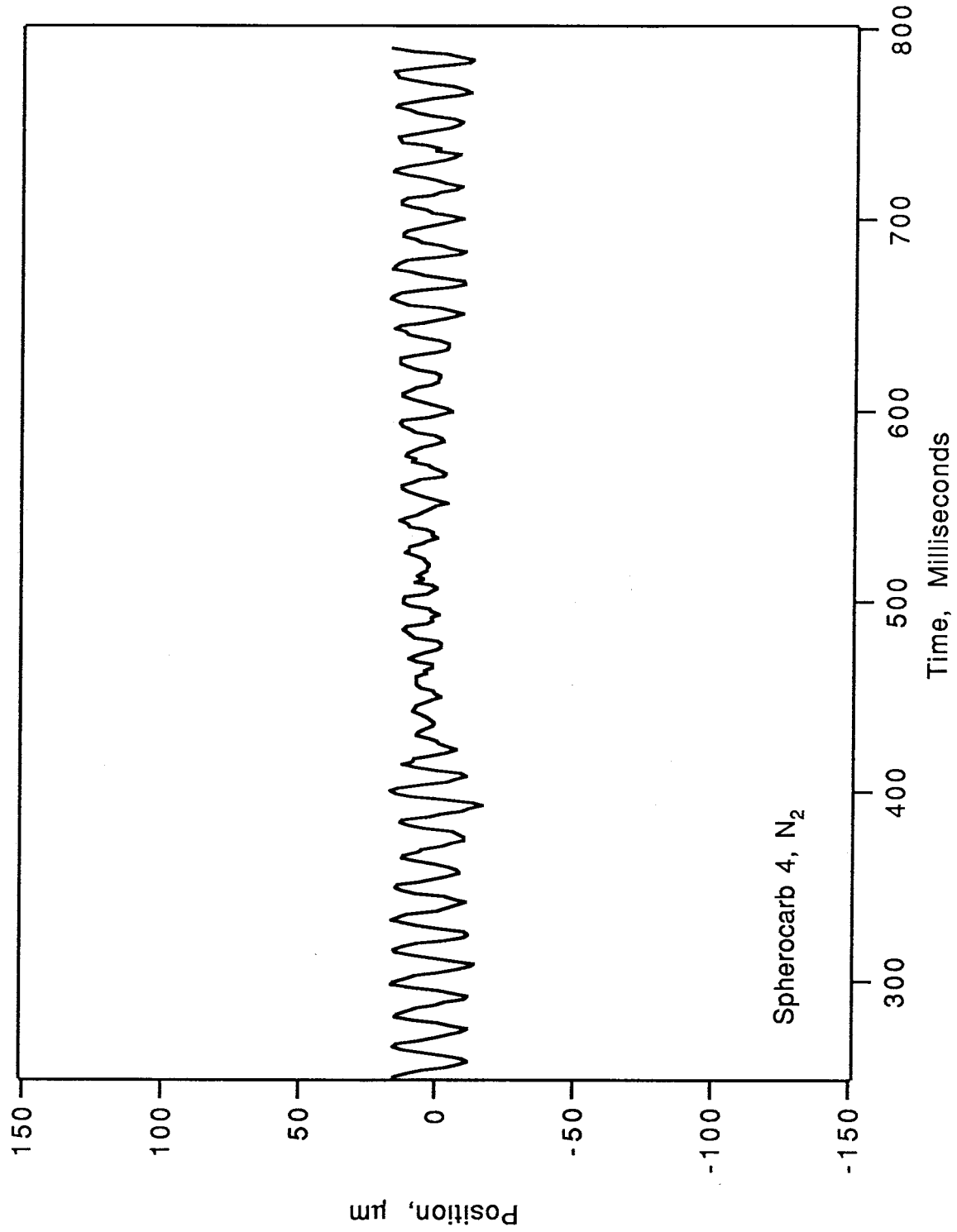
150
100
50
0
-50
-100
-150
Position, μm
300
400
500
600
700
800
Time, Milliseconds
Spherocarb 4, N_2

Figure 7b

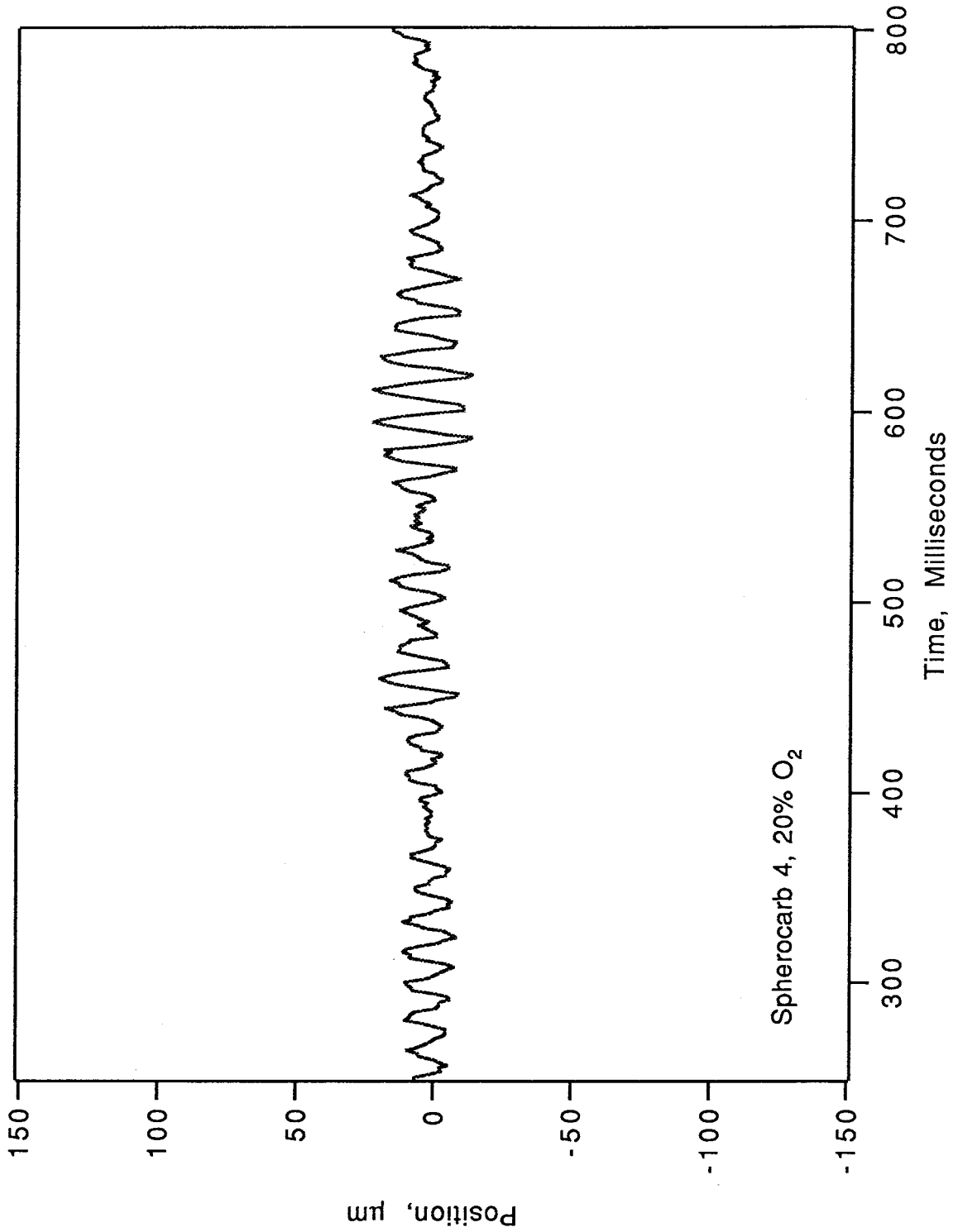
150
100
50
0
-50
-100
-150
Position, μm
300
400
500
600
700
800
Time, Milliseconds
Spherocarb 4, 20% O_2

Figure 7c

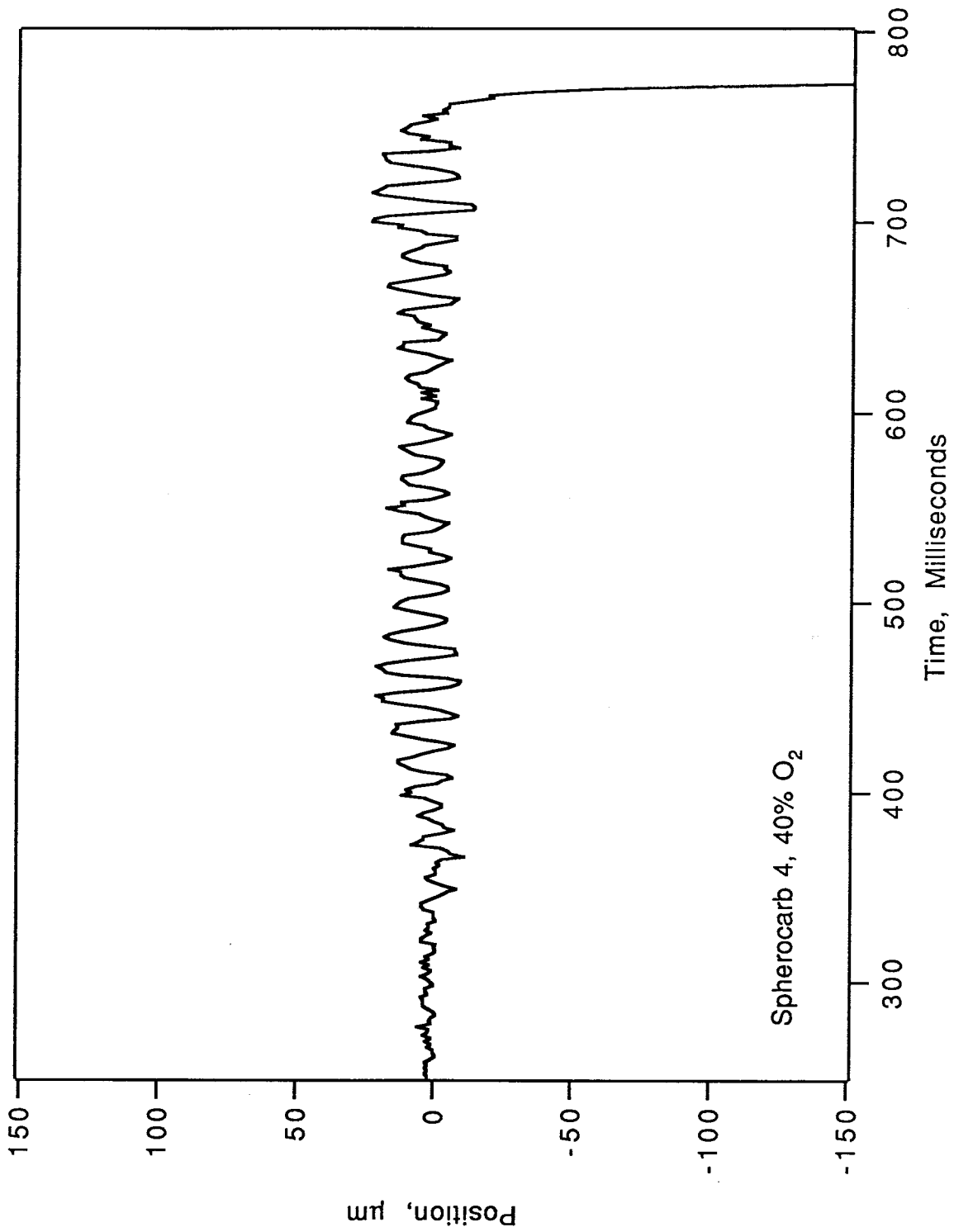
150
100
50
0
-50
-100
-150
Position, µm
300
400
500
600
700
800
Time, Milliseconds
Spherocarb 4, 40% O_2

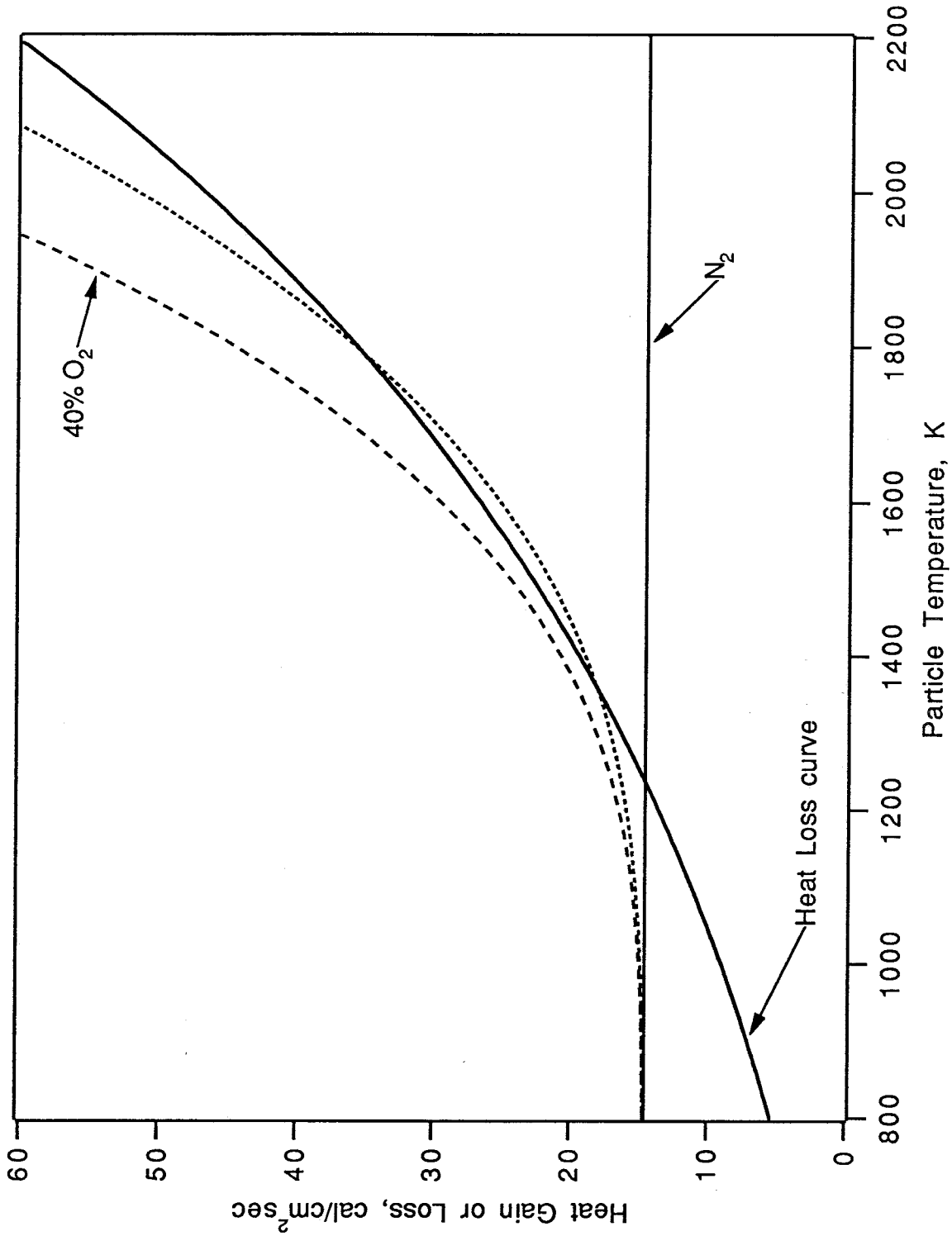
Heat Gain or Loss, cal/cm²sec
0
10
20
30
40
50
60
800
1000
1200
1400
1600
1800
2000
2200
Particle Temperature, K
40% O2
N2
Heat Loss curve

Figure 8

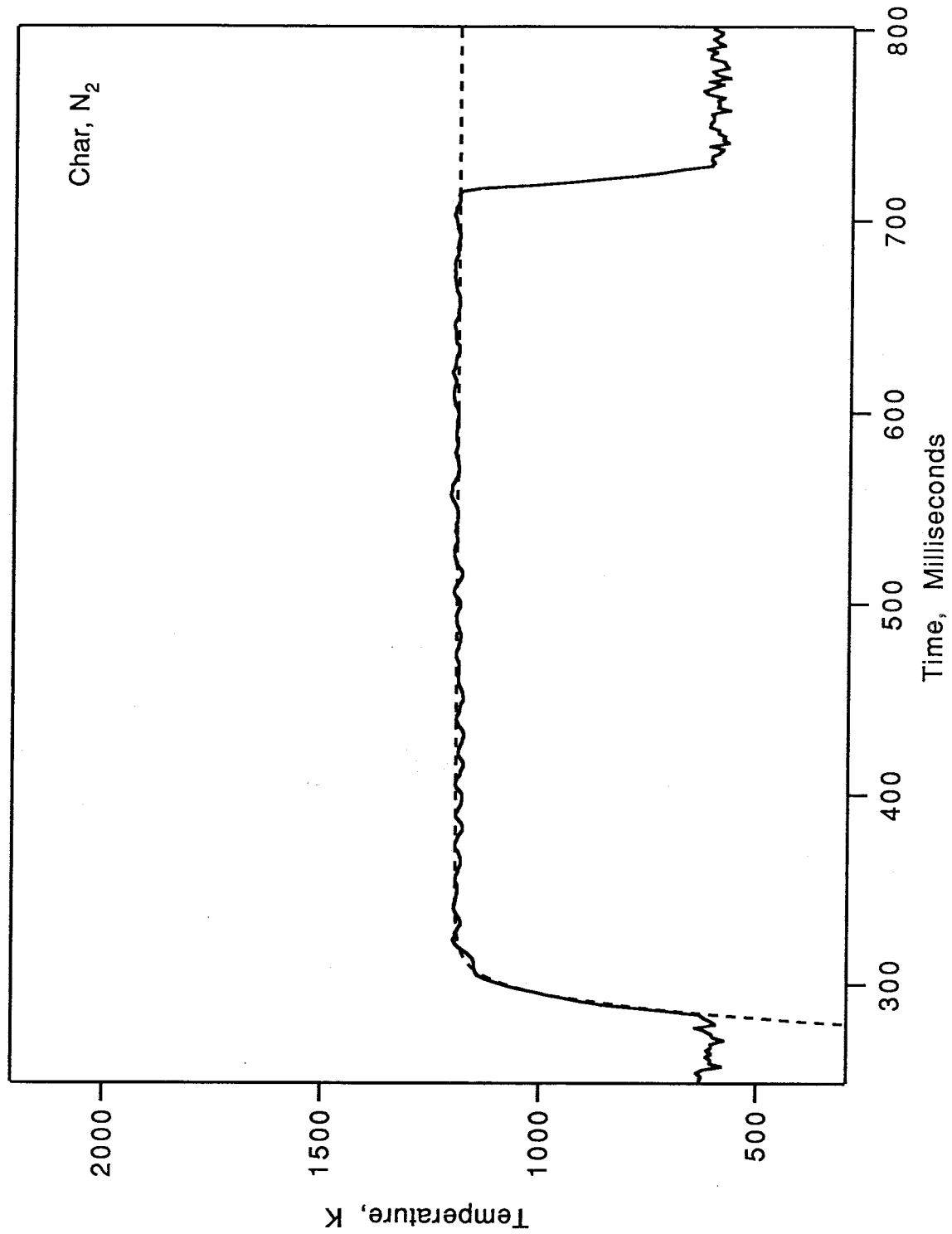
Char, N_2
Temperature, K
2000
1500
1000
500
300
400
500
600
700
800
Time, Milliseconds

Figure 9a

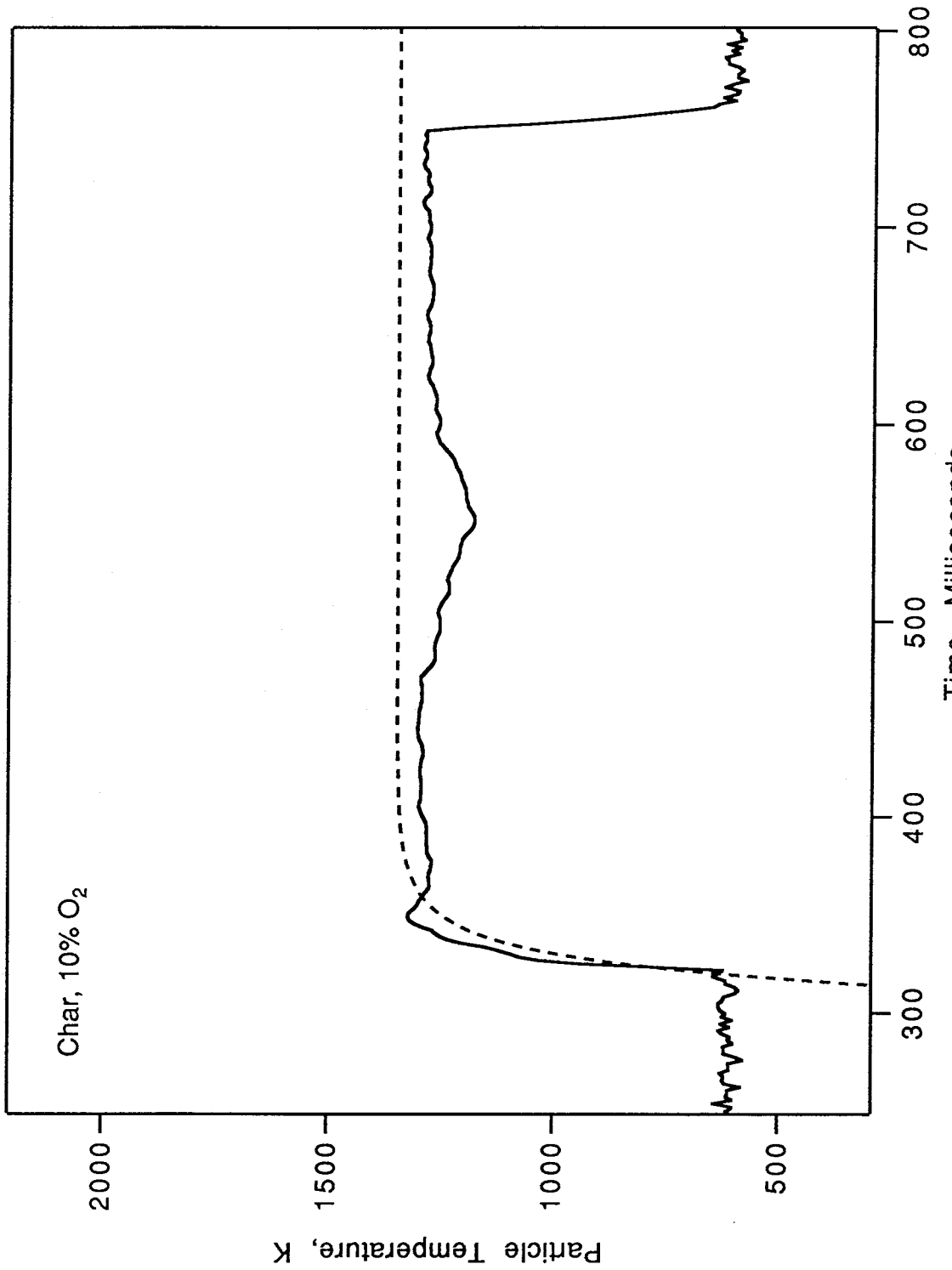
Char, 10% O_2
Particle Temperature, K
2000
1500
1000
500
300
400
500
600
700
800
Time, Milliseconds

Figure 9b

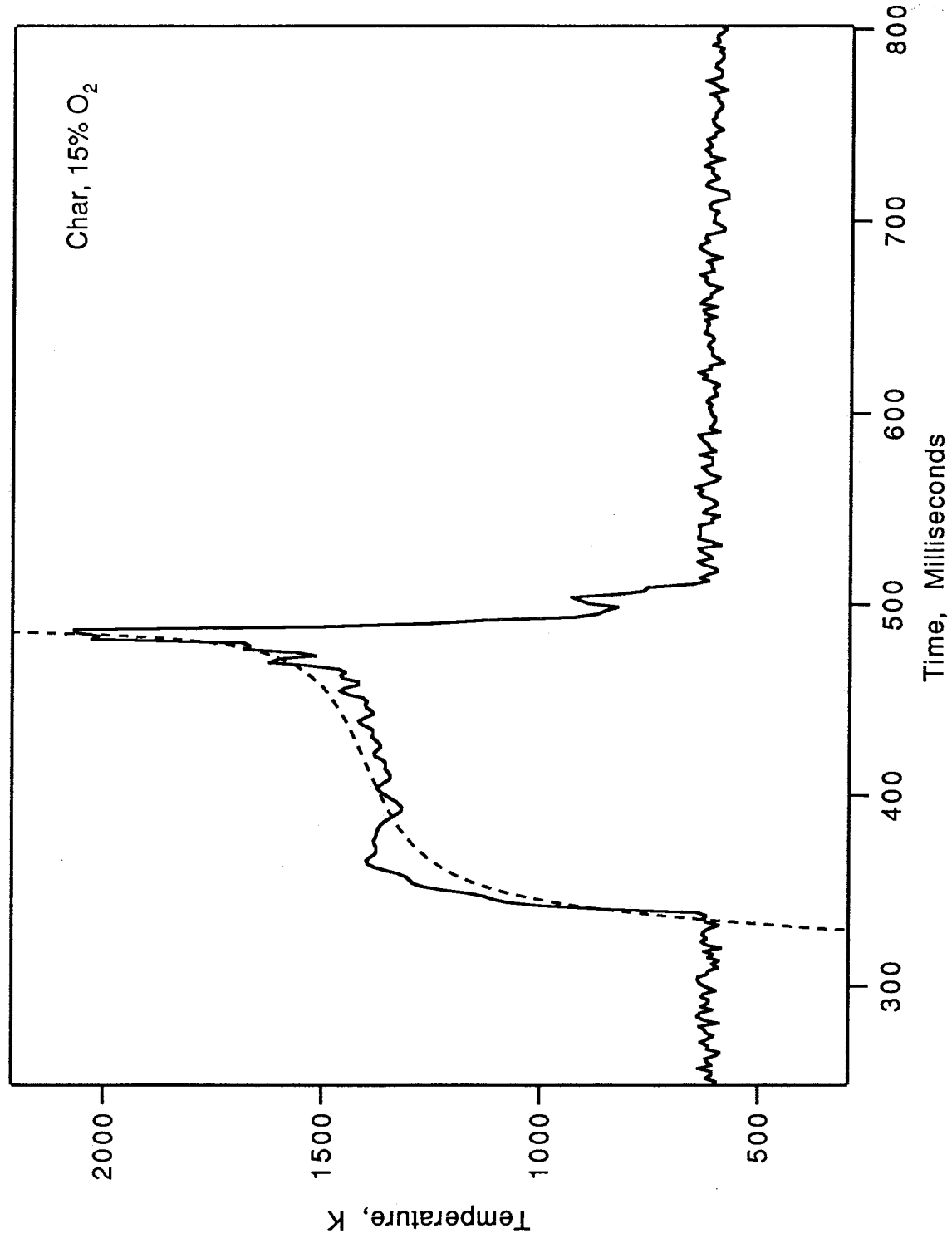
Char, 15% O_2
Temperature, K
2000
1500
1000
500
300
400
500
600
700
800
Time, Milliseconds

Figure 9c

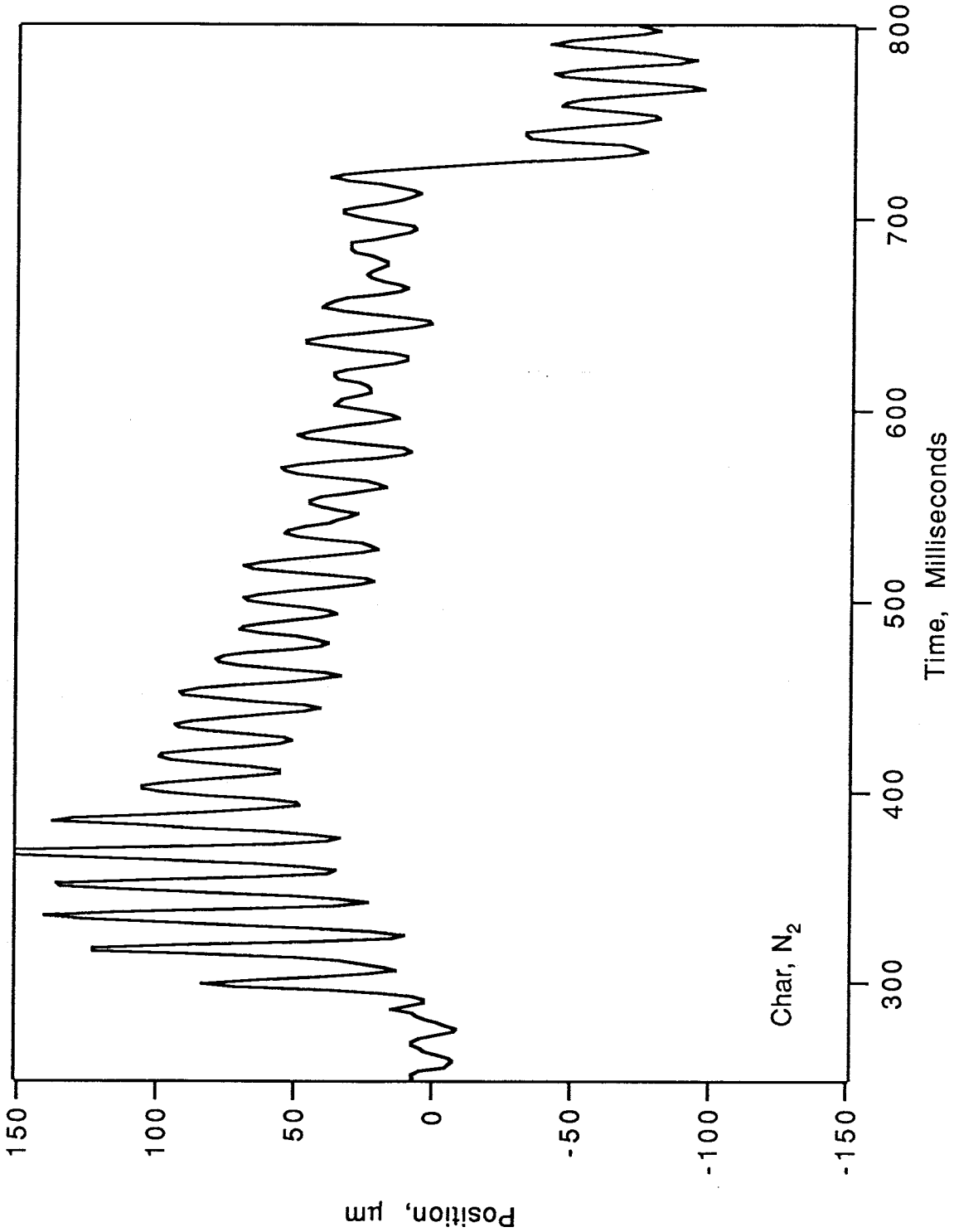
150
100
50
0
-50
-100
-150
Position, μm
300
400
500
600
700
800
Time, Milliseconds
Char, N_2

Figure 10a

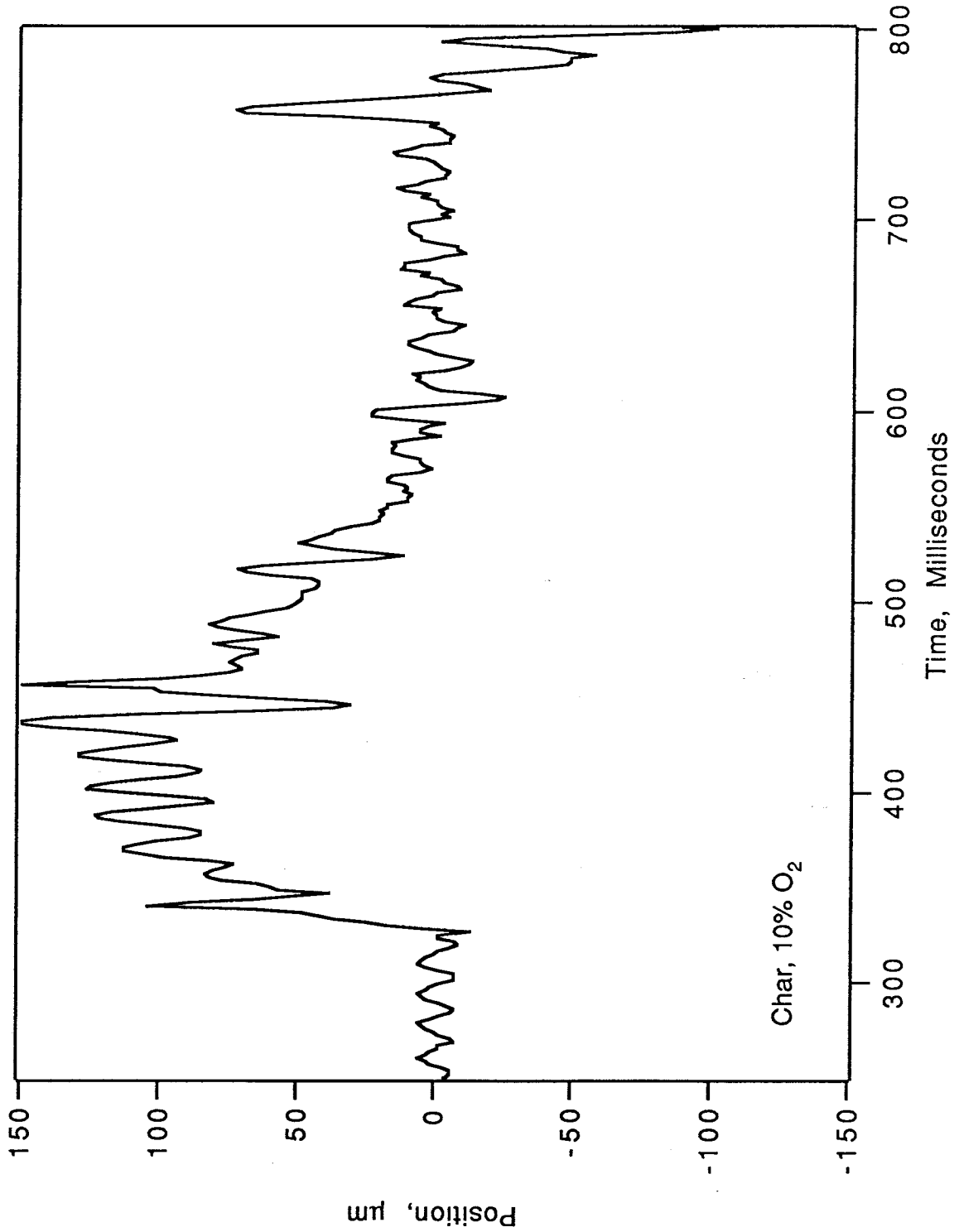
150
100
50
0
-50
-100
-150
Position, μm
300
400
500
600
700
800
Time, Milliseconds
Char, 10% O_2

Figure 10b

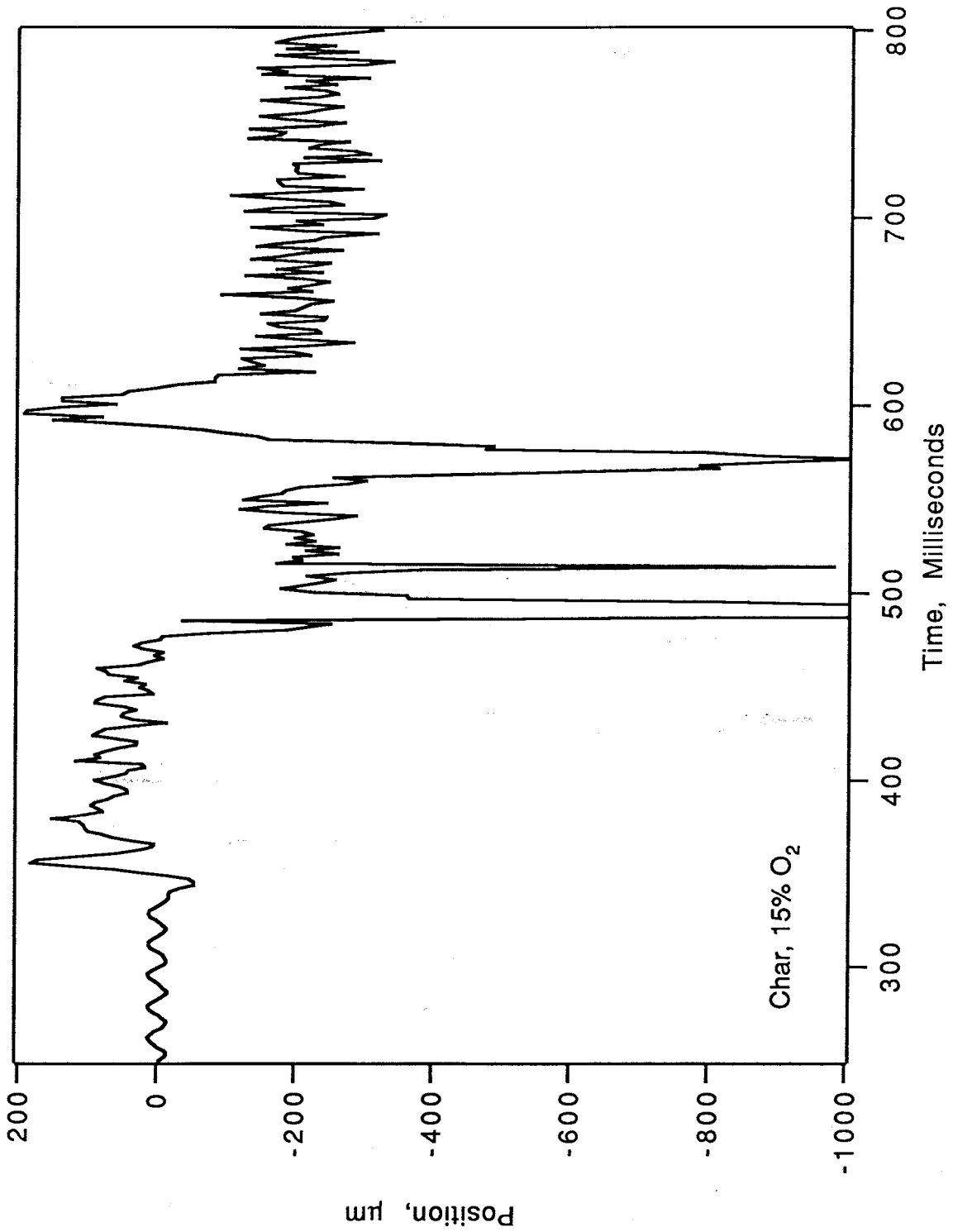
Position, μm
200
0
-200
-400
-600
-800
-1000
300
400
500
600
700
800
Time, Milliseconds
Char, 15% O_2

Figure 10c

Chapter 3

The Effect of Char formation Temperature on the Densification of a Bituminous Coal Char during Gasification

Introduction

The combustion of pulverized coal occurs in two steps: First, as the coal particle heats up, devolatilization occurs. Moisture and low vapor pressure organic components are first driven off, and thermal decomposition of some of the carbonaceous structure occurs (Field, 1967; Smoot and Smith, 1985) resulting in tar evaporation. The residual material, termed char, is enriched in carbon and mineral components. The char reacts with oxygen and burns out until only the mineral matter remains. Depending on the particle temperature, char oxidation occurs in one of three regimes. The first, at low temperatures, is the kinetically limited regime (regime I). The reaction rate is controlled by the kinetics of the surface reaction of carbon with oxygen. The oxygen can diffuse through the pores of the particle faster than it reacts, so the oxygen concentration is uniform throughout the porous particle. At higher particle temperatures, the reaction rate becomes so fast that the oxidation is controlled by the diffusion of oxygen through the porous particle as well as by the surface reaction. In this diffusion limited regime (regime II), oxygen from the bulk gas penetrates only partially through the particle, and the oxygen concentration goes to zero at the center of the particle (Walker, et al., 1959). In the third regime (regime III), boundary layer diffusion controls the oxidation rate. The reaction of carbon with oxygen is so fast that the oxygen concentration is essentially zero at the surface of the

particle, and the rate is controlled by the diffusion of oxygen through the boundary layer surrounding the char particle (Smoot and Smith, 1985).

If we define χ as the conversion, or the ratio of mass of carbon reacted to the initial carbon mass, m_0

$$\chi = \frac{m_0 - m}{m_0} \tag{1}$$

then

$$(1 + \frac{m_a}{m_0} - \chi) = \frac{\rho d^3}{\rho_0 d_0^3} \tag{2}$$

where m_a is the mass of the ash in the particle. Equation 2 can be divided into two equations

$$d = d_0 \, (1 + \frac{m_a}{m_0} - \chi)^{\alpha} \tag{3}$$

$$\rho = \rho_0 \, (1 + \frac{m_a}{m_0} - \chi)^{\beta} \tag{4}$$

where $3\alpha + \beta = 1$ (Smith, 1982). In the kinetically limited regime, carbon loss occurs throughout the particle, provided that the temperature of the particle is uniform, and oxygen is able to penetrate through to all of the inside surface area, i.e., there are no closed pores. In regime I, the diameter stays essentially constant and $\alpha = 0$, while the density decreases linearly and $\beta = 1$, until the conversion is nearly complete. In Figure 1, showing the relative volume, $(d/d_0)^3$ as a function of conversion, the top line corresponds to regime I. If a particle burns in Regime III, carbon loss will occur only near the external surface of the particle. The density will remain constant and the diameter of the particle will decrease, so $\alpha = 1/3$ and $\beta = 0$ (constant density line in Figure 1). The area in between, then corresponds to Regime II and the transitions between I and II and between II and III. In theory, then, following the diameter or density of a particle as a function

of conversion should provide information about the regime of reaction. Note that the calculations and data presented in Figure 1 describe an ash–free material, i.e., Spherocarb. For a mineral–bearing material, the volume would decrease to that of the mineral residue at 100% conversion.

Smith (1971) observed that for a semi-anthracite in the temperature range 1400-2200K, the particles decreased in size and density as they reacted. This was also observed by Waters et al. (1988) for Spherocarb particles in the same temperature range. Smith cited the fact that the particles decreased in size and density as an indication that the particles were burning between regimes I and II. Smith and Waters calculated $\alpha = 0.25$ and $\beta = 0.25$. Neither Smith (1971) nor Waters et al. (1988) observed any influence of temperature on the particle size or density change because of the experimental scatter in the data.

Hurt et al. (1988), observed that some chars, notably Spherocarb and sucrose char, did not gasify at a constant diameter in regime I (temperature less than 873K), as expected, but instead "shrank." At 60% conversion, the spherocarb particle diameter was about 81 to 87% of the initial diameter. For a sucrose char, the particle shrank to about 88 to 92% of the initial diameter, at 60% conversion. The particle density was not measured directly but, based on the change in size with mass loss, the density did not decrease as much as predicted, hence, the particles of both materials were said to have "densified." Other chars (Montana Lignite, Pittsburgh #8 bituminous) did not shrink, but maintained their initial diameter through 60% conversion.

The Spherocarb data of Waters et al. (1988) is shown with the Spherocarb data of Hurt et al. (1988), in Figure 1. The best fit line for Water's data, with $\alpha = 0.25$ is compared with the best fit line for Hurt's data, with $\alpha = 0.177$

(calculated by the authors). The line shifts towards the constant diameter line at higher temperatures, as expected. The observed shrinkage either means that the coal structure changed, as they postulated, or the particles did not burn in the kinetically limited regime. Since Hurt et al. observed, at the same low temperatures as the shrinking chars, that some chars did oxidize without shrinkage, the former possibility is the more likely. They also observed that external features, such as pore diameters, decreased in size at the same rate as the particle diameter (Hurt et al., 1988). If the reaction was occurring without shrinking, the pore diameters might be expected to enlarge as the particle reacted. In a later paper, Hurt et al. (1991) presented evidence that oxygen penetrates completely into the microporous regions of the spherocarb at temperatures of 673 to 873K. The reactivity of the Spherocarb carbon was found to be independent of particle size with the calculated effectiveness factor equal to unity, indicating that all the pore surface participated in the reaction. The adsorption equilibrium time in BET gas adsorption measurements of the char surface area was much shorter for Spherocarb than for sucrose char, a completely microporous char. From this evidence, Hurt et al. (1991) concluded that the oxygen penetrated completely through the micropores of the Spherocarb and reacted there under kinetically limited conditions.

Hurt observed shrinkage and densification in some but not all chars. Presumably, then, structural changes that a char may undergo during oxidation depend on the initial coal or carbon structure. Some coals, particularly bituminous coals, appear to be quite "plastic" and upon devolatilization, may swell to several times their original size (Field et al., 1967). The resulting chars may have very large macropores, and become cenospheric. It might seem, then, that chars made from such swelling coals would be prone to structural changes

during subsequent oxidation. This study was undertaken to determine if a swelling coal char from the bituminous coal PSOC 1451 does indeed densify, and if so, the effect of char formation temperature on the densification phenomenon.

Experimental

The particles used in this study were Spherocarb and char made from a high volatile bituminous coa (Pittsburgh seam – PSOC 1451). Spherocarb is a commercially available carbon material (sold as Carbosphere by Alltech Associates, Inc.). It consists of spherical particles of high purity carbon with a high specific surface area (nominally 1000 m^2/g). Spherocarb has networks of both micro– and macropores with 0.39 cm^3/g in micropores, and a porosity of 0.33 in pores > 200 Å (Floess et al., 1988).

Coal char particles were made from PSOC 1451 bituminous coal by Sahu et al. (1988). Briefly, the chars were made as follows: PSOC 1451 coal was ground and sieved. Coal particles in the 104 to 125μm fraction were entrained in a stream of nitrogen and passed through a drop tube furnace to a temperature of 1200 or 1600K for two seconds. The collected particles were washed in tetrahydrofuran and resieved. Chars in the 125 to 175μm, 175 to 208μm and 208 to 295μm size ranges were selected for study.

Table 1 lists measurements by Sahu et al. (1988) of the apparent density, σ_A, total porosity, ε_A, porosity of pores less than 64 Å, and pore volume and pore surface area based on mercury porosimetry for PSOC 1451 coal and chars. The apparent density decreases as char formation temperature increases, as does the total porosity. Only the 1600K char shows an appreciable microporosity, i.e., 19%. The pore volume and surface area increase as the coal is converted to char,

however, there are only slight differences between chars. According to Sahu et al., chars formed at lower temperatures developed bimodal pore size distributions, while high temperature chars developed trimodal pore size distributions. The 1200K char showed a bimodal distribution of pore volume and pore area with significant volume in the macropore region and significant area in the micropore region. The 1600K char contained similar micro- and macroporosity, but, additionally, showed significant area and volume in the so-called transition pore region, around a pore diameter of 500 Å (Sahu et al., 1988). For the 127 to 175μm fraction of the 1600K char, the total porosity was 47%, while the pore volume fraction contained in pores smaller than 64Å was 19%. The total porosity of 1200K char was 33%, with no significant microporosity. The physical properties listed for the chars are average values for the entire size range. As we chose to work with the larger char particles, it is expected that the macroporosity for these particles are even larger than that listed in the table. The large chars, particularly the 208 to 295μm diameter particles, were cenospheres.

The use of the electrodynamic balance for studying char oxidation has been described elsewhere by Spjut et al., (1985), Hurt et al., (1988) and Bar-Ziv et al., (1989). A brief description of the system used in this study is presented here. The electrodynamic balance consists of two endcap electrodes with a DC voltage across the electrodes. A charged particle is suspended in the electric field against gravity. A ring at midplane between the endcap electrodes is charged with an AC voltage. If the particle deviates in any direction from the center of the cell, the particle is subject to a time-averaged force from the AC field that pushes the particle back toward the center (Davis, 1987).

A microscope with a total magnification of 15x was used to view the

particle. A 10x eyepiece micrometer (American Optical Co.) was used to measure the size of the particle in the horizontal and vertical directions. The suspended particles were videotaped using a catadioptric microscope (Questar QM-1) and a video camera (COHU, Inc., model 4810). The output from the video camera was shown on a monitor (Electrohome, EVM) and recorded by a videotape recorder (Panasonic AG-1830). Still photographs were obtained by photographing the monitor, or by using an adapter coupled to a standard 35mm SLR camera that fit over the viewing microscope and a standard 15x eyepiece.

The particle suspended in the EDB was heated with the radiation from a 20 Watt carbon dioxide laser emitting at 10.6μm. The beam was split and directed by mirrors into the chamber vertically to heat the particle from top and bottom. The intensity of the beam intercepted by the particle was controlled by ZnSe lenses and by moving the focal point closer or farther from the particle.

The temperature of the particle was measured using a two-color optical pyrometer. Radiation emitted from the heated particle is collimated by a CaF_2 lens and split by a grating beam splitter. One arm of the split beam was focused by a CaF_2 lens through a 3.4 $\pm$ 0.0685 μm interference filter onto a liquid nitrogen cooled InSb detector. The other arm was focused through a $1.5 \pm .0037$ μm interference filter onto a thermoelectrically cooled InGaAs detector. The outputs from the detectors was sent to a log–ratio amplifier (Analog Devices 757). The output from the log–ratio amplifier was monitored on an oscilloscope and sent to a data acquisition system.

A typical experimented started by trapping a single particle in the electrodynamic balance. The size of the particle was measured in the horizontal and vertical directions using the eyepiece micrometer. Photographs were taken

through the viewing microscope. The CO_2 laser was allowed to stabilize with an external shutter closed. Particle heating was then initiated by opening the shutter. The pyrometer signal was monitored on the oscilloscope and recorded by the data acquisition system. The particle position was balanced manually. The heating pulse was ended by closing the external shutter. Photographs were again taken to record any changes in particle size and shape. In many cases, after heating, the particle was rotating about a vertical axis. If the particle was very irregularly shaped, photographs were attempted when the particle rotated through its original position, if that could be determined. Particle sizing was repeated, at the same orientation, if possible.

Results

The Spherocarb and char particles were heated at temperatures up to 1000K. Figures 2 and 3 show the temperature traces of a Spherocarb and a 1600K char heated in air. The particle temperature could be maintained only to within ± 50K. Irregular particle shape, strong photophoretic forces, and long term fluctuations in the intensity of the laser contributed to the temperature fluctuations. The primary focus of this paper is on the structural rearrangements of the char during kinetically limited oxidation. As long as the peak temperature experienced did not take the particle out of Regime I oxidation, the fluctuations should not affect the basic results.

The effectiveness factor was calculated for the Spherocarb and char particles at 1000K to verify that the oxidation reaction was occurring in the kinetically limited regime. The classical calculation of the Thiele modulus and effectiveness factor (Smith, 1970) were carried out using the effective diffusivity

reported by Hurt et al. (1991) and Arrhenius rate parameters for the intrinsic rate coefficient reported by Floess et al. (1988). A Thiele modulus of 0.15 at 1000K was calculated, which gives an effectiveness factor of unity. The method discussed by Smith (1978) was used to calculate the effectiveness factor for the bituminous char particles. Based on the measured reaction rates and the effective diffusivities reported by Sahu et al. (1988), the effectiveness factors for all the char particles studied were also unity at 1000K.

Photographs of the backlit particles showing their silhouettes are shown next. Figures 4a and 4b show a Spherocarb particle, before and after heating for 10 minutes in nitrogen. The particle has clearly retained its size and general surface features. Another Spherocarb particle before heating in air is shown in Figure 4c. The same particle, after 62% conversion is shown in Figure 4d. Note that the top and bottom of the particle are flattened, at the locations of the incident laser beams where the temperature was higher and the oxidation faster. The horizontal diameter is reduced from 196 μm to 175 μm, and is indicative of the shrinking of Spherocarb.

Figures 5a and 5b show PSOC 1451 coal char made at 1200K before and after 10 minutes heating in nitrogen. This particle clearly retains its size, shape and overall features. Figure 5c shows a photograph of a 1200K char, before heating in air, while Figure 5d shows the same char, at 48% conversion. The diameter decreased from 230 μm to 200 μm, clearly showing some shrinkage.

Figures 6a and 6b show PSOC 1451 coal char made at 1600 K before and after 11 minutes heating in nitrogen. Again, there is no change in the size or appearance of the particle after heating in nitrogen. Figure 6c shows a photograph of a 1600K char, before heating, and Figure 6d shows the same char,

at 56% conversion in air. The vertical dimension remains approximately the same at 222 μm, and the horizontal dimension also remains approximately the same at 160 μm. Note also, that the particle becomes lacy and translucent. As the cenospheric chars oxidize, the thin walls become more transparent.

The experiments in nitrogen show that the shrinkage of the particles is not due simply to heating, but in some way, is related to reaction with oxygen. When the char is heated in oxygen, some particles shrink, others do not. The relative volume as a function of conversion of Spherocarb is plotted in Figure 7. Each symbol represents a different Spherocarb particle. The dotted lines connect data from experiments on one particle. The particle volume was estimated by assuming that it was an oblate spheroid with volume $\frac{4}{3}\pi a^2 b$ where a is the major axis and b is the minor axis. The relative volume and conversion for Spherocarb particles is listed in Table 2. The relative volumes determined in the present experiment appear to lie somewhat lower than the measurements of Hurt et al. (1988) and approach the range of measurements of Smith (1971) and Waters et al. (1988). As noted above, a comparison of the data of Hurt et al. with Smith and Waters et al. suggest that the shrinkage increases with increasing temperature. The slightly higher temperatures of the present experiments may account for the differences with the observations of Hurt et al. (1988), but experimental differences cannot be ruled out. Unfortunately, the uncertainties in each data set preclude quantitative determination of this temperature dependence within each set of measurements.

Figure 8 shows the relative volume versus conversion for the bituminous char. The points for the 1200K char (the open squares) are scattered, but generally show significant shrinkage, roughly along the same line as the data of

Hurt et al. (1988) for Spherocarb. The points for the 1600K char (solid circles) mostly lie very close to the constant density line along the top of the graph. In cases where the particles were irregularly shaped, the size was measured from the extreme points in the vertical or horizontal directions. Volumes were calculated assuming that the particles could be modeled as oblate or prolate spheroids. Table 3 lists the relative volumes and conversions for the char particles.

Discussion and Conclusions

The reasons for the observed shrinkage or densification of some chars are as yet unknown. It has been shown that the particles are reacting in the kinetically limited regime and not the diffusion limited regime. The 1200K and the 1600K char both contained macropores, but only the 1600K char contained significant microporosity. Hence, it might be expected that the 1600K char show some diffusion limitations, but this is not the case. The larger coal char particles that were used in this experiment were quite cenospheric in nature, and should be even more macroporous than the average values listed in Table 1. Smith (1982) indicated that a cenosphere should burn at constant diameter and decreasing density, even if the reactions were limited to the outer surface. Thus, it seems unlikely that oxygen diffusion limitations would be a cause of shrinkage of the cenospheric 1200K but not the cenospheric 1600K char. Clearly then, the 1200K char is shrinking as it is reacting, while the 1600K char is reacting at constant diameter.

If diffusion limitations can be ruled out, then structural changes in the carbon must be occurring. Hurt et al. (1988) speculated that as the char loses carbon, atomic rearrangements causes the loss of pore volume in the fine pores.

These atomic rearrangements lead to a graphitization accompanied by an increase in the density. Sahu et al. (1988) also speculated that charring at the higher temperatures led to a loss of the finer pores. They noted that as a PSOC 1451 bituminous coal char was oxidized, the total surface area increased and reached a maximum at around 60% conversion. When examined as a function of char devolatilization temperature, it was observed that the surface area at 50% conversion was greater for the chars formed at lower temperatures. They postulated that the reduction of surface area at higher charring temperatures resulted from a closure of the smaller pores due to a structural ordering of carbon. The 1600K char, then may be more graphitized and less prone to shrinking than the 1200K char. In a study of the oxidation kinetics of synthetic chars (amorphous carbon), Levendis et al. (1989) observed that as the oxidation temperature increased, there was increased graphitization of the synthetic chars. Oxygen accelerated the graphitization process. Thus, there is evidence that as chars react, the carbonaceous material undergoes graphitization. The extent to which a char shrinks during low temperature oxidation may depend on the extent of graphitization of the initial carbon particle during the devolatilization process.

The reactions that take place during devolatilization may provide some information about the difference in behavior between the 1600K char and the 1200K. Solomon et al. (1988) describe a two-step devolatilization process in which the raw coal is pictured as a complex of aromatic and hydroaromatic carbon clusters linked by aliphatic bridges. In the initial pyrolysis step, the weakest bridges are broken. The lightest molecular weight fragments may vaporize, the heavier fragments may remain with the parent coal. During this time, functional group decomposition also releases CO_2, H_2O, methane and other light gases. In the second step of pyrolysis, cross-linking between the remaining aromatic clusters

occurs. Solomon et al. (1990) found that there are two distinct cross-linking events, occurring at different temperatures. At a heating rate of 0.5°C/s, the low temperature cross-linking occurs between about 200 and 450°C, and the moderate temperature cross-linking occurs between 450 and 600°C. It is conceivable that at the much higher heating rates and short exposure time (2 s) used to produce the bituminous char used in these studies, the cross-linking is less complete for the 1200K char than for the 1600K char. Thus, as a char undergoes subsequent oxidation, cross-linking also occurs, leading to the shrinkage. However, as the heating in nitrogen showed, the densification effect requires reaction with oxygen and not simply heating to elevated temperatures. Therefore, in this scenario, the cross-linking is assisted by the carbon-oxygen reaction.

There is a significant implication of these results for researchers using or producing char oxidation models. Most models assume that, as char oxidation progresses, the pores enlarge and the surface recedes, but the basic carbon structure does not change. Results from this experiment and those from the Spherocarb densification study of Hurt et al. (1988) show that the models must account for changes in density which can not be characterized simply by the oxidation regimes in which the reaction is taking place. These density changes are not only dependent on the initial coal structure, but also upon on the temperature time history of char formation. Thus, a complete description of char oxidation will require both the information about the basic structure (density, porosity, surface area, etc.) and knowledge of the history of the char to account for possible carbon structural changes and shrinking during the oxidation process.

Acknowledgements

This work was supported by the U.S. Department of Energy University Coal Research Program under grant number DE-FG22-89PC89765.

References

Bar-Ziv, E., Jones, D. B., Spjut, R. E., Dudek, D. R. and Sarofim, A. F.(1989). *Comb. and Flame.* 75:81-106.

Davis, E. J. (1987). In *Surface and Colloid Science* (E. Matijevic, ed.). Vol. 14. Plenum Press, New York.

Field, M. A., Gill, D. W., Morgan, B. B. and Hawksley, P. G. W. (1967). *Combustion of Pulverized Coal*, The British Coal Utilisation Research Association, Leatherhead.

Floess, J. K., Longwell, J. P. and Sarofim, A. F. (1988). *Energy and Fuels.* 2:18-26.

Levendis, Y. A., Flagan, R. C. and Gavalas, G. R. (1989). *Comb. Flame.* 76:221-241.

Hurt, R. L., Dudek, D. R., Longwell, J. P. and Sarofim, A. F. (1988). *Carbon.* 26:433-449.

Hurt, R. L., Sarofim, A. F. and Longwell, J. P. (1991). *Energy and Fuels.* 5: 290-299.

Sahu, R., Levendis, Y. A., Flagan, R. C. and Gavalas, G. R. (1988). *Fuel.* 67:275-283.

Smith, I. W. (1971). *Comb. Flame.* 17: 421-428.

Smith, I. W. (1978). *Fuel.* 57:409-414.

Smith, I. W. (1982). *Nineteenth Symp. (Int.) Comb.* The Combustion Institute. pp. 1045-1065.

Smith, J. M. (1970). *Chemical Engineering Kinetics.* McGraw-Hill Book Company, NewYork.

Smoot, L. D. and Smith, P. J. (1985). *Coal Combustion and Gasification.* Plenum Press, New York.

Solomon, P. R., Hamblen, D. G., Carangelo, R. M., Serio, M. A. and Deshpande, G. V. (1988). *Energy and Fuels.* 2:405-422.

Solomon, P. R., Serio, M. A., Deshpande, G. V. and Kroo, E. (1990). *Energy and Fuels.* 4:42-54.

Spjut, R. E., Sarofim, A. F. and Longwell, J. P. (1985). *Langmuir.* 1:355-360.

Waters, B. J., Squires, R. G., Laurendreau, N. M. and Mitchell, R. E. (1988). *Comb. and Flame.* 74:91-106.

Table 1

Properties of Chars

Coal or Char	σ_A	ε_a <7μm	ε <32 Å	V_{Hg}	S_{Hg}
	g/cm^3	%	%	cm^3/g	m^2/g
PSOC 1451 coal	1.18	17	–	0.14	7.9
1200K char	1.0	33	0	0.43	11.6
1400K char	0.9	40	0	0.57	11.4
1600K char: 53-90μm from 53-90μm	0.98	47	2	0.46	14.7
127-147μm from 90-125μm	0.92	47	19	0.35	14.9
Spherocarb	0.56	33[1]	.39[2]	–	864[3]

[1]Pores larger than 200 Å by mercury porosimetry (Floess et al., 1988).

[2]Micropore volume, cm^3/g for an average pore radius of 6.7 Å, determined by nitrogen adsorption (Floess et al., 1988).

[3]BET surface area by N_2 adsorption (Waters et al., 1988).

Table 2

Spherocarb Data

Particle	Series	Temperature K	Conversion %	Relative Volume $(d/d_0)^3$
A	TS0372	930 ± 20	17.6	.77
		920 ± 20	32.2	.70
		950 ± 50	42.3	.60
		880 ± 30	64.0	.45
		890 ± 30	71.7	.31
B	TS0373	1000 ± 50	60.8	.75
C	TS0374	1010 ± 15	8.9	.94
		990 ± 30	30.9	.79
		940 ± 40	43.9	.62
		930 ± 30	53.9	.54
		900 ± 40	63.5	.47
D	TS0471	970 ± 20	12.2	.94
		960 ± 20	36.8	.81
		930 ± 30	55.2	.60
		910 ± 30	75.6	.31
E	TS0473	900 ± 10	24.0	.79
		820 ± 20	55.1	.63
		900 ± 100	67.2	.41
F	TS0474	820 ± 20	4.4	.92
		860 ± 40	40.1	.65
G	TS0475	760 ± 100	11.7	.88
		790 ± 100	23.8	.86
		790 ± 100	41.8	.80
H	TS0512	910 ± 20	9.8	.92
		900 ± 20	21.4	.79
		890 ± 25	31.8	.76
I	TS0513	980 ± 30	12.3	.90
		960 ± 20	36.0	.80
		930 ± 20	55.8	.54

Table 2, Continued

Particle	Series	Temperature K	Conversion %	Relative Volume $(d/d_0)^3$
J	TS0921	980 ± 15	4.0	.95
		1030 ± 30	52.1	.60
K	TS0522	920 ± 40	78.9	.27
L	TS0523	1000 ± 20	43.9	.82
		1000 ± 100	82.6	.39
M	TS0524	1070 ± 100	61.3	.62
N	TS0525	890 ± 15	17.4	.95
		880 ± 15	52.4	.67

Table 3

Char Data

Particle	Series	Temperature K	Conversion %	Relative Volume $(d/d_0)^3$
A (1200K)	TC0771	790 ± 50	9.6	1.00
			42.9	.85
B (1200K)	TC0781	790 ± 50	63.5	.46
C (1200K)	TC0782	790 ± 50	33.6	.69
D (1200K)	TC0783	790 ± 50	79.5	.28
E (1200K)	TC0784	790 ± 50	70.5	.54
F (1200K)	TC0785	790 ± 50	48.3	1.00
G (1200K)	TC0786	790 ± 50	15.4	.82
			43.2	.72
H (1600K)	TC0861	$\sim$	17.9	.99
		$\sim$	52.1	.76
I (1600K)	TC0871	$\sim$	29.3	.98
J (1600K)	TC0872	$\sim$	19.4	.93
K (1600K)	TC0874	$\sim$	38.4	1.00
L (1600K)	TC0875	700 ± 100	10.7	.95
M (1600K)	TC0881	880 ± 100	28.3	.95
N (1600K)	TC0882	880 ± 100	42.4	1.00
		850 ± 100	76.0	.95
O (1600K)	TC0902	840 ± 100	63.8	.95
P (1200K)	TC0911	780 ± 100	51.4	.77
Q (1400K)	TC0913	840 ± 100	51.6	.51
R (1200K)	TC1041	770 ± 100	48.2	.64

Figure Captions

Figure 1. Graph of relative volume of particle vs. conversion. The top line is the line of constant diameter. The diagonal line is the line of constant density.

Figure 2. Temperature trace for a Spherocarb particle heated in the electrodynamic balance.

Figure 3. Temperature trace for a char particle made at 1600K from PSOC 1451 bituminous coal.

Figure 4. Photograph of backlit Spherocarb particle before being heated in the electrodynamic balance; b. Photograph of the same Spherocarb particle after 62% conversion. Note the flattened top and bottom, where the laser beam was heating the particle; c. Photograph of Spherocarb before reacting; d. Photograph of Spherocarb after heating in nitrogen.

Figure 5. a. Photograph of 1200K char before reacting; b. Photograph of 1200K char after heating in nitrogen; c. Photograph of 1200K char before reacting; d. Photograph of 1200K char after 48% conversion. Note the relatively uniform size change.

Figure 6. a. Photograph of 1600K char before heating; b. Photograph of 1600K char after heating in nitrogen; c. Photograph of 1600K char before reacting; d. Photograph of 1600K char after 56% conversion. The char now looks lacy or translucent. The exterior dimensions are nearly the same.

Figure 7. Relative volume of Spherocarb particles reacted at low temperatures.

Figure 8. Relative volume of bituminous char vs. conversion. The x are 1200K char, and the circles are 1600K char.

Figure 1

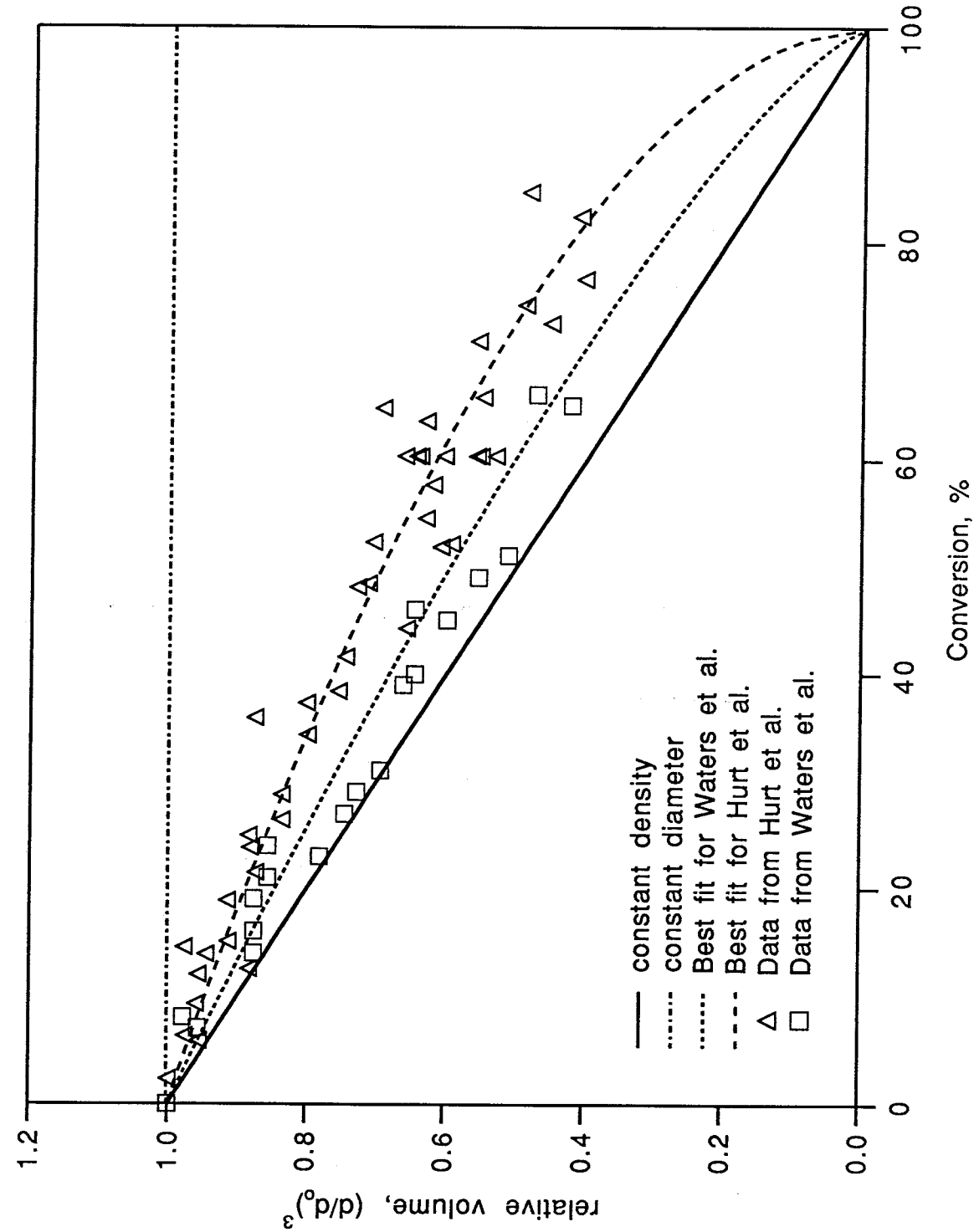
relative volume, $(d/d_o)^3$
1.2
1.0
0.8
0.6
0.4
0.2
0.0
0
20
40
60
80
100
Conversion, %
constant density
constant diameter
Best fit for Waters et al.
Best fit for Hurt et al.
Data from Hurt et al.
Data from Waters et al.

Figure 2

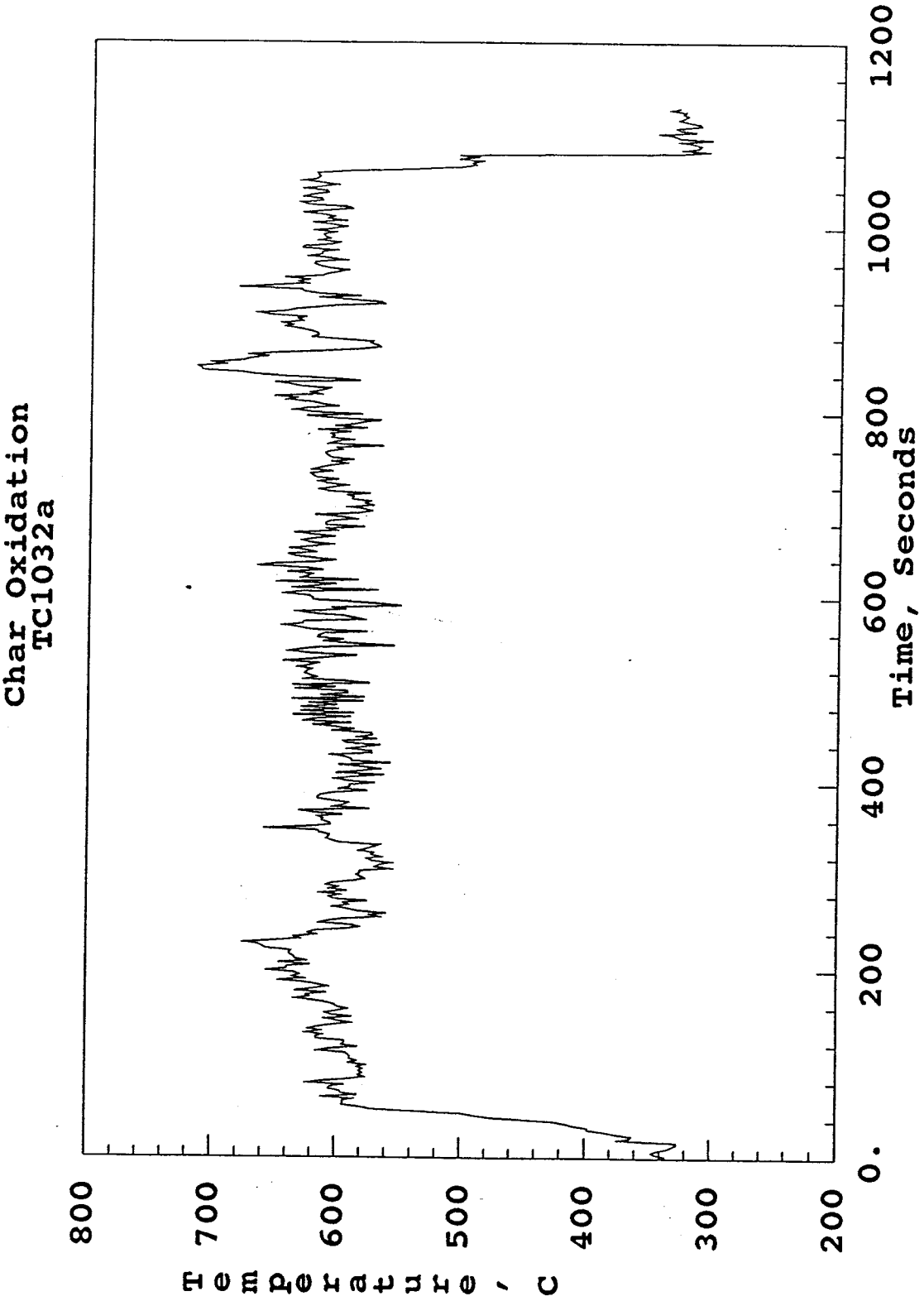
Char Oxidation
TC1032a
Temperature, C
800
700
600
500
400
300
200
0.
200
400
600
800
1000
1200
Time, Seconds

Figure 3

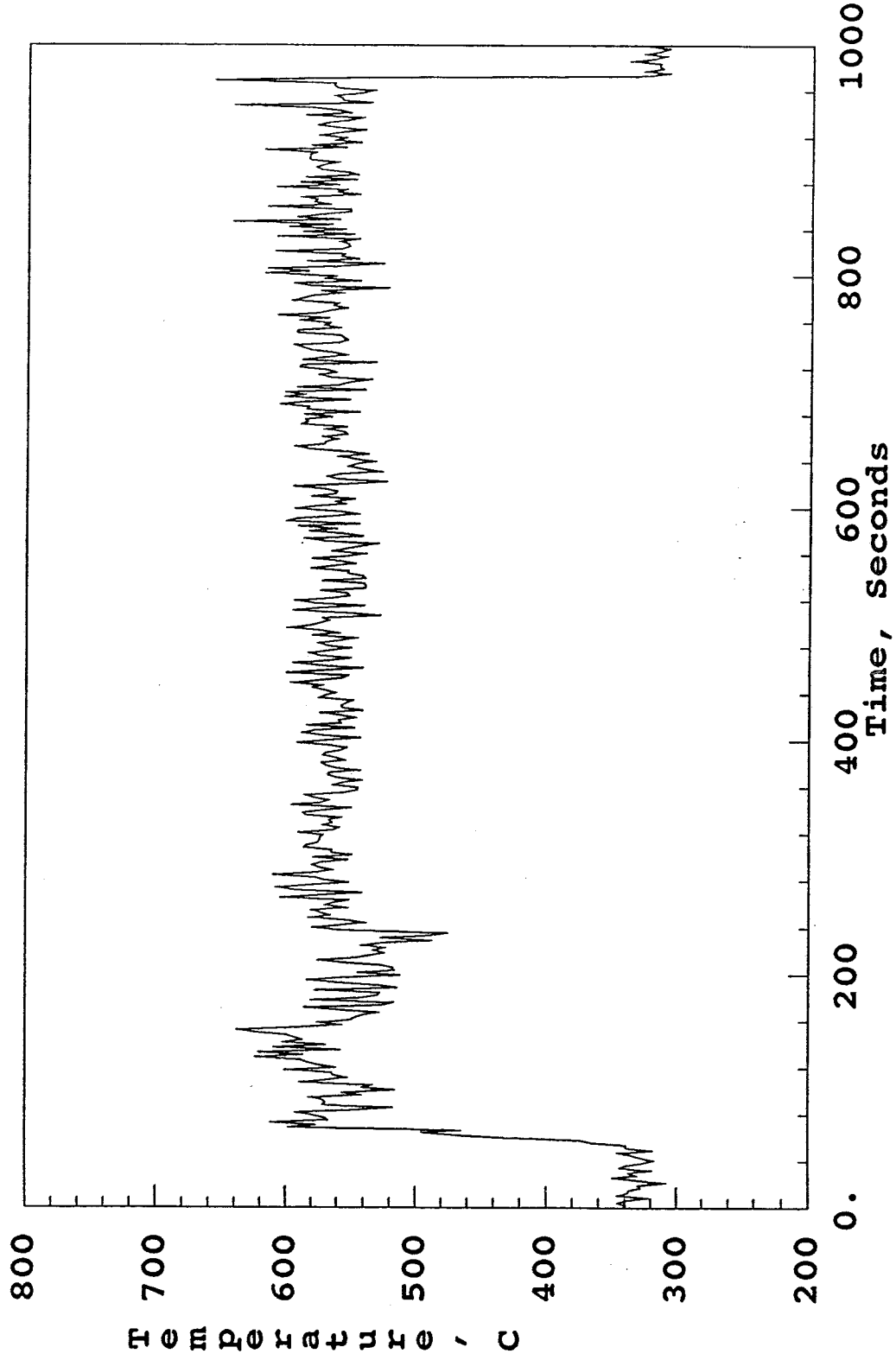
Char Oxidation
TC0873a
Temperature, C
800
700
600
500
400
300
200
0.
200
400
600
800
1000
Time, Seconds

Figure 4a. Spherocarb before heating in N_2	Figure 4c. Spherocarb before heating in air
Figure 4b. Spherocarb after heating in N_2	Figure 4d. Spherocarb after heating in air
Figure 5a. 1200K Char before heating in N_2	Figure 5c. 1200K Char before heating in air
Figure 5b. 1200K Char after heating in N_2	Figure 5d. 1200K Char after heating in air
Figure 6a. 1600K Char before heating in N_2	Figure 6b. 1600K Char before heating in air
Figure 6b. 1600K Char after heating in N_2	Figure 6d. 1600K Char after heating in air

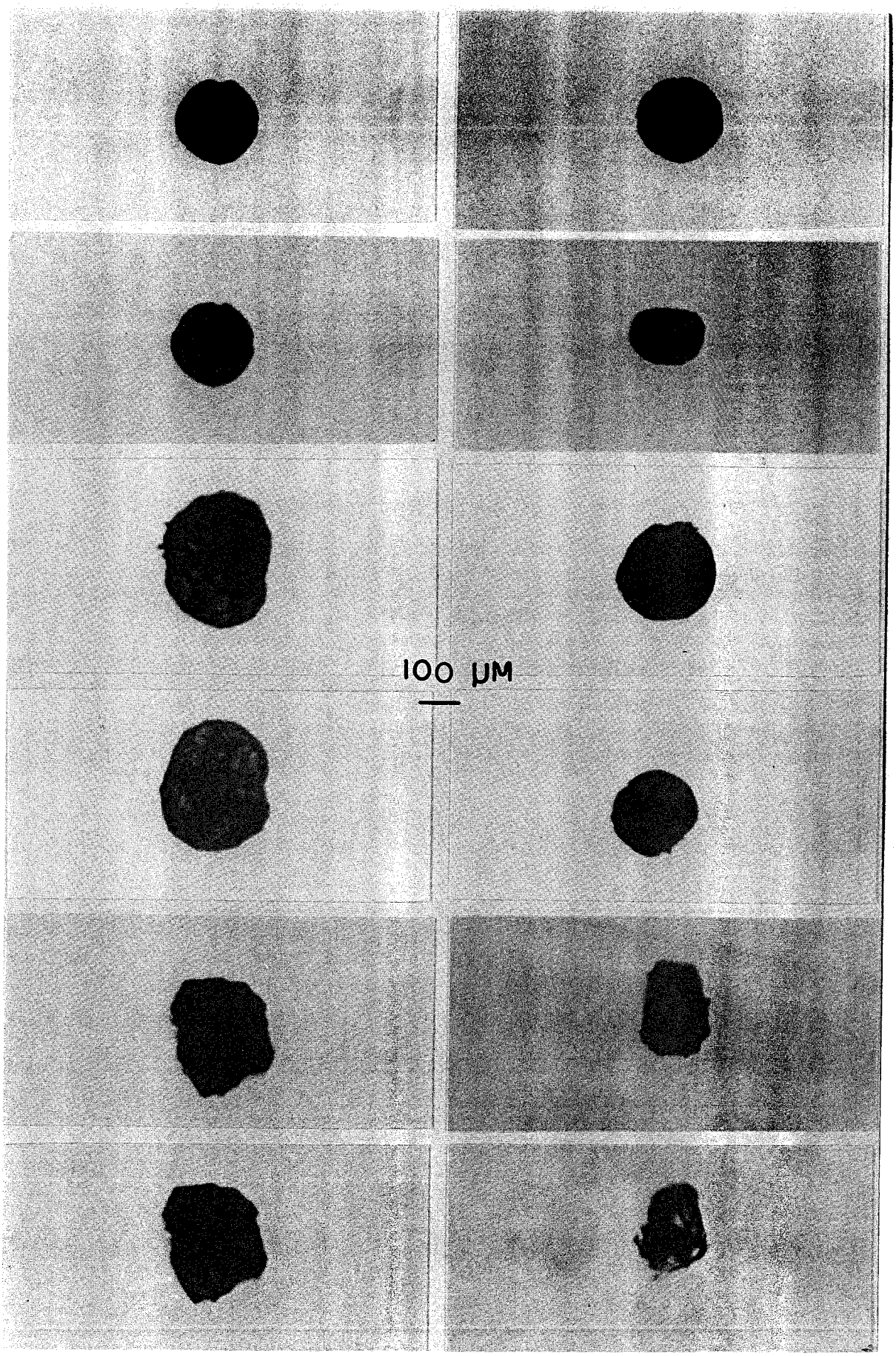
100 µM

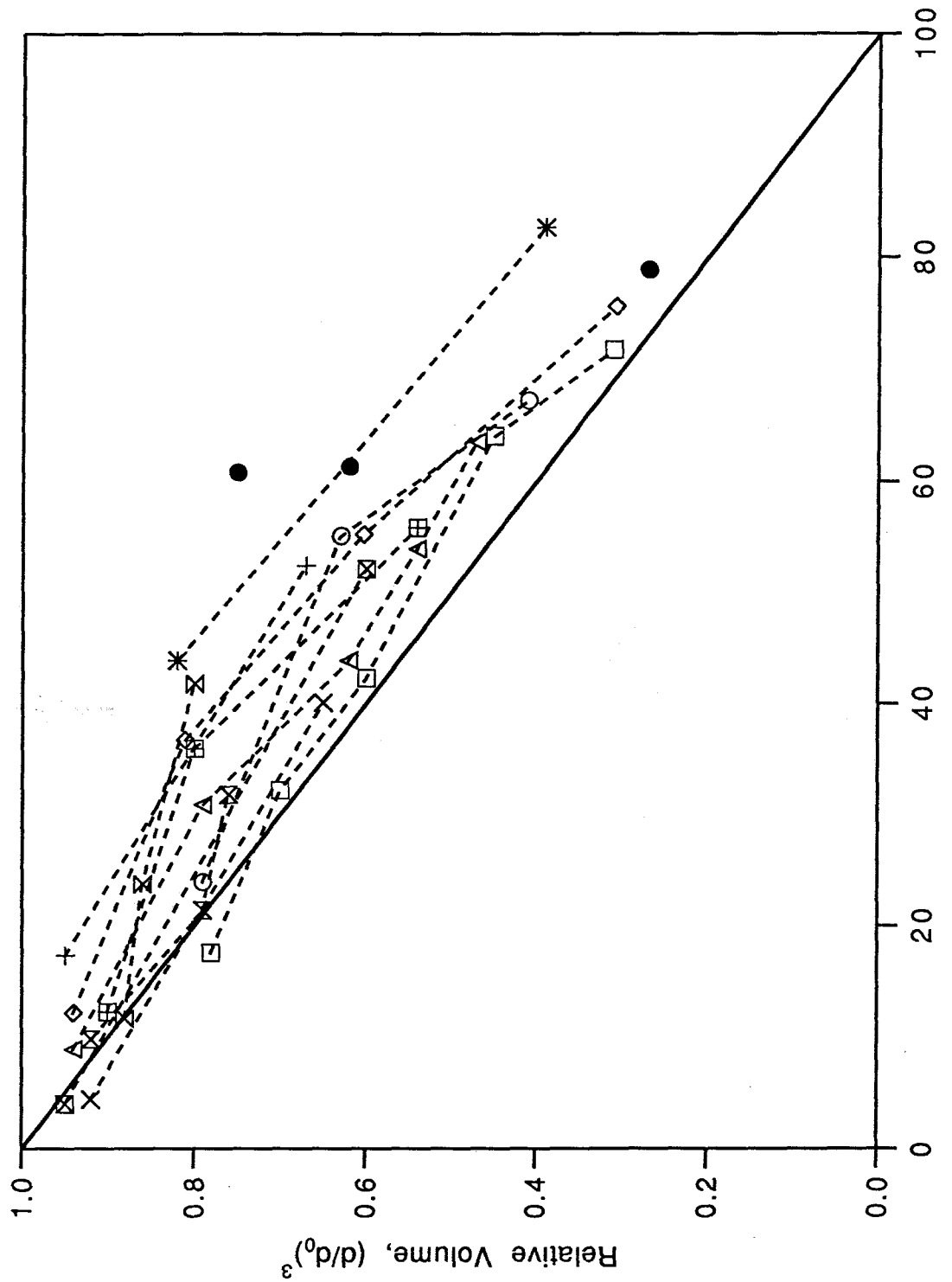
Relative Volume, $(d/d_0)^3$
1.0
0.8
0.6
0.4
0.2
0.0
0
20
40
60
80
100
Conversion, %

Figure 7

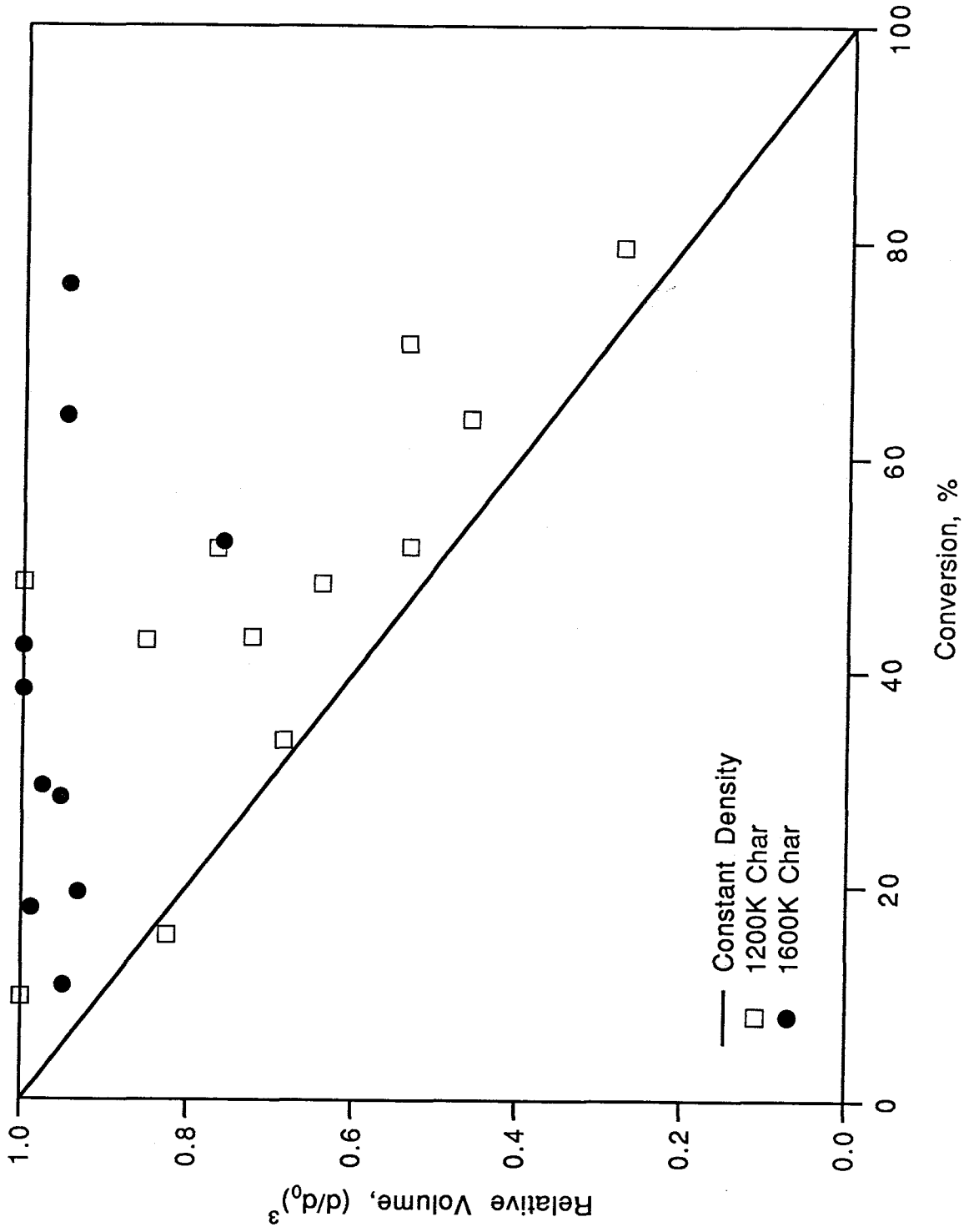
Relative Volume, $(d/d_0)^3$
1.0
0.8
0.6
0.4
0.2
0.0
0
20
40
60
80
100
Conversion, %
Constant Density
1200K Char
1600K Char

Figure 8

Chapter 4

Conclusions

The results from these studies are somewhat contradictory for the field of char oxidation. On the one hand, the ignition experiments showed that the experimental data could be explained by the simple thermal explosion model. The Spherocarb and the char showed the ignition delay predicted by the model. The ignition temperature trace was modeled by using existing literature data. Thus, the ignition experiments indicate that using an isothermal sphere model is adequate for char oxidation modeling. On the other hand, the low temperature oxidation of the Spherocarb and char showed that an isothermal sphere model may not be adequate, because the particles of Spherocarb and char shrank unexpectedly. The size and density of the particles both changed when the porous structure of the particle and low temperatures of reaction predicted that the diameter should remain constant and the density decrease. In fact, chars made under different conditions from the same coal behaved differently. The char made at 1200K shrank and densified as it was oxidized, while the char made at 1600K oxidized at constant diameter and decreased in density. Hence, it would appear that the charring history has an effect on the subsequent oxidation behavior. A model of char oxidation cannot simply take a particle and predict its oxidation behavior and size change with conversion based solely on the temperature and the reaction rate regime. This has important implications for char oxidation models. First of all, the size of the particle cannot be used as a measure of carbon conversion, since the particle is shrinking as it is reacting. Secondly, the change

in size can alter the heat balance since the heat loss and heat gain terms are dependent on the size of the particle. Thirdly, the density changes during oxidation depend on the temperature history of the char formation. Further study is needed, then to determine the precise factors, such as devolatilization temperature and heating rate, that cause a char particle to possibly shrink upon subsequent char oxidation. Study is also needed to determine the molecular reactions that are occurring and causing the particle to shrink and densify.

Appendix I

Design of the Electrodynamic Balance

Historically, the electrodynamic balance can be traced back to Millikan's apparatus for determining the charge of the electron (Davis, 1987). In his apparatus, Millikan applied a DC voltage across two horizontal brass disks. A charged oil droplet was trapped between the two plates. The vertical velocity attained by the oil droplet depends on the drop size, the viscosity of the ambient gas (air), and the electric field. By measuring the velocity of the same particle with different numbers of electrons at the same electric field strengths, Millikan was able to determine the charge of an electron. Although the vertical force of gravity was counteracted by the electrical field, the particle can move laterally due to Brownian forces (Davis, 1987). Fletcher placed a small disk in the center of the top electrode. When electrified, the disk attracted the particle back to the center axis (Davis, 1987).

Straubel (1956) inserted a simple ring in the midplane between the upper and lower plates of the Millikan cell. An AC voltage was applied to the ring to retain the particles. Wuerker et al. (1959) described an electrodynamic cell based on the quadrupole mass filter of Paul and Raether (1955). Their cell consisted of electrodes with hyperbolic surfaces described by the following equations:

$$z^2 - \frac{r^2}{2} = z_0^2 \tag{1}$$

for the endcap, and

$$z^2 - \frac{r^2}{2} = -z_0^2 \tag{2}$$

for the ring electrode (see Figure 1), where $2z_0$ is the distance between the endcaps.

When one considers the electric field due to the ring, there is a time varying voltage, however, at any one instant, it can be that steady state has been achieved, so that the Laplace equation holds:

$$\frac{1}{r}\frac{\partial}{\partial r}\left(r\frac{\partial V}{\partial r}\right) + \frac{\partial^2 V}{\partial z^2} = 0 \tag{3}$$

A solution which satisfies equations 1,2 and 3 is

$$V = \left(\frac{V_{DC} - V_{AC}\cos\Omega t}{z_0^2}\right)\left(z^2 - \frac{r^2}{2}\right) \tag{4}$$

The electric field that results from equation 4 is

$$E_{AC,r} = V_{AC}\cos\Omega t\frac{r}{2z_0^2} \tag{5}$$

$$E_{AC,z} = -V_{AC}\cos\Omega t\frac{z}{z_0^2} \tag{6}$$

It can be seen that the electric field in the horizontal and vertical directions is linear. The electrode configuration producing this result is a hyperbola of revolution. The field produced by a DC voltage across the endcaps is more complex, but essentially linear near the center of the cell.

Other cell configurations have been used (Straubel, 1956; Berg and

Gaukler, 1969). Other cell geometries are considerably easier to machine than machining hyperboloids. Therefore, it was desirable to see how the electric fields for two different geometries compared. An analytical solution could be found for a cylindrical geometry cell (see Figure 2). Begin again with Laplace's equation 3. Assume that there is no variation with θ, and that variables r and z can be separated. The boundary equations are:

$$V(0,z) = \text{finite}$$

$$V(r,0) = \text{ symmetric}$$

$$V(r,z_0) = V_1$$

$$V(r,-z_0) = V_2$$

$$V(r_0,z) = V_r\left(\left(\frac{z_0-z}{z_0-b}\right)+\left(1-\frac{z_0-z}{z_0-b}\right)\cdot(1-\text{ u }_b(z))\right)$$

$$\text{u}_b = \begin{cases} 0 \text{ if} \leq z \leq b \\ 1 \text{ if } b < z \leq z_0 \end{cases}$$

The last term is a ramp function to describe the voltage drop-off from the endcap electrode to the ring.

The solution to the equations can be found in terms of Bessel Functions. The potential due to the voltage on the ring is

$$V(r,z) = \frac{2V_{AC}z_0}{z_0-b}\sum_{m=1}^{\infty}\left(\frac{2}{(2m-1)\pi}\right)^2 \cos\left(\frac{(2m-1)\pi}{2z_0}b\right)\cos\left(\frac{(2m-1)\pi}{2z_0}z\right)\frac{\text{I}_0\left(\frac{(2m-1)\pi}{2z_0}r\right)}{\text{I}_0\left(\frac{(2m-1)\pi}{2z_0}r_0\right)}$$

The potential due to the voltage on the top endcap electrode is

$$V(r,z) = 2V_1 \sum_{m=1}^{\infty} \frac{\left(e^{-\lambda_m \frac{z}{r_0}} - e^{\lambda_m \frac{2z_0 + z}{r_0}} \right)}{\left(e^{-\lambda_m \frac{z_0}{r_0}} - e^{3\lambda_m \frac{z_0}{r_0}} \right)} \frac{J_0\left(\lambda_m \frac{r}{r_0}\right)}{\lambda_m J_1(\lambda_m)}$$

The potential due to the voltage on the bottom endcap electrode is

$$V(r,z) = 2V_2 \sum_{m=1}^{\infty} \frac{\left(e^{-\lambda_m \frac{z}{r_0}} - e^{\lambda_m \frac{z-2z_0}{r_0}} \right)}{\left(e^{\lambda_m \frac{z_0}{r_0}} - e^{-3\lambda_m \frac{z_0}{r_0}} \right)} \frac{J_0\left(\lambda_m \frac{r}{r_0}\right)}{\lambda_m J_1(\lambda_m)}$$

The potential due to the voltage ramp used in the last boundary condition is

$$V(r,z) = \sum_{m=1}^{\infty} 2V_1 \left[-(-1)^m \frac{1}{m\pi} - \frac{z_0}{z_0 - b} \left(\frac{1}{m\pi}\right)^2 \sin\left(m\pi \frac{b}{z_0}\right) \right] \sin\left(m\pi \frac{z}{z_0}\right) \frac{I_0\left(m\pi \frac{r}{z_0}\right)}{I_0\left(m\pi \frac{r_0}{z_0}\right)}$$

The electric field is defined from the voltages by

$$E = -\nabla V$$

The electric field in the vertical and radial directions for the ring electrode becomes:

$$E_r^R = -\sum_{m=1}^{\infty} \frac{2V_R}{z_0 - b} \left(\frac{2}{(2m-1)\pi}\right) \cos\left(\frac{(2m-1)\pi}{2z_0} b\right) \cos\left(\frac{(2m-1)\pi}{2z_0} z\right) \frac{I_1\left(\frac{(2m-1)\pi}{2z_0} r\right)}{I_0\left(\frac{(2m-1)\pi}{2z_0} r_0\right)}$$

$$E_z^R = \sum_{m=1}^{\infty} \frac{2V_R}{z_0 - b} \left(\frac{2}{(2m-1)\pi}\right) \cos\left(\frac{(2m-1)\pi}{2z_0} b\right) \sin\left(\frac{(2m-1)\pi}{2z_0} z\right) \frac{\mathbf{I_0}\left(\frac{(2m-1)\pi}{2z_0} r\right)}{\mathbf{I_0}\left(\frac{(2m-1)\pi}{2z_0} r_0\right)}$$

The electric field due to the top electrode in vertical and radial directions is:

$$E_r^T = 2V_1 \sum_{m=1}^{\infty} \frac{\left(e^{-\lambda_m \frac{z}{r_0}} + e^{\lambda_m \frac{2z_0 + z}{r_0}}\right)}{\left(e^{-\lambda_m \frac{z_0}{r_0}} - e^{\lambda_m \frac{3z_0}{r_0}}\right)} \frac{\mathbf{J_1}(\lambda_m \frac{r}{r_0})}{r_0 \mathbf{J_0}(\lambda_m)}$$

$$E_z^T = 2V_1 \sum_{m=1}^{\infty} \frac{\left(e^{-\lambda_m \frac{z}{r_0}} + e^{\lambda_m \frac{2z_0 + z}{r_0}}\right)}{\left(e^{-\lambda_m \frac{z_0}{r_0}} - e^{\lambda_m \frac{3z_0}{r_0}}\right)} \frac{\mathbf{J_0}(\lambda_m \frac{r}{r_0})}{r_0 \mathbf{J_1}(\lambda_m)}$$

The electric field due to the bottom electrode in the radial and vertical directions is:

$$E_r^B = 2V_1 \sum_{m=1}^{\infty} \frac{\left(e^{-\lambda_m \frac{z}{r_0}} - e^{\lambda_m \frac{z - 2z_0}{r_0}}\right)}{\left(e^{\lambda_m \frac{z_0}{r_0}} - e^{-\lambda_m \frac{3z_0}{r_0}}\right)} \frac{\mathbf{J_1}(\lambda_m \frac{r}{r_0})}{r_0 \mathbf{J_0}(\lambda_m)}$$

$$E_z^B = 2V_1 \sum_{m=1}^{\infty} \frac{\left(e^{-\lambda_m \frac{z}{r_0}} + e^{\lambda_m \frac{z - 2z_0}{r_0}}\right)}{\left(e^{\lambda_m \frac{z_0}{r_0}} - e^{-\lambda_m \frac{3z_0}{r_0}}\right)} \frac{\mathbf{J_0}(\lambda_m \frac{r}{r_0})}{r_0 \mathbf{J_1}(\lambda_m)}$$

The electric field due to the voltage ramp in the last boundary condition is

$$E_r = -\sum_{m=1}^{\infty} 2V_1\left[-(-1)^m\frac{1}{z_0} - \frac{1}{z_0-b}\left(\frac{1}{m\pi}\right)\sin\left(m\pi\frac{b}{z_0}\right)\right]\sin\left(m\pi\frac{z}{z_0}\right)\frac{\mathbf{I_1}(m\pi\frac{r}{z_0})}{\mathbf{I_0}(m\pi\frac{r_0}{z_0})}$$

$$E_z = -\sum_{m=1}^{\infty} 2V_1\left[-(-1)^m\frac{1}{z_0} - \frac{1}{z_0-b}\left(\frac{1}{m\pi}\right)\sin\left(m\pi\frac{b}{z_0}\right)\right]\cos\left(m\pi\frac{z}{z_0}\right)\frac{\mathbf{I_0}(m\pi\frac{r}{z_0})}{\mathbf{I_0}(m\pi\frac{r_0}{z_0})}$$

Figure 3 shows the electric field in the vertical and radial directions for the hyperboloidal geometry and for the cylindrical geometry. It can be seen that near the center of the cell, the two fields are essentially identical. Therefore, the cylindrical system should behave essentially identically to the hyperboloidal system.

The equations of motion for a particle in the cell have been analyzed by Davis, Frickel et al. (1978) and Bar-Ziv et al. (1991). The equations of motion in the vertical direction are

$$m\,\frac{d^2z}{dt^2} = \frac{-3\pi\eta d}{C_c}\,\frac{dz}{dt} + qE_{AC}\cos\omega t + qE_{DC} - mg$$

where m is the mass of the particle, η is the gas viscosity, d is the particle diameter, C_c is the Cunningham slip correction factor, and q is the charge on the particle. If the equation is non-dimensionalized and rearranged, an equation results which is a form of the Mathieu equation (Bar-Ziv, 1991; Davis, 1987; Frickel, 1978). The solution of the Mathieu equation yield sets of solutions which are stable and unstable. The regions of stability and instability depend on the

electrical field, which in turns, depends on the geometry of balance. Therefore, for the cylindrical balance, the regions of stability and instability are not predictable a priori, but can be determined experimentally.

The original design of the balance was of a cylindrical geometry, as shown in Figure 2. The design of the balance was subject to the following constraints: size of the chamber in which the cell would sit, size of the viewing ports, contributing to the size of the ring, electrical arcing between electrodes, determining the spacing between the electrodes, etc.

After the balance was in use for a while, certain deficiencies were noted, e.g., inability to go to high AC fields, desire for more DC field strength (to hold larger particles, or particles with smaller charge to mass ratio). The simplest modification was to make endcap electrodes with a hemispherical shape. The electrical field was not recalculated, since the field should be somewhere between that of the hyperboloid and the cylindrical geometry. The hemispherical geometry is currently being used, and is the geometry used in the main experiments.

References

Bar-Ziv, E., de Boton, G., Bar-Ziv, R. H., Martsiano, Y. and Ben-dor, G. (1991). *Aerosol Sci. Technol.* 14:127-137.

Davis, E. J. (1987). In *Surface and Colloid Science* (E. Matijevic, ed.) vol. 14, Plenum Press, New York.

Frickel, R. H., Shaffer, R. E. and Stamatoff, J. B. (1978). *Chambers for the Electrodynamic Containment of Charged Aerosol Particles.* Tech Report ARCSL-TR77041, U.S. Army Armament Research and Development command, Aberdeen, MD.

Straubel, H. (1956). *Z. Elektrochemie*, 60:1033-1036.

Wuerker, R. F., Shelton, H. and Langmuir, R. V. (1959). *J. Appl. Phys.* 30:342-349.

Paul, W. and Raether, M. (1955). *Z. Phys.* 140:262-273.

Figure Captions

Figure 1. The hyperboloidal electrodes used in the electrodynamic balance.

Figure 2. A cylindrical geometry electrodynamic balance

Figure 3. Graph of the electric field near the center of the hyperboloidal geometry and cylindrical geometry electrodynamic balance.

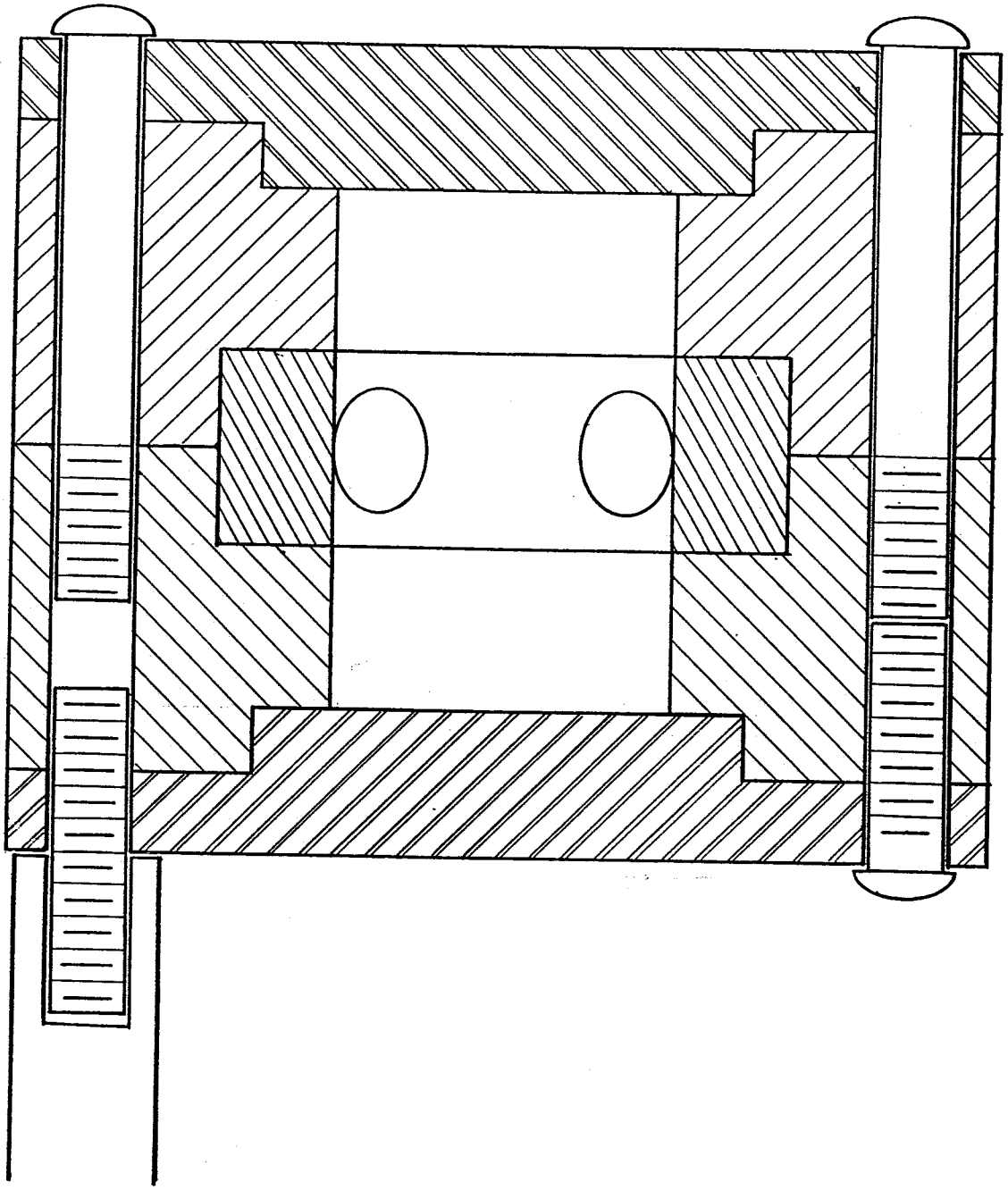

Figure 2

The Electrodynamic Balance with Hyperboloidal Electrodes

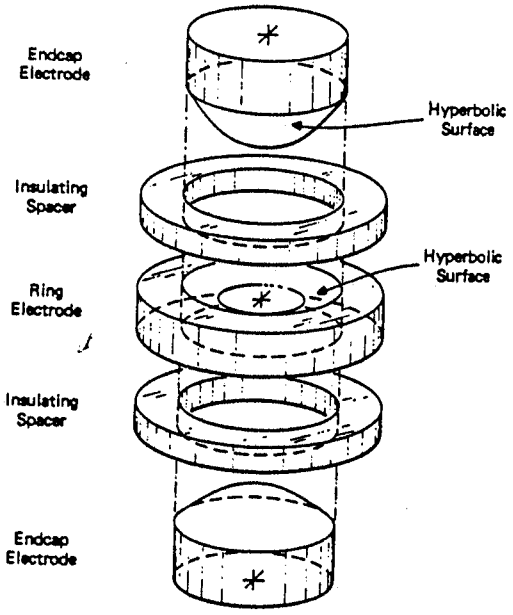

FIG. 1. Exploded view of quadrupole.

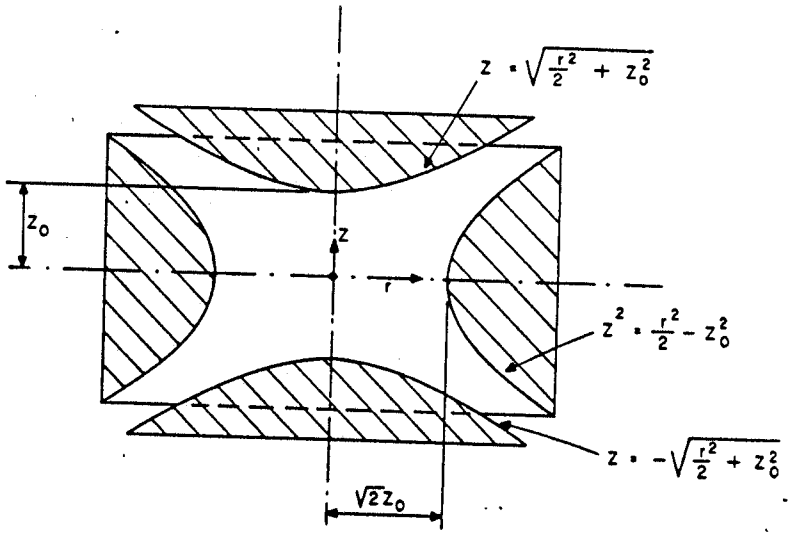

$$E_{AC,r} = V_{AC}cos(\omega t)\frac{r}{2z_0^2}$$

$$E_{AC,z} = -V_{AC}cos(\omega t)\frac{z}{z_0^2}$$

$$V_{DC} = \frac{m}{q}\frac{gz_0}{C}$$

Figure 1

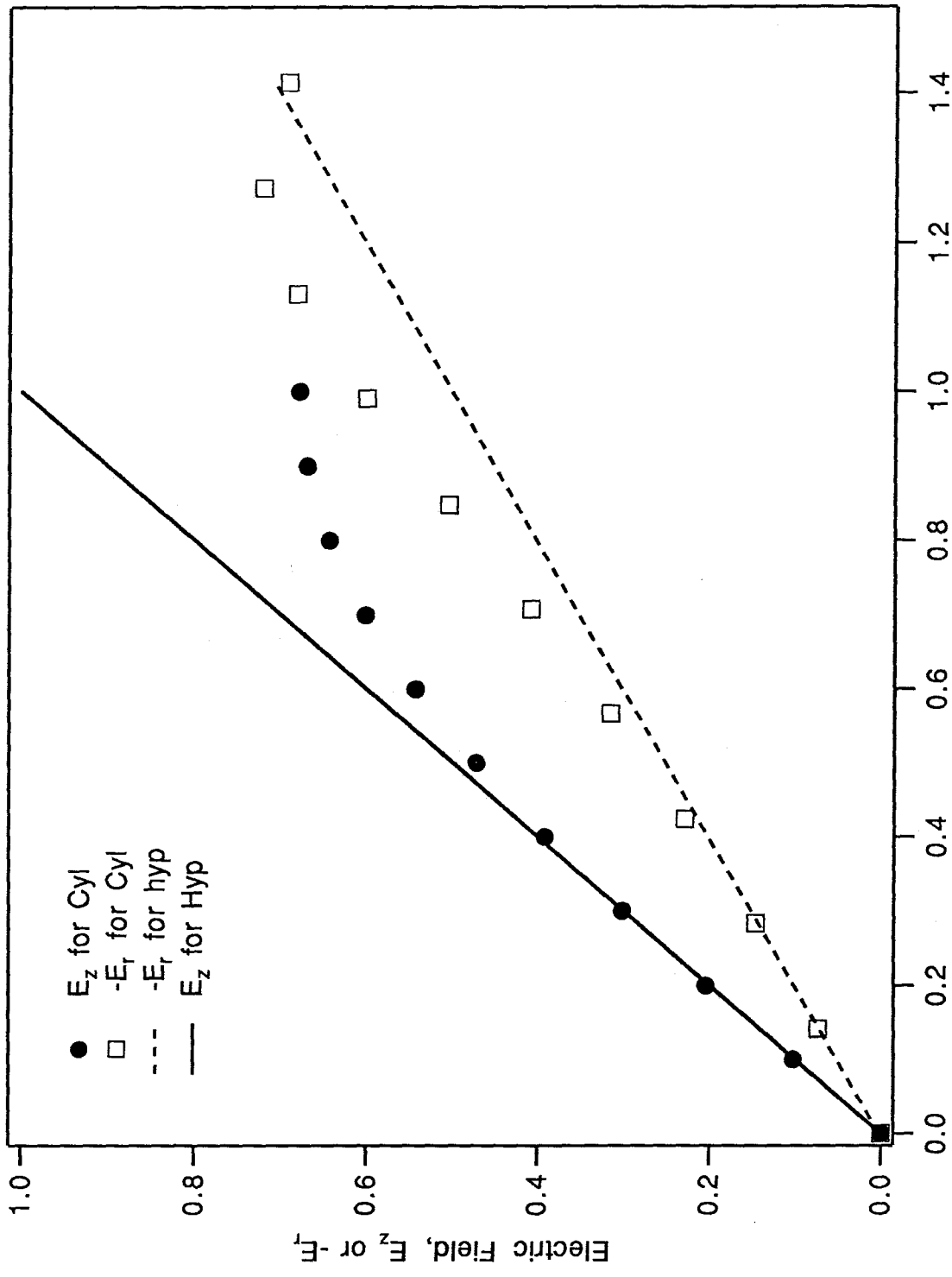
Electric Field, E_z or $-E_r$
r or z
E_z for Cyl
$-E_r$ for Cyl
$-E_r$ for hyp
E_z for Hyp
0.0
0.2
0.4
0.6
0.8
1.0
1.2
1.4

Figure 3

Appendix 2

Particle Trapping

Trapping particles in the electrodynamic balance is one of the more important techniques to master. A particle of the desired properties must be produced with a sufficient charge so that it can be held by the electrodynamic balance. Important considerations in determining the techniques used to trap particles are the nature of the particle (liquid or solid), the size of the particles, and the shape of the particle, if solid. A wide variety of techniques exist to produce liquid droplets, and these techniques may be adapted to produce particles suitable for trapping in the electrodynamic balance. Solid particles are a little more difficult to work with and trap in the balance. All of the trapping techniques work by introducing a charged particle or particles in the vicinity of the center of the electrodynamic cell. If the particle or particles have the appropriate charge-to-mass ratio, then the AC voltage will capture the particle.

Historically, more experiments have been performed on liquid droplets, hence a variety of techniques have proven successful in generating and trapping droplets. One is to generate a quantity of the droplets in a space above the apparatus, and allow a particle to drop past the top plate via a small opening. This technique is especially useful with small droplets with a slow settling velocity. Millikan used this technique in his experiment (Davis, 1987). Allen and Raabe (1985) and Cheng et al. (1988) used a variation of this technique in which a vertical glass tube leads from the aerosol reservoir to the particle trap. Another

technique is to use a droplet injection system to shoot droplets directly into the cell. Arnold (1986) made a droplet injector from a thin stainless steel tube lined with a piezo-electric strip. An electric pulse transmitted to the piezo-electric strip causes a mechanical pulse on the stainless steel tubing. A droplet or droplets are injected out through a glass nozzle. Davis and Ravindran (1982) used a charged syringe to form a small droplet at the syringe tip, then inject the droplet into the balance. Rubel (1982) applied a high voltage to a wire embedded in a glass capillary tube. The ejected droplets were captured in a three-rail transport system, also used by Frickel (1978), to carry the particle to the electrodynamic balance.

Liquid droplet trapping techniques may be used if the solid is soluble in a liquid. Cohen et al. (1987) and Grader et al. (1987) used this technique to capture liquid droplets containing various dissolved salts. Manipulation of the humidity in the chamber then caused the droplets to grow, or dry out to salt particles. Other solids, such polystyrene latex, may be diluted and injected into the chamber and dried (Davis and Ravindran, 1982).

Other solids may be introduced into the chamber via some technique which puts a charge onto the particle during the introduction process. D'Amore et al. (1988) used a syringe to inject solid particles into the cell. The particles acquire charge by friction with the syringe needle wall as they are blown into the cell. Wuerker et al. (1959) applied a high voltage to a small quantity of conducting particles to inject them into the cell from beneath. The charging of small particles has been considered by researchers in the micrometeorite field. (Vedder, 1963; Shelton et al., 1960; Cho, 1964).

The technique used in these experiments was a variation on the high

voltage injection technique. An electrode was fashioned to slide under the bottom endcap electrode. A small amount of particles were placed onto this electrode. The electrode was slid underneath the bottom electrode. The AC voltage was set to an experimentally determined value. The DC voltage was also set, if needed. A "Zerostat" static ion generator (Discwasher, Inc.) was used to generate a high voltage. The Zerostat is a commercially available product, normally used to remove static charges from LP vinyl records. It consists of a piezo-electric element connected to a pointed needle. The entire device is in the shape of a gun. A trigger is used to apply pressure to the piezo crystal. When the trigger is pulled, a high voltage positive charge is generated. When the trigger is released, a high voltage negative charge is generated. The tip of the Zerostat is electrically connected to the injection electrode. When the trigger is pulled, the positive charge generates positively charged particles on the electrode, which are then repelled by the positively charged electrode surface, and attracted to the neutral bottom endcap electrode. The particles accelerate upwards, some particles enter the cell, and are captured by the AC field. If multiple particles are captured, the DC field is adjusted to approximately center one particle vertically. The AC is slowly reduced. The particles which are unbalanced oscillate with higher and higher amplitude, further and further from the center until they are lost, and the one balanced particle remains. If a negatively charged particle is desired, then the Zerostat trigger is pulled and released so that there is a residual negative charge on the Zerostat tip. The tip is then connected to the injection electrode.

The particle injection technique must be adjusted to suit each type of particle. For example, the char from PSOC 1451 coal can be captured by setting the AC to about 20 on the variac(about 800 volts) and using very small trigger motions. Spherocarb, on the other hand, requires an AC setting of about 120

(about 5000 volts), and a preset DC voltage of about 2 to 300 volts, and somewhat larger trigger motions.

A variety of other particle injection techniques were tried. The first was a variation on the high-voltage injection system actually used. In this, a 2000 V high voltage power supply was used to charge the particles. A high voltage relay was used to briefly make a connection from the power supply to the injection electrode. This technique worked adequately for small, or very low density particles, such as the char cenospheres.

Several systems for electrifying syringes and capillary tubes were also experimented upon, for injecting liquid particles. In some cases, the syringe needle was electrified directly, or the particle passed through an electric field to induce particle charging. In another case, a standard transfer pipet was modified to produce a smaller nozzle, and filled with a liquid. A thin wire was inserted into the pipet. When a charge was applied to the wire, the liquid squirted out the nozzle. The major difficulties encountered with these techniques was the control of the droplet size, and velocity of the injected particles. In most cases, the droplets were too large (order 100 μm). The trapping AC voltage was not large enough to hold these particles. Also, the velocity of the particles flying off the needles was too great. Ideally, the syringes should be mounted upside down, and a sufficient distance from the chamber that gravity has a chance to slow the particles. This could not be done with the current chamber and electrode set-up.

A system for injecting solid particles through a syringe capillary tubing was tried. A capillary tube with a 90° bend was filled with particles, and slid underneath the cell, so that the bent end pointed upwards into the cell. A small puff of air blew the particles into the chamber. A wire was connected to the

tubing, so that it could be electrified, if desired. This system did not work satisfactorily, perhaps because the particles blew into the chamber with too high a velocity to be captured, or because a greater AC voltage was required.

Particles were placed on an electrified plate above the cell. The plate was vibrated slightly, so that some particles fell into the cell. A few of the particles were captured by the AC voltage. This technique worked best when the top electrode was removed. This technique was abandoned because of the inconvenience of removing and replacing the top electrode, and the hazards of the exposed high voltage plate.

Suggestions for improvement

In the ideal situation, a single particle could be trapped, and then recovered. Thus characterization of the particle could be done prior to insertion (such as electron microscopy, pre-treatment, etc.) then the particle inserted into the cell and reacted. Then the particle could be recaptured, withdrawn from the cell, and additional characterization performed. The withdrawal phase appears to be feasible. An electrode could be inserted close to the particle, and an opposite charge placed on the electrode. The AC and DC voltages would be reduce, then turned off when the particle landed on the capturing electrode. The particle insertion is more difficult, because a certain amount of charge must be placed on the particle.

References

Allen, M. D. and Raabe, O. G. (1985). *Aerosol Sci. Tech.* 4:269-286.

Arnold, S. and Folan, L. M. (1986). *Rev. Sci. Instrum.* 57:2250-2253.

Cheng, Y. S., Allen, M. D., Gallegos, D. P., Yeh, H. C. and Peterson, K. (1988). *Aerosol Sci. Technol.* 8:199-214.

Cho, A. Y. H. (1964). *J. Appl. Phys.* 35: 2561-2564

Cohen, M. D., Flagan, R. C. and Seinfeld, J. H. (1987). *J. Phys. Chem.* 91:4563-4574.

D'Amore, M., Dudek, D. R., Sarofim, A. F. and Longwell, J. P. (1988). *Powder Tech.* 56:129-134.

Davis, E. J. (1987). In *Surface and Colloid Science* (E. Matijevic, ed.). Vol. 14. Plenum Press, New York.

Davis, E. J. and Ravindran, P. (1982). *Aerosol Sci. Tech.* 1:337-350.

Frickel, R. H., Shaffer, R. E. and Stamatoff, J. B. (1978), *Chambers for the electrodynamic containment of charged aerosol particles*, Tech Report, ARCSL TR 77041. U.S. Army Armament Research and Development Command, Aberdeen, MD.

Grader, G. S., Arnold, S., Flagan, R. C. and Seinfeld, J. H. (1987). *J. Chem. Phys.* 86:5897-5903.

Rubel, G. O. (1982). *J. Colloid Interface Sci.* 85:549-555.

Shelton, H., Hendricks, C. D. and Wuerker, R. F. (1960). *J. Appl. Phys.* 31:1243-1246.

Vedder, J. F. (1963). *Rev. Sci. Instrum.* 34:1175-1183.

Wuerker, R. F., Shelton, H. and Langmuir, R. V. (1959). *J. Appl. Phys.* 30:342-349.

Appendix 3

Heating System

A Carbon Dioxide Laser, producing radiation in the infrared at 10.6μm, was used to heat the particles. To determine the approximate laser power required, some calculations were made, based on a very simple heat transfer model. It was assumed that a sphere was undergoing heating by the laser. The sphere was assumed to be isothermal, so that only heat transfer at the surface would have to be considered. The primary mechanisms of heat transfer were assumed to be absorption from the laser beam, conduction to the surrounding gas, and radiation from the particle to the surrounding chamber. From Newton's law of cooling,

$$q_C = (Nu)K\frac{\Delta T}{d} \tag{1}$$

From the assumption that the sphere is in a stagnant gas, $Nu = 2$. The heat loss due to radiative transfer is:

$$q_r = \varepsilon\sigma(T_p^4 - T_\infty^4) \tag{2}$$

where ε = emissivity and σ = Stefan-Boltzmann constant. The heat input from the laser beam is the intensity, I multiplied by an absorbtivity, here assumed to be the same as the emissivity.

$$q_l = \varepsilon I \tag{3}$$

At steady state, the heat input must equal the heat output. The laser intensity to produce a the given temperature is shown for three different particle sizes in Table I.

To estimate the heating rate, the unsteady state situation is considered:

$$\frac{dT}{dt} = \frac{\pi r_p^2 \varepsilon I - 4\pi r_p K(T_p - T_\infty) - 4\pi r_p^2 \varepsilon \sigma (T_p^4 - T_\infty^4)}{mC_p} \tag{4}$$

A Runge-Kutta integration routine was used to numerically solve equation 4. Figure 1 shows the temperature for three particles heated by a laser beam with an intensity of $1.0 \times 10^7 W/m^2$. The solid line represents a 50 μm particle, the small dashed line a 25 μm particle, and the large dashed line a 10 μm particle.

The CO_2 laser beam was steered by front surface pyrex mirrors coated with aluminum (Janos Technology). A beam combiner (Laser Power Optics) was used to co-align a helium neon laser beam with the CO_2 laser beam. A 75mm fl zinc selenide lens (Janos Technology) was used to focus the laser beam. The optics are outlined in schematic form in Figure 2. Three different schemes were used to admit the laser beam into the chamber. In the first case, the beam was split and brought into the chamber horizontally, from opposite sides, as shown in Figure 2. In the second, the beam was also split, but brought into the chamber vertically, from top and bottom. In the third scheme, the laser beam was brought in vertically, but only from the top.

The different schemes were employed in an attempt to deal with problems of particle motion and uneven heating. Photophoretic forces act on the particle and tend to move the particle out of the beam (Greene et al., 1985). The log of the ratio of the photophoretic force to the particle weight versus particle radius is plotted in Figure 3. The solid line represents a particle with a density of 0.5 g/cm^3, while the dashed line represents a particle with a density of 0.05 g/cm^3. Figure 4 is a similar plot, with the log of the ratio of photophoretic force to particle weight plotted against temperature. The solid line represents a particle with a density of 0.5 g/cm^3, while the dashed line represents a particle with a density of 0.05 g/cm^3. The particle radius for both particles is 100 μm. With a Gaussian beam, the intensity is greatest at the center. Therefore, a particle experiencing photophoretic forces will tend to move out of the beam. If the beam diameter is of the same order as the particle size, the gradient experienced by the particle will strongly encourage the particle to move. A wider beam will alleviate this problem since the localized gradient will be less. This latter problem could be solved by using a more powerful laser and less focusing, however, we were limited to the 20 Watt laser on hand.

When the beam is brought in vertically, the photophoretic and thermophoretic forces are directed in the vertical direction, and compensated for by the particle positioning system. The particle still moved laterally, however, to get out of the beam. Again, a more powerful laser, with a wider beam and a more even distribution of power across the beam would solve this problem. With a less powerful laser, we decided to go with a different mode laser - a TEM-01*, or doughnut mode laser. In such a mode, the cross-section of the laser beam appears as a ring, or doughnut. Thus, a particle heated by this beam will tend to remain trapped in the ring.

References

Greene, W. M., Spjut, R. E., Bar-Ziv, E., Longwell, J. P. and Sarofim, A. F. (1985). *Langmuir.* 1:361-365.

Table I

Laser Intensity Required

Particle Radius (μm)	Temperature K	Beam Intensity W/m^2
50	1500	4.04×10^6
	2000	7.72×10^6
25	1500	6.93×10^6
	2000	1.18×10^7
10	1500	1.56×10^7
	2000	2.41×10^7

Figure Captions

Figure 1. Particle Temperature as a function of time when heated by a carbon dioxide laser. The solid line shows a particle of 50 μm radius being heated. The small dashed line shows a particle of 25 μm radius. The large dashed line represents a 10 μm radius particle. The incident laser intensity is 1.0×10^7 W/m^2.

Figure 2. Schematic of the Laser optics for directing the beams horizontally into the chamber.

Figure 3. Photophoretic force when a particle is heated from one side only. The log of the ratio of the photophoretic force to the particle weight is plotted against particle radius. The solid line represents particles with a density of 0.5 g/cm^3. The dashed line represents particles with a density of 0.05 g/cm^3.

Figure 4. Photophoretic force when a particle is heated from one side only. The log of the ratio of the photophoretic force to the particle weight is plotted against temperature. The solid line represents a particle 200 μm in diameter and 0.5 g/cm^3 density. The dashed line represents a particle 200 μm in diameter and 0.05 g/cm^3 density.

Figure 1

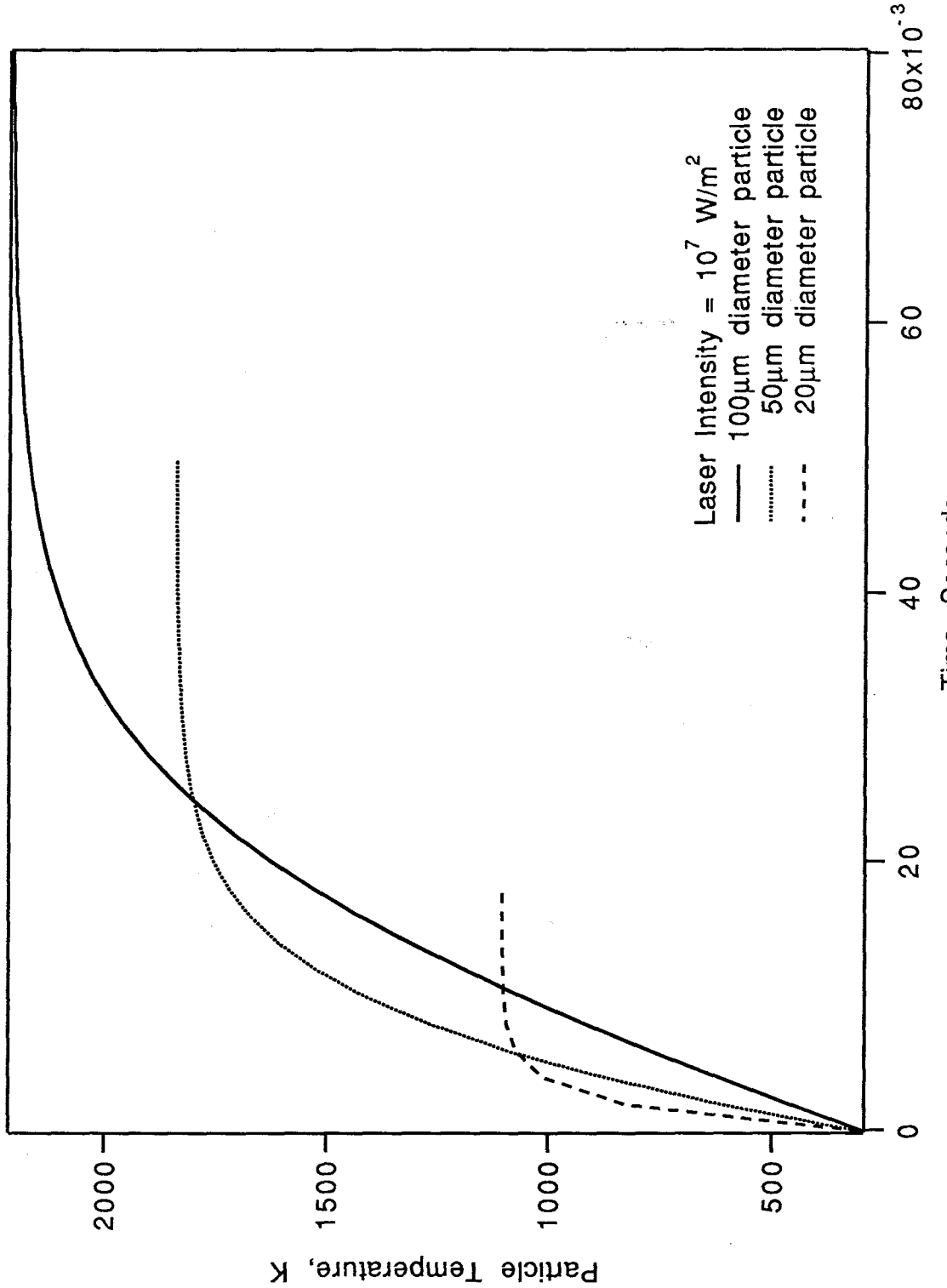
Particle Temperature, K
2000
1500
1000
500
0
20
40
60
80x10-3
Time, Seconds
Laser Intensity = 10^7 W/m^2
100µm diameter particle
50µm diameter particle
20µm diameter particle

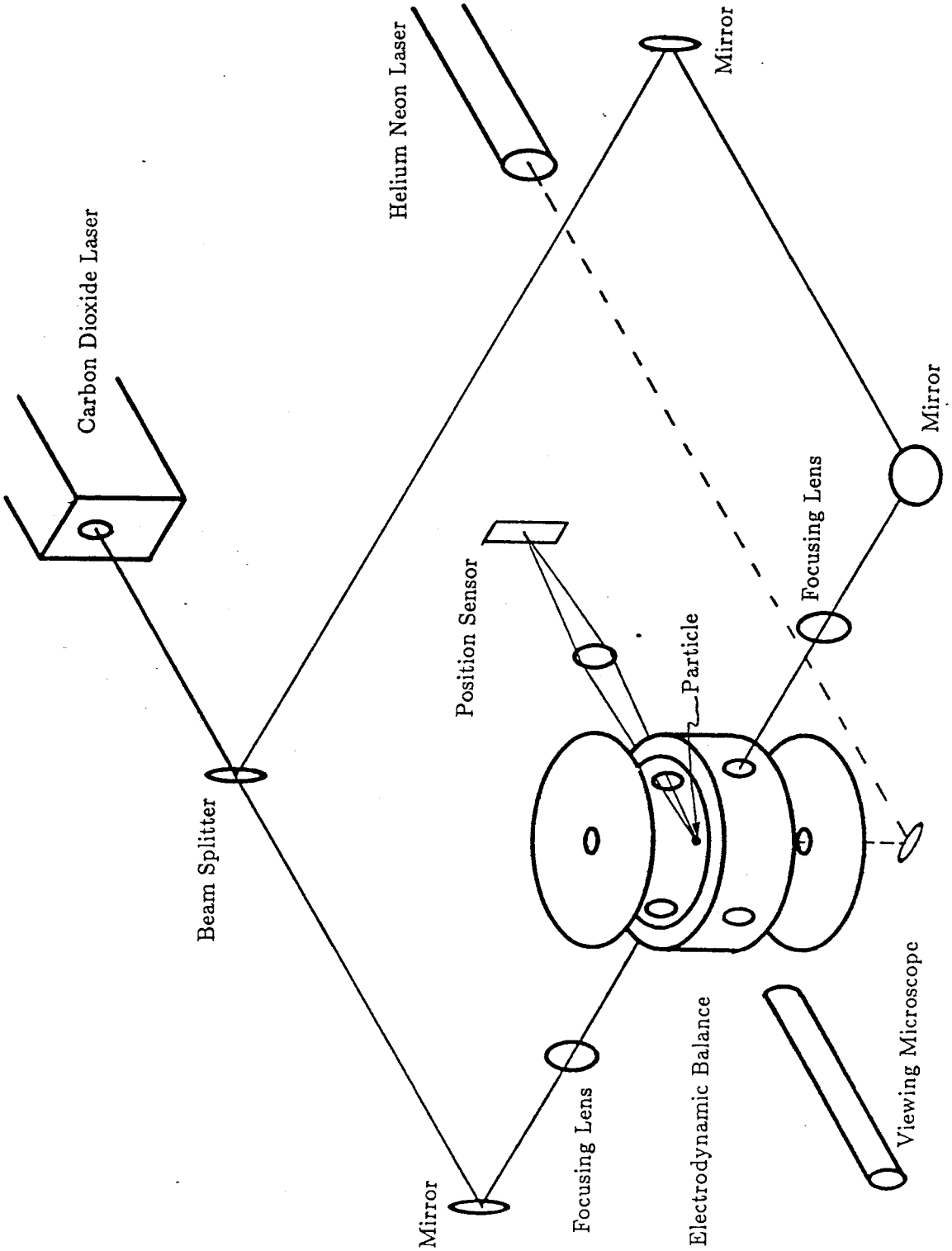

Heating and Illumination Systems

Figure 2

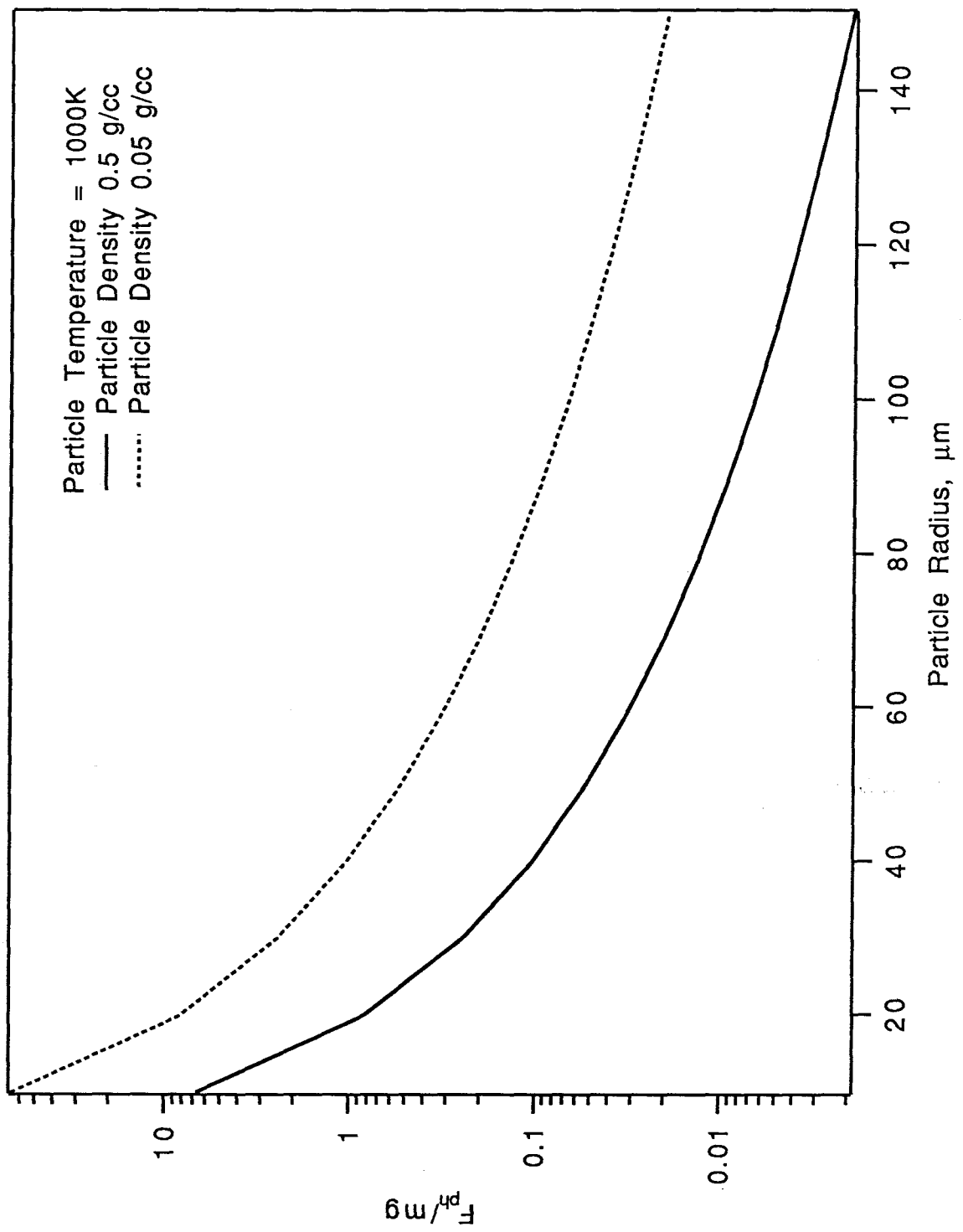
Particle Temperature = 1000K
Particle Density 0.5 g/cc
Particle Density 0.05 g/cc
F_{ph}/mg
10
1
0.1
0.01
20
40
60
80
100
120
140
Particle Radius, μm

Figure 3

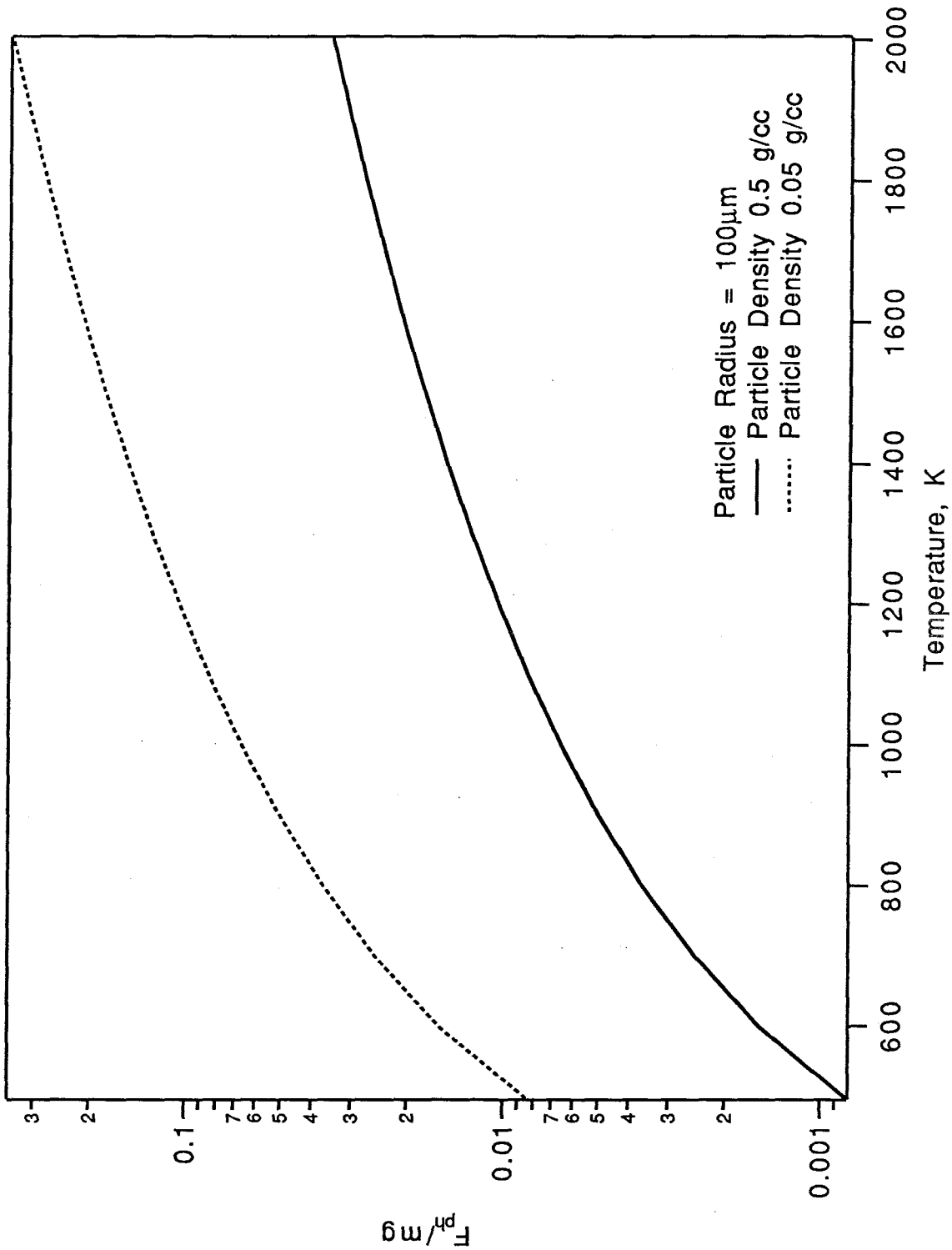
Particle Radius = 100μm
Particle Density 0.5 g/cc
Particle Density 0.05 g/cc
T_{ph}/mg
0.1
0.01
0.001
600
800
1000
1200
1400
1600
1800
2000
Temperature, K

Figure 4

Appendix 4

Particle Position Sensing and Control

When a particle is trapped and balanced in the electrodynamic balance, it is subject to two equal and opposing forces, gravity in the downward direction, and the DC electrical force in the upward direction. The AC field has a null point in the center, and the particle is not subject to the AC force when it is exactly balanced in the center of the chamber. If the particle is subjected to other forces, such as a buoyancy force due to heating by a laser, the particle will be accelerated. As the particle moves from the center, the AC field increases in strength, causing the particle to oscillate. In the vertical direction, the DC potential can be changed to compensate for any disturbing forces, and bring the particle back to the center of the cell. Systems have been developed to monitor the position of the particle and generate a correction signal to feed back to the DC voltage control to restore the particle to the center. The particle position control system is based on standard process control theory. It has been thoroughly discussed by Spjut (1985), Bar-Ziv et al. (1980). The system requires a technique to sense the position of the particle, a controller, and a feedback loop to the DC voltage supply.

A feedback system was developed to sense the position of the particle and feed back the position deviation signal to a control system to change the DC voltage whenever the particle moved away from the center of the balance in the vertical direction. In this electrodynamic balance, such a control system was

constructed, based on a linear position-sensitive photodiode (Hamamatsu S1544). The position sensitive detector consists of a resistive photosensitive solid state detector. When a spot is imaged onto the surface of the detector, a current is generated, which is transmitted to two electrodes at either end of the detector through a uniform resistive layer. The strength of each current is dependent on the location of the spot along the resistive linear detector. Thus, an imaged spot in the center of the detector generates an equal current at either end, while a spot at one end generates a strong current at that end, and a weak current at the other. The two currents can be processed to generate a nearly linear voltage response to position displacement.

The particle is illuminated by a Helium Neon Laser, brought in vertically. The image of the particle is focused by a 25mm fl lens (f1 lens) onto the PSD, in an approximately 1.5:1 magnification. The signal from the two current outputs are suitably amplified to give a voltage output in response to the displacement. The output goes to a PID controller, which generates a control signal, proportional to the displacement, and also integrates over the time the signal is displaced. The control signal is split and then goes to the DC power amplifier which controls the DC voltage. A schematic of the system is shown in Figure 1.

References

Bar-Ziv, E., Jones, D. B., Spjut, R. E., Dudek, D. R., Sarofim, A. F. and Longwell, J. P., *Combust. Flame*, 75: 81-106 (1989).

Davis, E. J., *ISA Transactions*, 26: 1-5 (1987).

Maloney, D. J., Fasching, G. E., Lawson, L. O. and Spann, J. F., *Rev. Sci. Instrum.* 60: 450-455 (1989).

Richardson, C. B., *Rev. Sci. Instrum.*, 61: 1334-1335 (1990).

Spjut, R. E., *Heat Transfer to and Position Control of electrodynamically suspended micron-sized particles,* Ph.D. Thesis, Massachussetts Institute of Technology, Cambridge, MA (1985).

Figure Captions

Figure 1. Schematic of the Position Sensitive Detector and PID electronics.

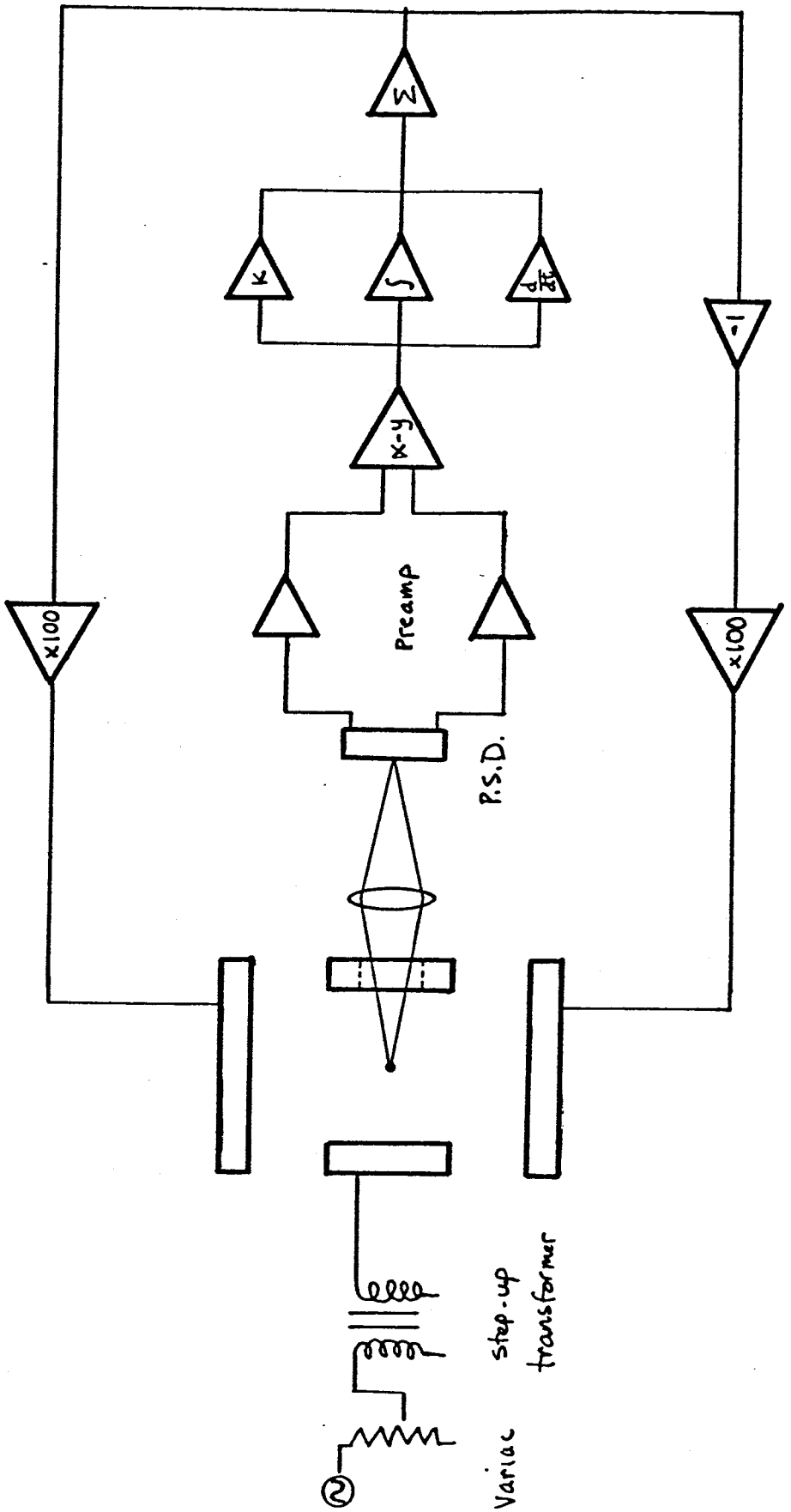

Electronic Systems
Figure 1

Appendix 5

Video System

A system was assembled so that the particles undergoing study could be videotaped for future reference. A catadioptric long range microscope (Questar QM1) was used to view the particle from approximately 22 inches. A CCD monochrome video camera (COHU Model 4180) was coupled to the microscope. Output from the video camera went to a videotape recorder (Panasonic AG1830), and then to a monitor (Electrohome EVM). Various techniques were used to videotape a particle, depending on the illumination conditions, and the kind of video record desired. In one technique, the particle was illuminated only by the helium neon laser. On the video monitor, the particle appears as a bright body against a dark background. This technique was useful for observing smoke or clouds of particulates condensing from vapor emitted by a heated particle, because the tiny particulates would scatter the helium neon radiation. The cloud would appear as a brightly lit sphere or halo around the particle.

In another technique, a helium neon laser radiation blocking filter (Micro-coatings) was used between the particle and the microscope, to prevent the HeNe radiation from reaching the camera. A white light source (an ordinary flashlight, or microscope illuminator) was placed opposite the video system with the particle in between. A diffusor, a translucent piece of plastic was put in front of the light source. In some instances it was necessary to attach an infrared blocking filter to the white light source to prevent infrared radiation from the incandescent light

from interfering with the optical pyrometer. The particle appeared as a dark object against a light background. This technique was used when the particle was likely to glow as it is heated and the servo system was being used. The HeNe laser was used to operate the servo, but the HeNe blocking filter prevented the illumination from the HeNe from swamping out the glow of the particle.

Finally, the particle was illuminated by a diffuse white light source and observed directly by the video camera. This technique was used to record particles that were not under servo control.

Appendix 6

Optical Pyrometer

Introduction

One of the objectives in constructing the electrodynamic TGA is to measure the temperature of the suspended particle. As physical methods involving contact with the particle are unusable, a noncontact means of measuring temperature must be used. Single and multi-wavelength optical pyrometry are commonly used to optically measure the temperature of surfaces (Baker et al., 1961). These techniques are based on Planck's law for the radiant power emitted by a black body in the wavelength range λ to $\lambda + \Delta\lambda$

$$i_{\lambda,b} = \frac{2C_1}{\lambda^5(e^{C_2/\lambda T} - 1)} \tag{1}$$

where C_1 and C_2 are the standard radiation constants and T is the temperature. The application of Wien's approximation to Planck's law, and assuming a non-blackbody radiator results in (Monazam et al., 1989)

$$W(\lambda,T) = \frac{C_3 A C_1 \varepsilon}{\lambda^5(e^{C_2/\lambda T} - 1)} \tag{2}$$

where $W(\lambda,T)$ is the measured radiant emissive power, C_3 contains the system calibration, A is the cross-sectional area of the emitting particle, and ε is the emissivity of the particle. If the emissivity of the surface is known, and the instrument efficiencies are known, then the temperature can be determined from

the intensity of the radiation at that wavelength.

Single wavelength pyrometry is sensitive to the emissivity and cross-sectional area of the particle. If the cross-sectional area changes, such as a reacting particle that is losing mass, measured intensity will change. This change could be misinterpreted as a change in temperature. This problem is solved by Monazam et al. (1989) by independently monitoring the particle size. An alternative is to measure the ratio between two different wavelengths

$$I = K \frac{\varepsilon_1}{\varepsilon_2} \frac{\lambda_1^5}{\lambda_2^5} \frac{(e^{C_2/\lambda_2 T} - 1)}{(e^{C_2/\lambda_1 T} - 1)} \tag{3}$$

where K contains the calibration constants. If the particle is a graybody emitter (emissivity is constant over the temperature span of interest and at the selected wavelengths), then the absolute value of the emissivity is irrelevant. There is no dependence on the cross-sectional area, so the particle can be changing size, or moving in the view volume of the detectors without causing serious error. If the viewed surface in not a graybody emitter, then there is potential for serious errors. Baxter et al. (1988) determined that coal exhibited non-gray behavior, and could cause errors in the hundreds of degrees, depending on the wavelengths chosen for the pyrometer. They also determined that coal particles became more gray as size, rank and extent of devolatilization increase. They determined that partially devolatilized samples of bituminous coal emitted as gray bodies over a large portion of the infrared spectrum.

Wavelength selection

The selection of the wavelengths to be used was based on three criteria, the

recommendations expressed by Baxter et al. (1988), the detectors available and the availability of interference filters of the proper wavelength. They stated that the errors in pyrometry measurement could be minimized by making one measurement in or near the visible region or increasing the separation between wavelengths. The wavelength selected near the visible region was 1.48 μm (6757 cm^{-1}). Figure 1 shows a spectrum of the filter. The other wavelength selected was 3.42 μm (2924 cm^{-1}), with a spectrum shown in Figure 2. The InSb detector shows a peak at approximately 5.0 μm (see Figure 3) and the InGaAs detector shows a peak at approximately 1.6 μm (Electro-Optical Systems) (see Figure 4).

The components of the optical pyrometer are mounted on rails on an elevated base. Figure 5 is a schematic of the optical system. The refractive optics and windows are all made of CaF_2, which transmits radiation from 0.15μm to 9μm. A 50 mm fl lens collimates the radiation emitted by the particle. The light is then split into two beams by a coarse grating splitter (Oriel). The grating beamsplitter is unique to this instrument. Other multicolor pyrometers have generally used partial reflector beamsplitters. The partial reflectors are generally wavelength sensitive, however. The grating beamsplitter is purely reflective. The incident light reflects off the grating in two different directions. Thus, the beamsplitter will split the incident beam, independent of wavelength (at least, throughout the range of reflectivity of the coating material). One of the reflected beams is directed through a 50 mm fl lens to a detector. Between the detector and lens is the appropriate interference filter.

The detectors were supplied with preamps. The voltage outputs from the preamps were converted to currents, and input into a log-ratio amplifier (Analog Devices 757N). Output from the InSb detector was first biased, to take care of

offset.

The optical pyrometer was calibrated with a type R thermocouple. The bead diameter was approximately 215 μm. The thermocouple bead was located in place of the particle. The bead was heated by the CO_2 laser, and observed by the optical pyrometer. The output from the thermocouple was converted to voltage, and then to temperature. The output from the optical pyrometer was compared with the output from the thermocouple. In practice, the laser was programmed to slowly increase and decrease power, so that the thermocouple would slowly heat and cool. Data from both the thermocouple and the optical pyrometer were acquired and stored. The data from several heating and cooling cycles is shown in Figure 6.

Corrections must be made for the non-graybody behavior of platinum. The voltage output from the optical pyrometer is the log of equation 3:

$$V = -G \log K \left(\frac{\varepsilon_{P,1}}{\varepsilon_{P,2}}\right)\left(\frac{\lambda_2^5}{\lambda_1^5}\right)\frac{(e^{C_2/\lambda_2 T_m} - 1)}{(e^{C_2/\lambda_1 T_m} - 1)} \tag{4}$$

where G is the gain of the log-ratio amplifier, $\varepsilon_{P,1}$ is the spectral emissivity of platinum at λ_1 and T_m, $\varepsilon_{P,2}$ is the spectral emissivity of platinum at λ_2 and T_m, and T_m is the temperature measured by the thermocouple. The output of the optical pyrometer when measuring the temperature of a suspended particle is:

$$V = -G \log K \left(\frac{\varepsilon_{C,1}}{\varepsilon_{C,2}}\right)\left(\frac{\lambda_2^5}{\lambda_1^5}\right)\frac{(e^{C_2/\lambda_2 T_C} - 1)}{(e^{C_2/\lambda_1 T_C} - 1)} \tag{5}$$

where $\varepsilon_{C,1}$ is the spectral emissivity of the particle at λ_1 and T_C, $\varepsilon_{C,2}$ is the spectral emissivity of the particle at λ_2 and T_C, and T_C is the temperature of the

suspended particle. Equating 4 and 5, we get

$$\left(\frac{\varepsilon_{C,1}}{\varepsilon_{C,2}}\right)\frac{(e^{C_2/\lambda_2 T_C}-1)}{(e^{C_2/\lambda_1 T_C}-1)} = \left(\frac{\varepsilon_{P,1}}{\varepsilon_{P,2}}\right)\frac{(e^{C_2/\lambda_2 T_m}-1)}{(e^{C_2/\lambda_1 T_m}-1)} \tag{6}$$

If $e^{C_2/\lambda T} >> 1$, then we can eliminate the -1 term. This assumption is reasonable for λ_1 out to $T = 1800$K, where the error is about 0.5%. For λ_2, at $T = 900$K, the error is about 1%. Thus, the assumption begins to break down beyond 1000K, but we will use it for now. Equation 6 can be solved by numerical means for greater accuracy. With the assumption, equation 6 becomes:

$$e^{C_2/\lambda_2 T_C} - C_2/\lambda_1 T_C = \left(\frac{\varepsilon_{C,2}}{\varepsilon_{C,1}}\right)\left(\frac{\varepsilon_{P,1}}{\varepsilon_{P,2}}\right) e^{C_2/\lambda_2 T_m} - C_2/\lambda_1 T_m \tag{7}$$

Finally,

$$T_C = \frac{\left(\frac{\lambda_1-\lambda_2}{\lambda_1\lambda_2}\right) C_2 T_m}{\left(\frac{\lambda_1-\lambda_2}{\lambda_1\lambda_2}\right) C_2 \; + \; ln\left(\frac{\varepsilon_{C,2}}{\varepsilon_{C,1}}\right)\left(\frac{\varepsilon_{P,1}}{\varepsilon_{P,2}}\right) T_m} \tag{8}$$

This equation is then used to correct the temperature obtained from Figure 6 for the emissivity of platinum. Values for the spectal emissivity of platinum at two different temperatures, 830 and 1400K, were obtained from Touloukian and Dewitt, 1970. Emissivity values for other temperatures were calculated, assuming a linear dependency on temperature. If the spectral emissivity of the chars was known, values can be substituted appropriately. Otherwise, as mentioned above, it is assumed that the chars radiate as graybodies.

References

Baker, H. D., Ryder, E. A. and Baker, N. H. (1961). *Temperature Measurement in Engineering*, J. Wiley and Sons, Inc, New York.

Baxter, L. L., Fletcher, T. H. and Ottesen, D. K. (1988). *Energy and Fuels.* 2:423-430.

Monazam, E. R., Maloney D. J. and Lawson, L. O. (1989). *Rev. Sci. Instrum.*, 60: 3460-3465.

Touloukian, Y. S. and DeWitt, D. P. (1970). *Thermal Radiation Properties of Metallic Elements and Alloys.* IFI/Plenum Press, New York, p. 536.

Figures

Figure 1

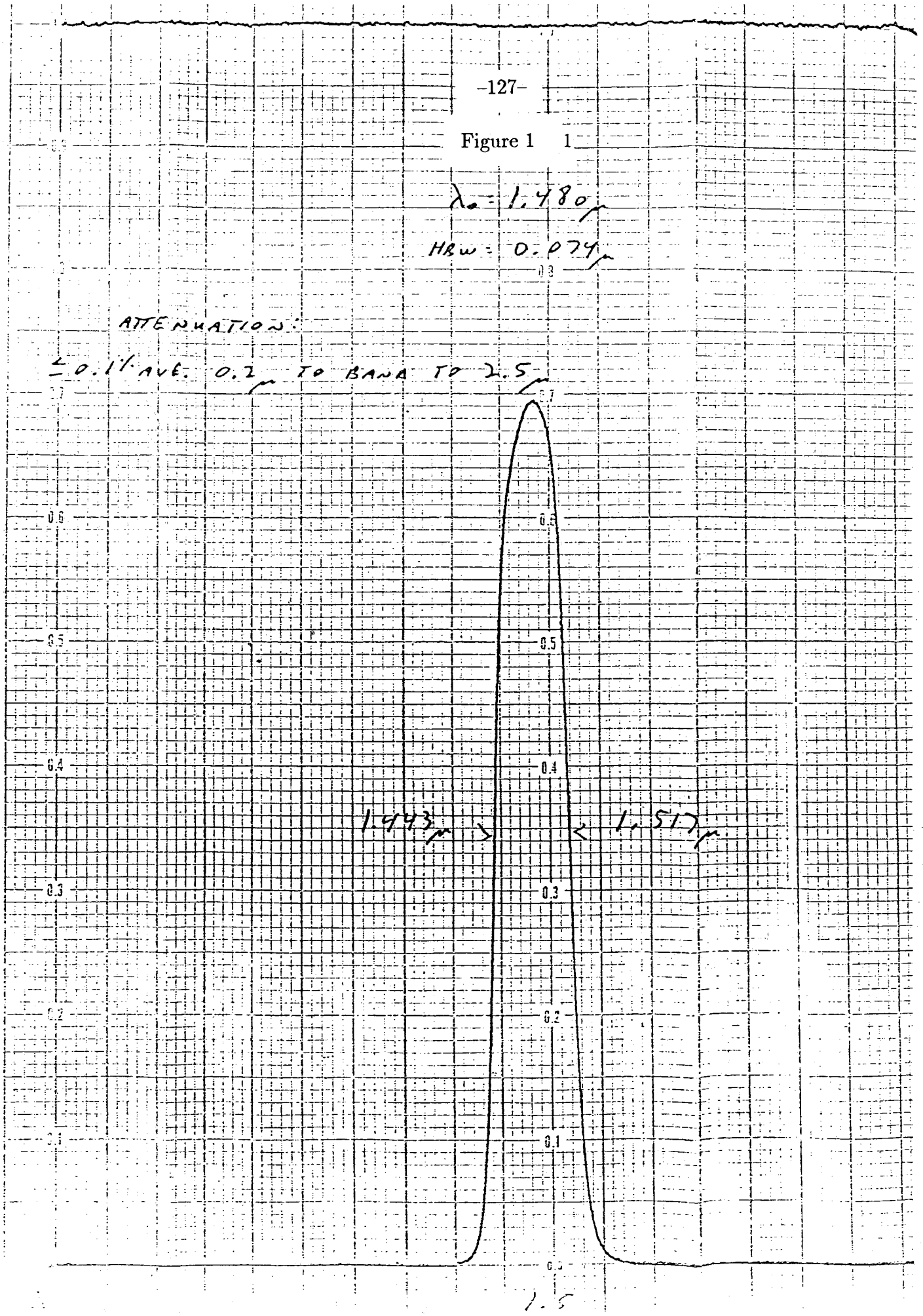
λo = 1.480 μ
HBW = 0.074 μ
ATTENUATION:
± 0.1% AVE. 0.2 μ TO BAND TO 2.5 μ
1.443 μ
1.517 μ
0.7
0.6
0.5
0.4
0.3
0.2
0.1
0.0
1.5

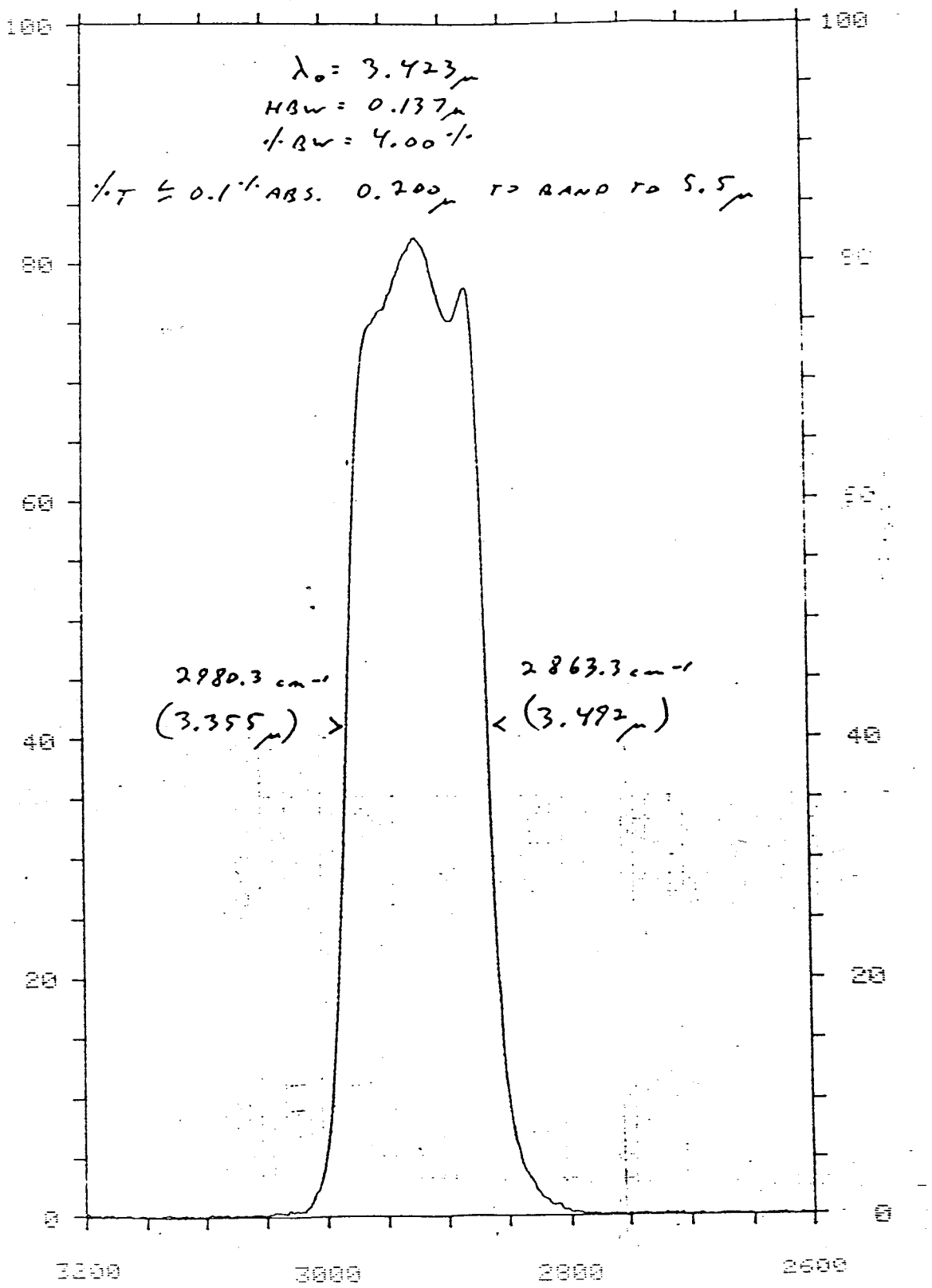

NC342

PERKIN-ELI

DATE 4-10

SAMPLE I

581-04

OPERATOR

SCAN MODE

NOISE FIL

RESOLUTIO

ORDINATE

RANGE 320

ANGLE :

SUBSTRA

TEMP:

Figure 2

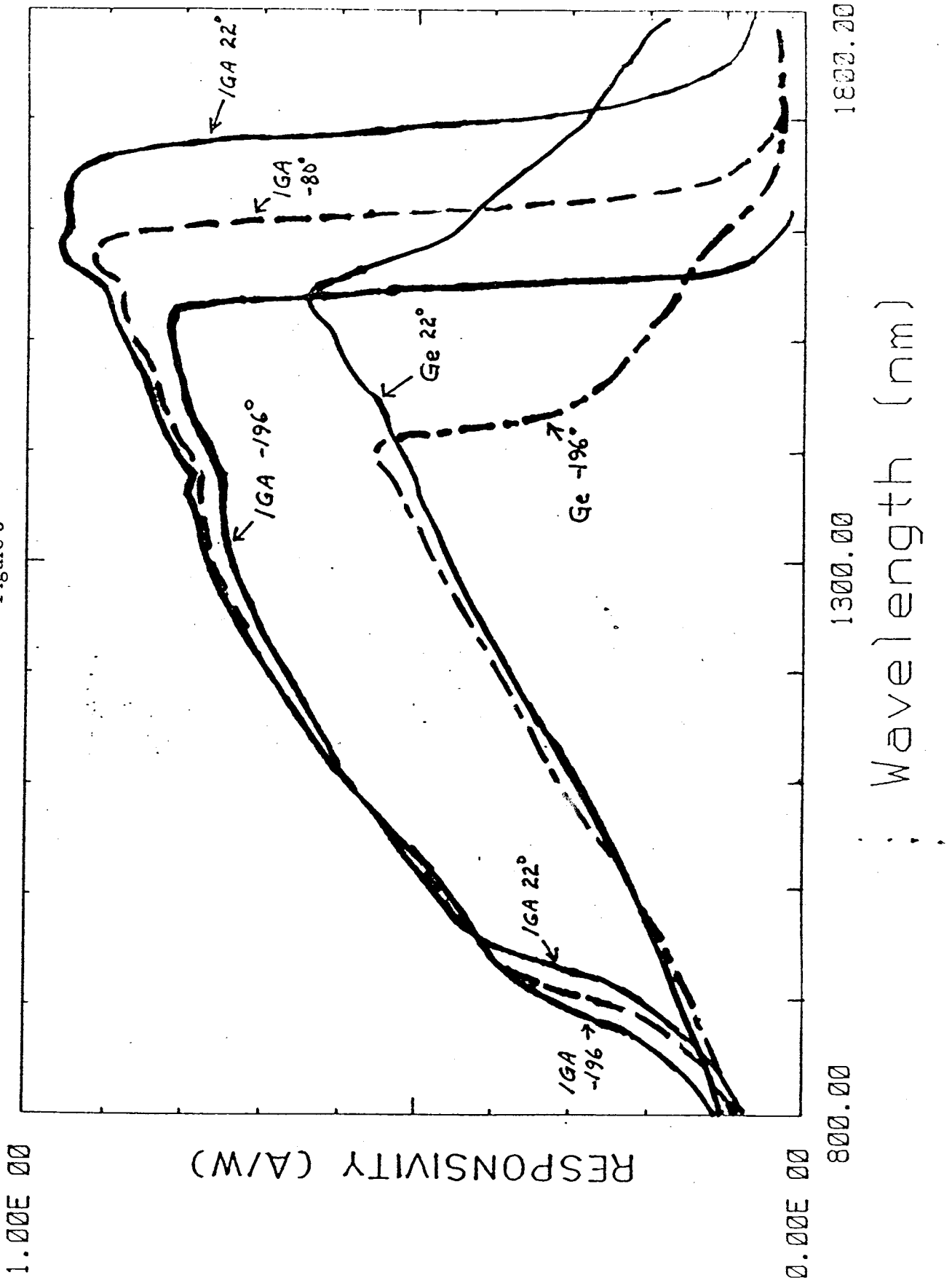
1.00E 00
0.00E 00
RESPONSIVITY (A/W)
800.00
1300.00
1800.00
Wavelength (nm)
IGA 22°
IGA -80°
Ge 22°
IGA -196°
Ge -196°
IGA 22°
IGA -196°

Figure 3

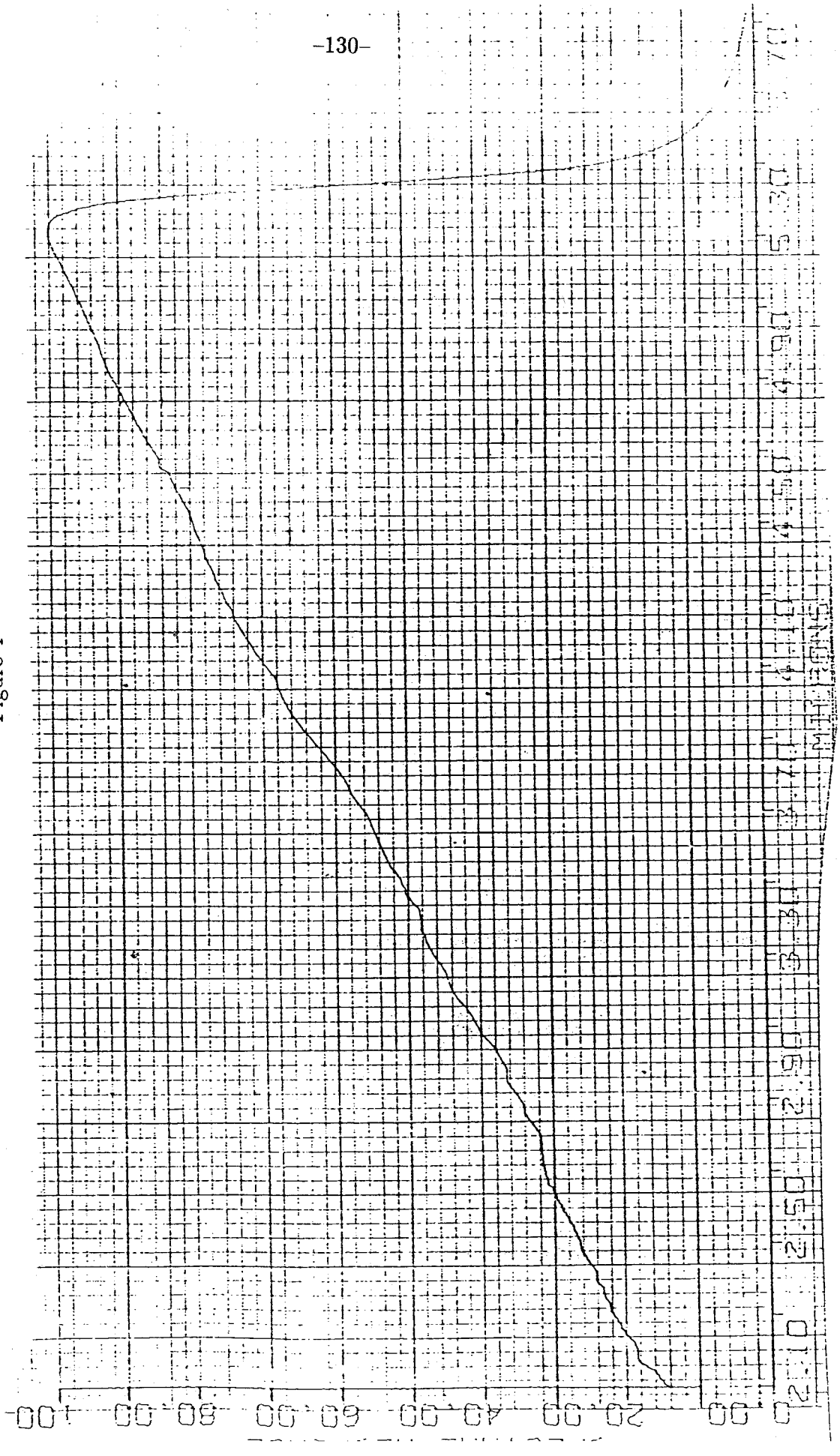

Figure 4

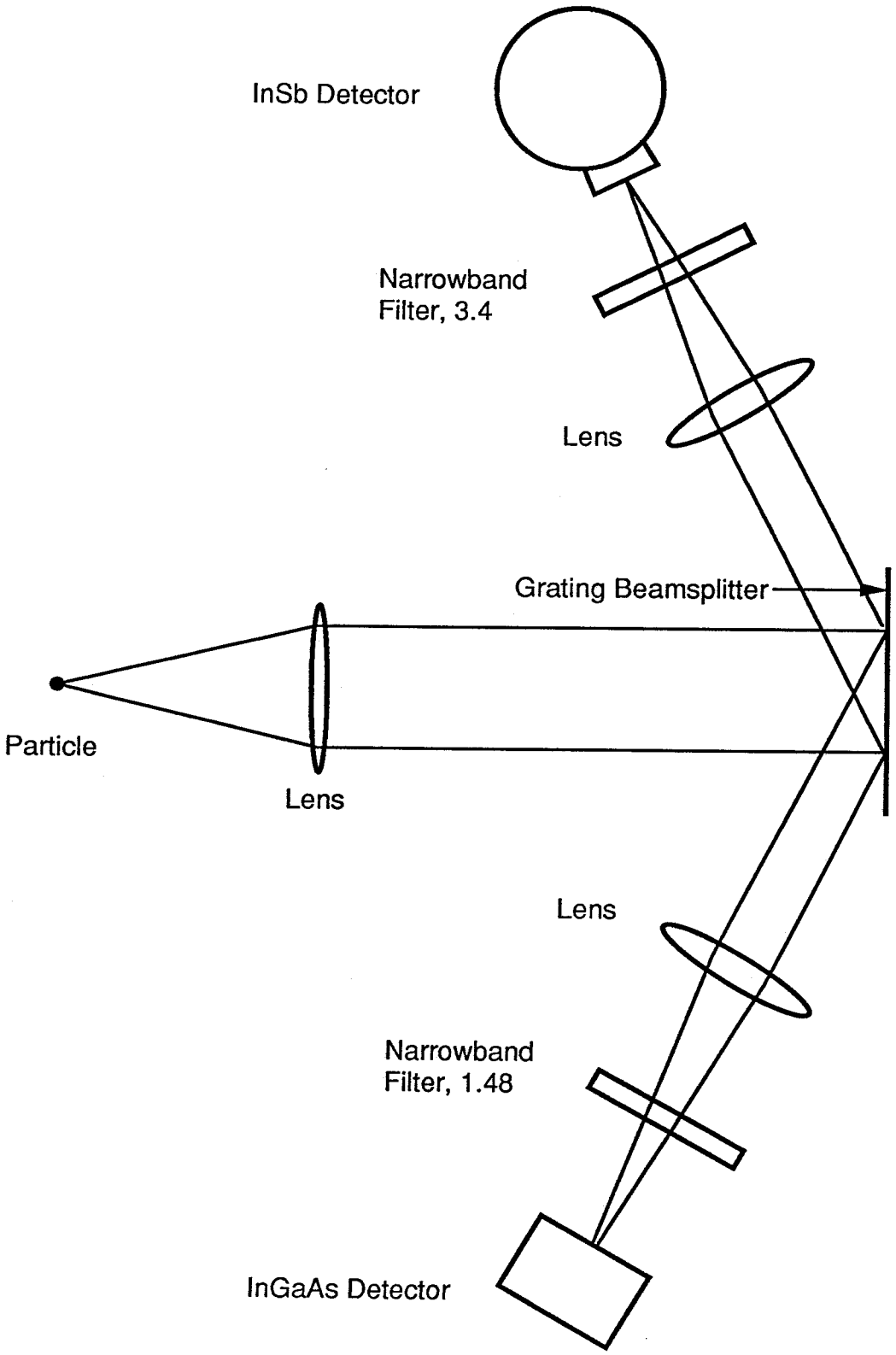

Figure 5. Pyrometer Schematic

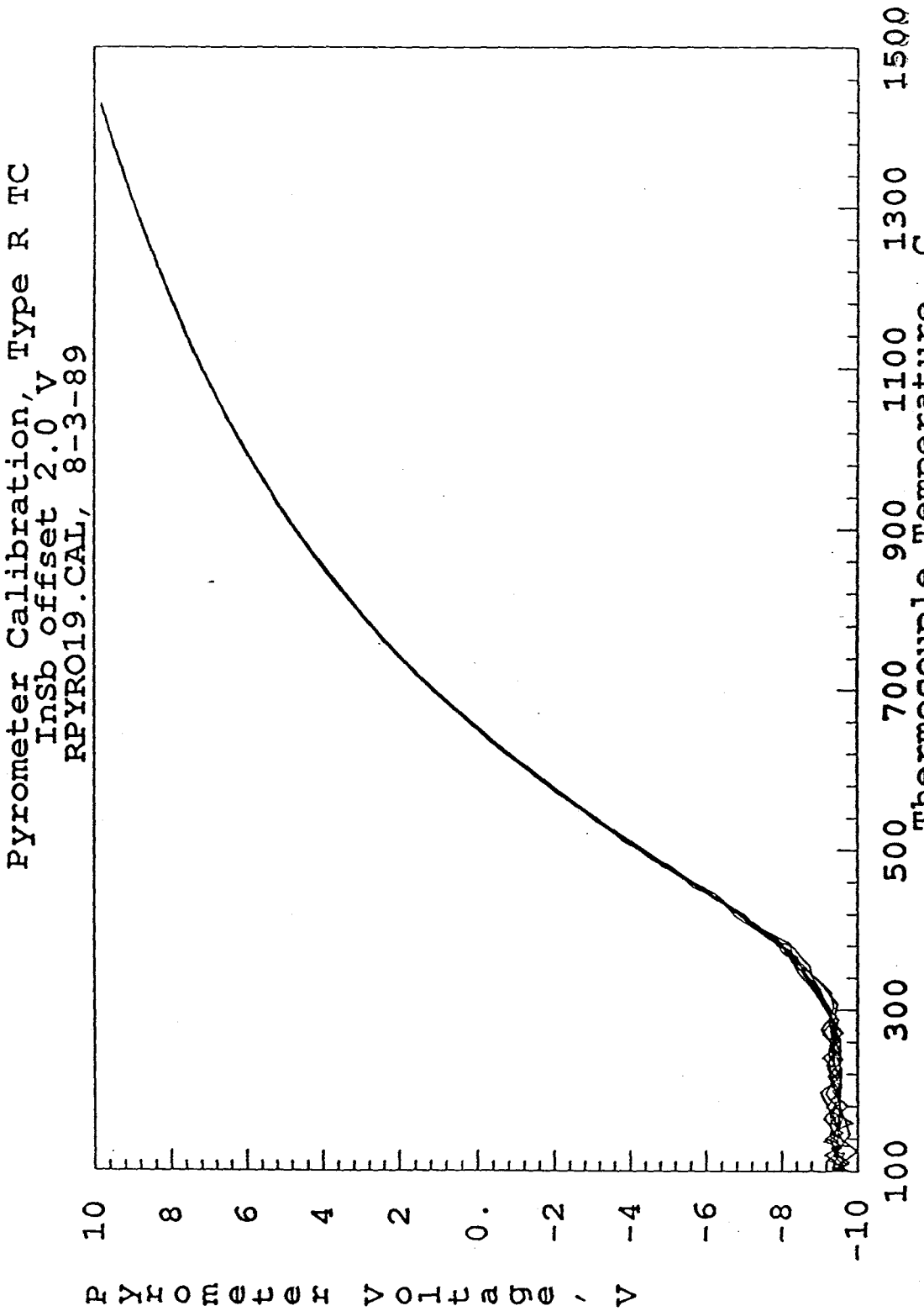
Pyrometer Calibration, Type R TC
InSb offset 2.0 V
RPYRO19.CAL, 8-3-89
Pyrometer Voltage, V
10
8
6
4
2
0.
-2
-4
-6
-8
-10
100
300
500
700
900
1100
1300
1500
Thermocouple Temperature, C

Figure 6

Appendix 7

The following graphs are temperature traces for the particles that were heated for the experiment described in Chapter 2.

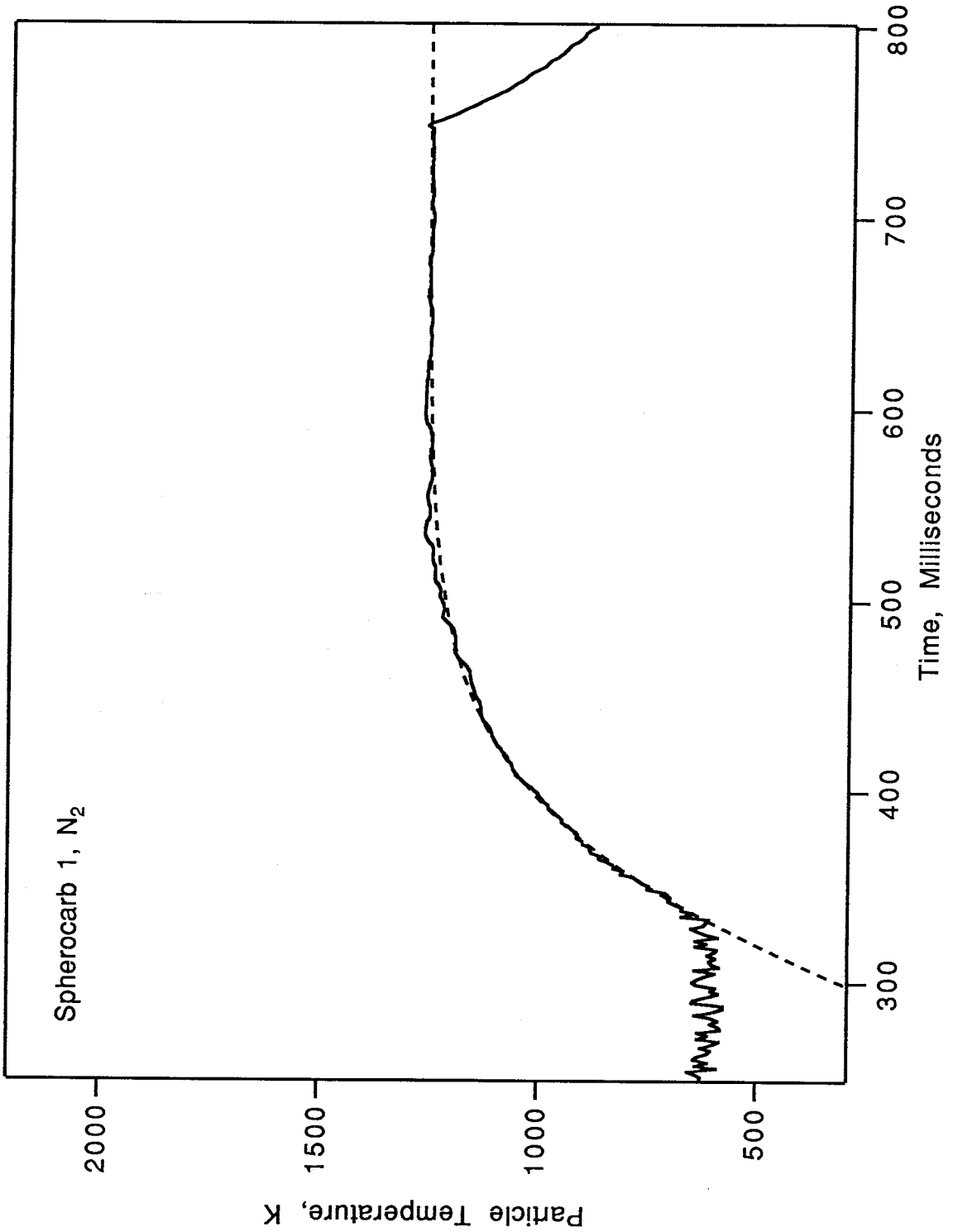
Spherocarb 1, N_2
Particle Temperature, K
2000
1500
1000
500
300
400
500
600
700
800
Time, Milliseconds

Figure 1

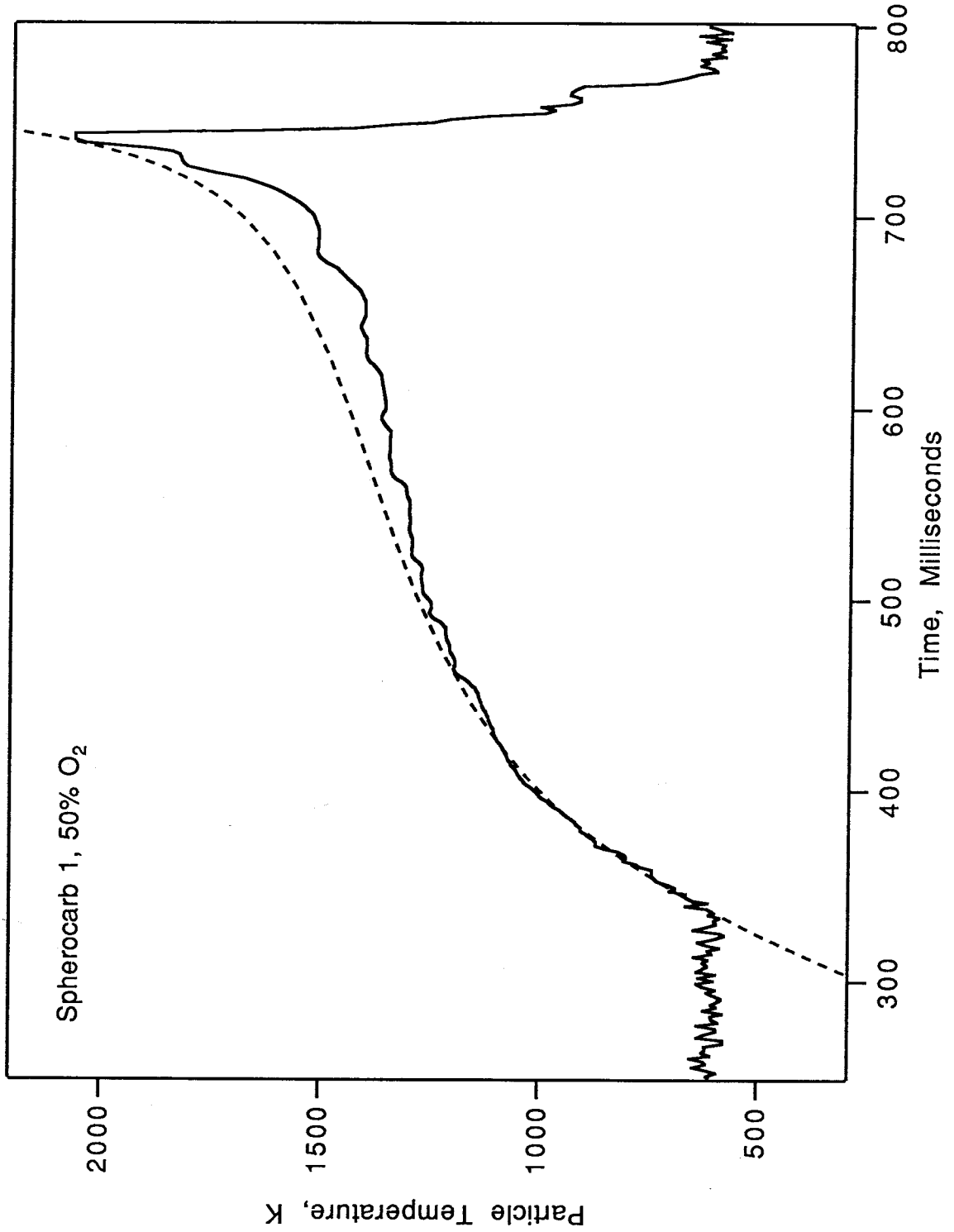
Spherocarb 1, 50% O_2
Particle Temperature, K
2000
1500
1000
500
300
400
500
600
700
800
Time, Milliseconds

Figure 2

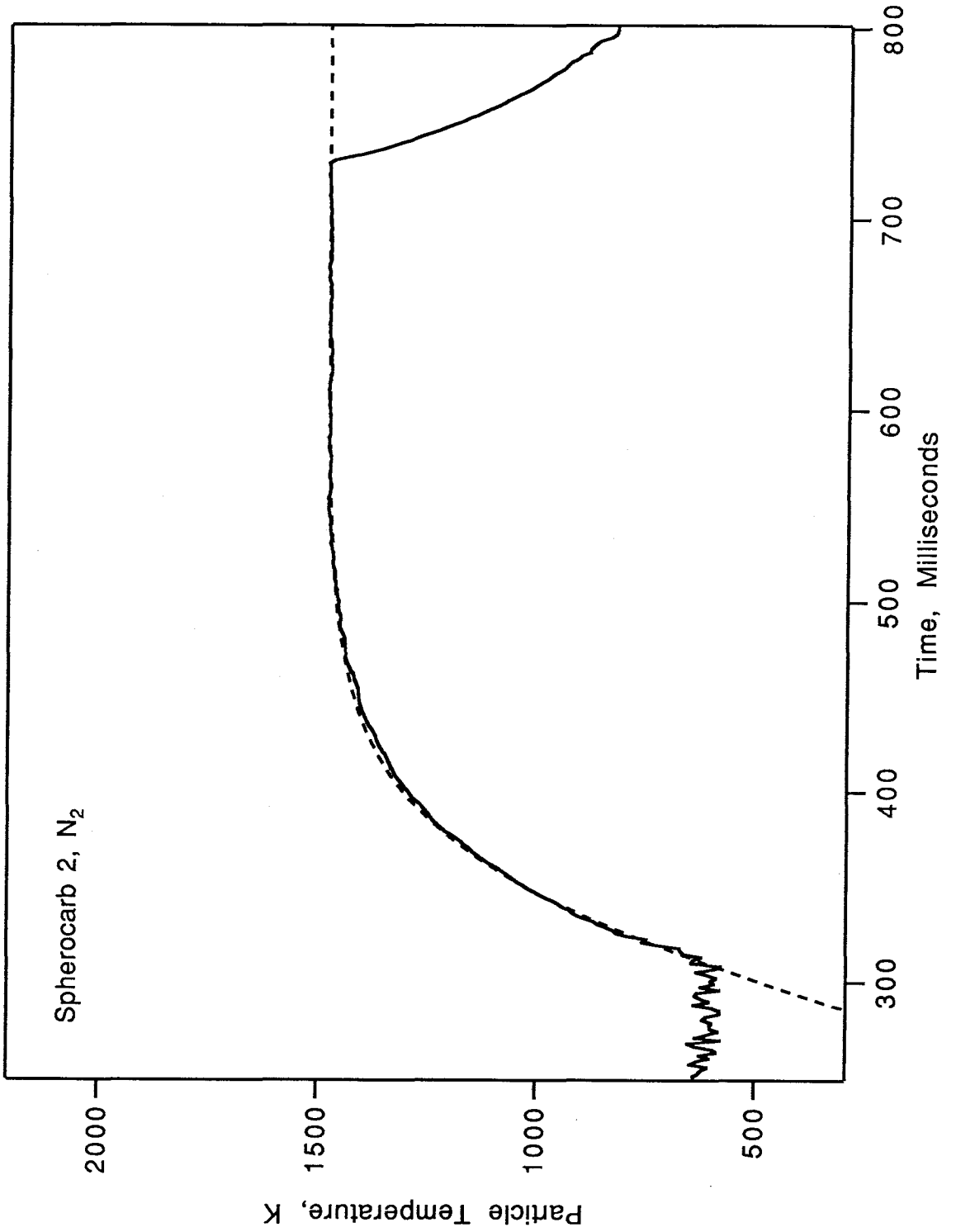
Spherocarb 2, N_2
Particle Temperature, K
2000
1500
1000
500
300
400
500
600
700
800
Time, Milliseconds

Figure 3

Figure 4

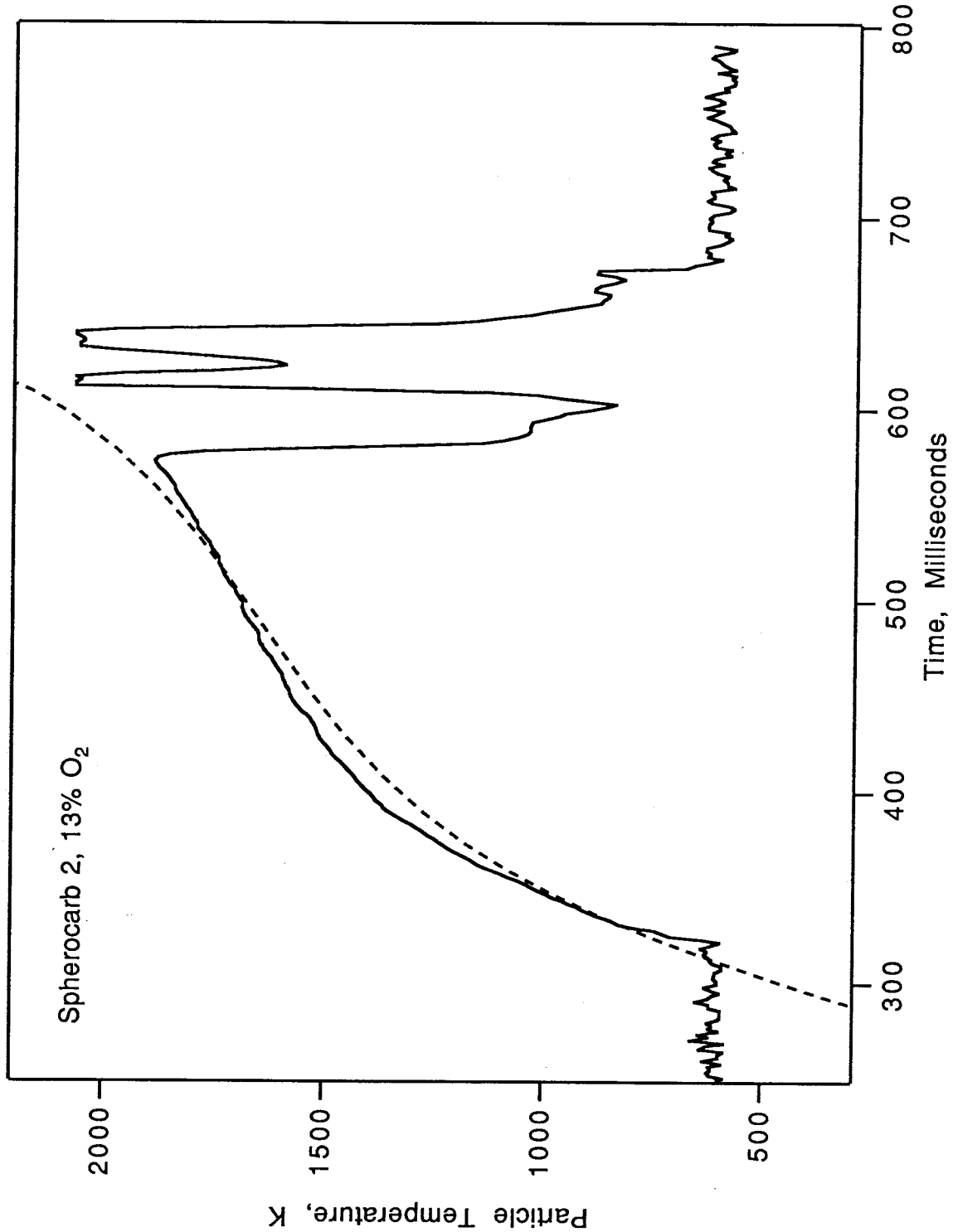
Spherocarb 2, 13% O_2
Particle Temperature, K
2000
1500
1000
500
300
400
500
600
700
800
Time, Milliseconds

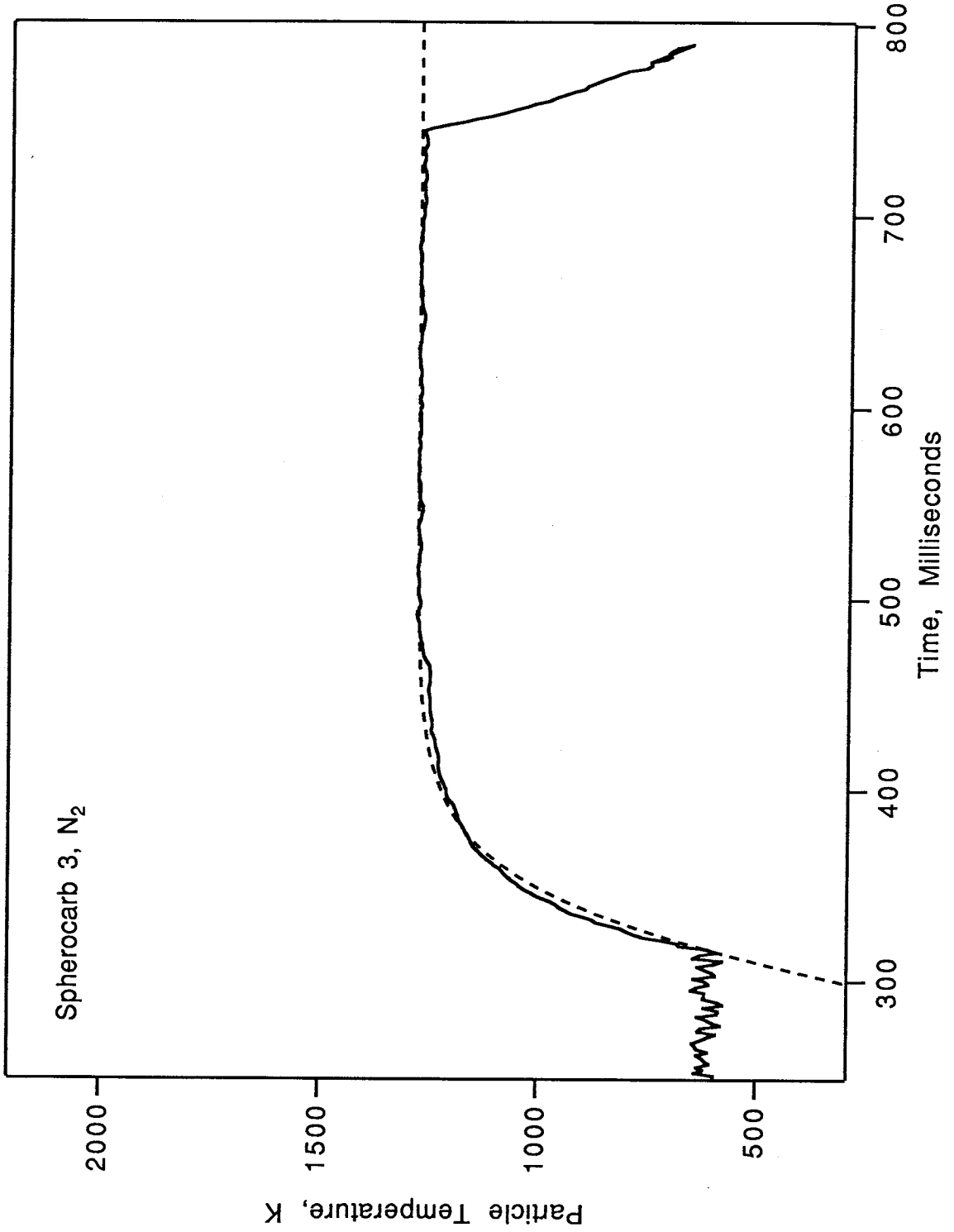
Spherocarb 3, N_2
Particle Temperature, K
2000
1500
1000
500
300
400
500
600
700
800
Time, Milliseconds

Figure 5

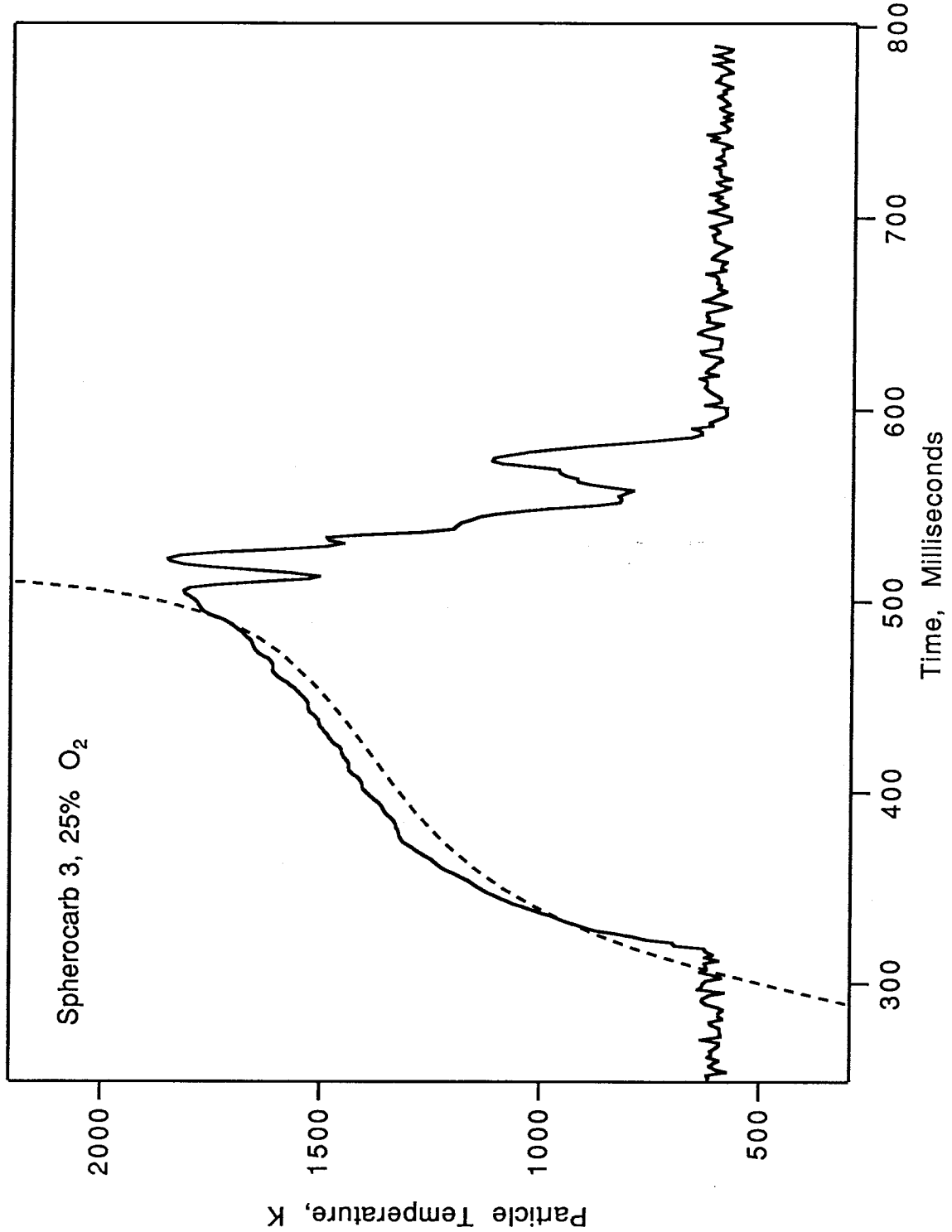
Spherocarb 3, 25% O_2
Particle Temperature, K
2000
1500
1000
500
300
400
500
600
700
800
Time, Milliseconds

Figure 6

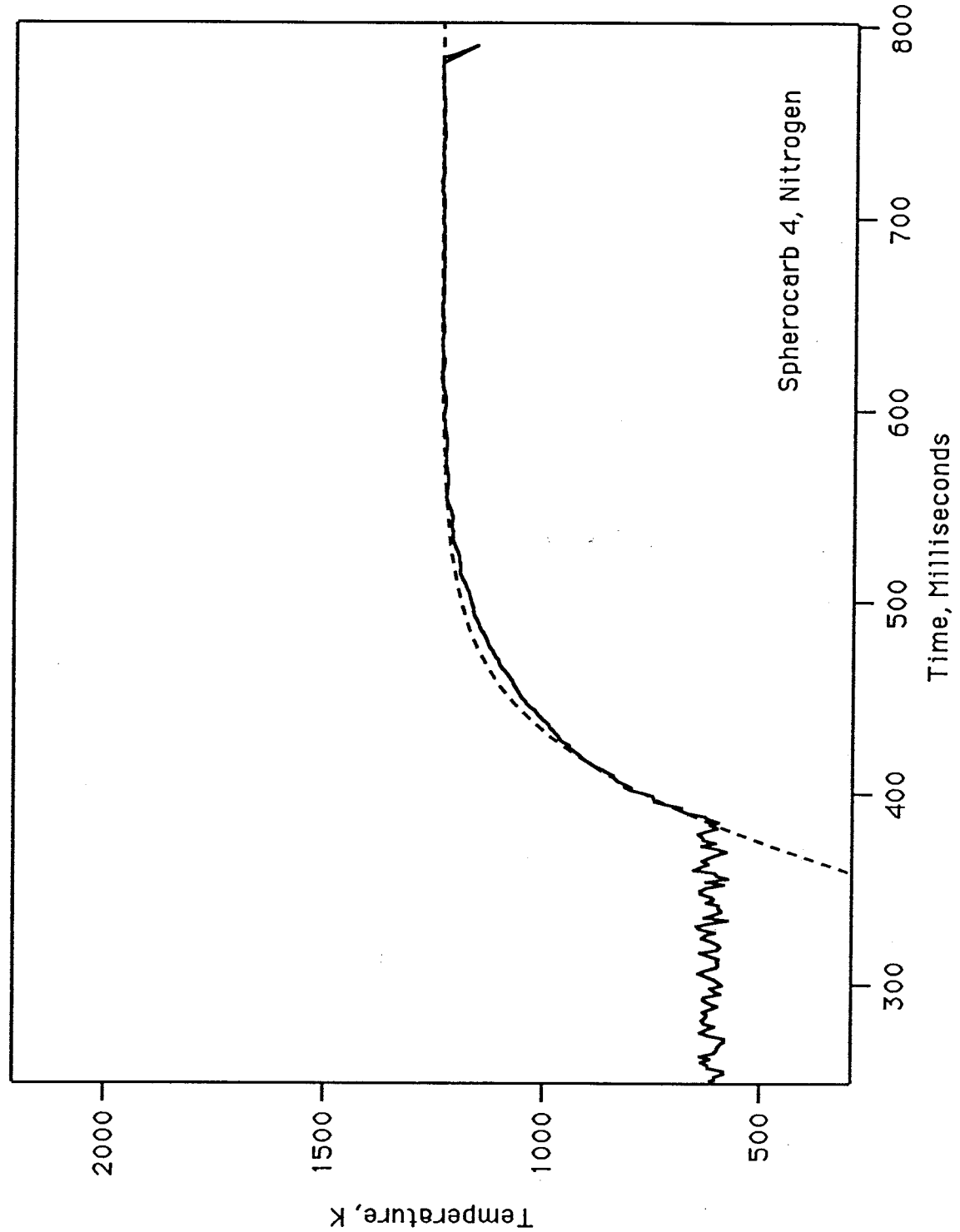
Temperature, K
2000
1500
1000
500
300
400
500
600
700
800
Time, Milliseconds
Spherocarb 4, Nitrogen

Figure 7

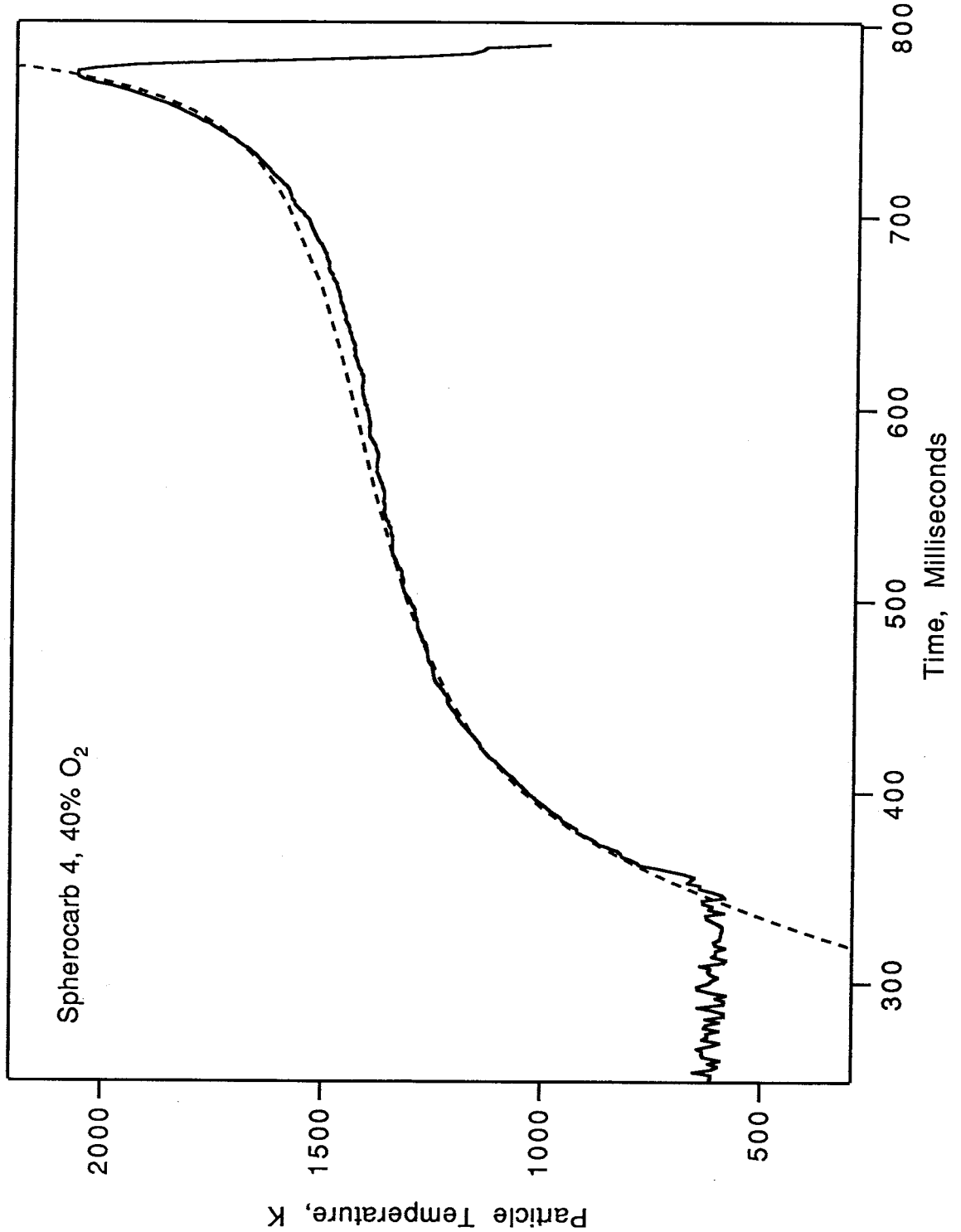
Spherocarb 4, 40% O_2
Particle Temperature, K
2000
1500
1000
500
300
400
500
600
700
800
Time, Milliseconds

Figure 8

Figure 9

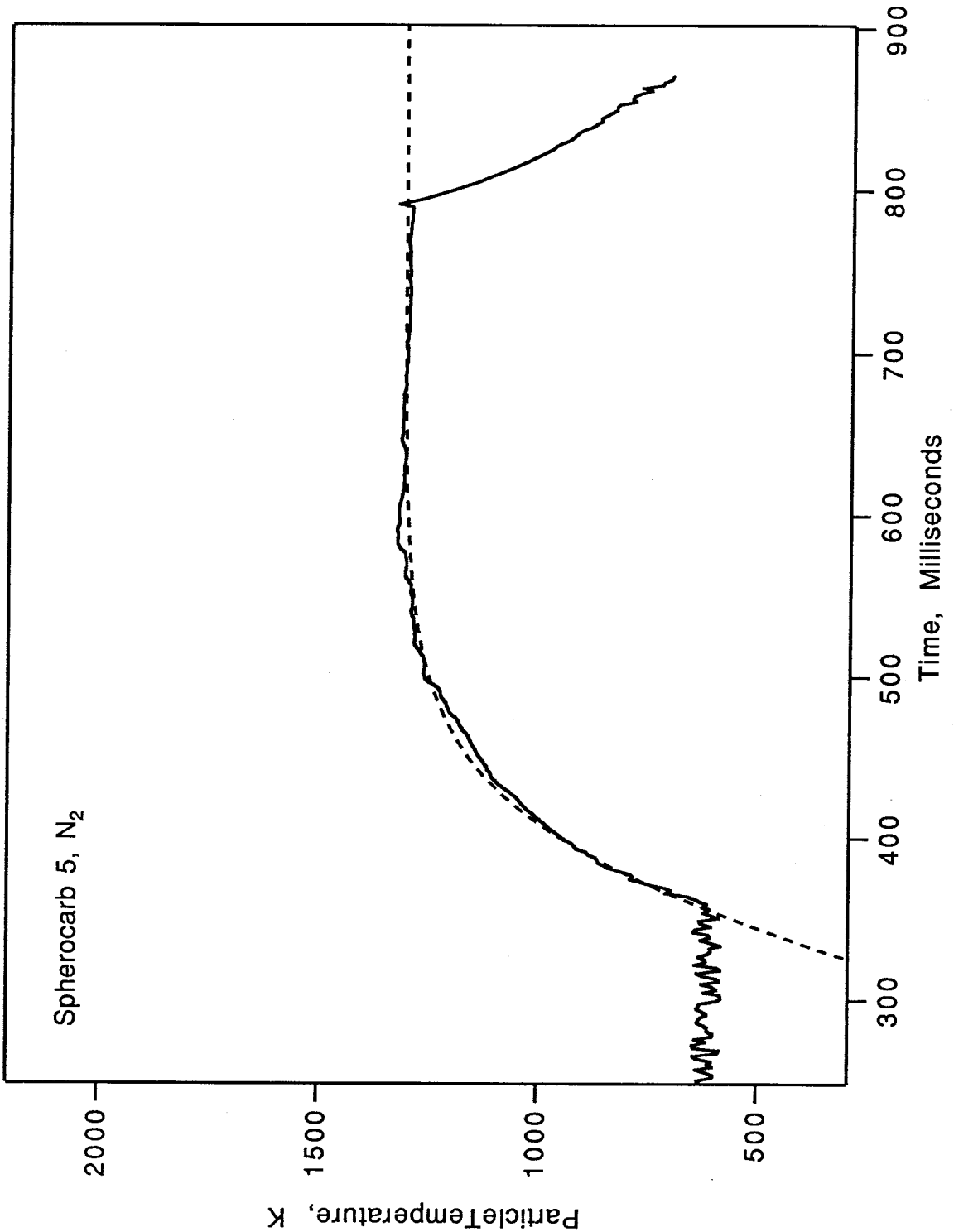
Spherocarb 5, N_2
ParticleTemperature, K
2000
1500
1000
500
300
400
500
600
700
800
900
Time, Milliseconds

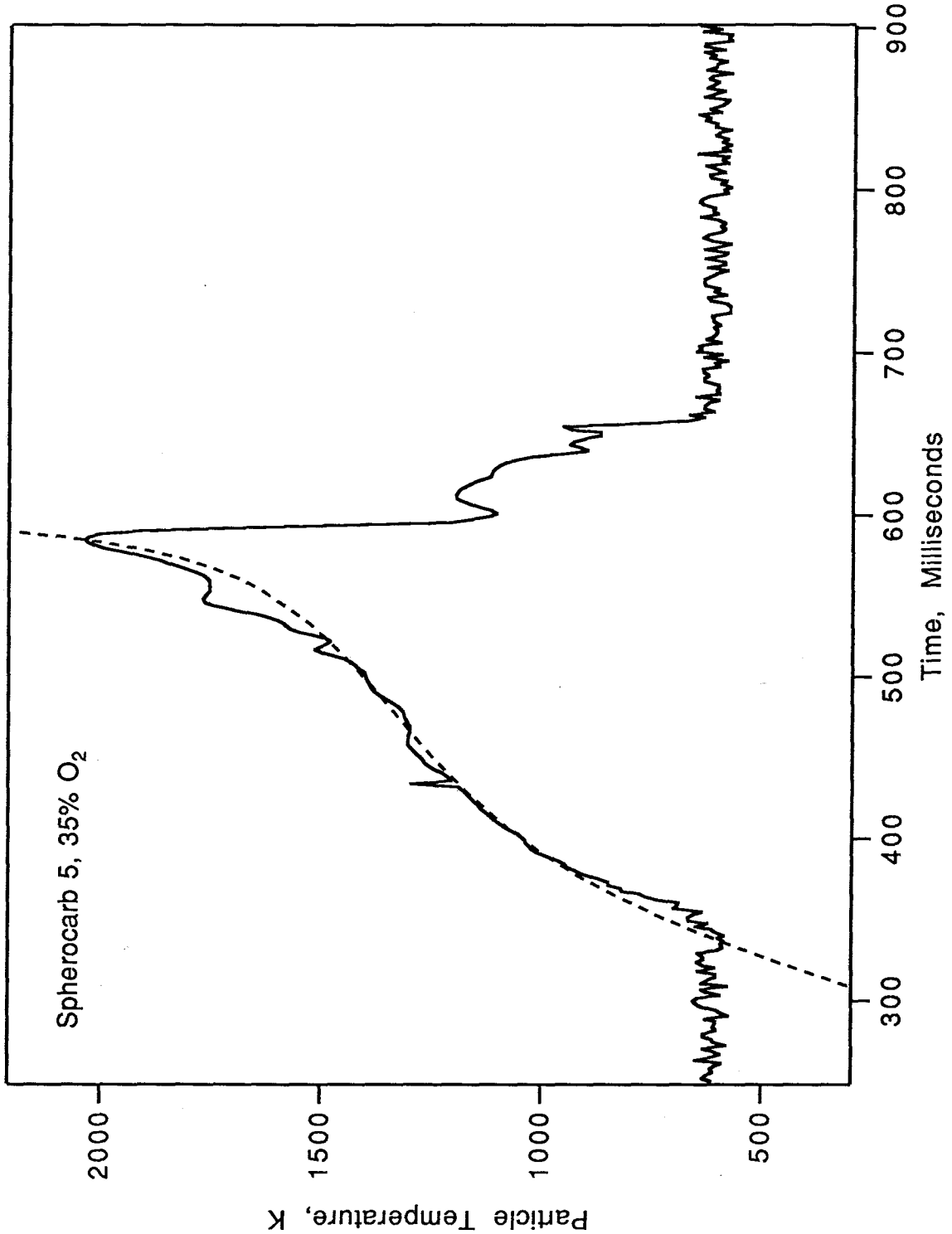
Spherocarb 5, 35% O_2
Particle Temperature, K
2000
1500
1000
500
300
400
500
600
700
800
900
Time, Milliseconds

Figure 10

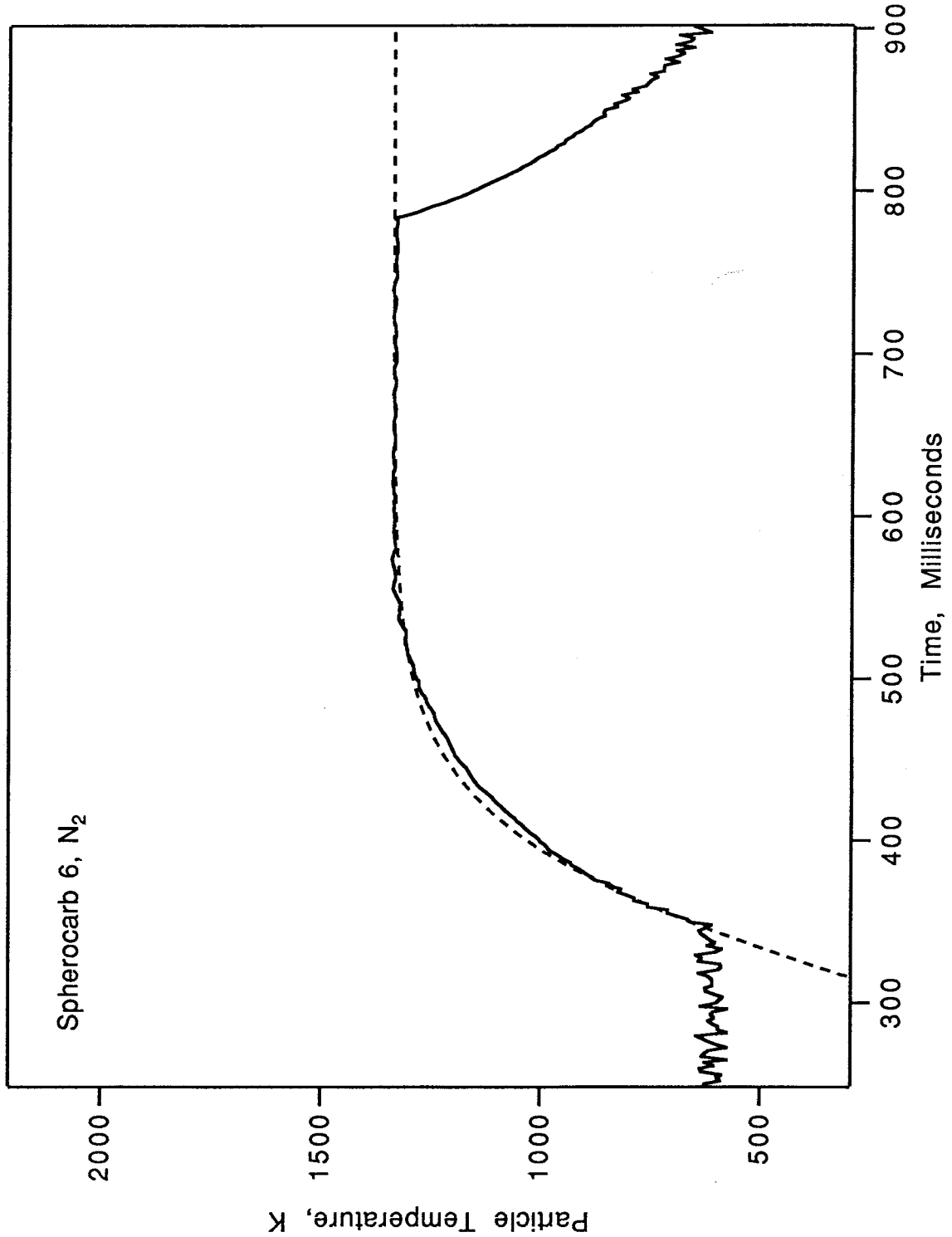
Spherocarb 6, N_2
Particle Temperature, K
2000
1500
1000
500
300
400
500
600
700
800
900
Time, Milliseconds

Figure 11

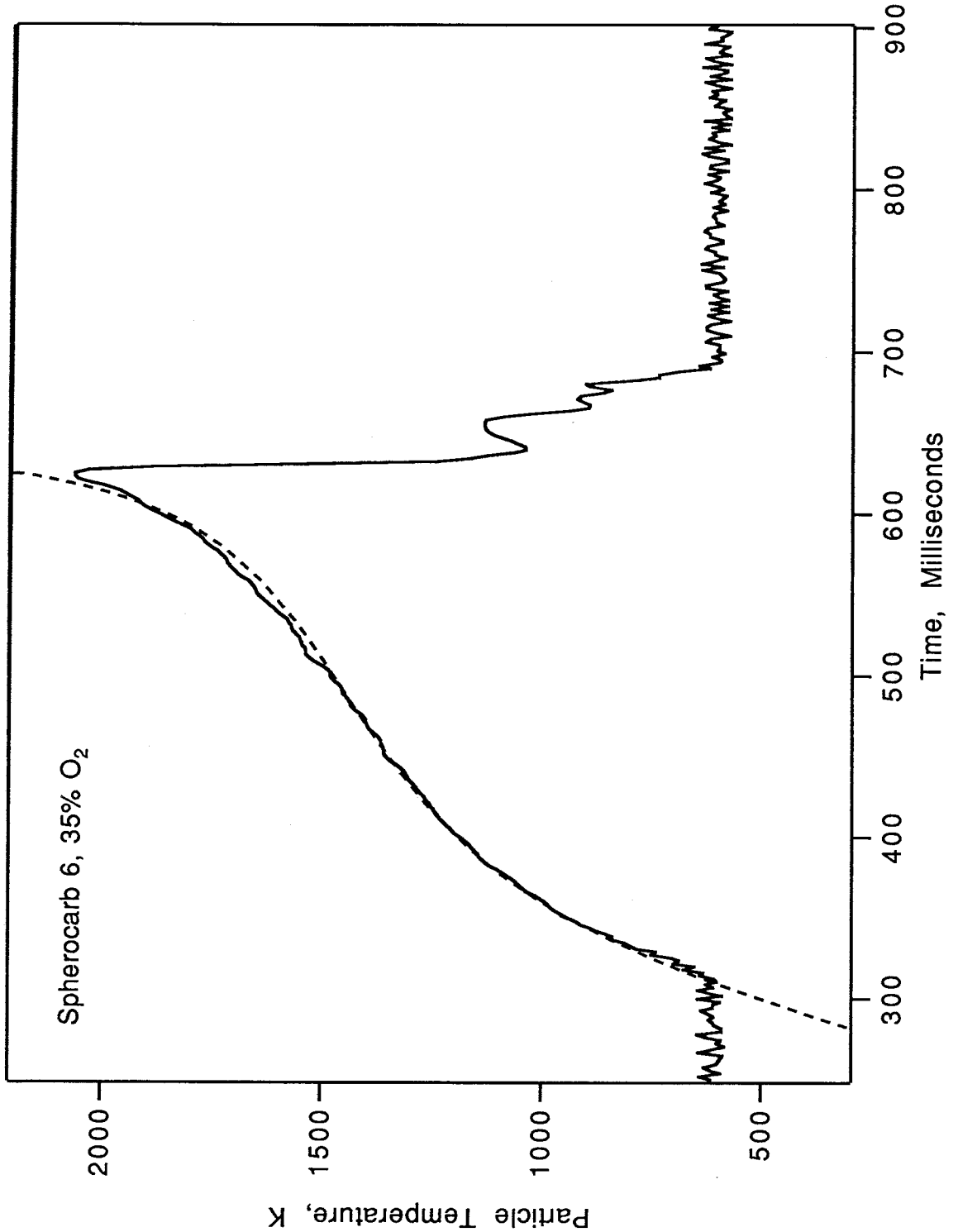
Spherocarb 6, 35% O_2
Particle Temperature, K
2000
1500
1000
500
300
400
500
600
700
800
900
Time, Milliseconds

Figure 12

Figure 13

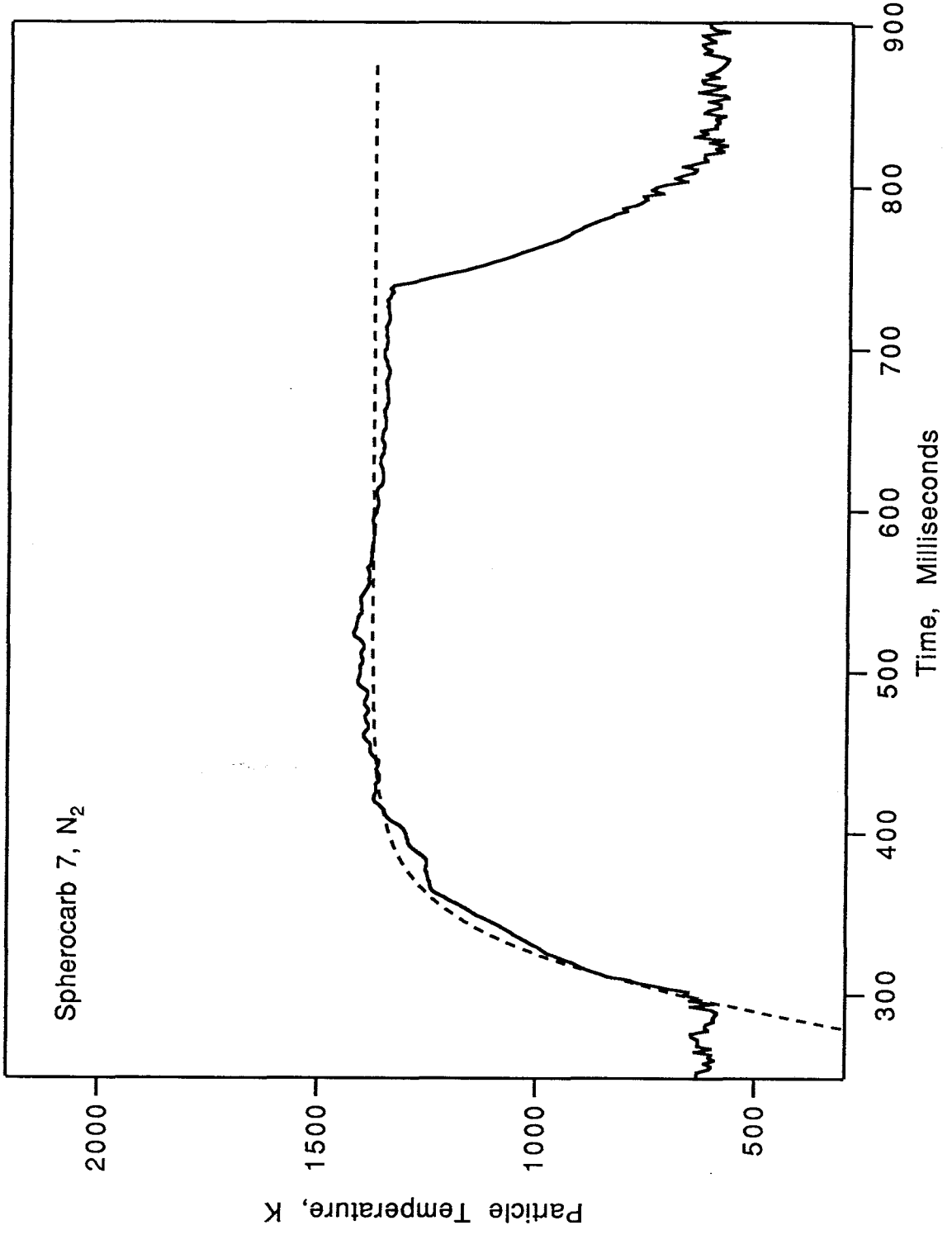
Spherocarb 7, N_2
Particle Temperature, K
2000
1500
1000
500
300
400
500
600
700
800
900
Time, Milliseconds

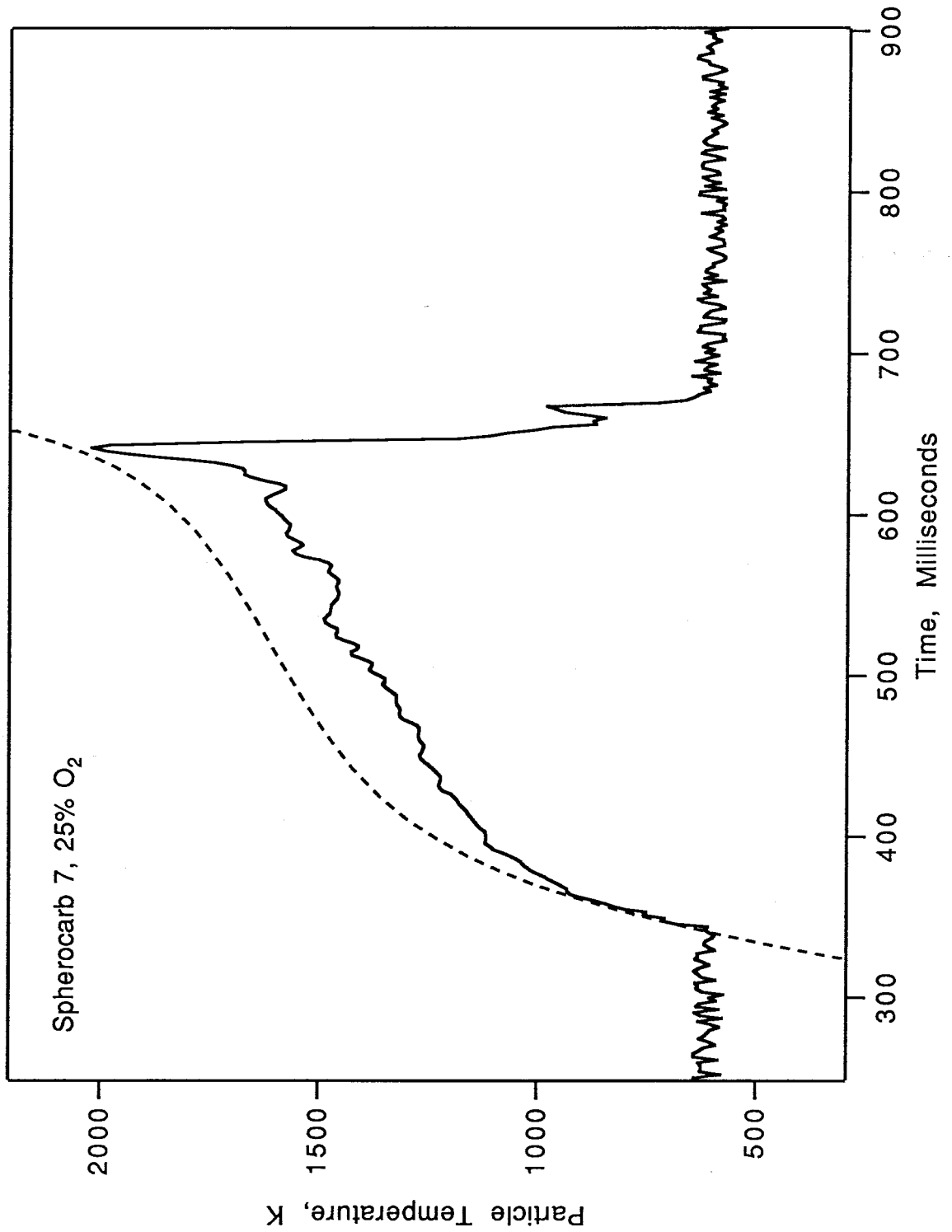
Spherocarb 7, 25% O_2
Particle Temperature, K
2000
1500
1000
500
300
400
500
600
700
800
900
Time, Milliseconds

Figure 14

Figure 15

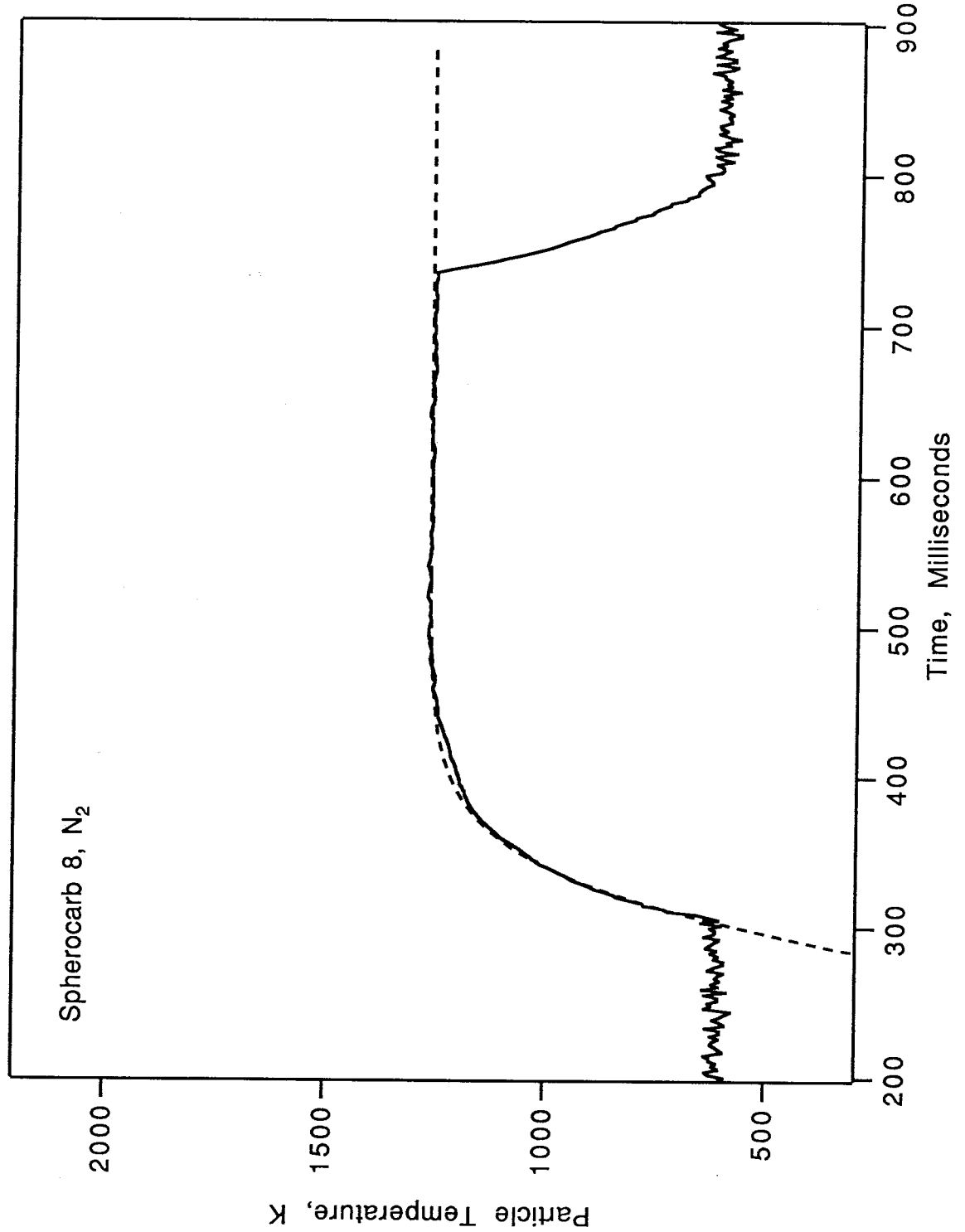
Spherocarb 8, N_2
Particle Temperature, K
2000
1500
1000
500
200
300
400
500
600
700
800
900
Time, Milliseconds

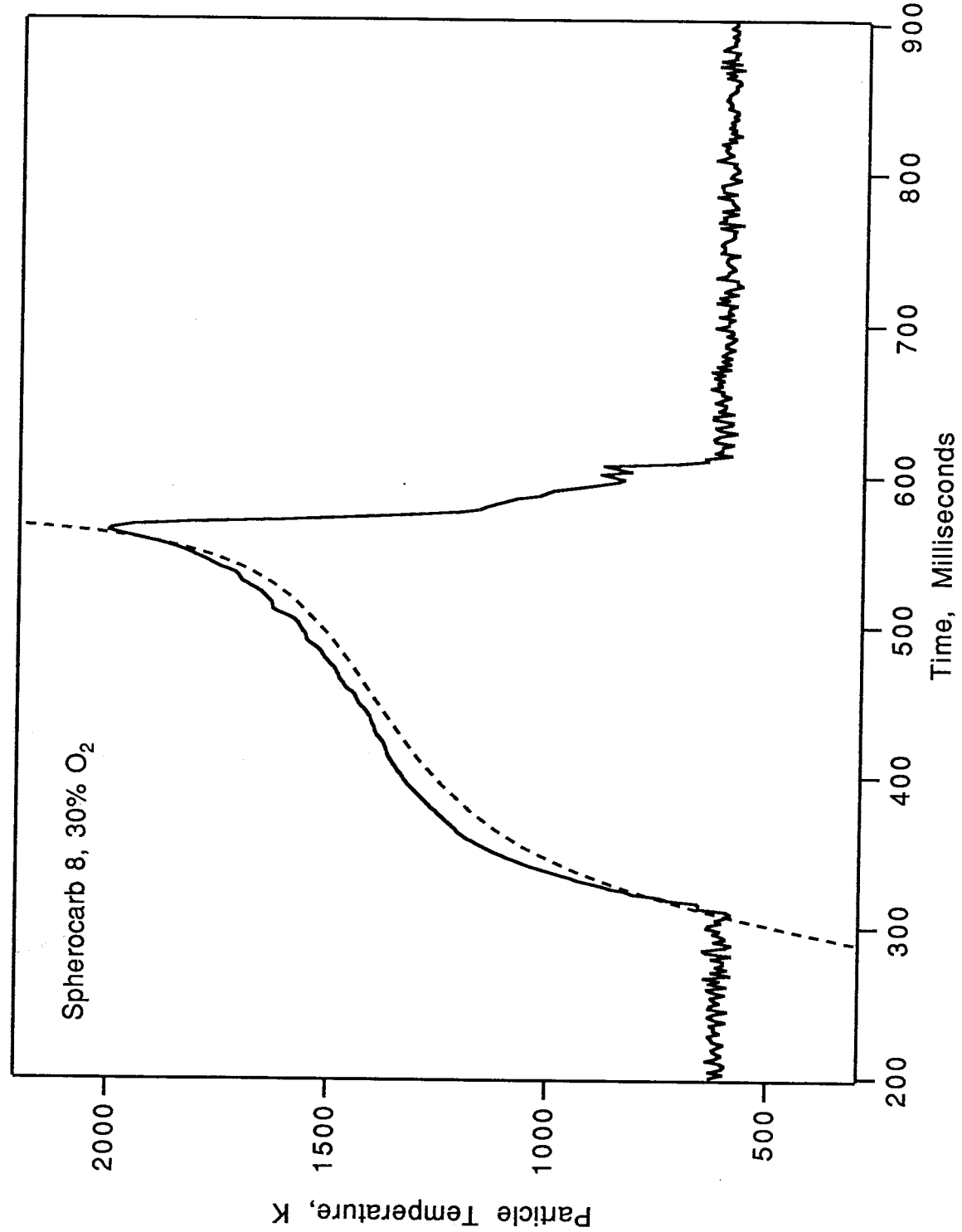
Spherocarb 8, 30% O_2
Particle Temperature, K
2000
1500
1000
500
200
300
400
500
600
700
800
900
Time, Milliseconds

Figure 16

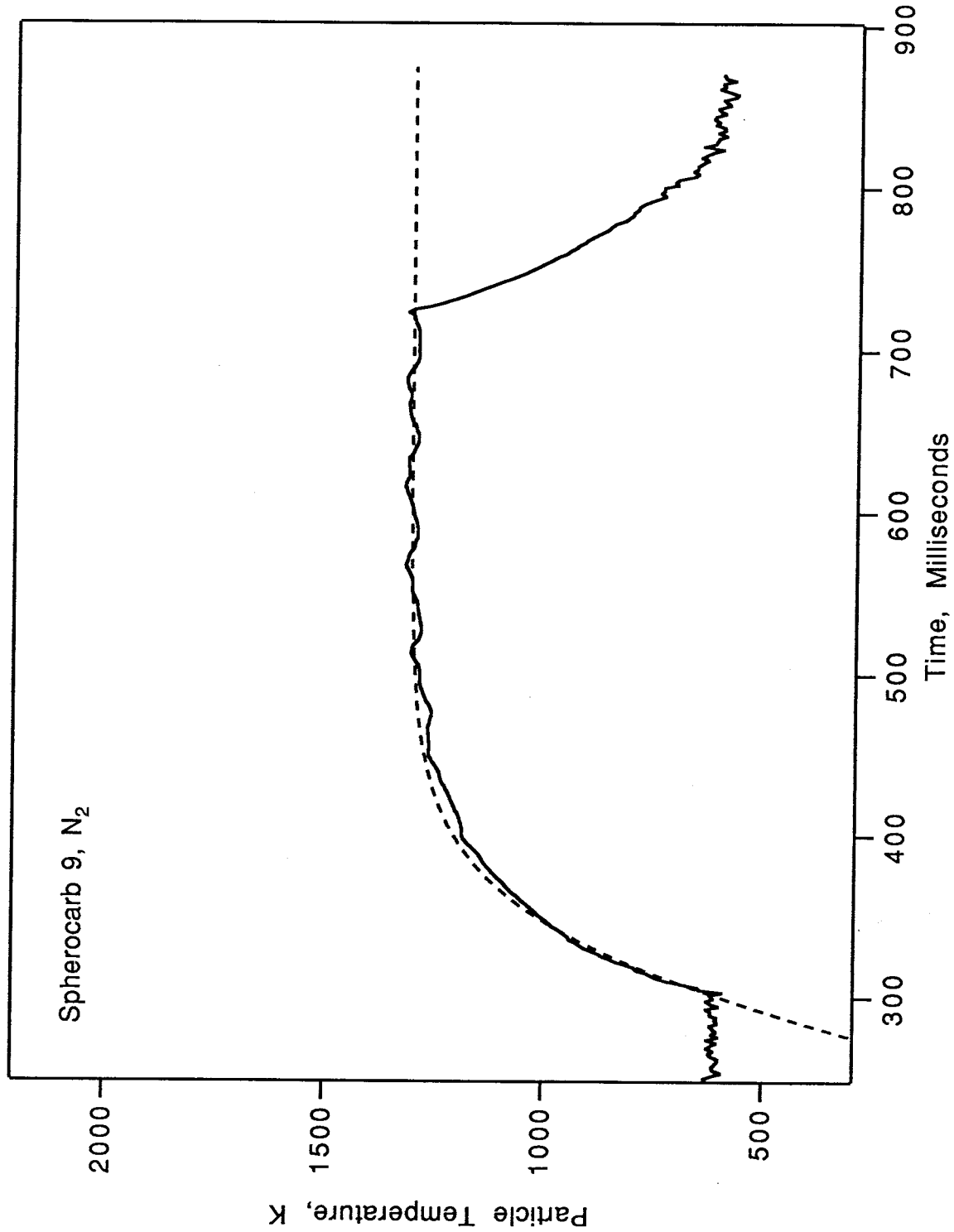
Spherocarb 9, N_2
Particle Temperature, K
2000
1500
1000
500
300
400
500
600
700
800
900
Time, Milliseconds

Figure 17

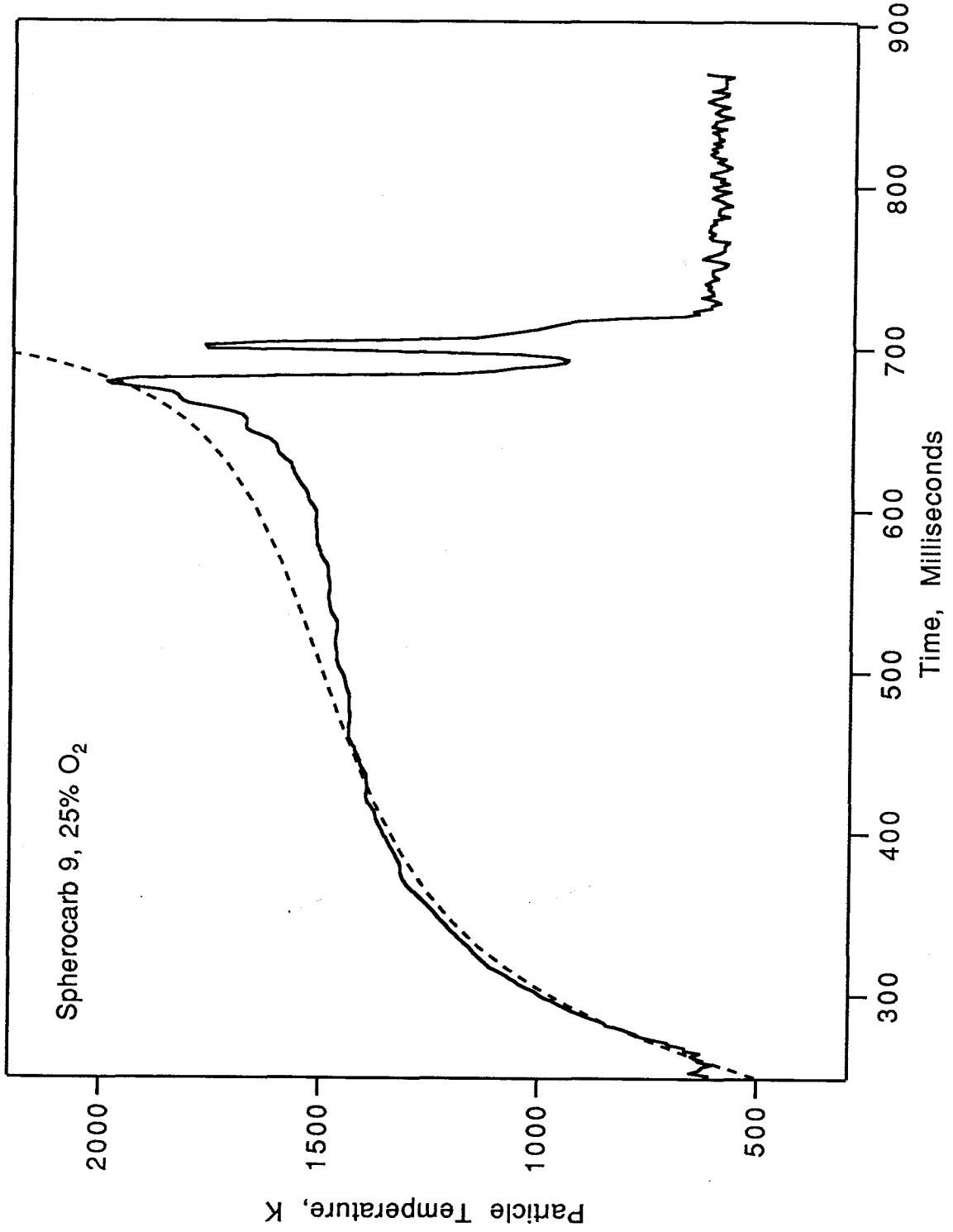
Spherocarb 9, 25% O_2
Particle Temperature, K
2000
1500
1000
500
300
400
500
600
700
800
900
Time, Milliseconds

Figure 18

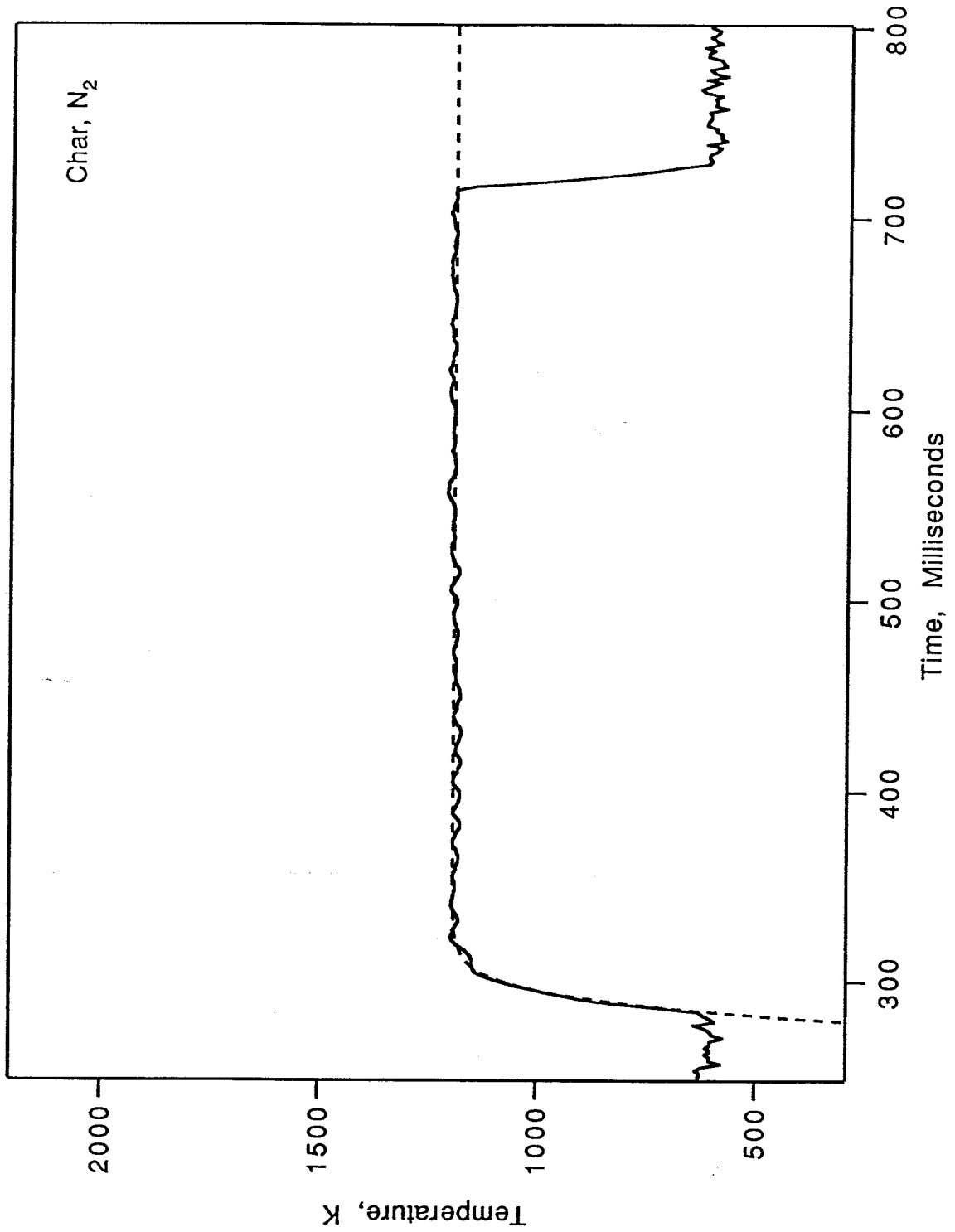
Char, N_2
Temperature, K
2000
1500
1000
500
300
400
500
600
700
800
Time, Milliseconds

Figure 19

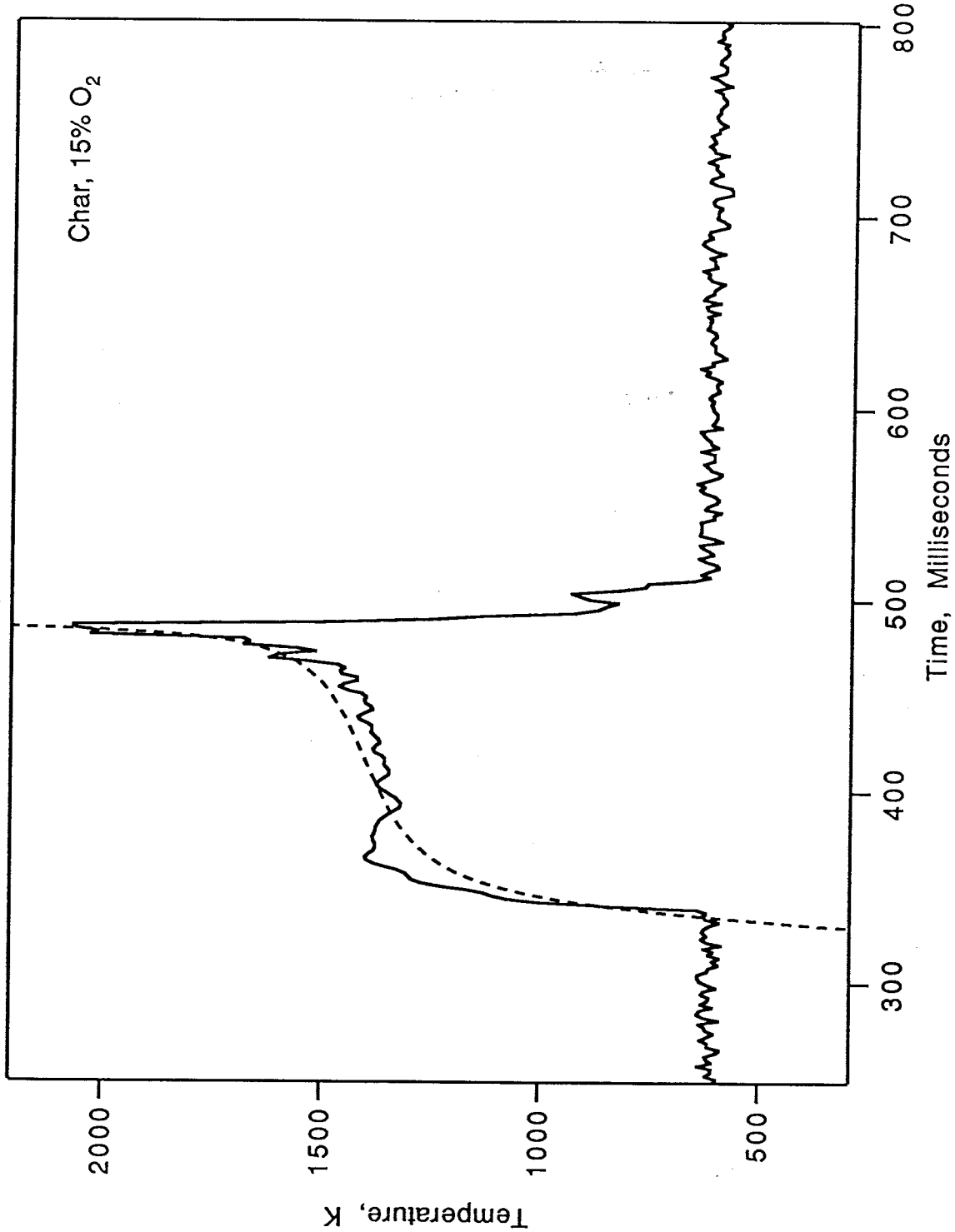
Char, 15% O_2
Temperature, K
2000
1500
1000
500
300
400
500
600
700
800
Time, Milliseconds

Figure 20

Appendix 8

The following graphs are temperature traces for the particles that were heated for the experiment described in Chapter 3.

Figure 1

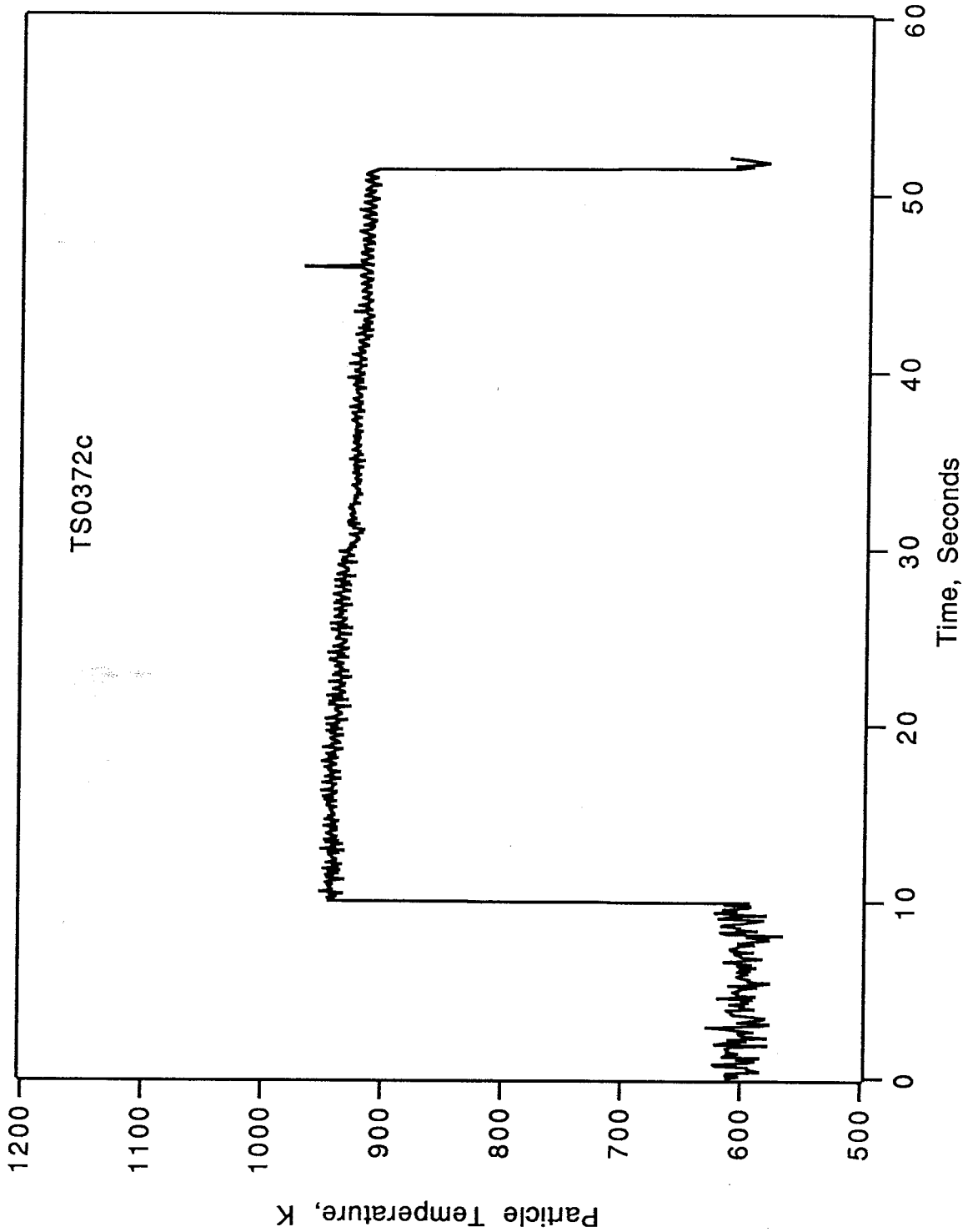
TS0372c
Particle Temperature, K
Time, Seconds
1200
1100
1000
900
800
700
600
500
0
10
20
30
40
50
60

Figure 2

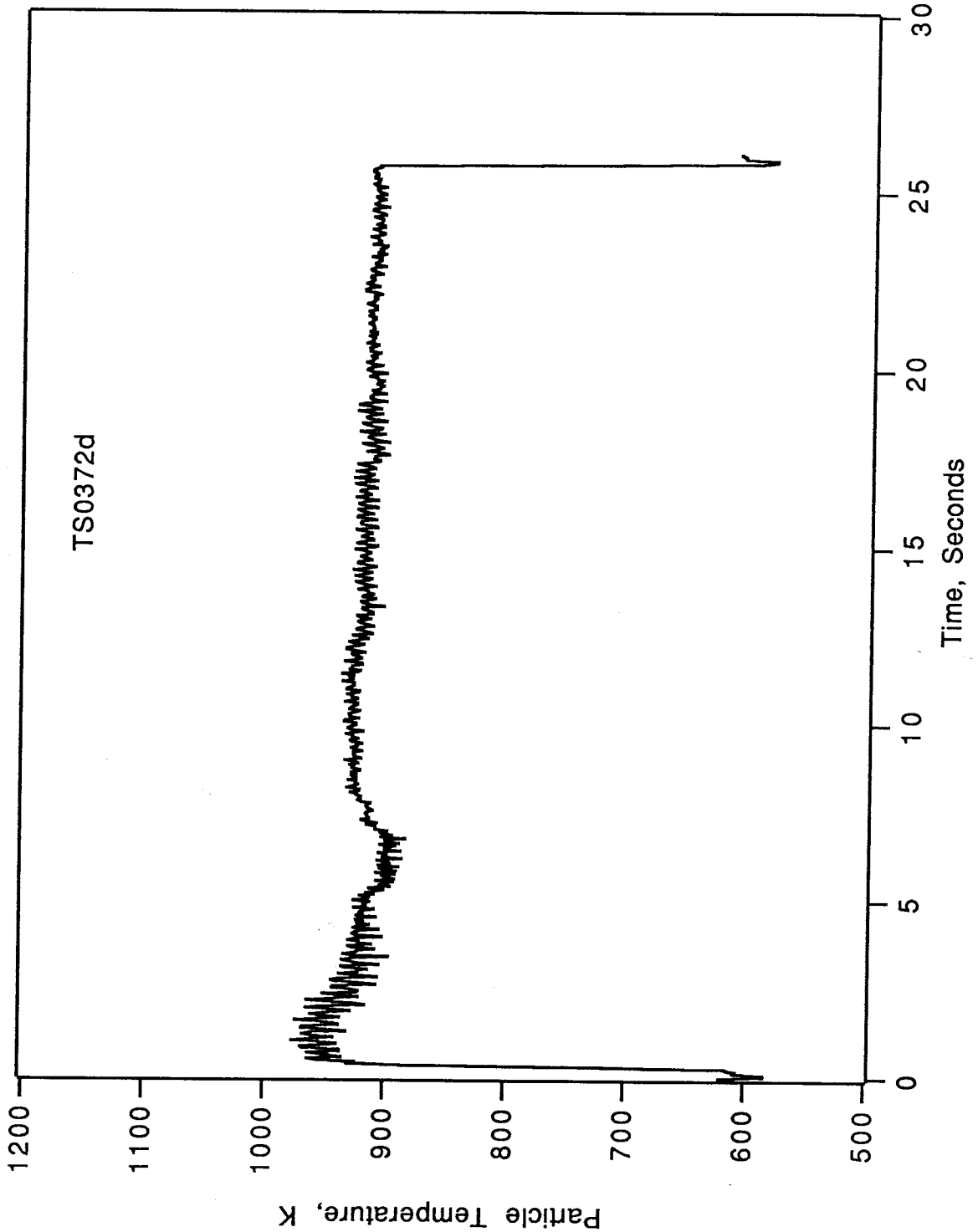
TS0372d
Particle Temperature, K
Time, Seconds
1200
1100
1000
900
800
700
600
500
0
5
10
15
20
25
30

Figure 3

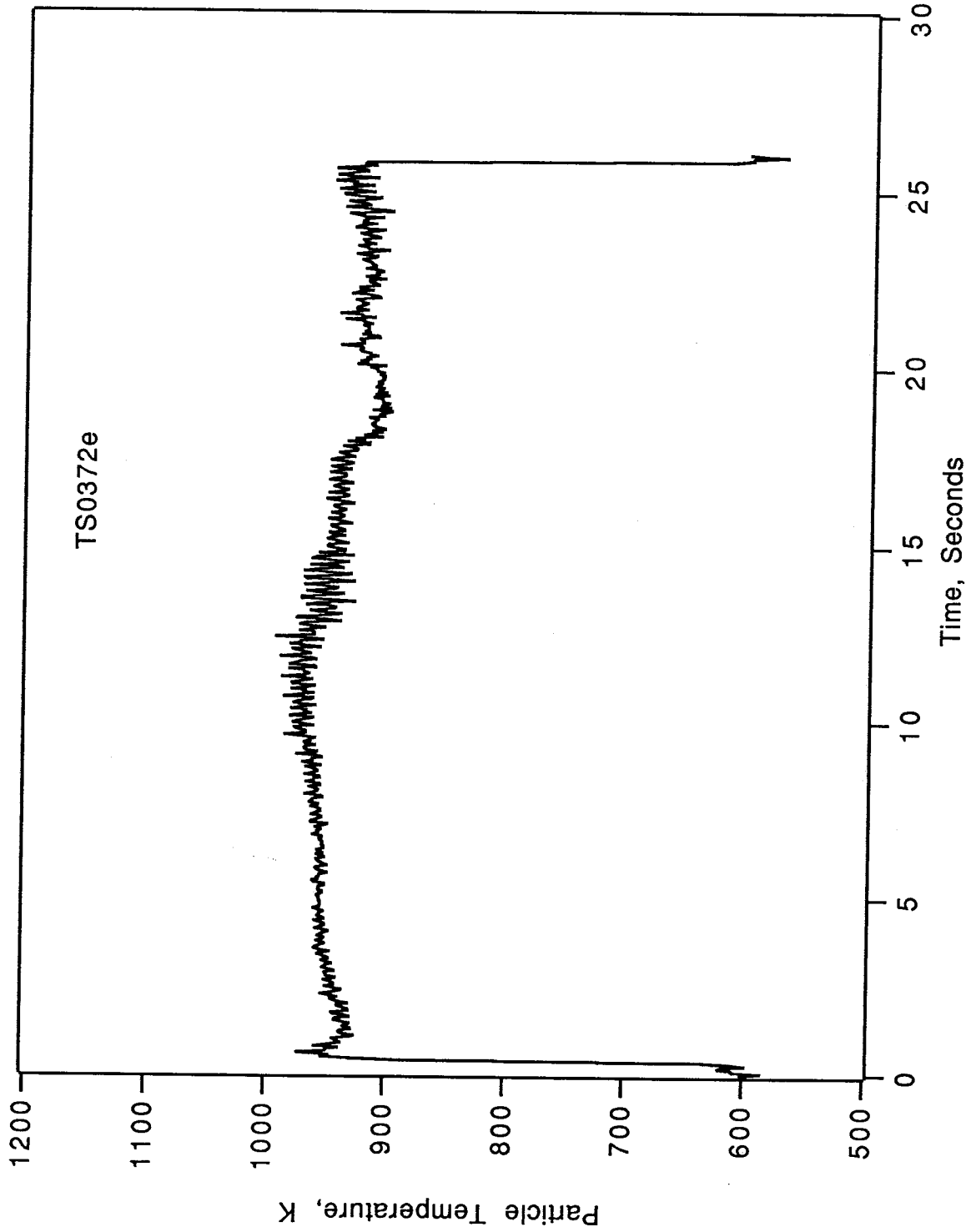
TS0372e
Particle Temperature, K
Time, Seconds
1200
1100
1000
900
800
700
600
500
0
5
10
15
20
25
30

Figure 4

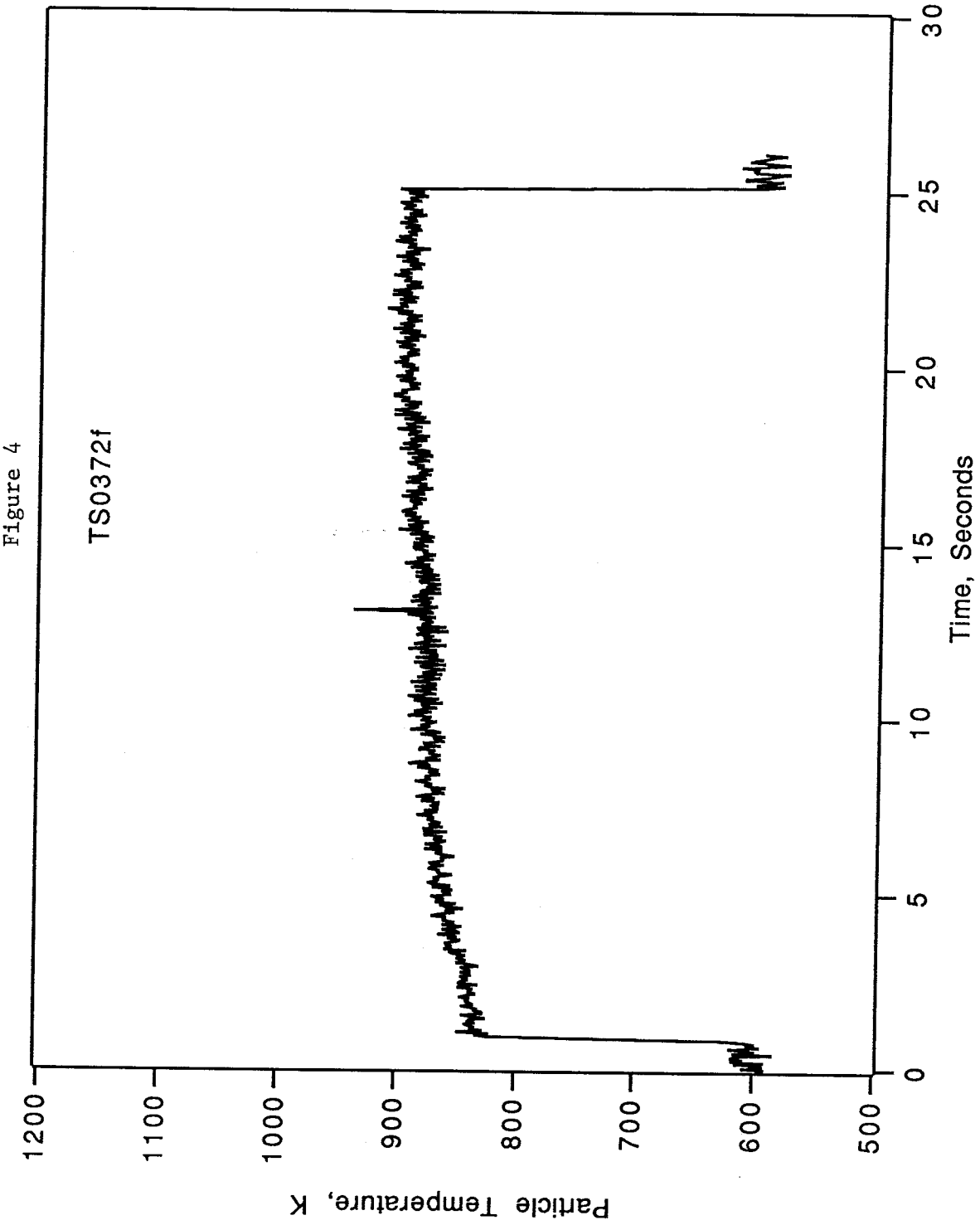
TS0372f
Particle Temperature, K
Time, Seconds
1200
1100
1000
900
800
700
600
500
0
5
10
15
20
25
30

Figure 5

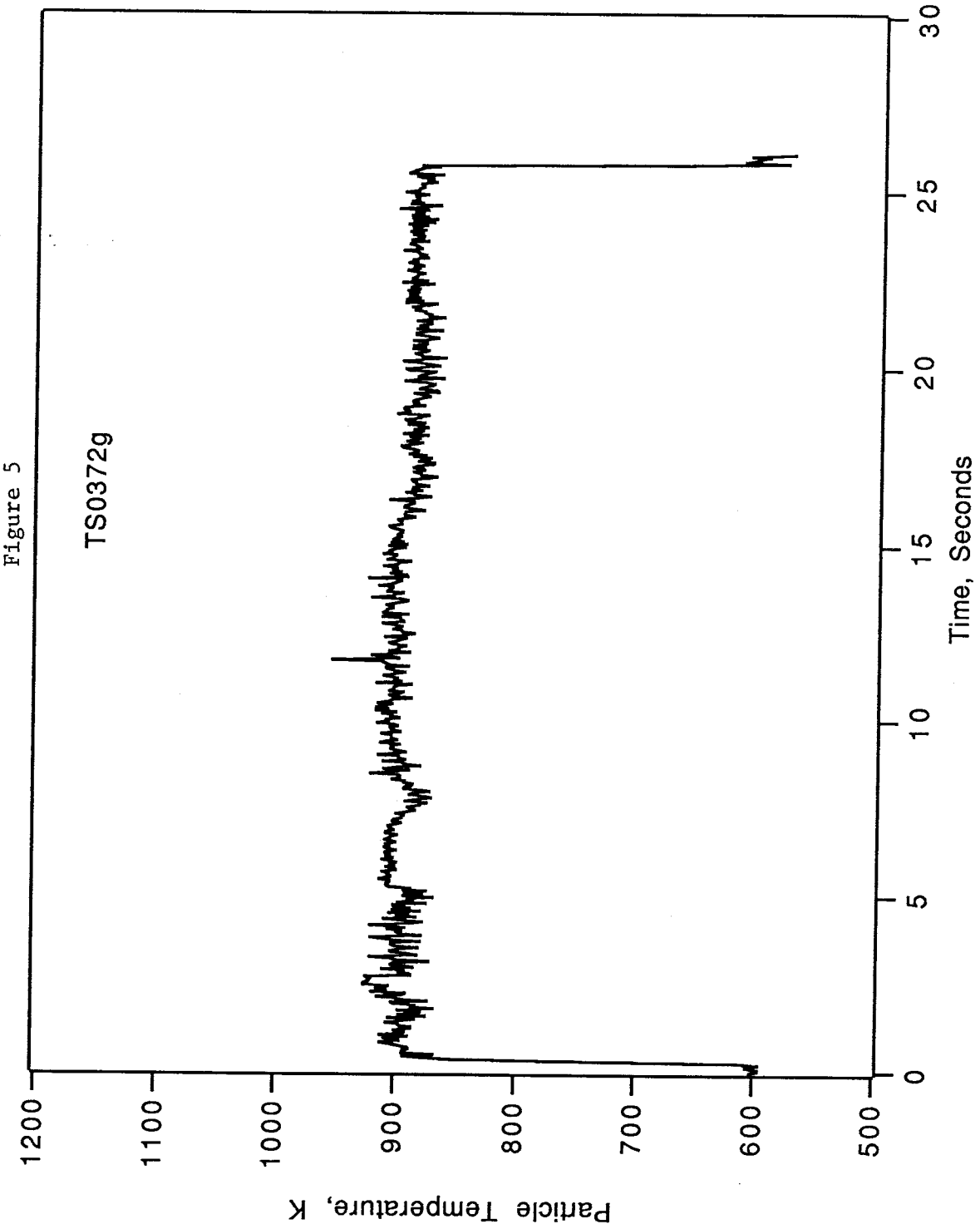
TS0372g
Particle Temperature, K
1200
1100
1000
900
800
700
600
500
0
5
10
15
20
25
30
Time, Seconds

Figure 6

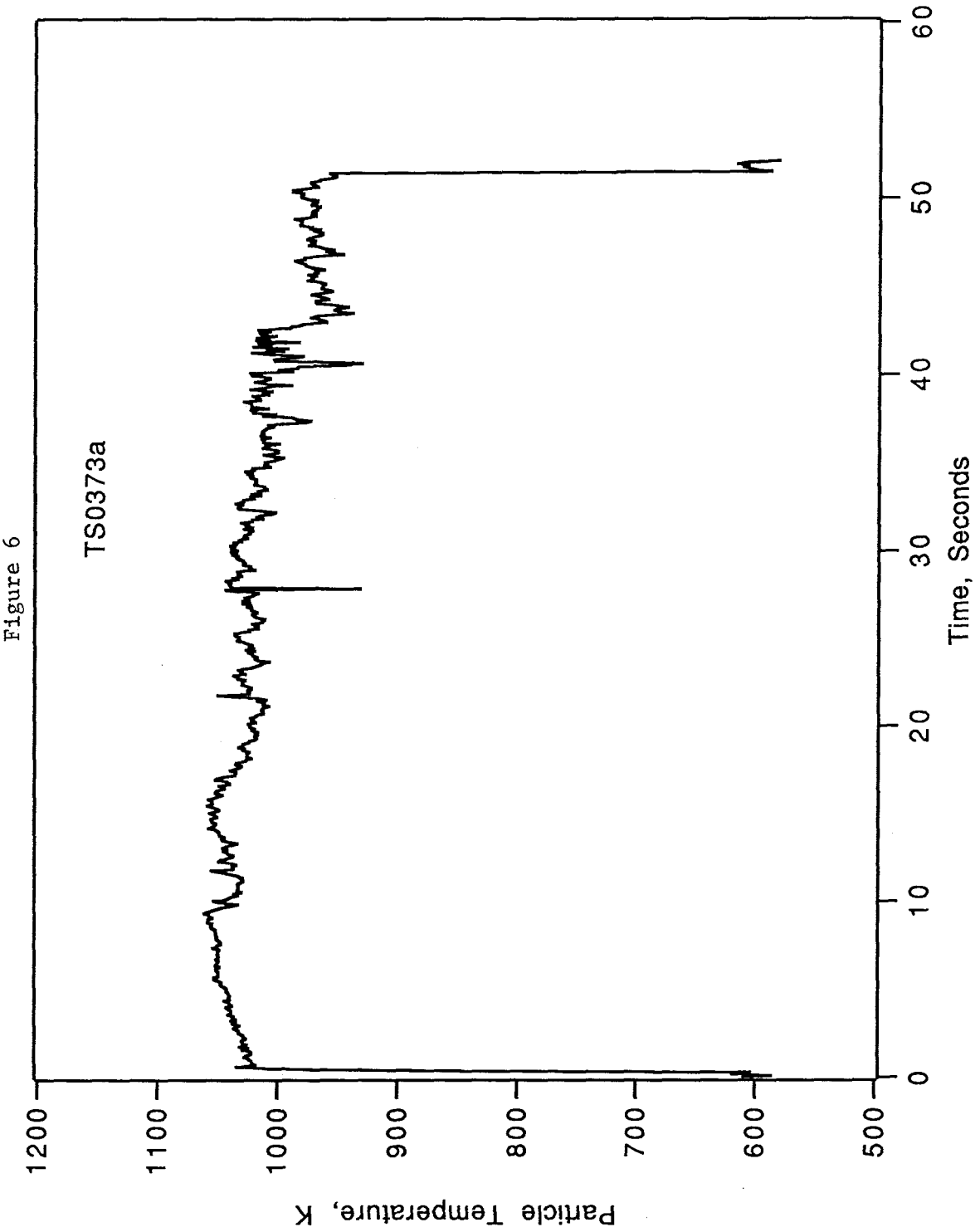
TS0373a
Particle Temperature, K
1200
1100
1000
900
800
700
600
500
0
10
20
30
40
50
60
Time, Seconds

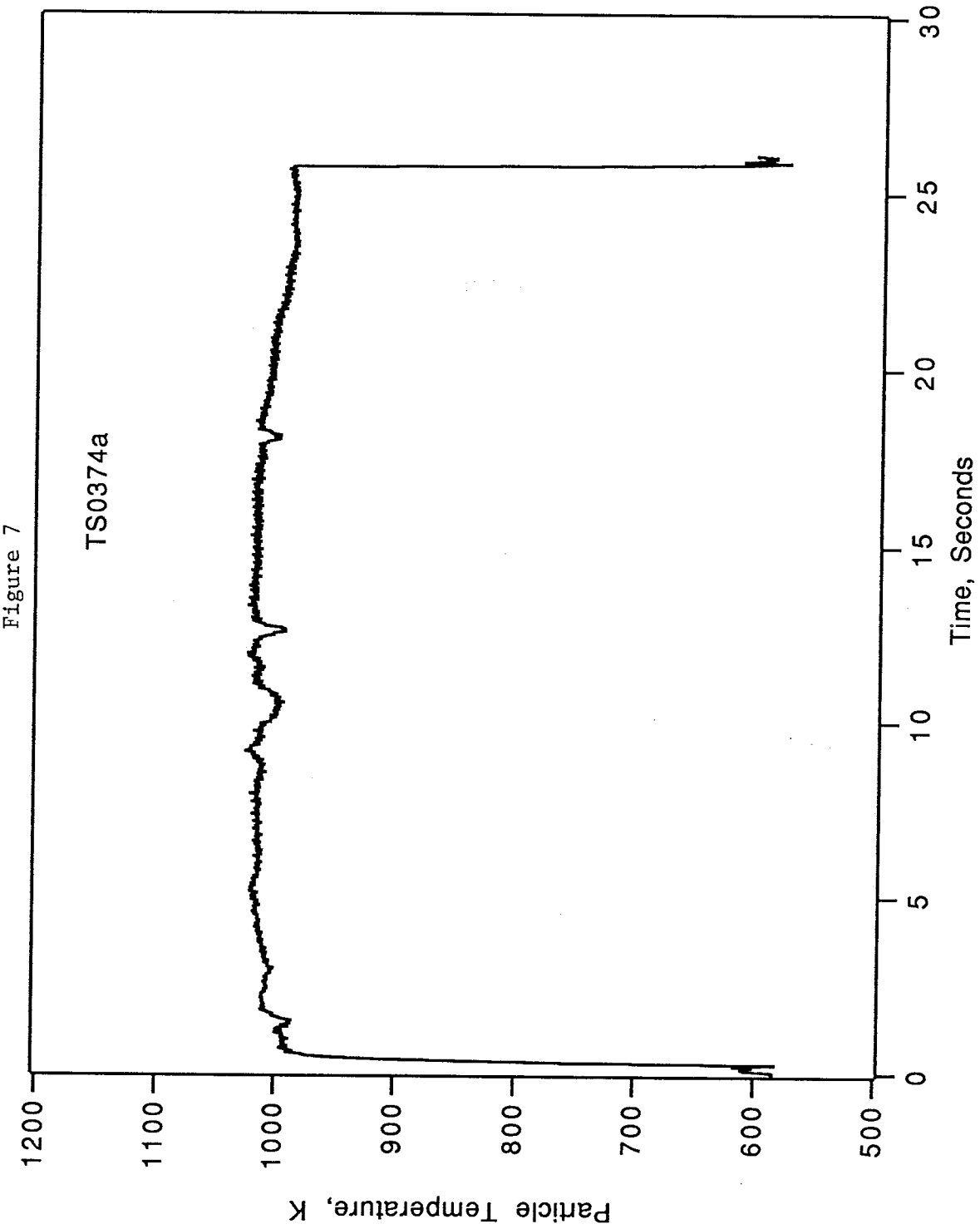
TS0374a
Particle Temperature, K
Time, Seconds
1200
1100
1000
900
800
700
600
500
0
5
10
15
20
25
30

Figure 7

Figure 8

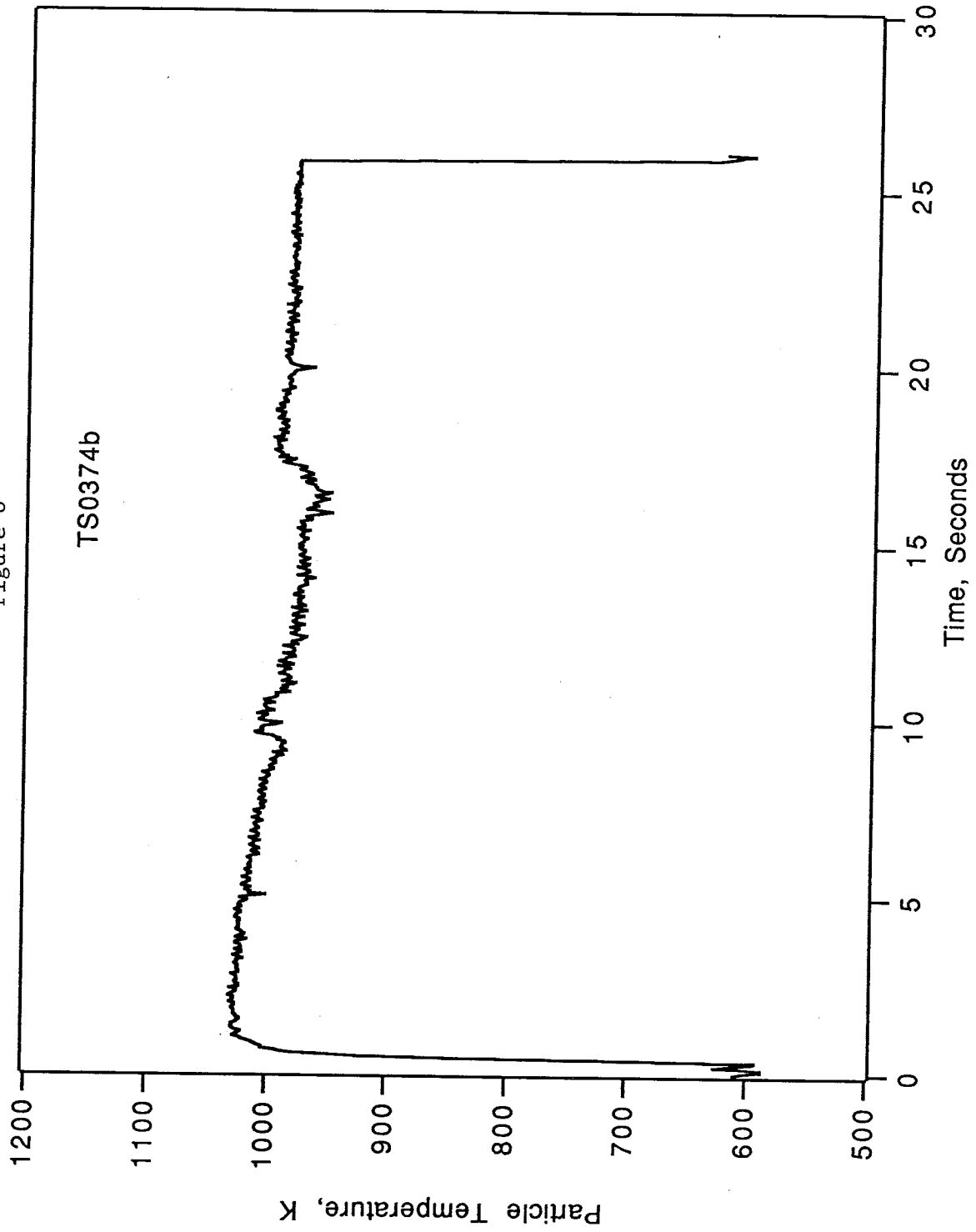
TS0374b
Particle Temperature, K
Time, Seconds
1200
1100
1000
900
800
700
600
500
0
5
10
15
20
25
30

Figure 9

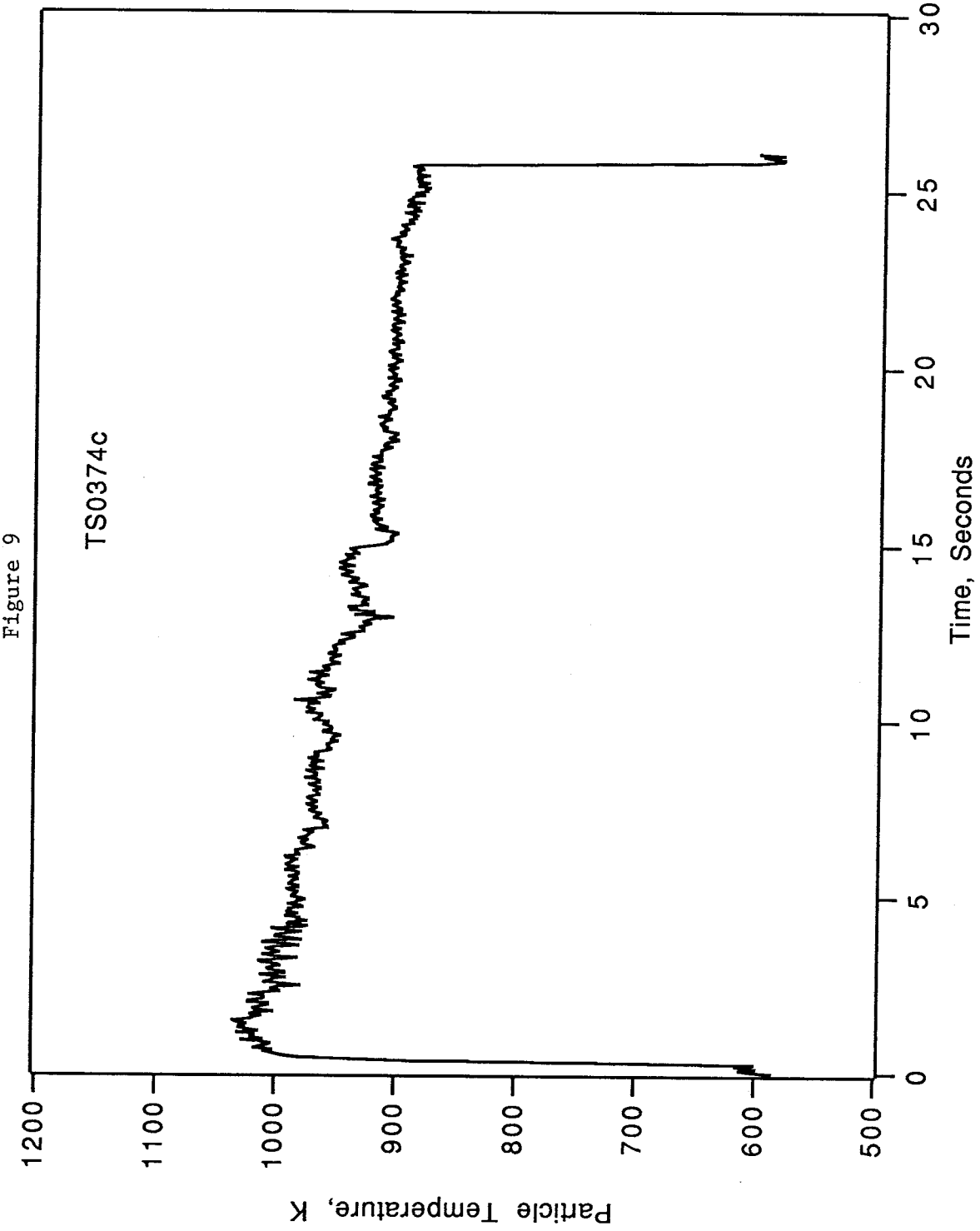
TS0374c
Particle Temperature, K
Time, Seconds
1200
1100
1000
900
800
700
600
500
0
5
10
15
20
25
30

Figure 10

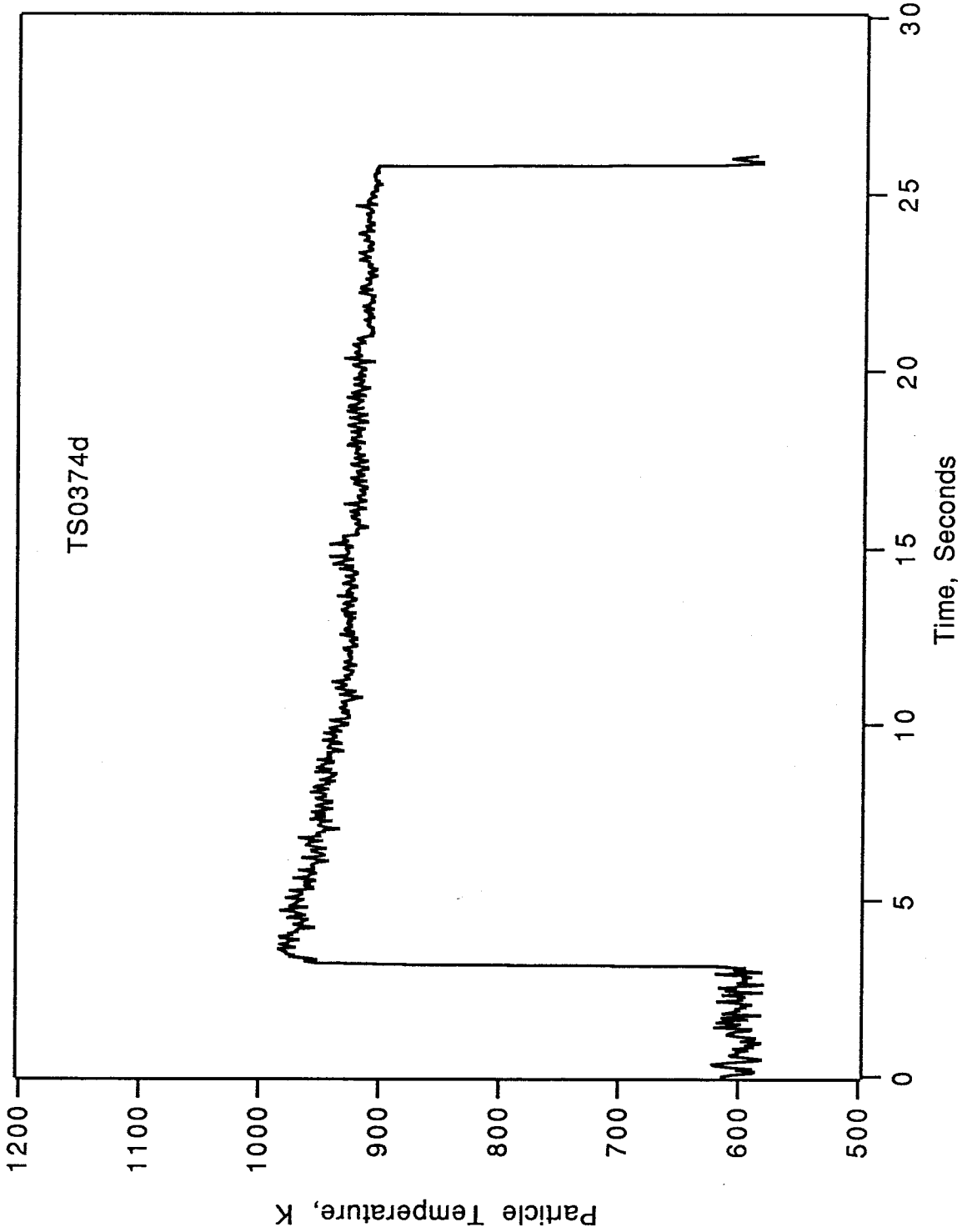
TS0374d
Particle Temperature, K
1200
1100
1000
900
800
700
600
500
0
5
10
15
20
25
30
Time, Seconds

Figure 11

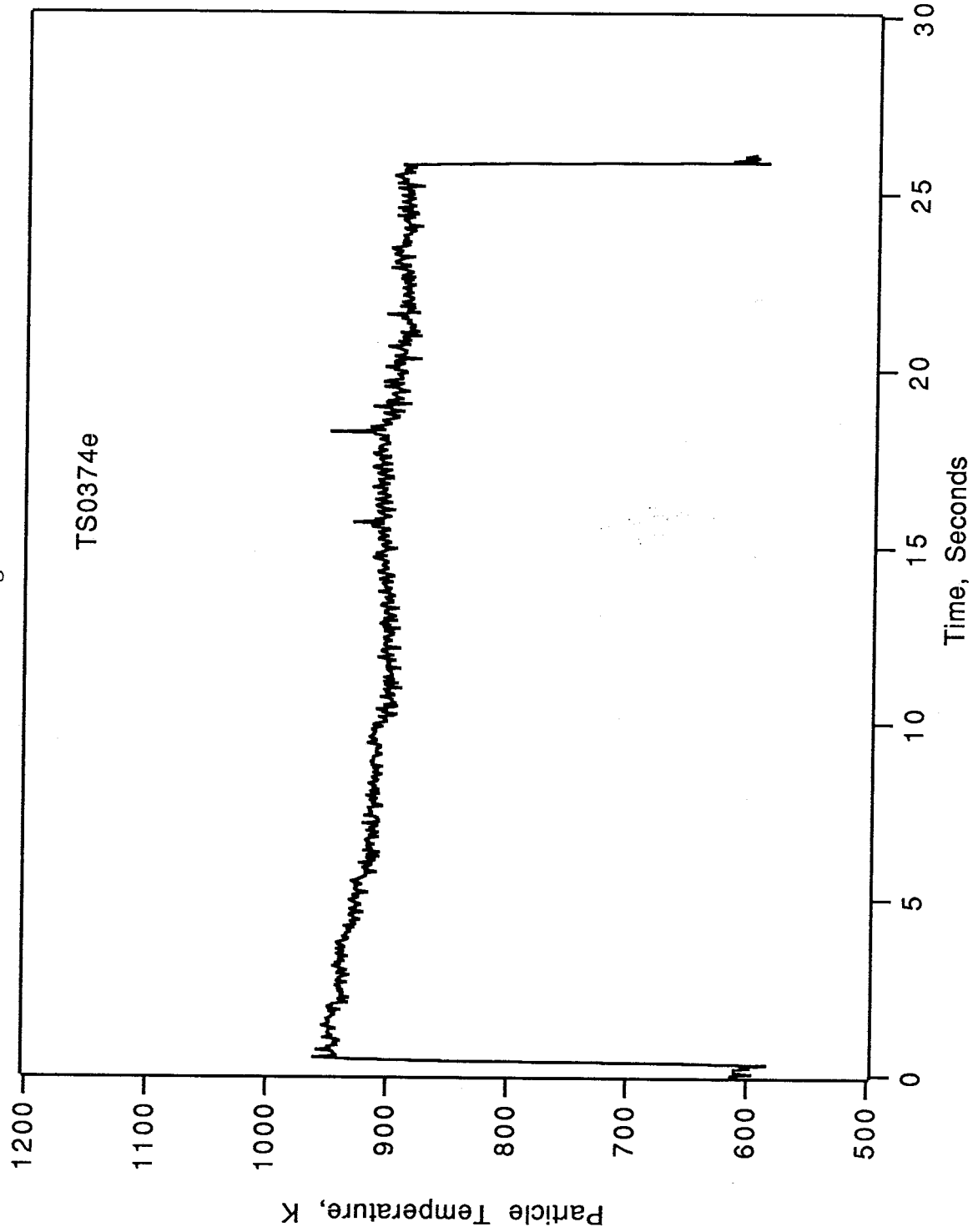
TS0374e
Particle Temperature, K
1200
1100
1000
900
800
700
600
500
0
5
10
15
20
25
30
Time, Seconds

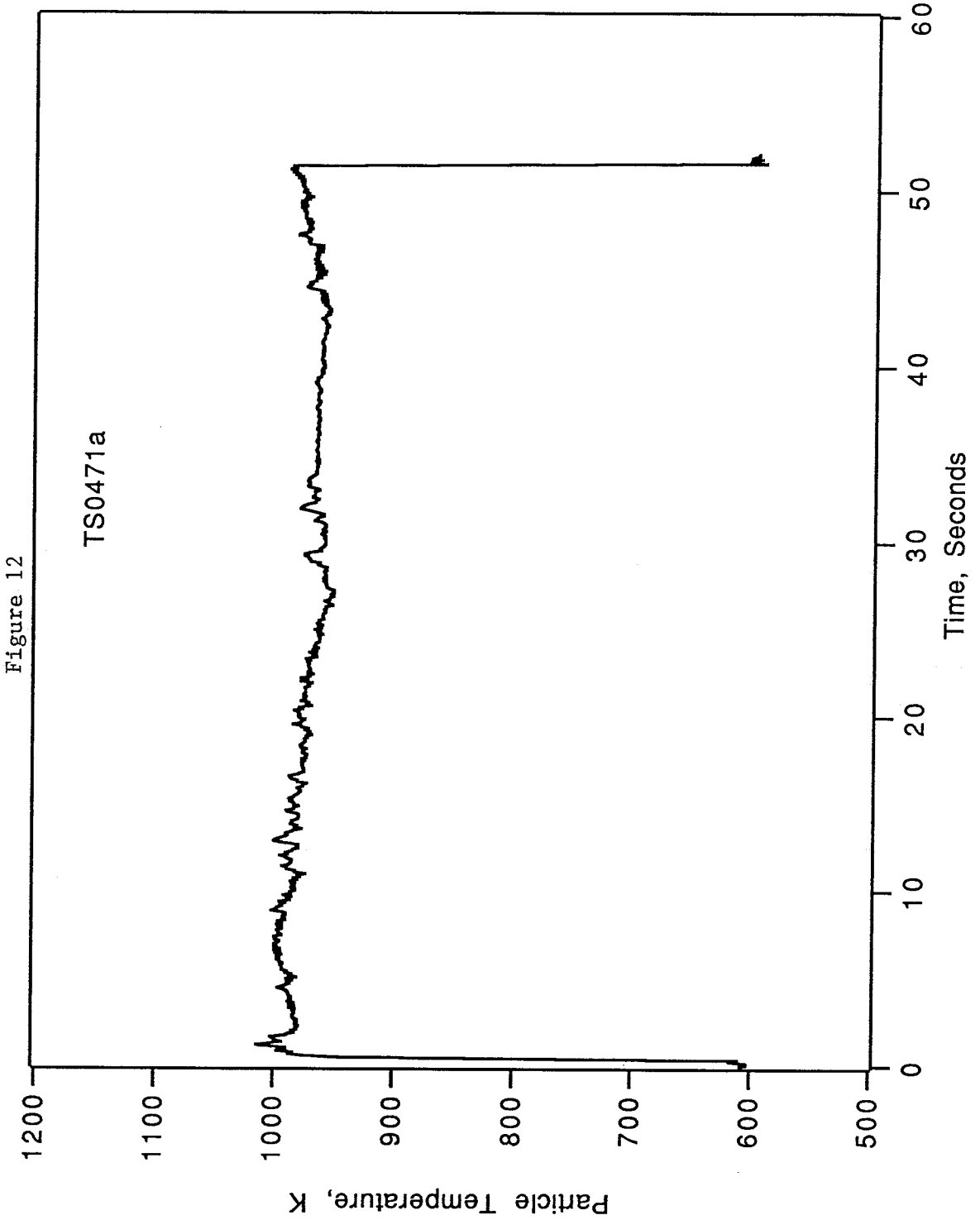
TS0471a
Particle Temperature, K
Time, Seconds
1200
1100
1000
900
800
700
600
500
0
10
20
30
40
50
60

Figure 12

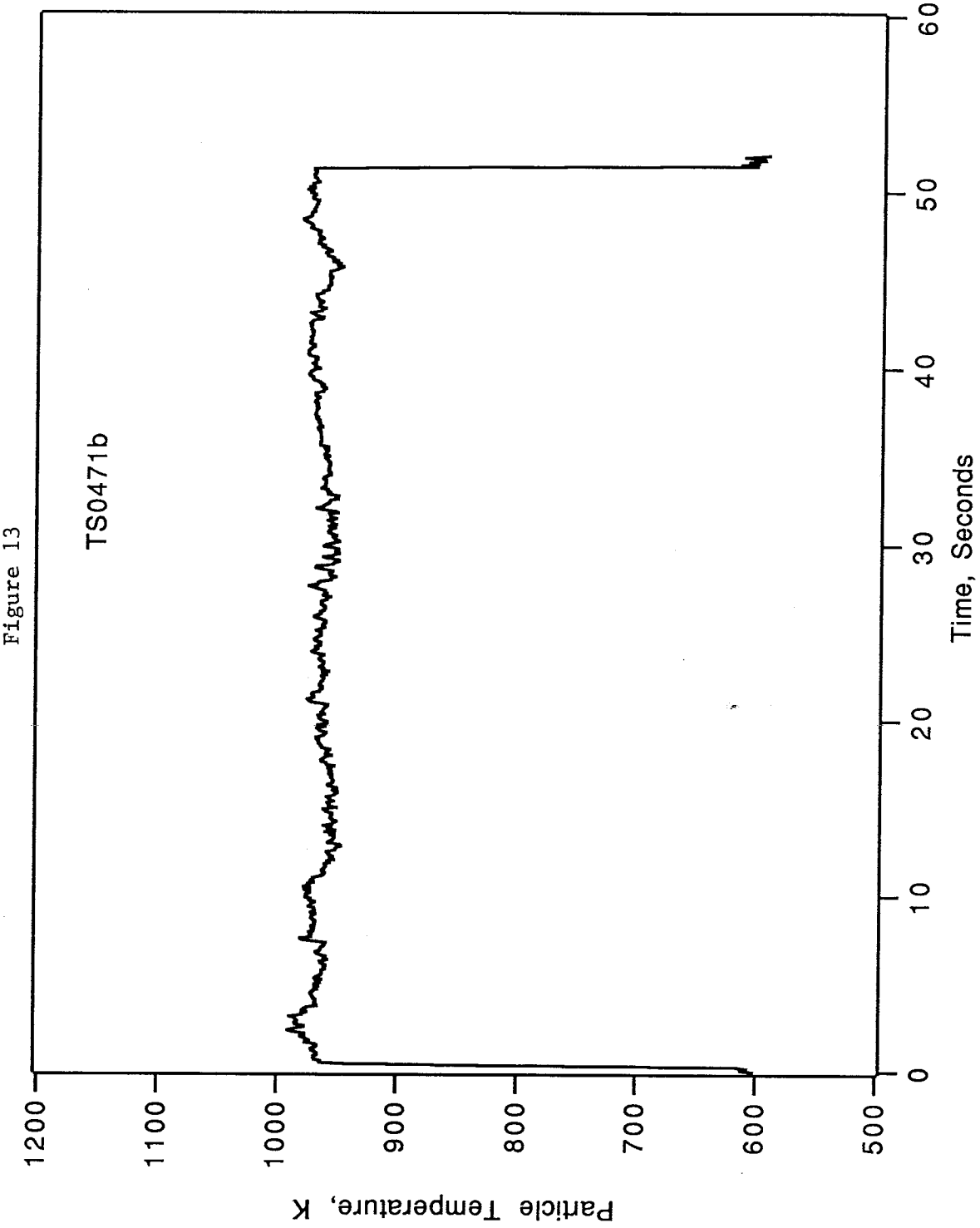
TS0471b
Particle Temperature, K
Time, Seconds
1200
1100
1000
900
800
700
600
500
0
10
20
30
40
50
60

Figure 13

Figure 14

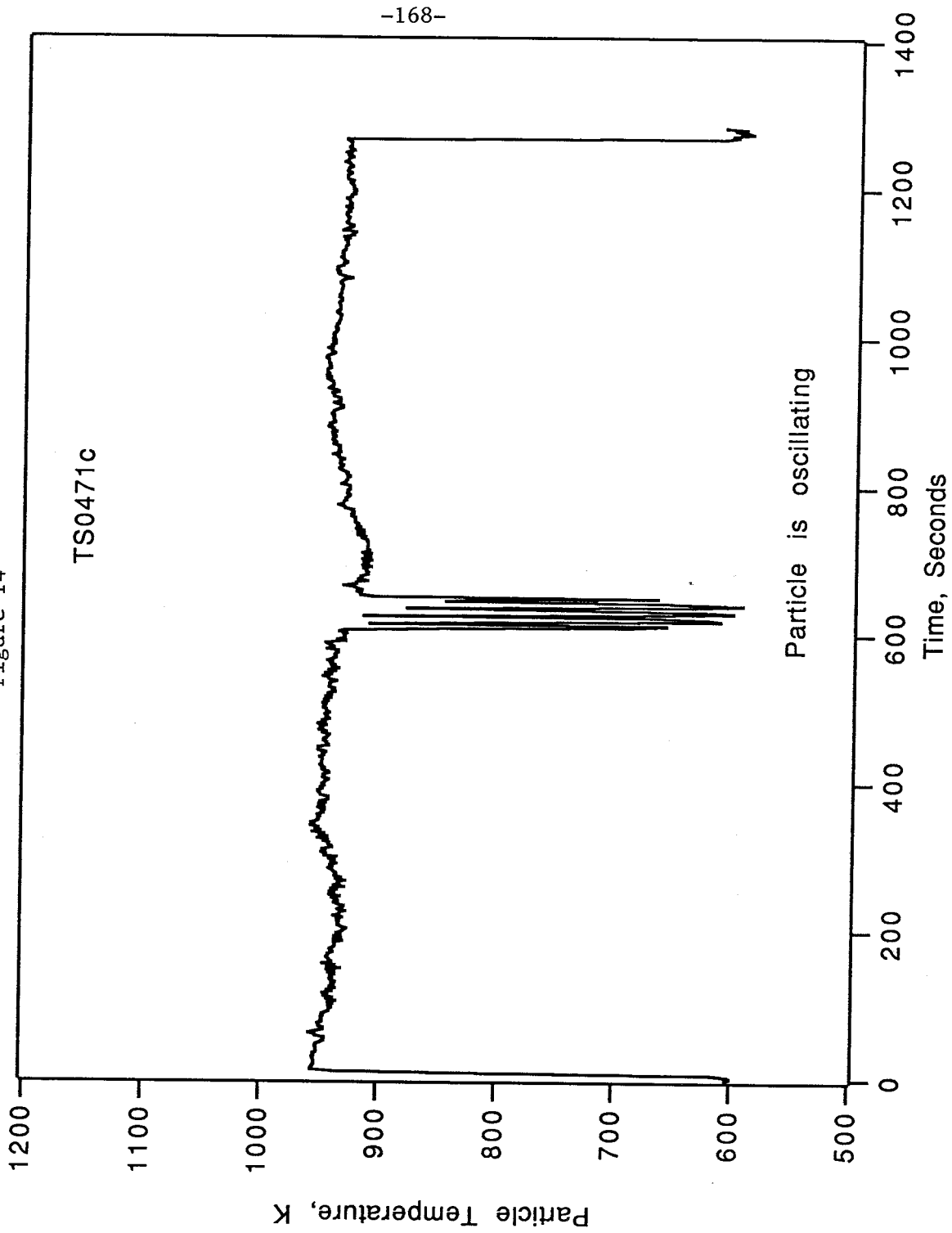
TS0471c
Particle is oscillating
Particle Temperature, K
Time, Seconds
1200
1100
1000
900
800
700
600
500
0
200
400
600
800
1000
1200
1400

Figure 15

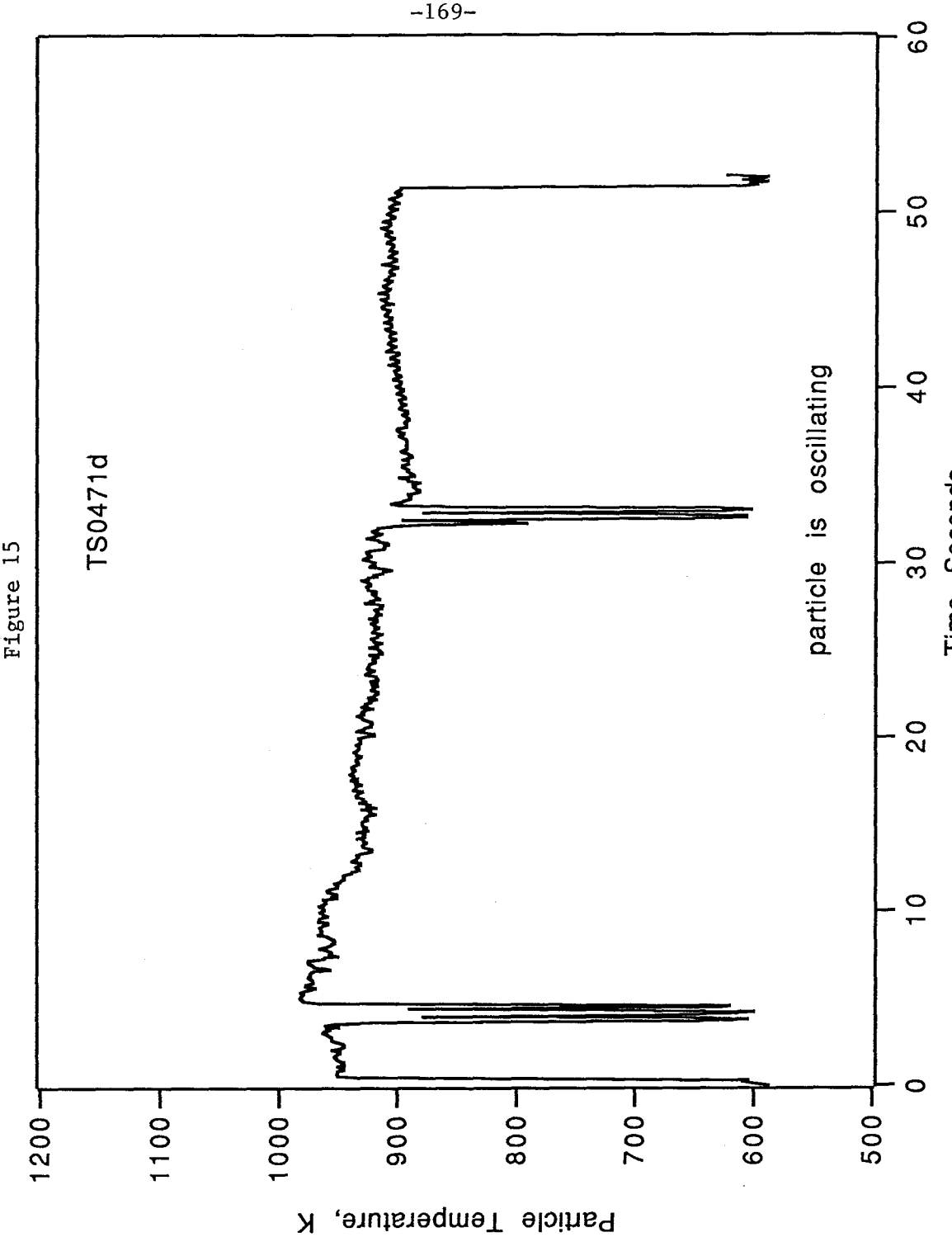
TS0471d
particle is oscillating
Particle Temperature, K
Time, Seconds
1200
1100
1000
900
800
700
600
500
0
10
20
30
40
50
60

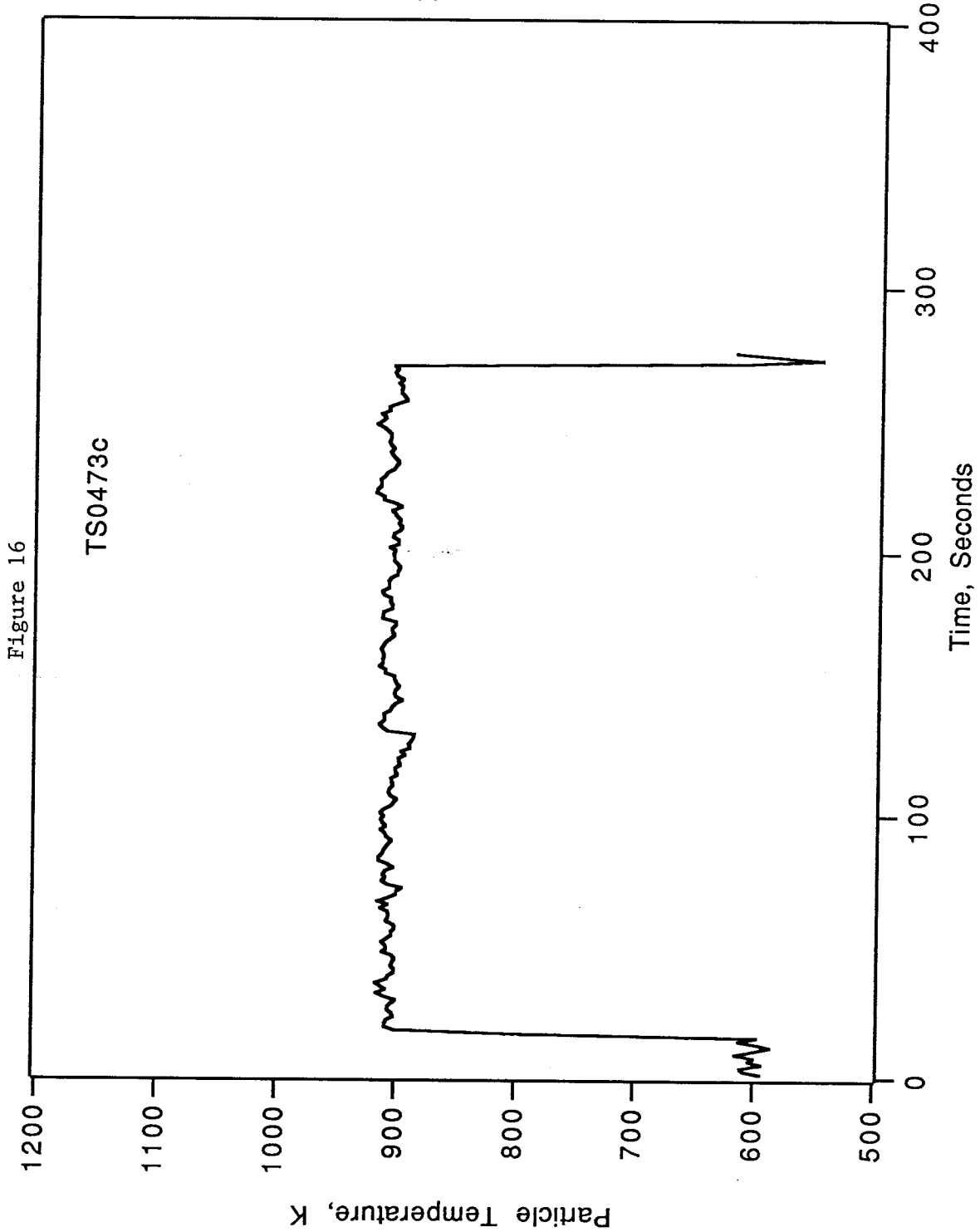
TS0473c
Particle Temperature, K
Time, Seconds
1200
1100
1000
900
800
700
600
500
0
100
200
300
400

Figure 16

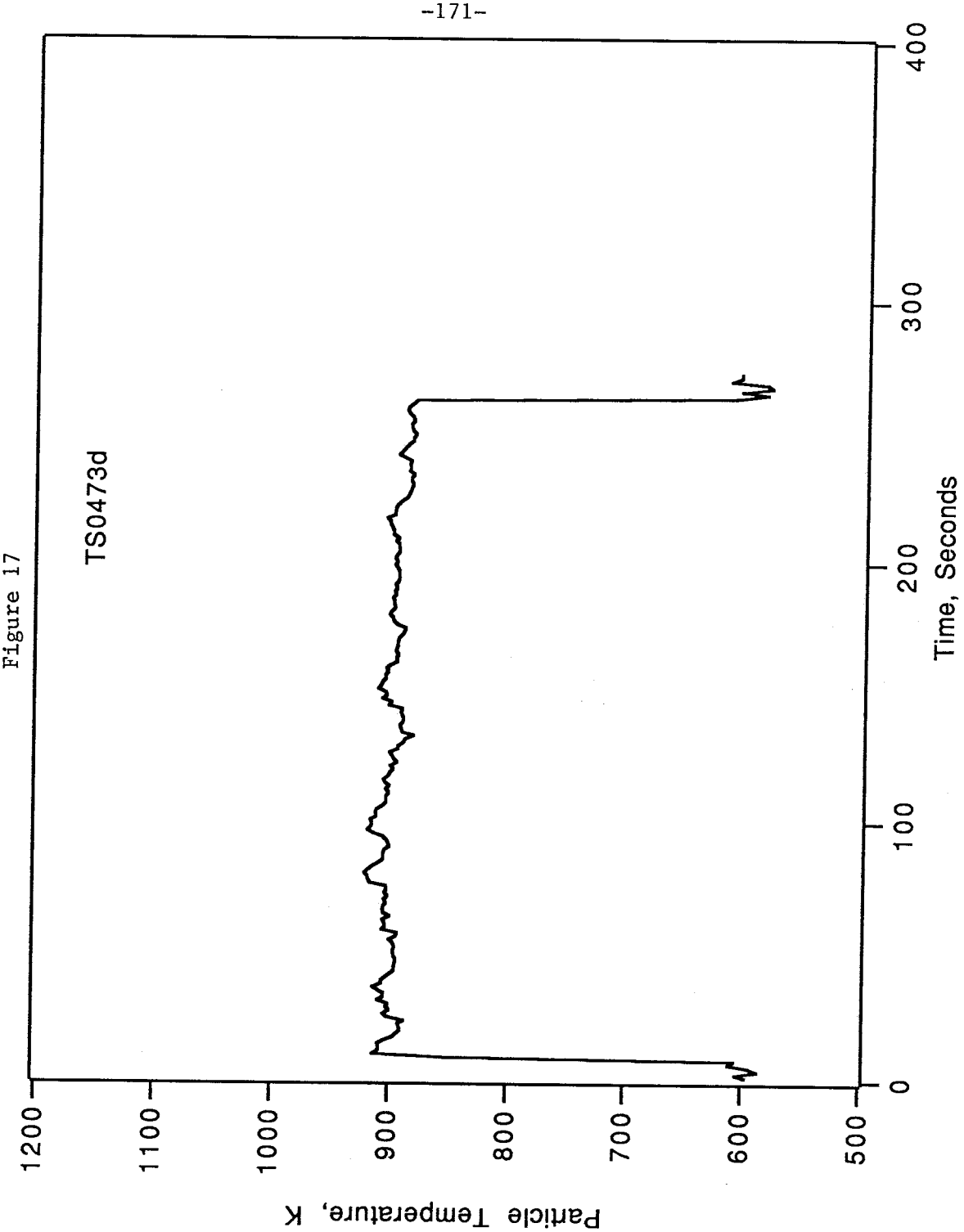
TS0473d
Particle Temperature, K
Time, Seconds
1200
1100
1000
900
800
700
600
500
0
100
200
300
400

Figure 17

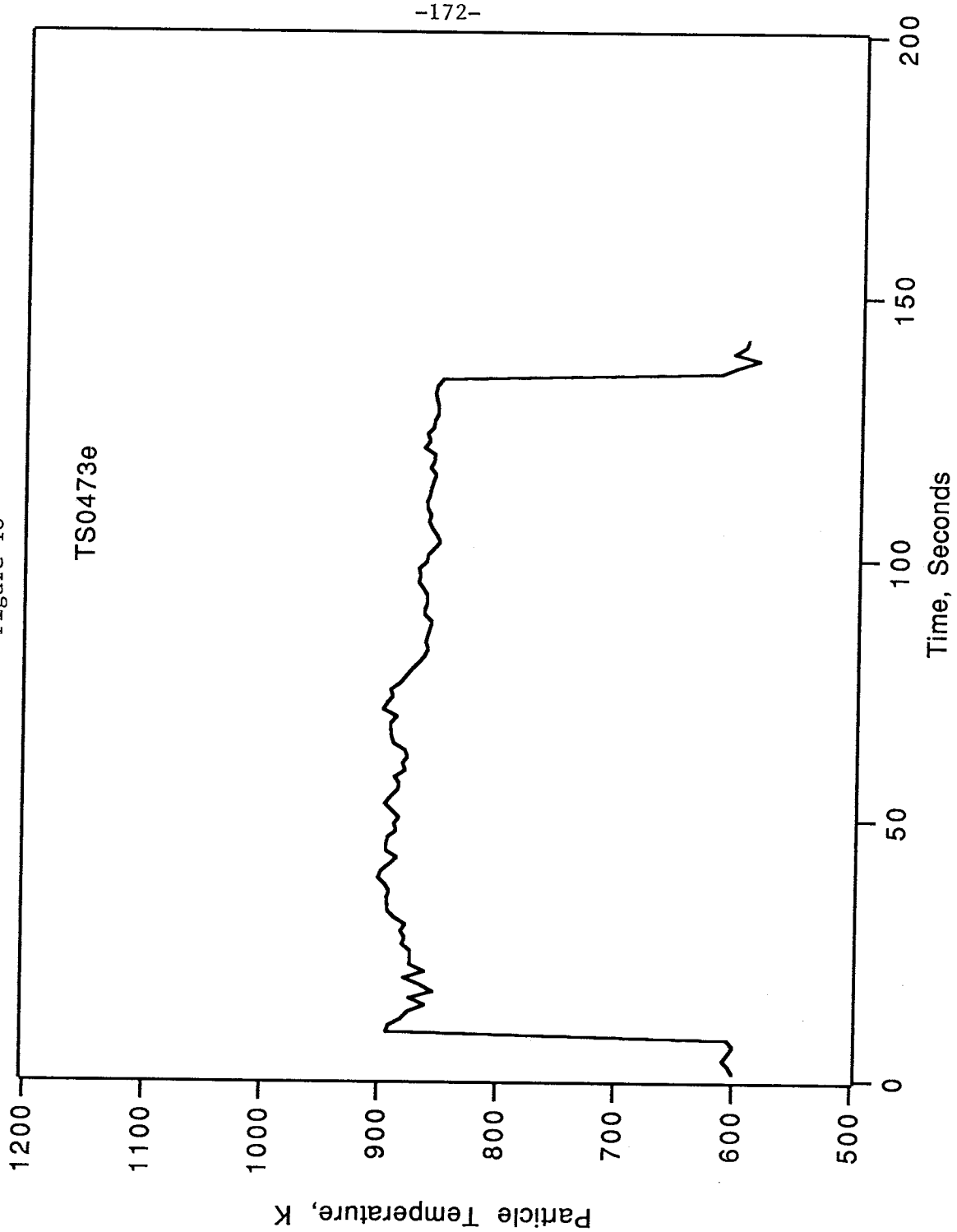
TS0473e
Particle Temperature, K
1200
1100
1000
900
800
700
600
500
0
50
100
150
200
Time, Seconds

Figure 18

Figure 19

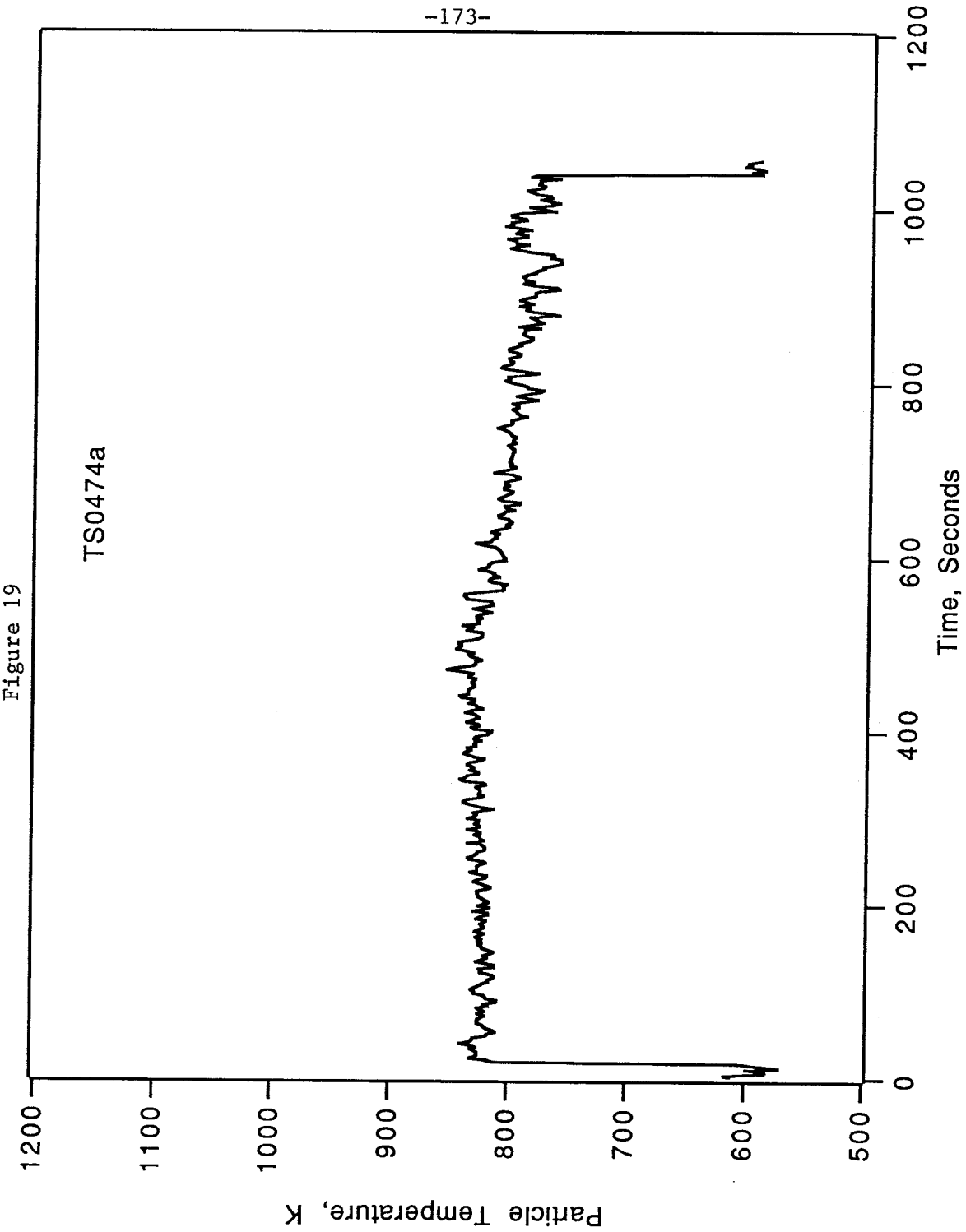
TS0474a
Particle Temperature, K
Time, Seconds
1200
1100
1000
900
800
700
600
500
0
200
400
600
800
1000
1200

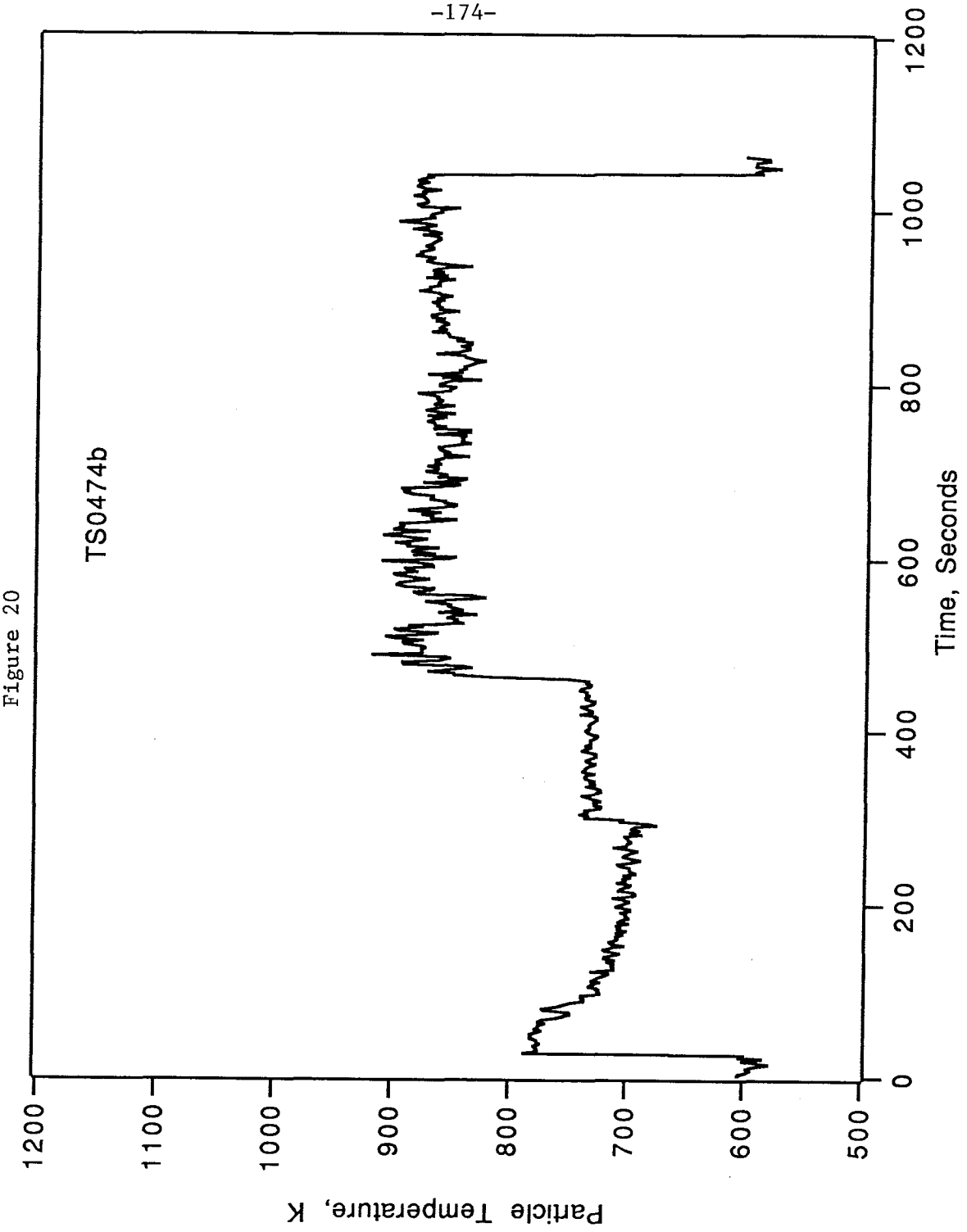
TS0474b
Particle Temperature, K
Time, Seconds
1200
1100
1000
900
800
700
600
500
0
200
400
600
800
1000
1200

Figure 20

Figure 21

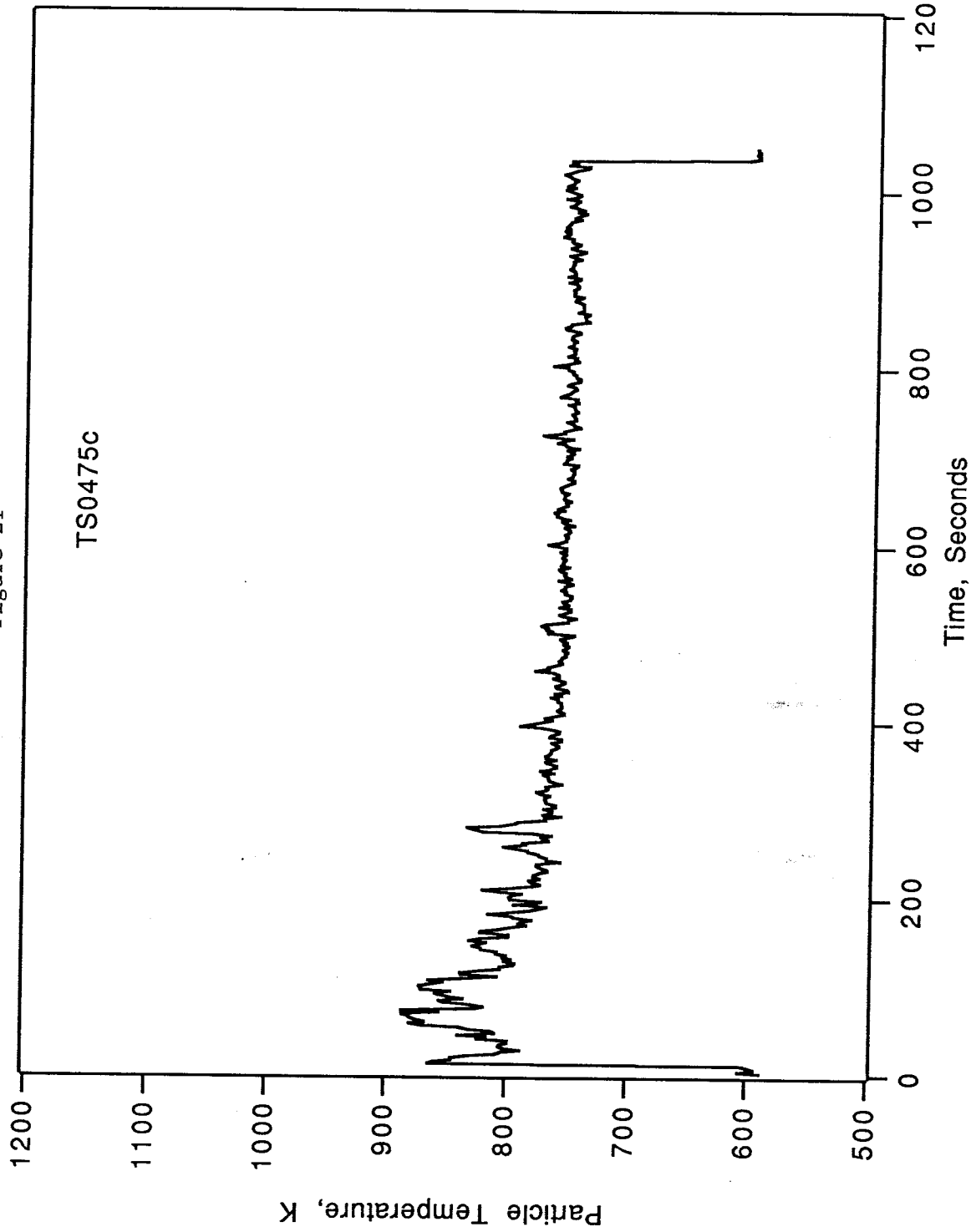
TS0475c
Particle Temperature, K
Time, Seconds
1200
1100
1000
900
800
700
600
500
0
200
400
600
800
1000
1200

Figure 22

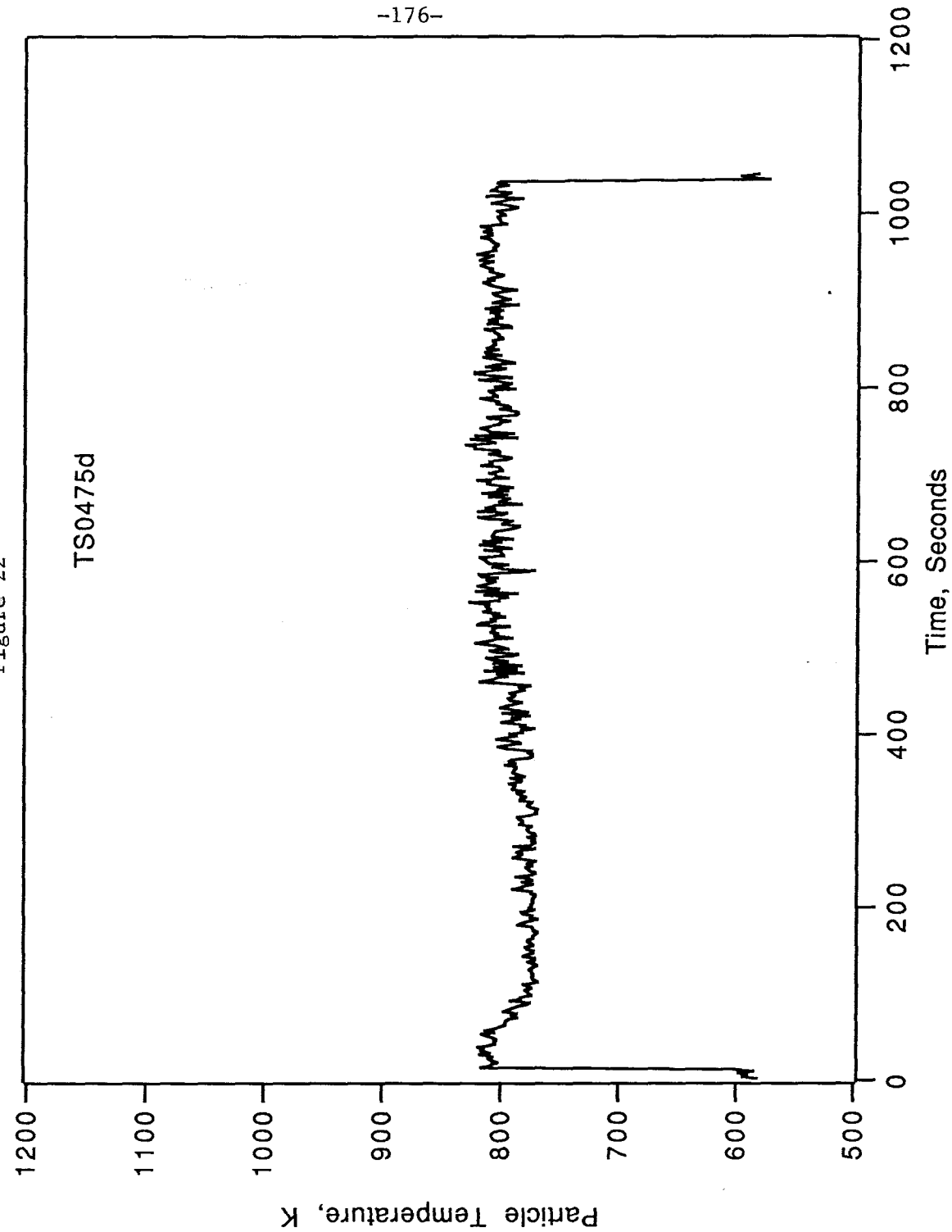
TS0475d
Particle Temperature, K
Time, Seconds
1200
1100
1000
900
800
700
600
500
0
200
400
600
800
1000
1200

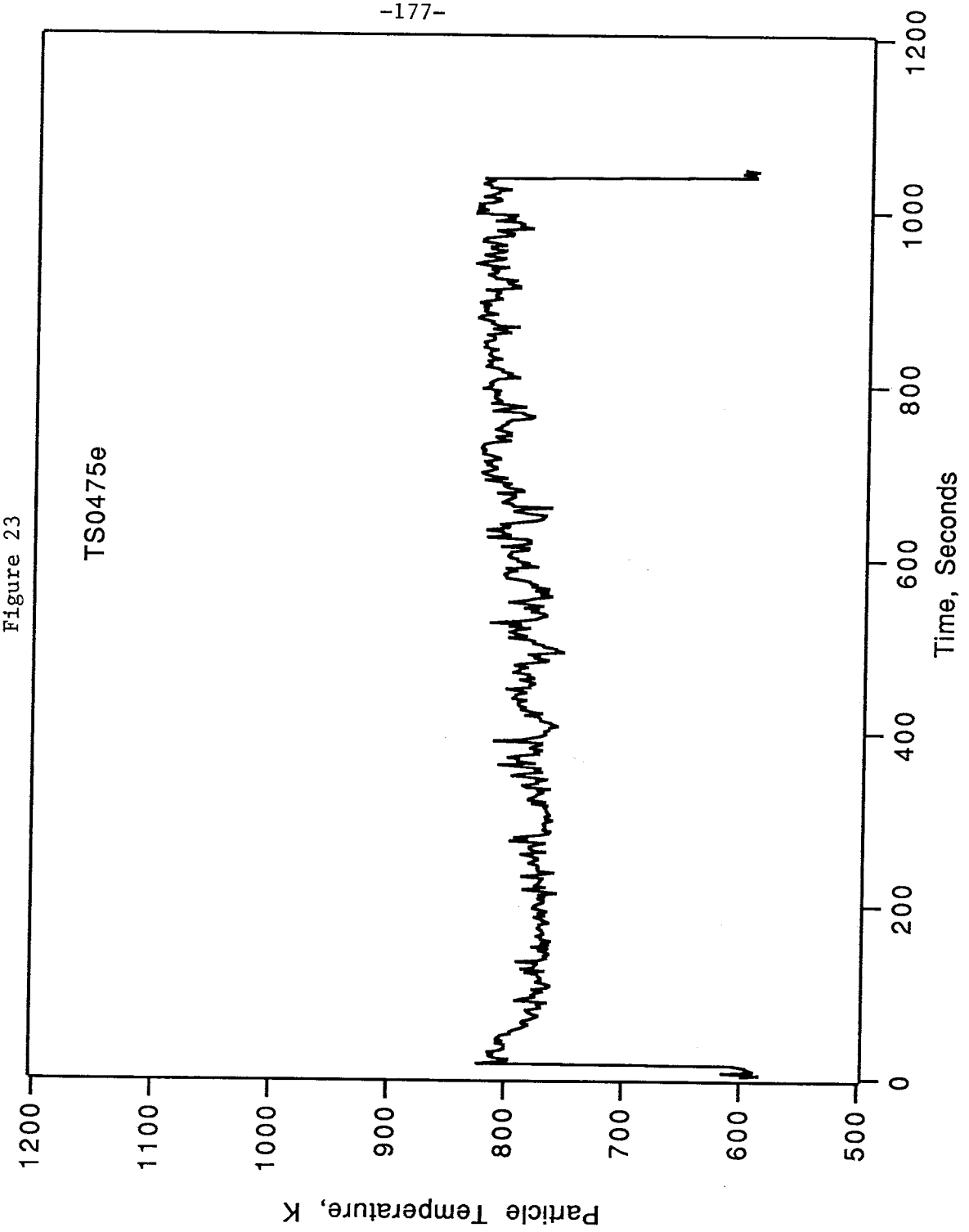
TS0475e
Particle Temperature, K
Time, Seconds
1200
1100
1000
900
800
700
600
500
0
200
400
600
800
1000
1200

Figure 23

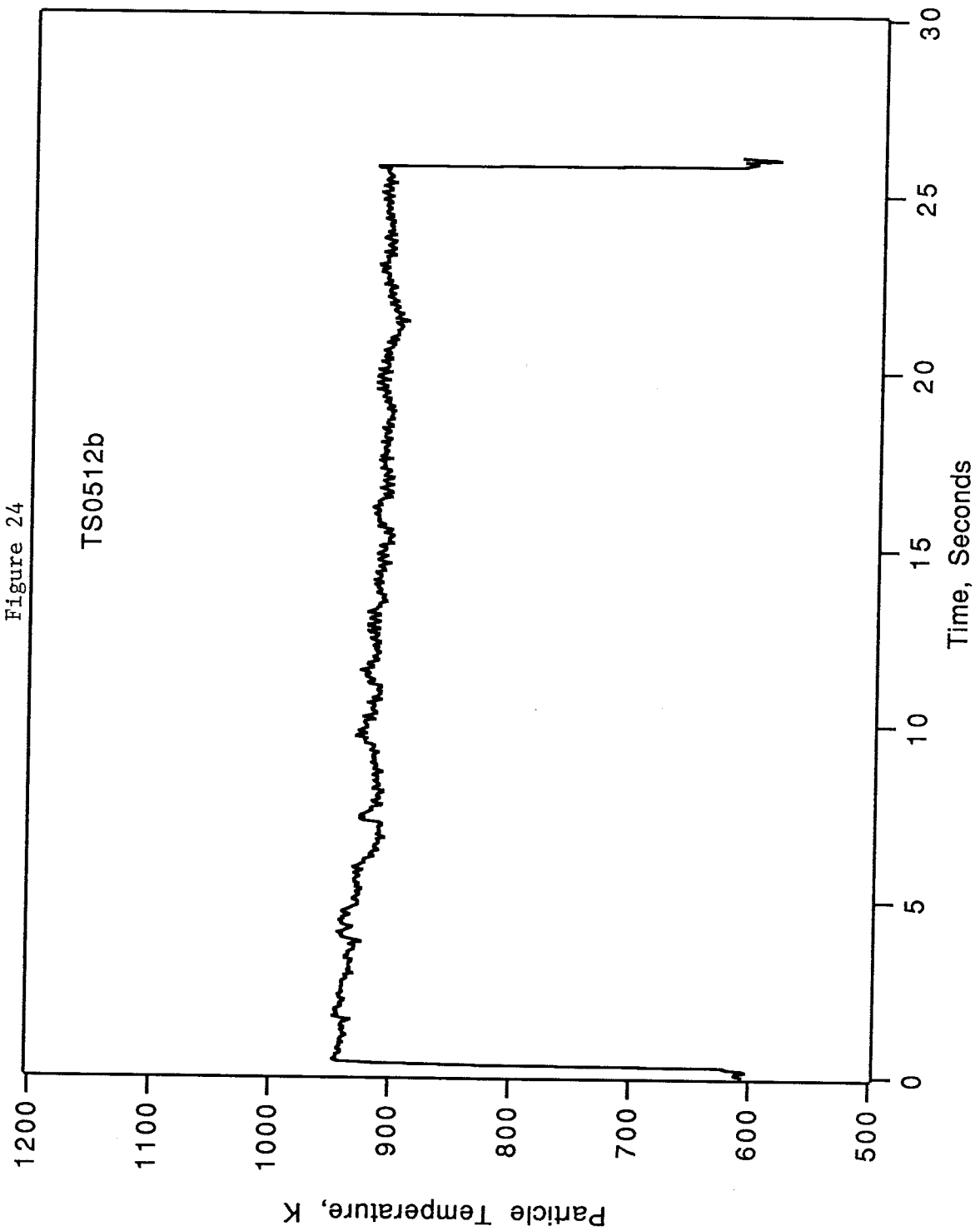
TS0512b
Particle Temperature, K
Time, Seconds
1200
1100
1000
900
800
700
600
500
0
5
10
15
20
25
30

Figure 24

Figure 25

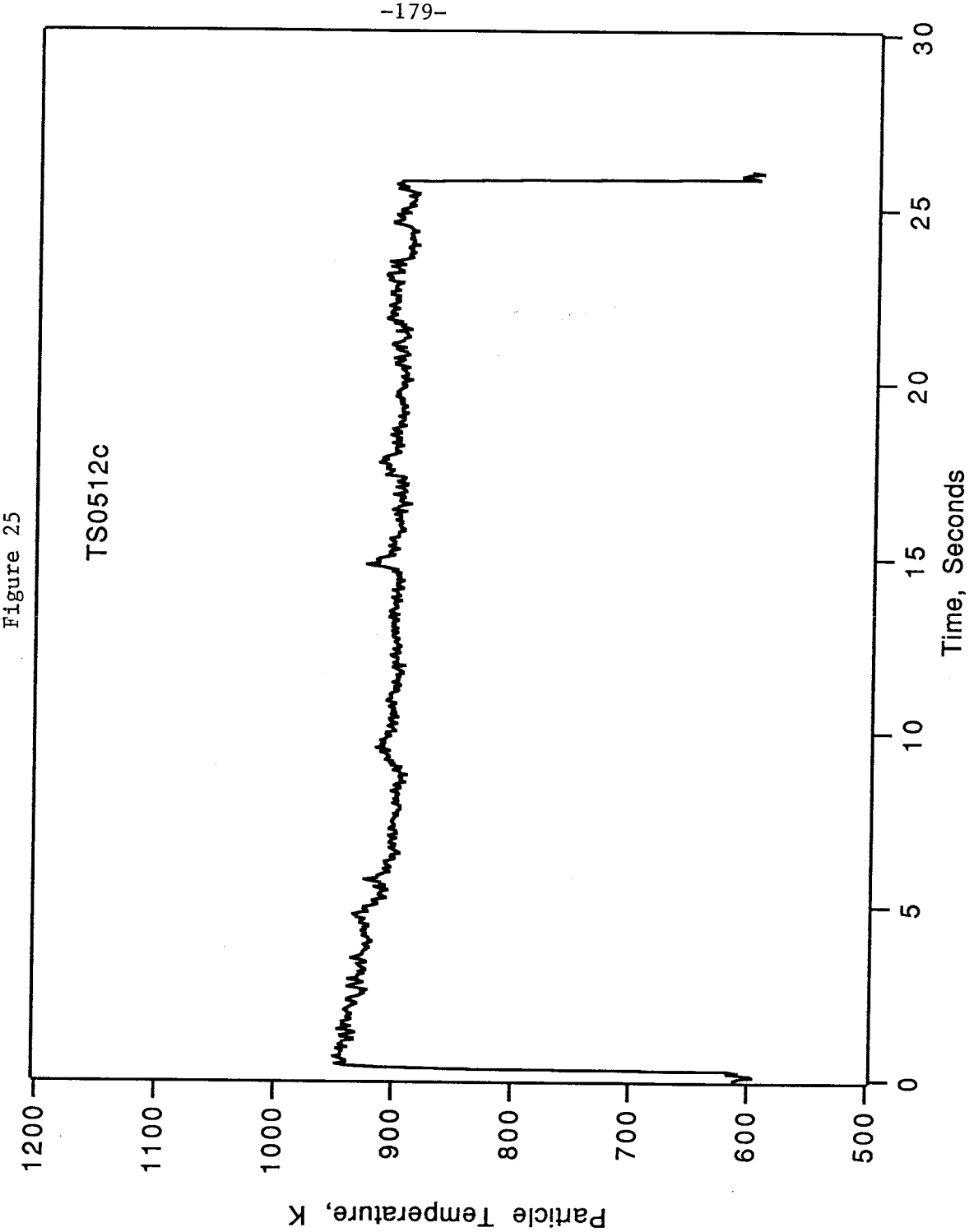
TS0512c
Particle Temperature, K
1200
1100
1000
900
800
700
600
500
0
5
10
15
20
25
30
Time, Seconds

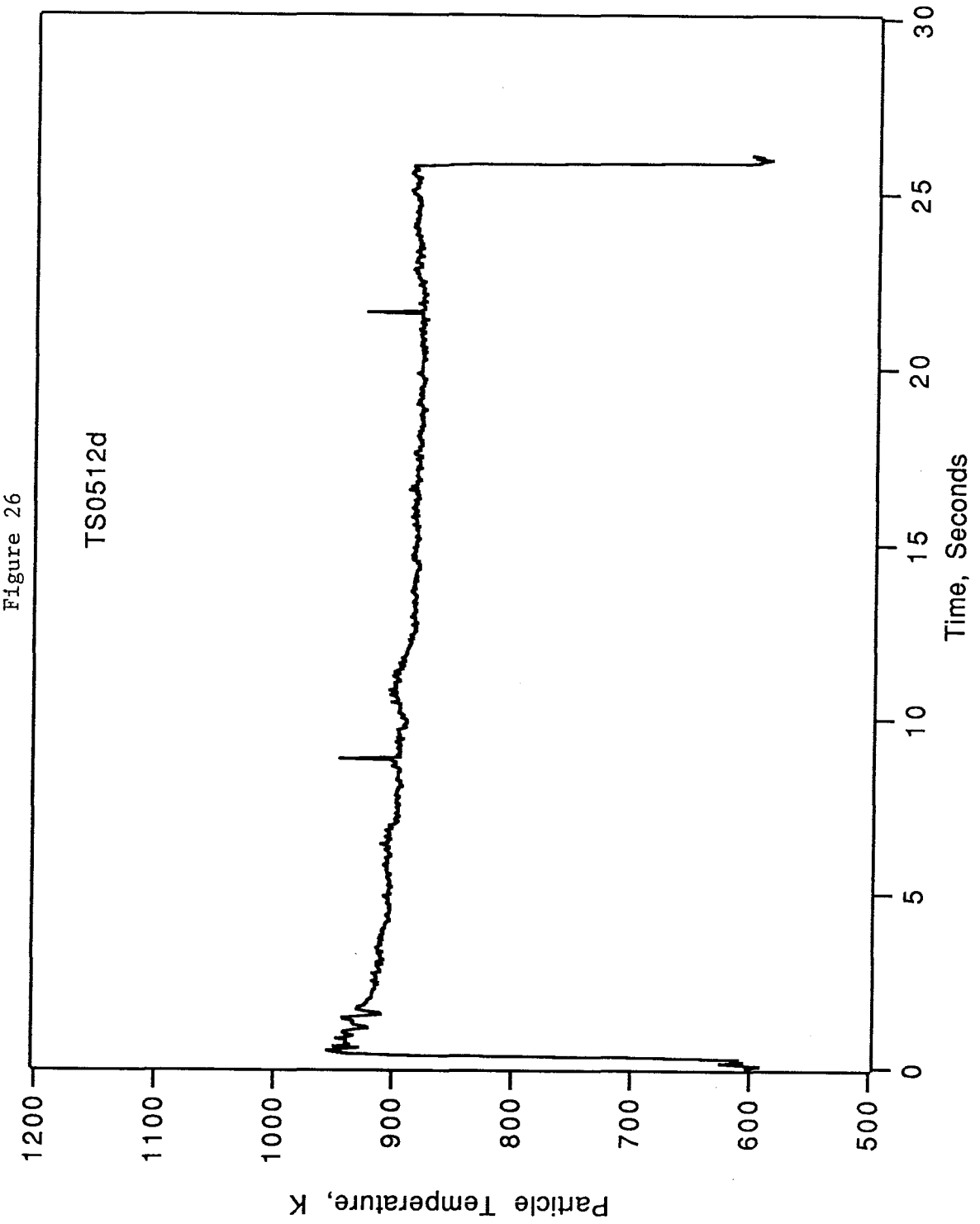
TS0512d
Particle Temperature, K
1200
1100
1000
900
800
700
600
500
0
5
10
15
20
25
30
Time, Seconds

Figure 26

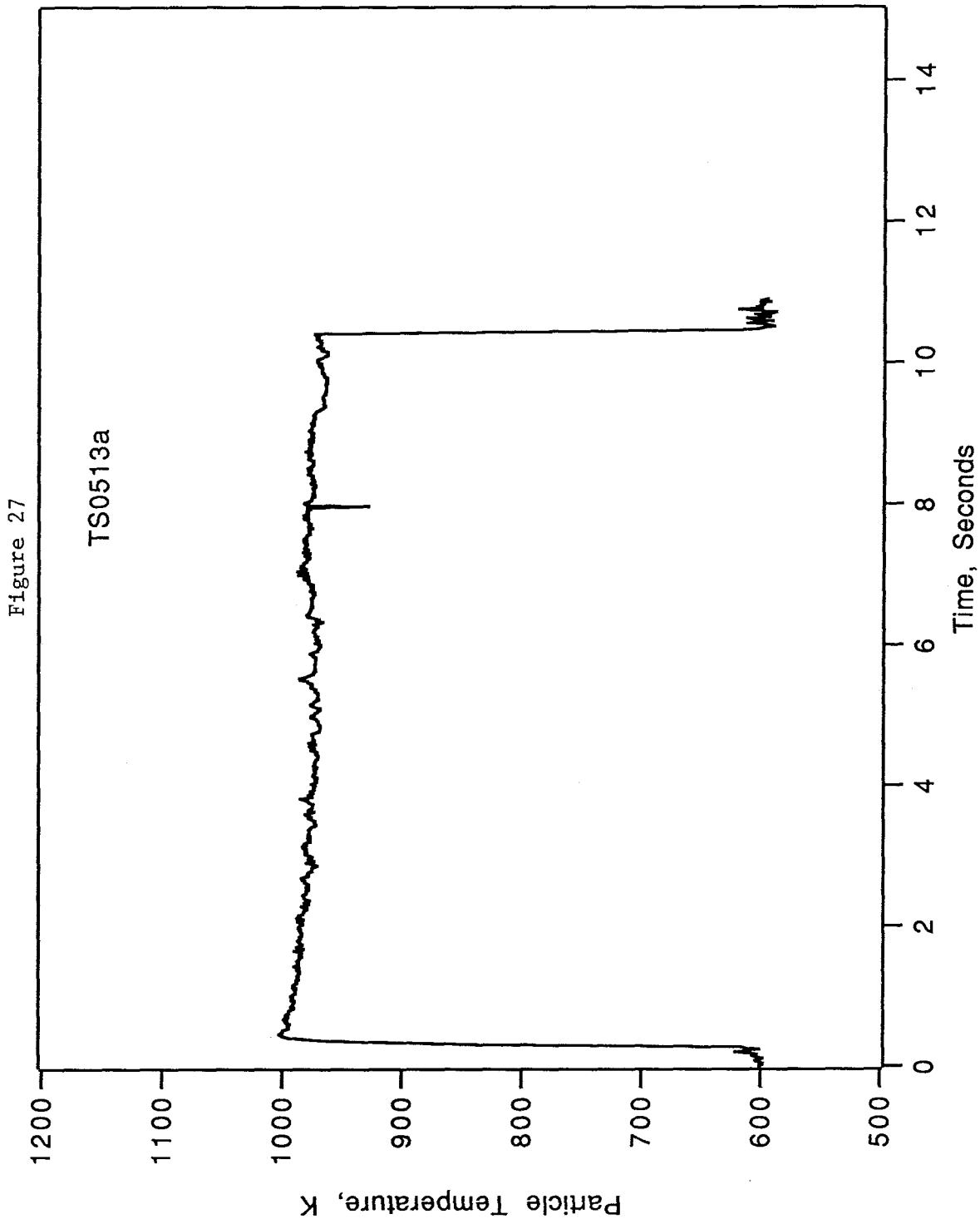
TS0513a
Particle Temperature, K
Time, Seconds
1200
1100
1000
900
800
700
600
500
0
2
4
6
8
10
12
14

Figure 27

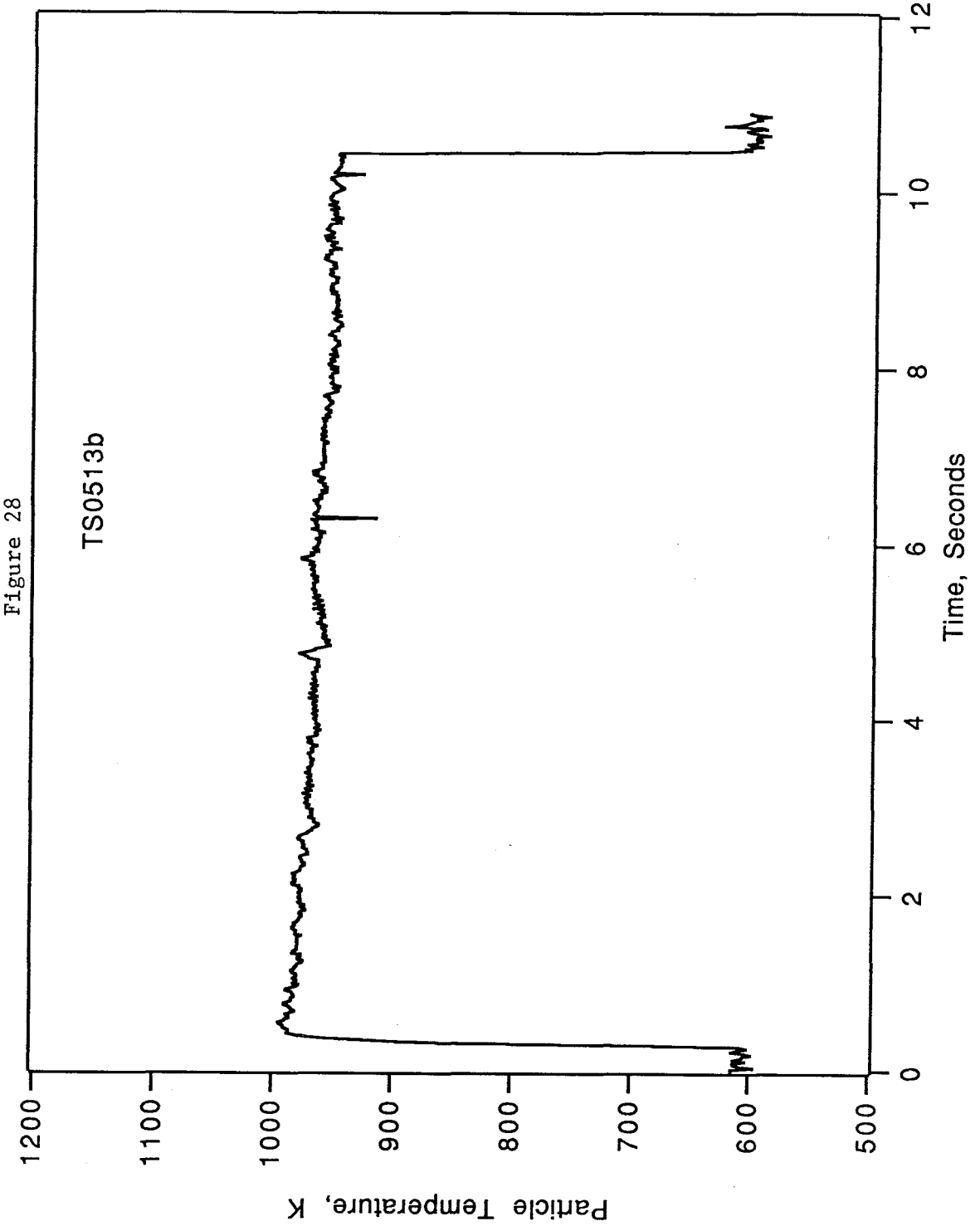
TS0513b
Particle Temperature, K
Time, Seconds
1200
1100
1000
900
800
700
600
500
0
2
4
6
8
10
12

Figure 28

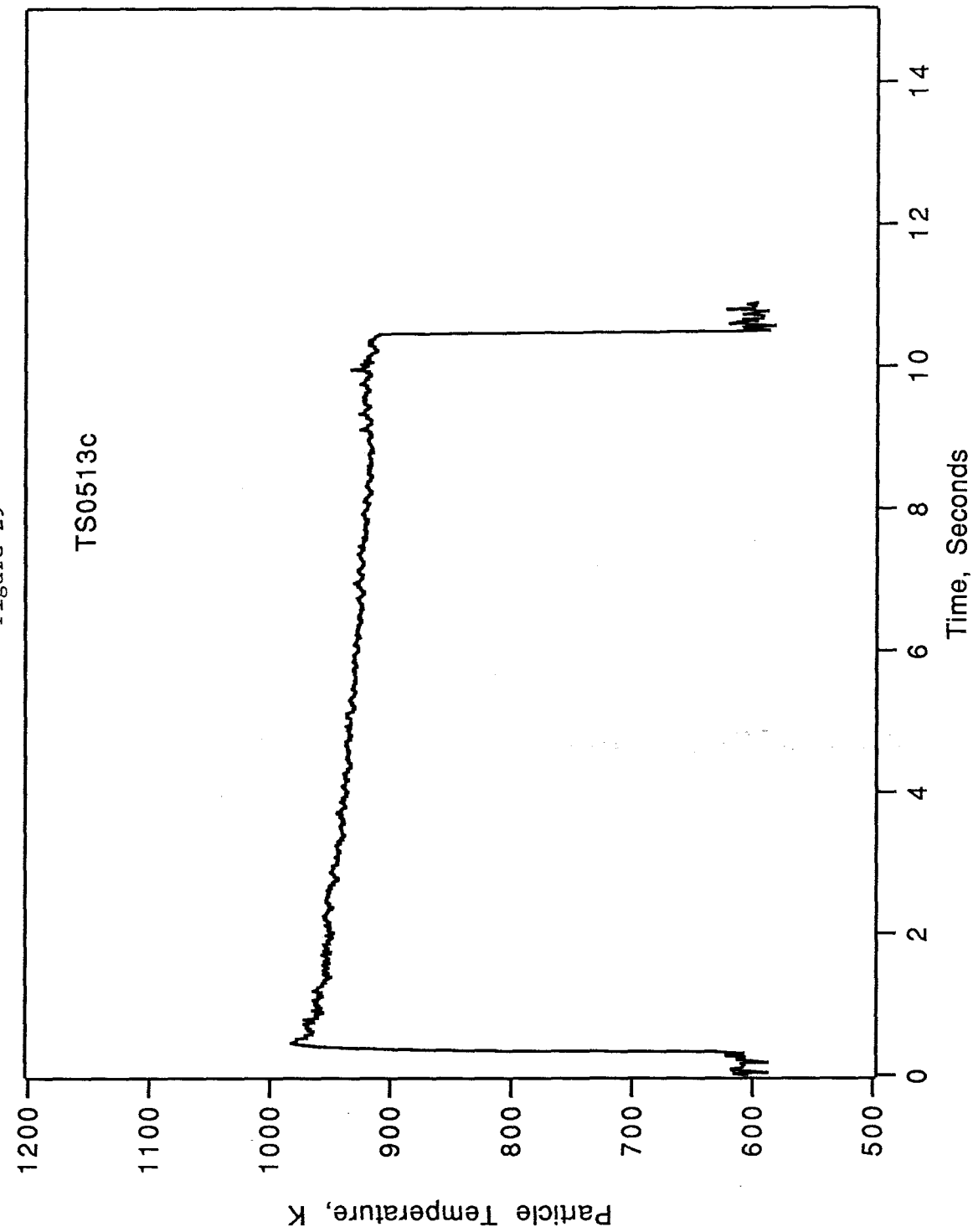
TS0513c
Particle Temperature, K
Time, Seconds
1200
1100
1000
900
800
700
600
500
0
2
4
6
8
10
12
14

Figure 29

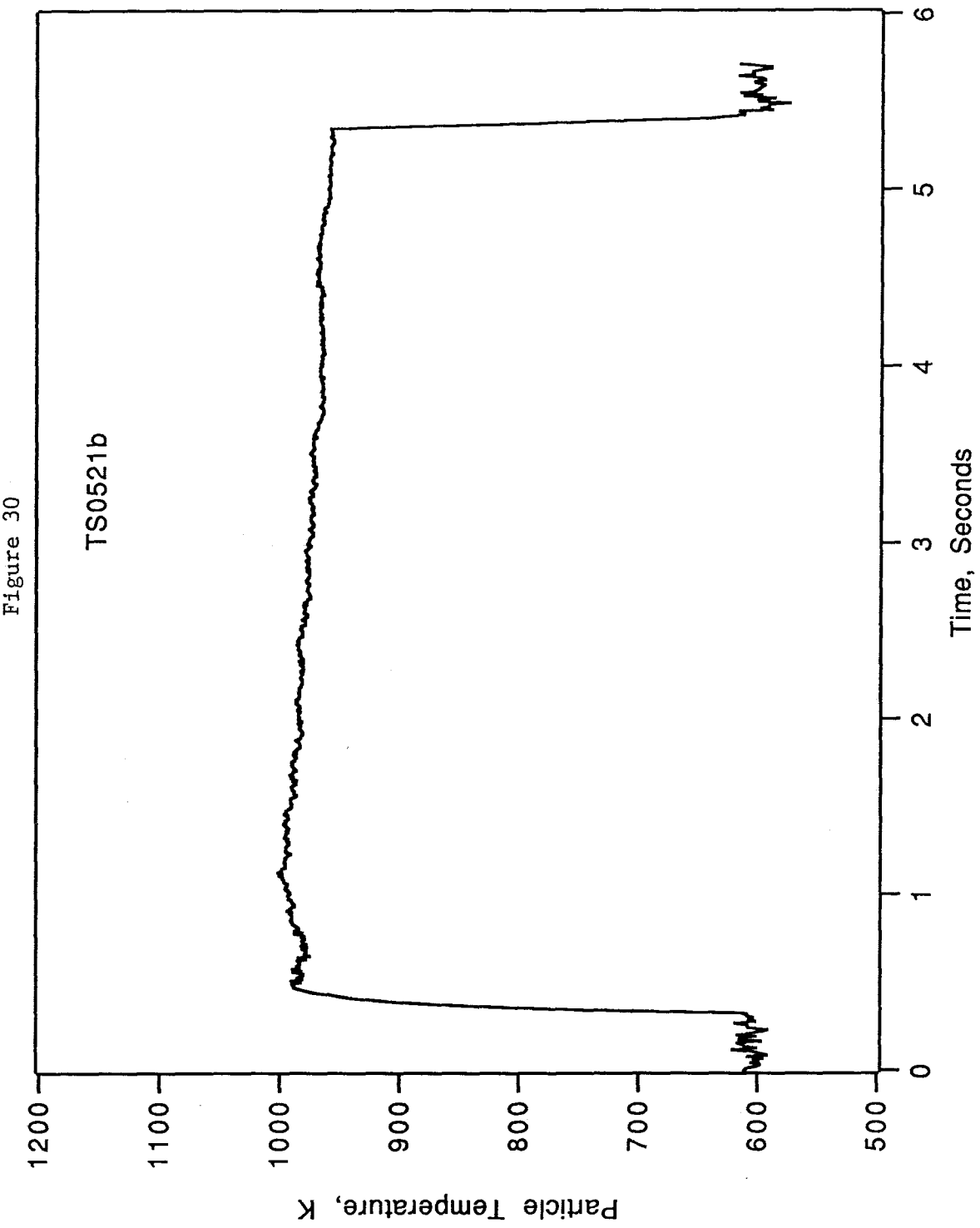
TS0521b
Particle Temperature, K
Time, Seconds
1200
1100
1000
900
800
700
600
500
0
1
2
3
4
5
6

Figure 30

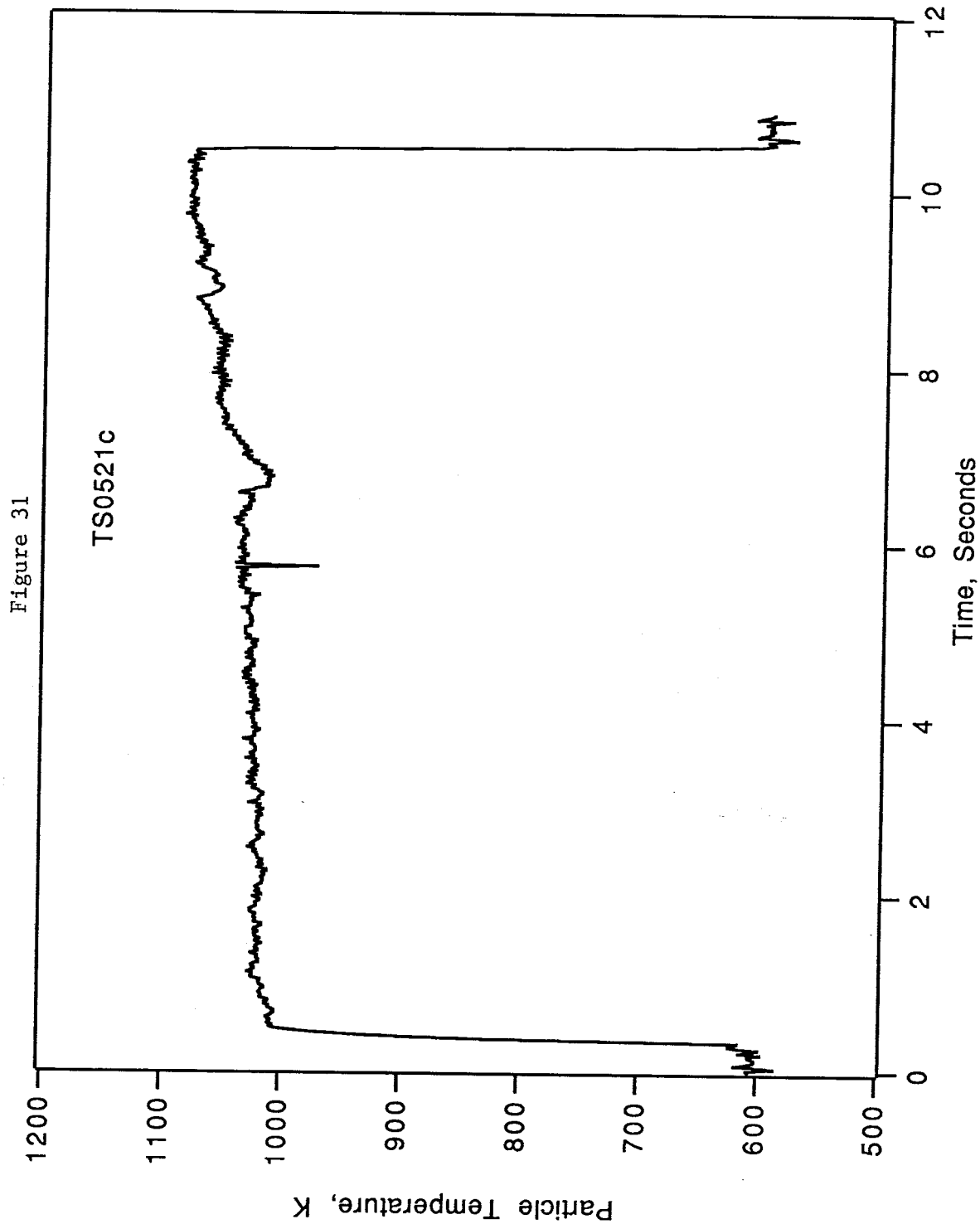
TS0521c
Particle Temperature, K
Time, Seconds
1200
1100
1000
900
800
700
600
500
0
2
4
6
8
10
12

Figure 31

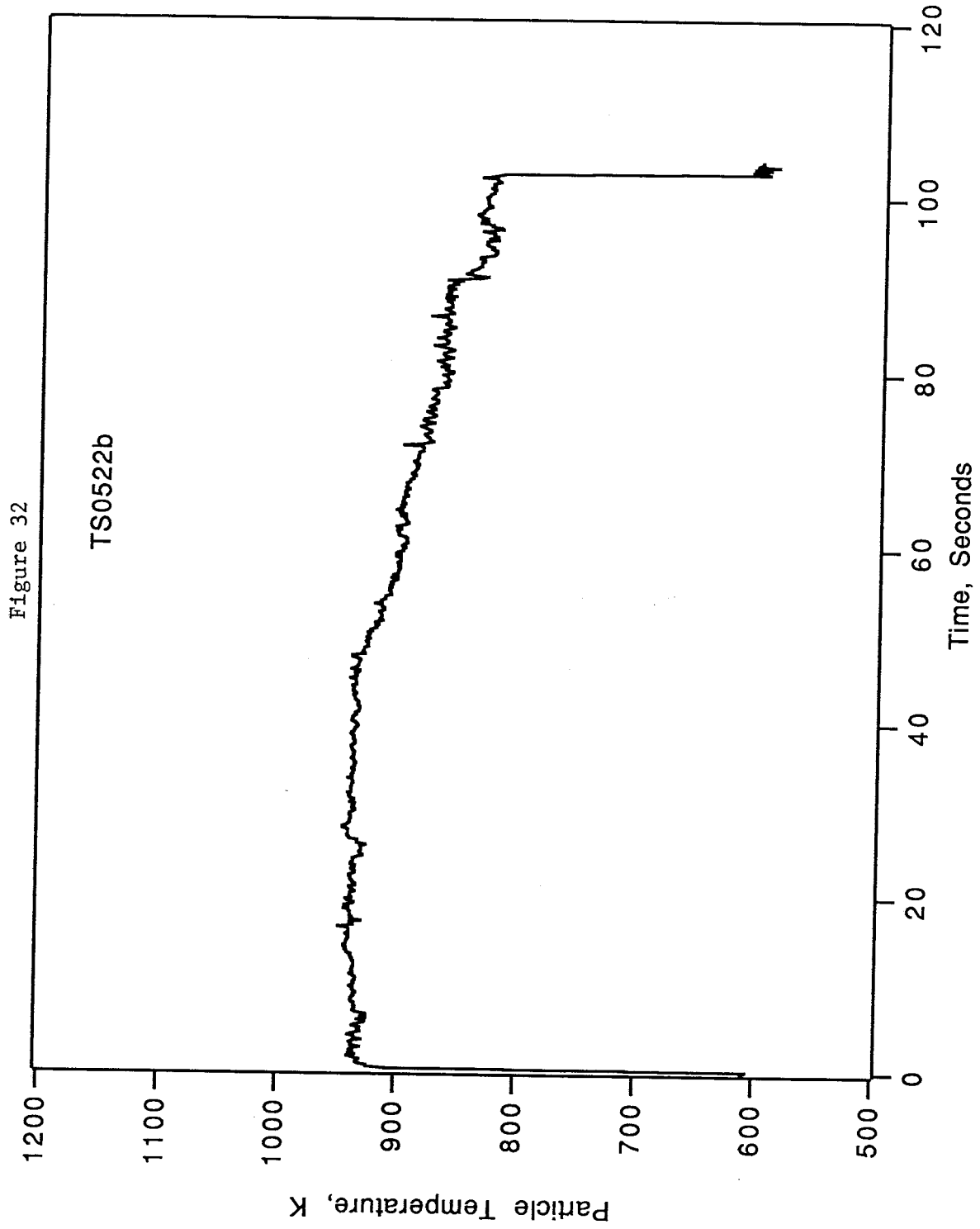
Figure 32
TS0522b
Particle Temperature, K
Time, Seconds
1200
1100
1000
900
800
700
600
500
0
20
40
60
80
100
120

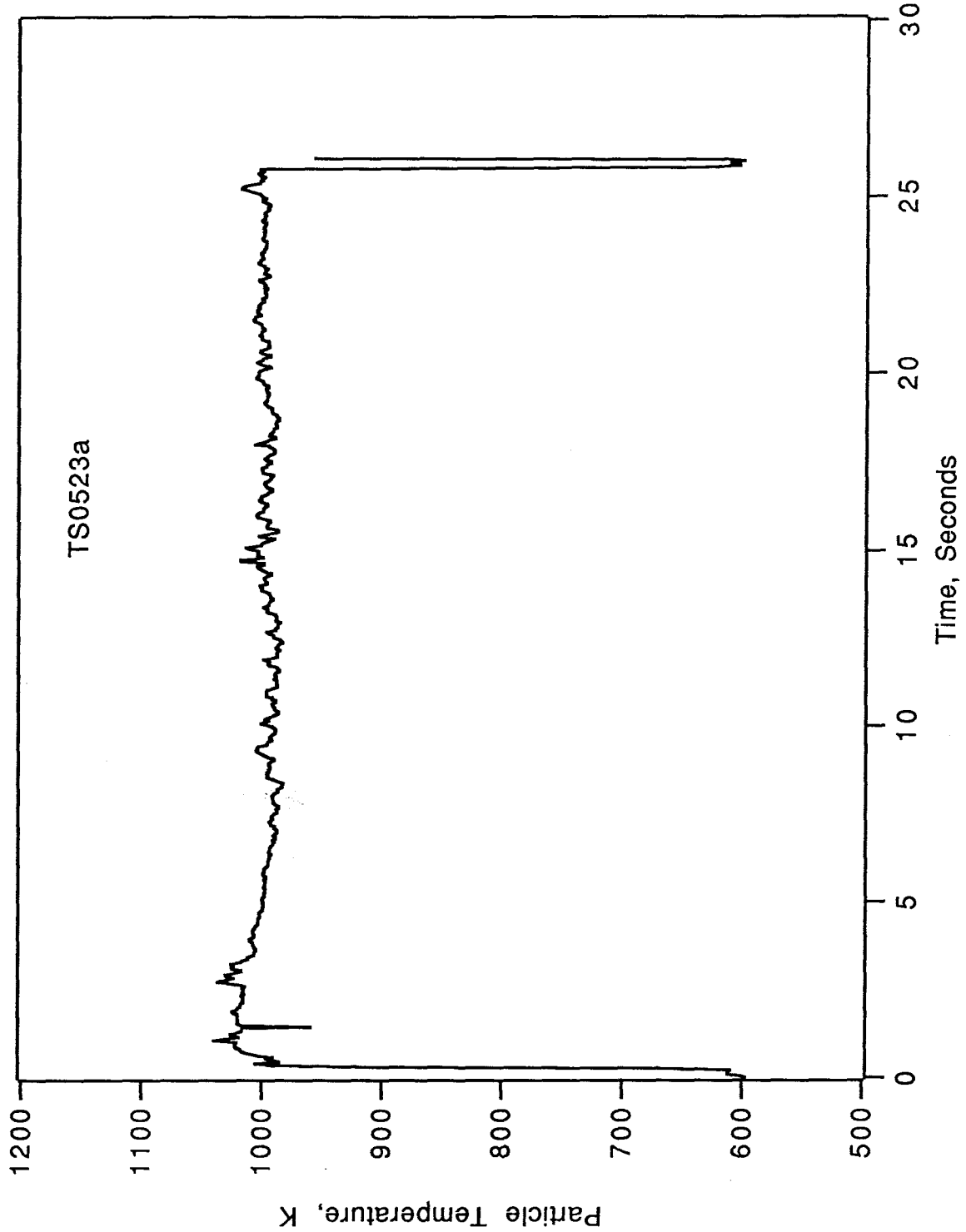
TS0523a
Particle Temperature, K
Time, Seconds
1200
1100
1000
900
800
700
600
500
0
5
10
15
20
25
30

Figure 33

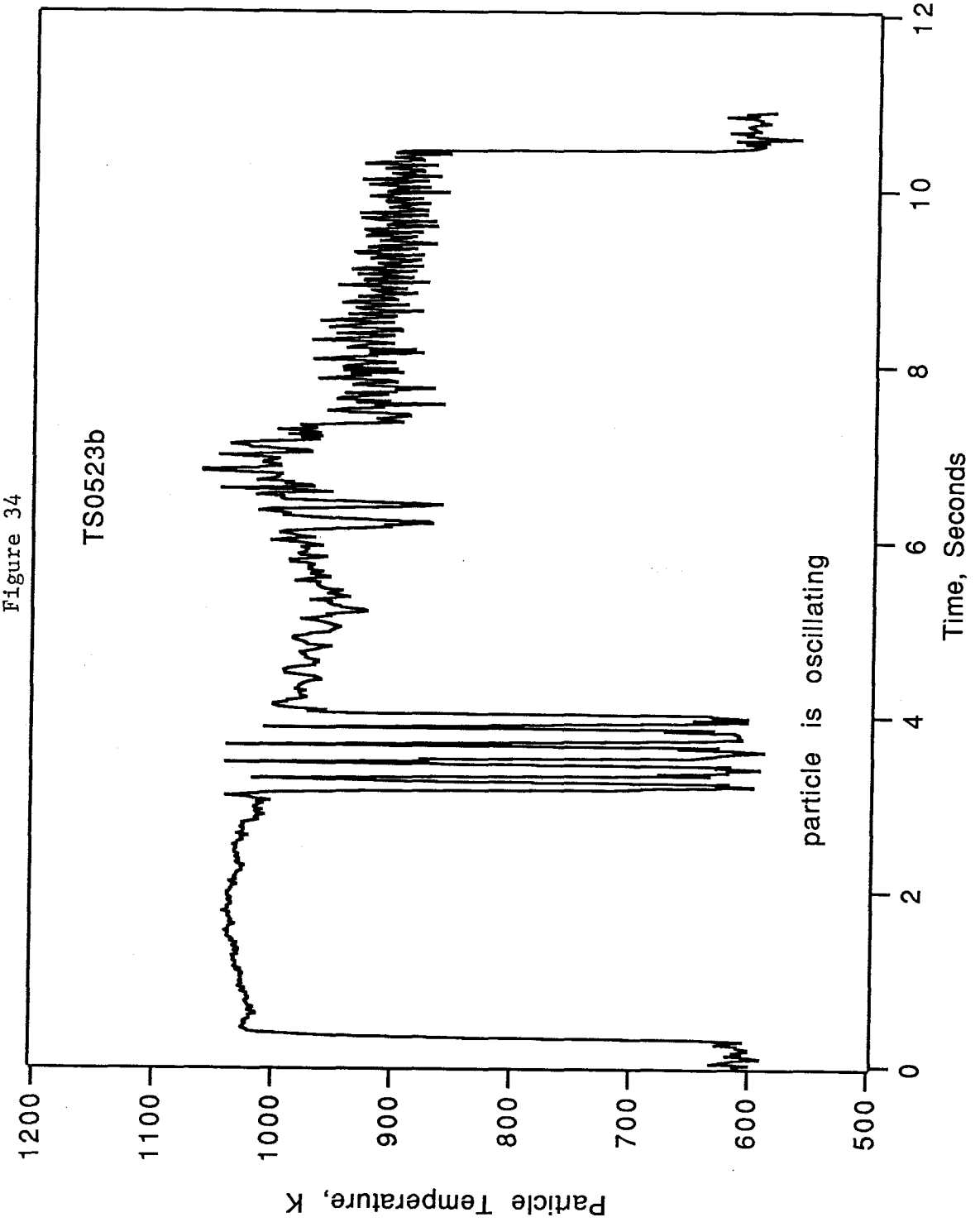
TS0523b
particle is oscillating
Particle Temperature, K
Time, Seconds
1200
1100
1000
900
800
700
600
500
0
2
4
6
8
10
12

Figure 34

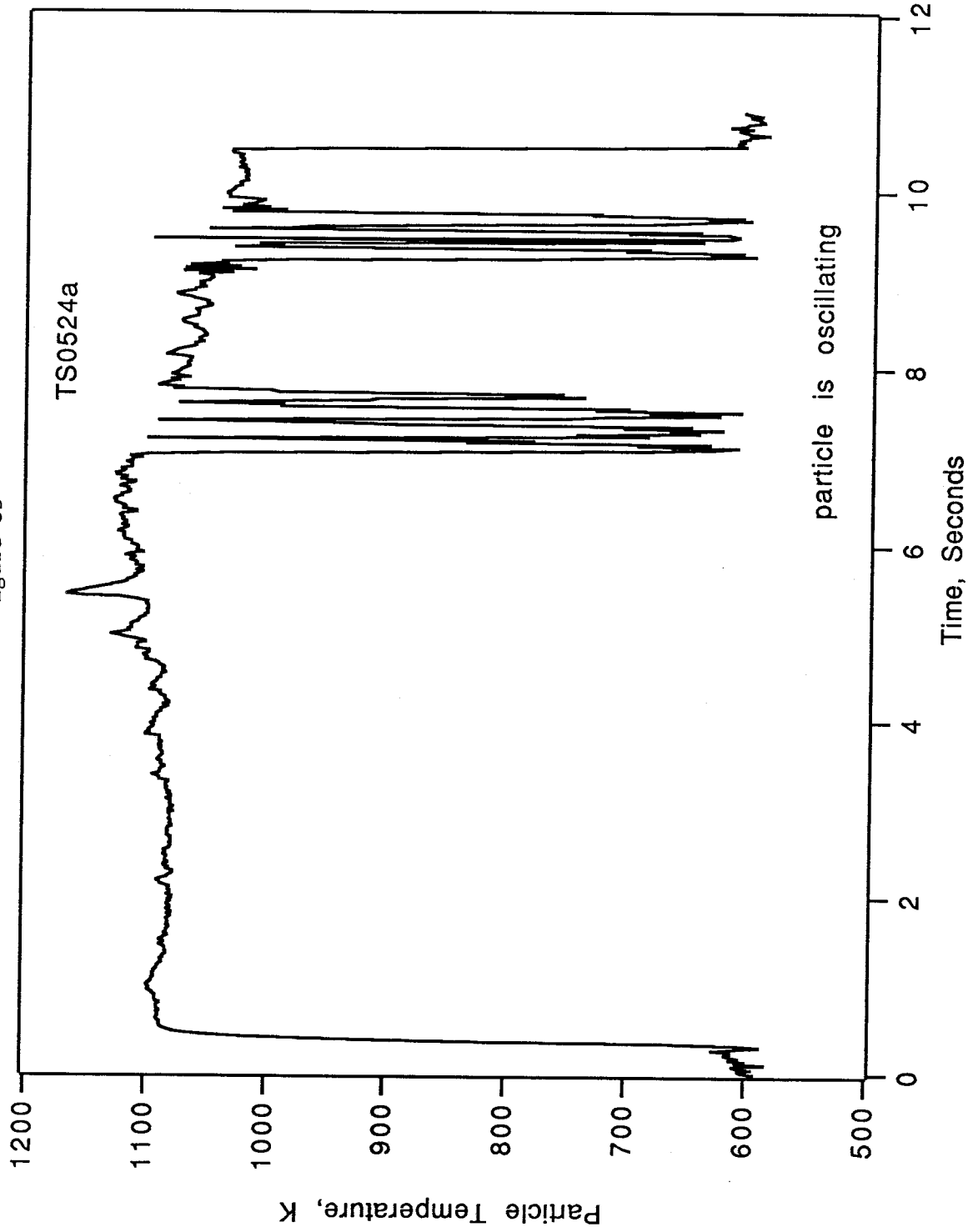
TS0524a
particle is oscillating
Particle Temperature, K
Time, Seconds
1200
1100
1000
900
800
700
600
500
0
2
4
6
8
10
12

Figure 35

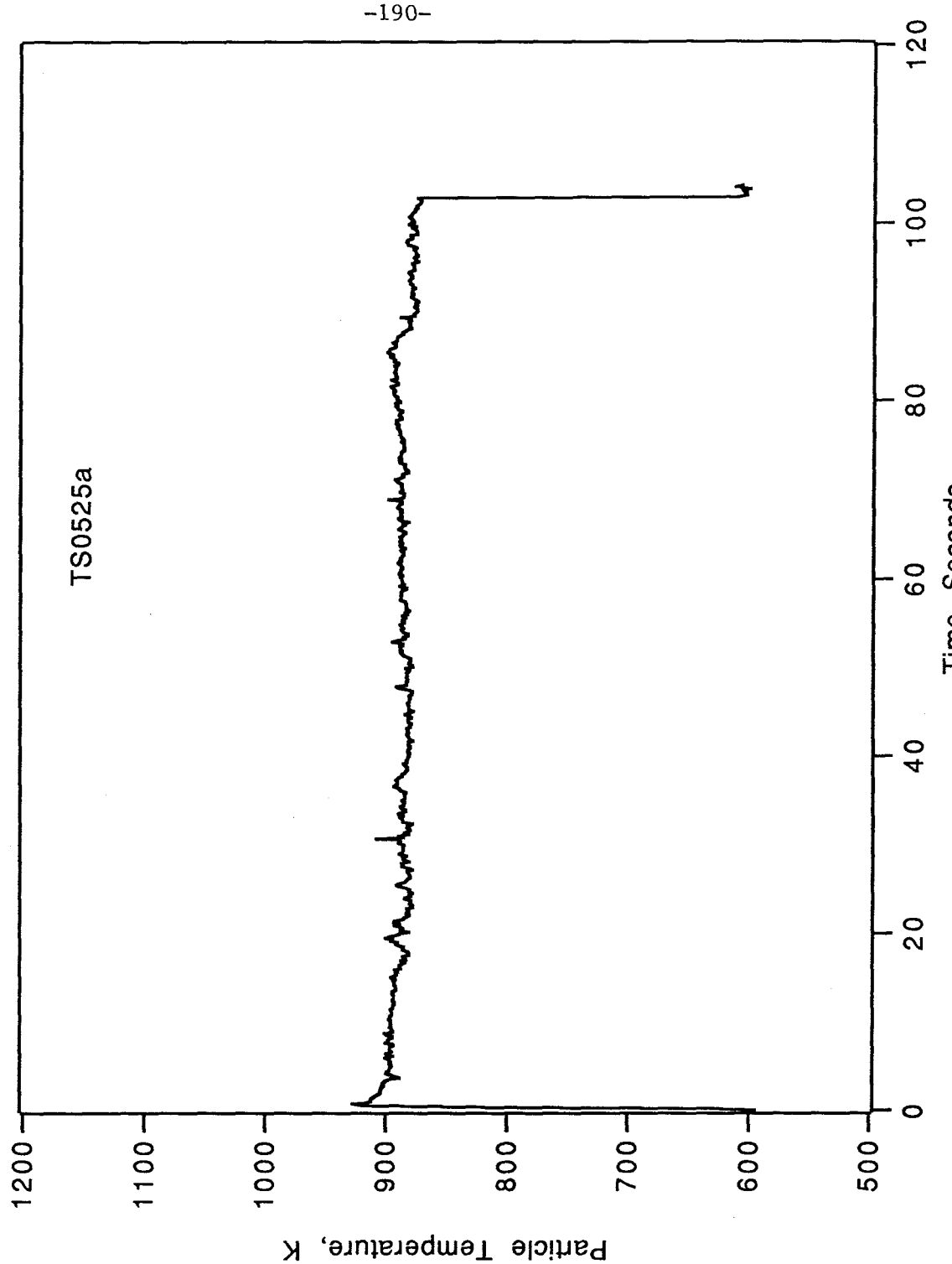
TS0525a
Particle Temperature, K
Time, Seconds
1200
1100
1000
900
800
700
600
500
0
20
40
60
80
100
120

Figure 36

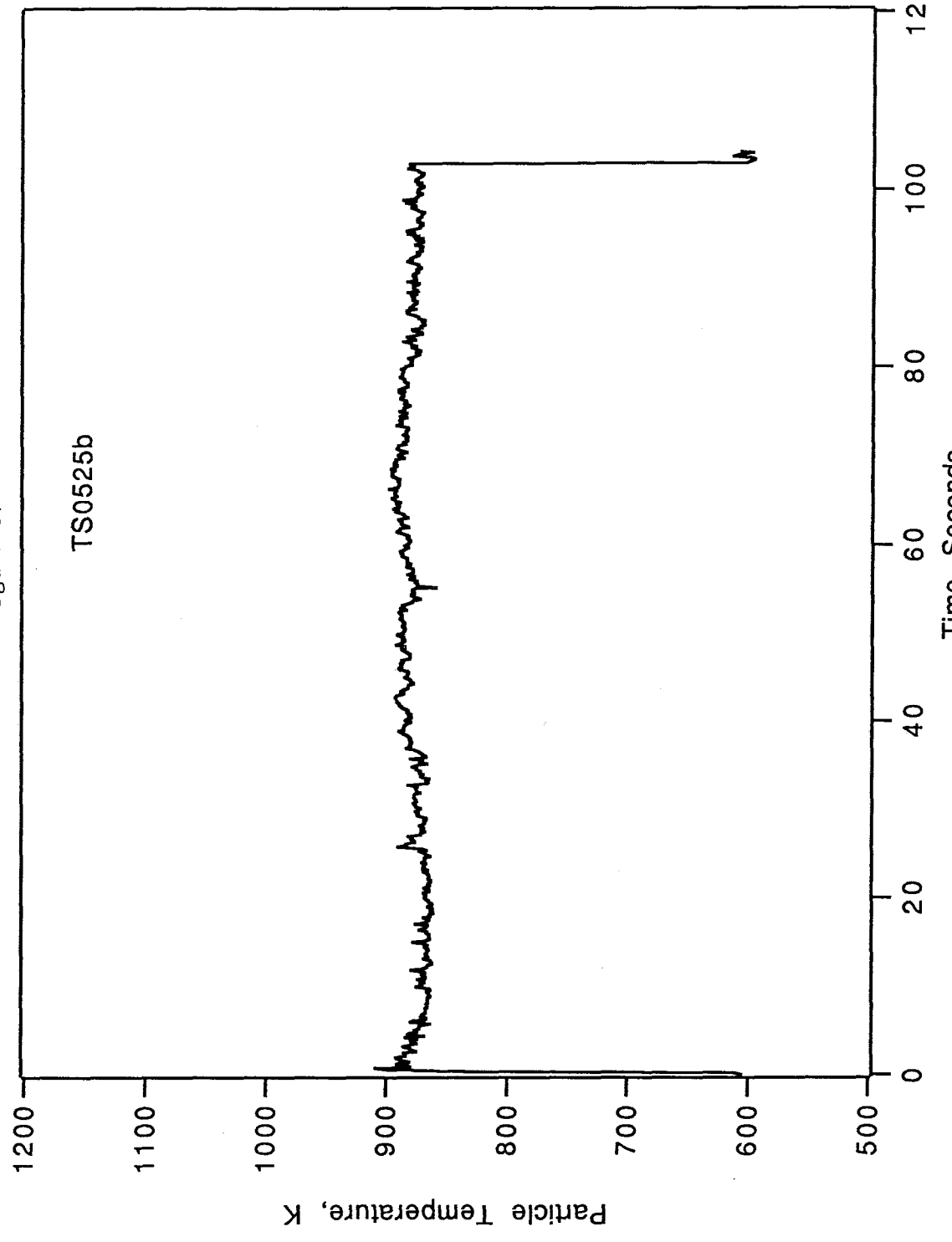
TS0525b
Particle Temperature, K
1200
1100
1000
900
800
700
600
500
0
20
40
60
80
100
120
Time, Seconds

Figure 37

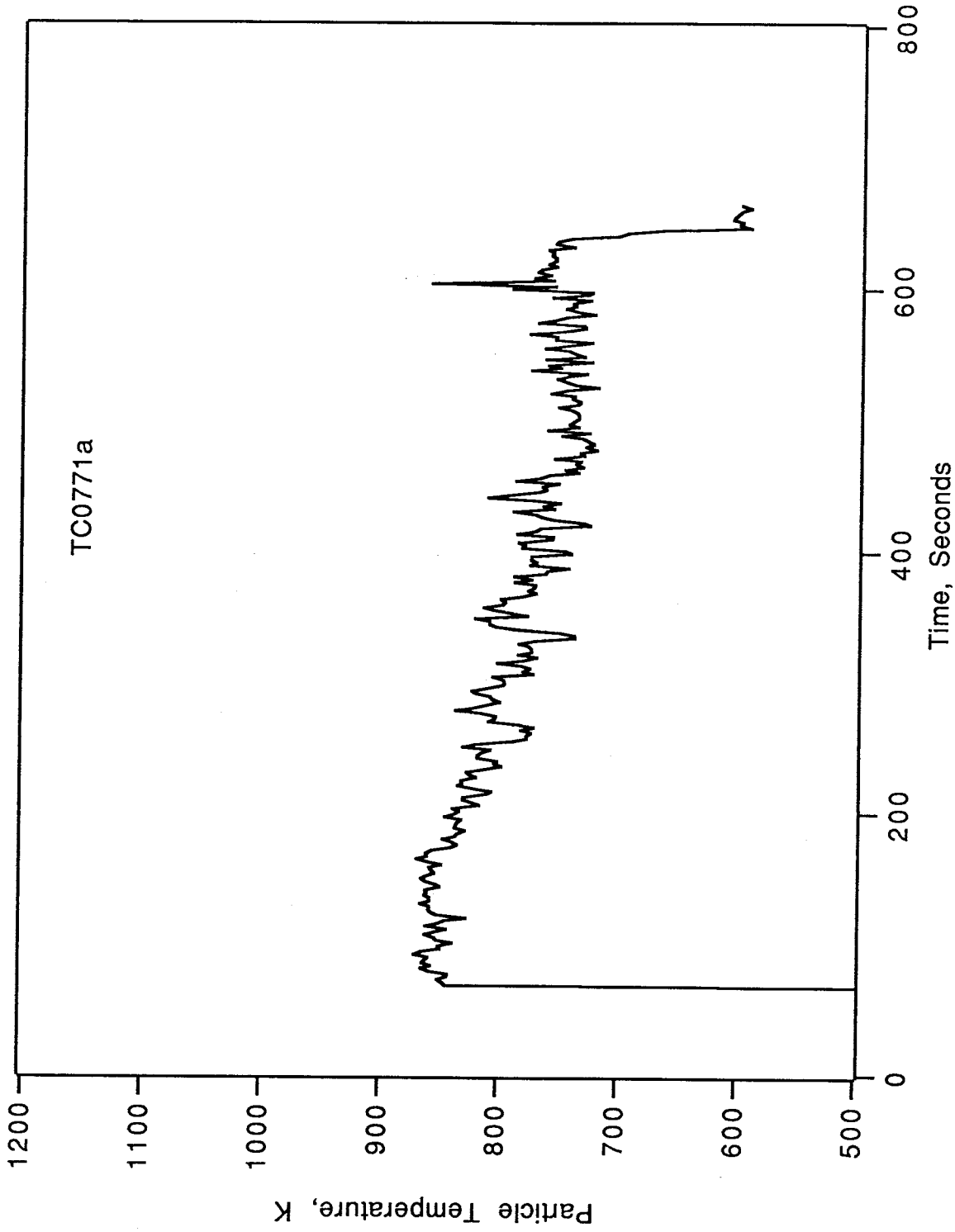
TC0771a
Particle Temperature, K
1200
1100
1000
900
800
700
600
500
0
200
400
600
800
Time, Seconds

Figure 38

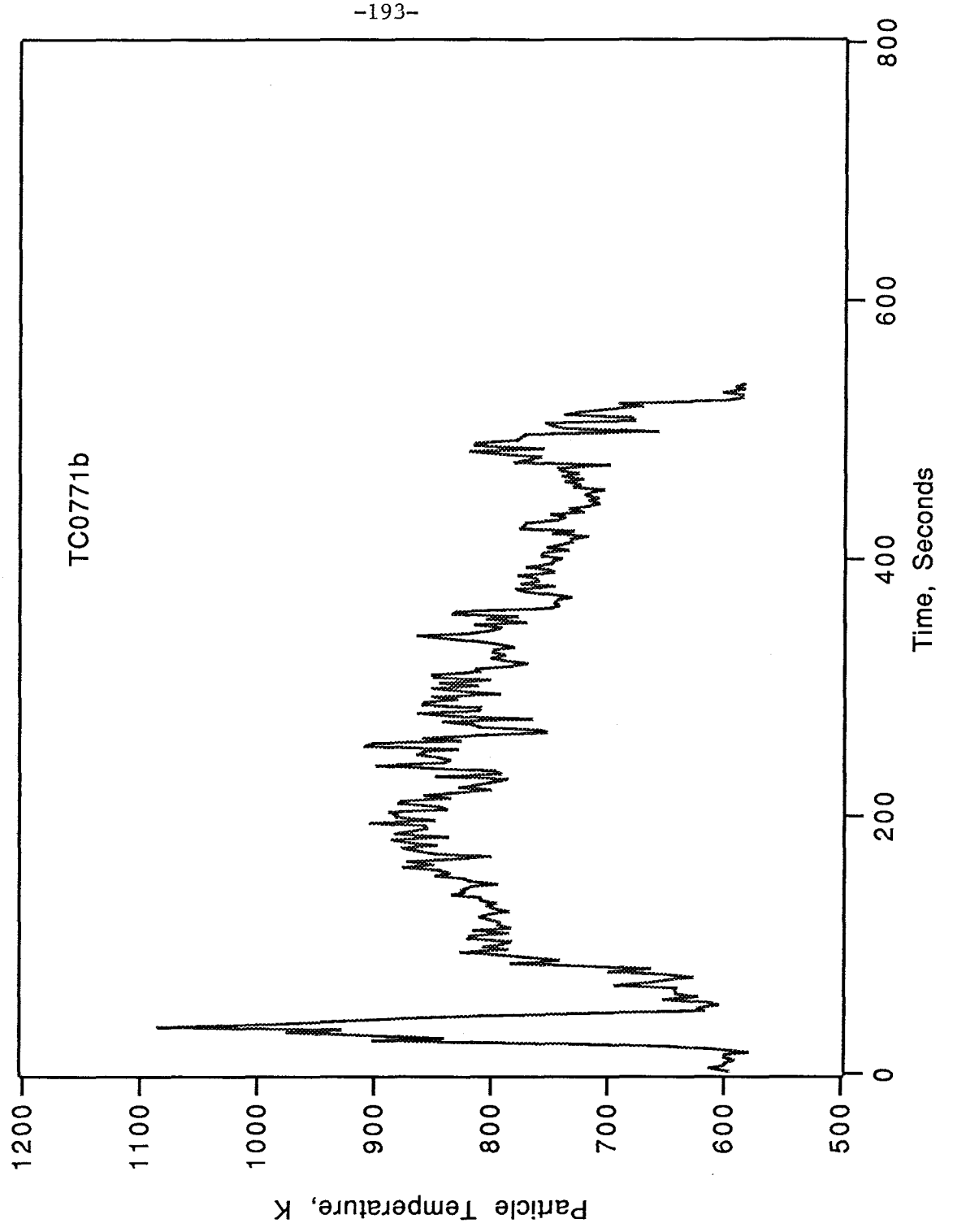
TC0771b
Particle Temperature, K
Time, Seconds
1200
1100
1000
900
800
700
600
500
0
200
400
600
800

Figure 39

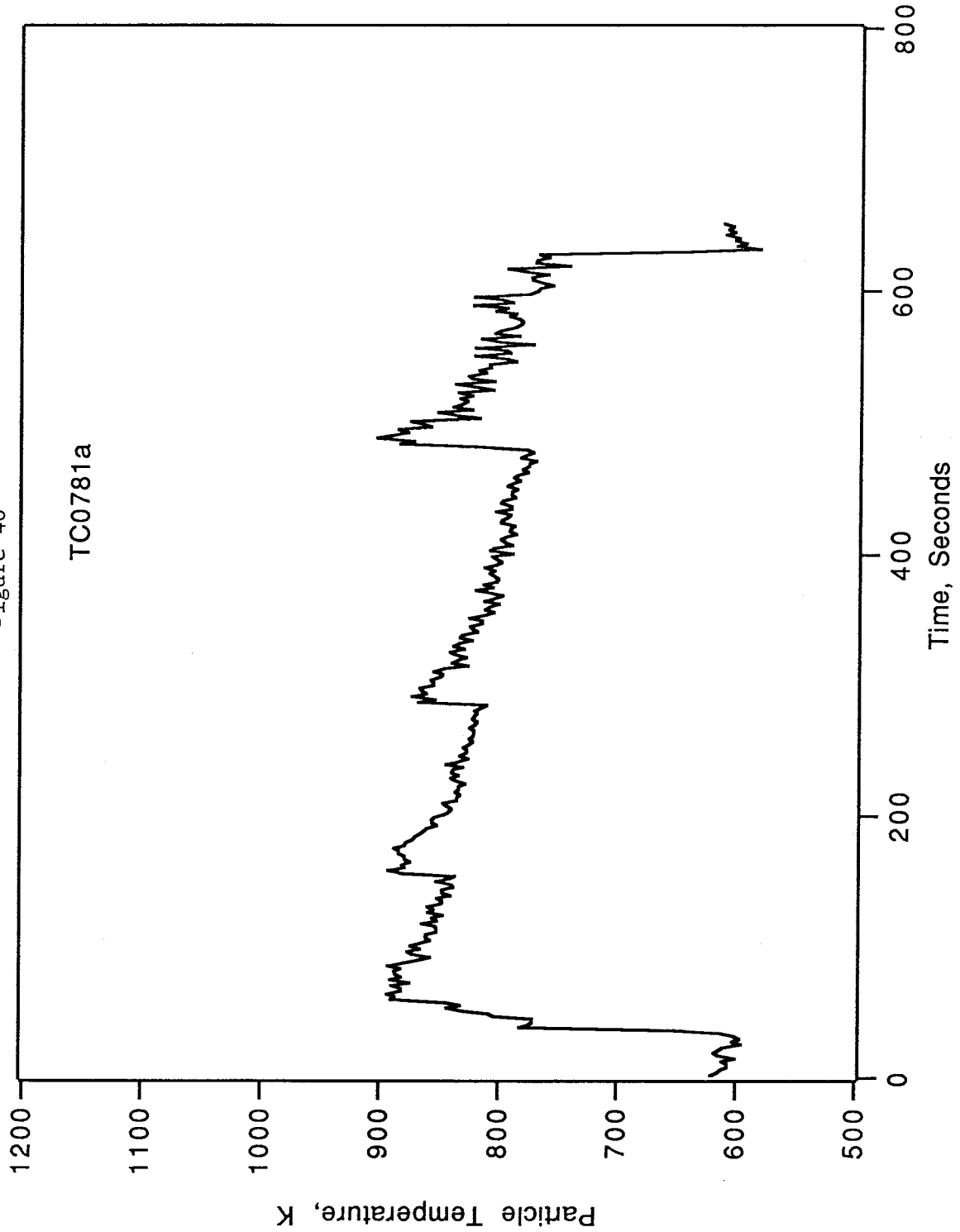
TC0781a
Particle Temperature, K
Time, Seconds
1200
1100
1000
900
800
700
600
500
0
200
400
600
800

Figure 40

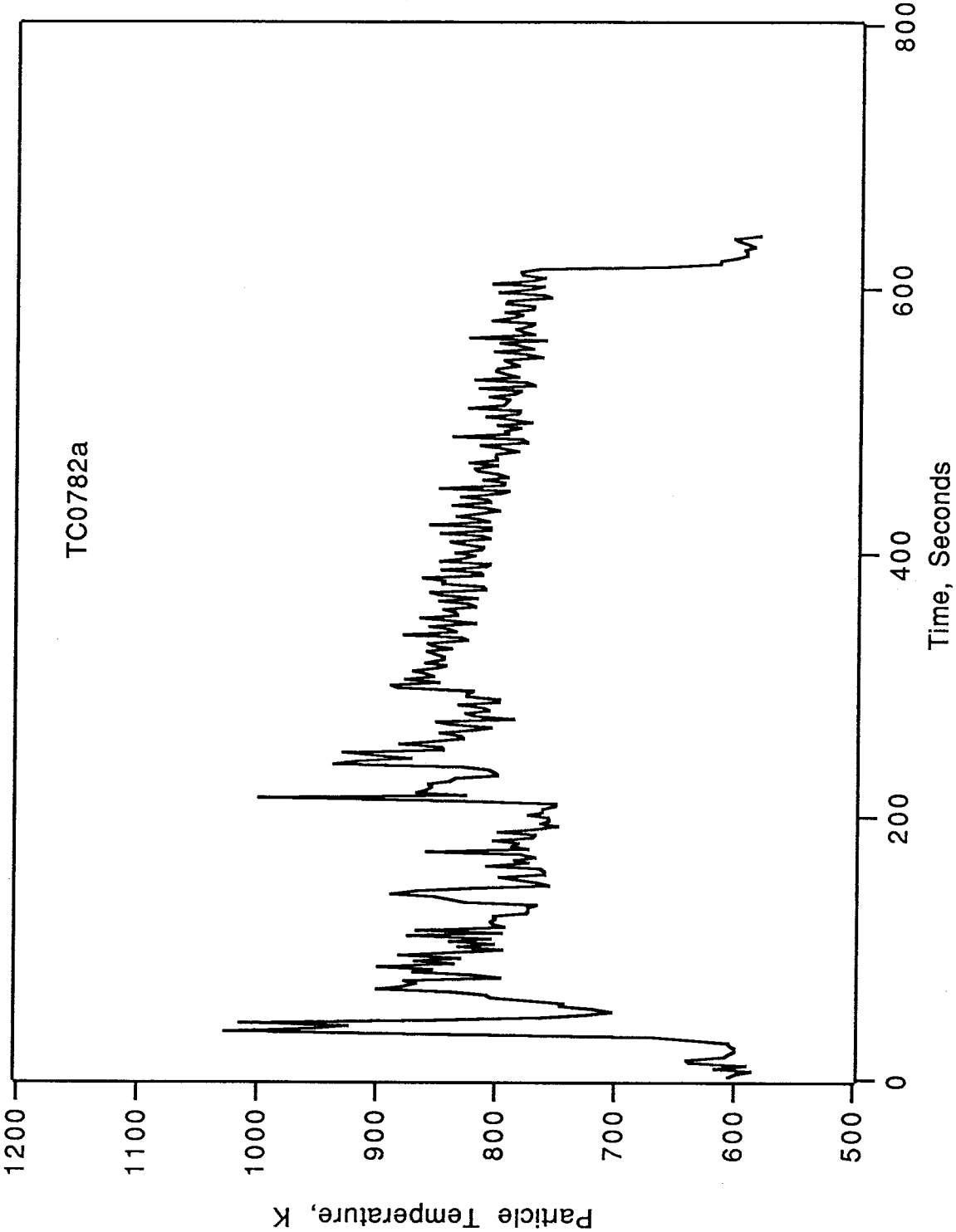
TC0782a
Particle Temperature, K
1200
1100
1000
900
800
700
600
500
0
200
400
600
800
Time, Seconds

Figure 41

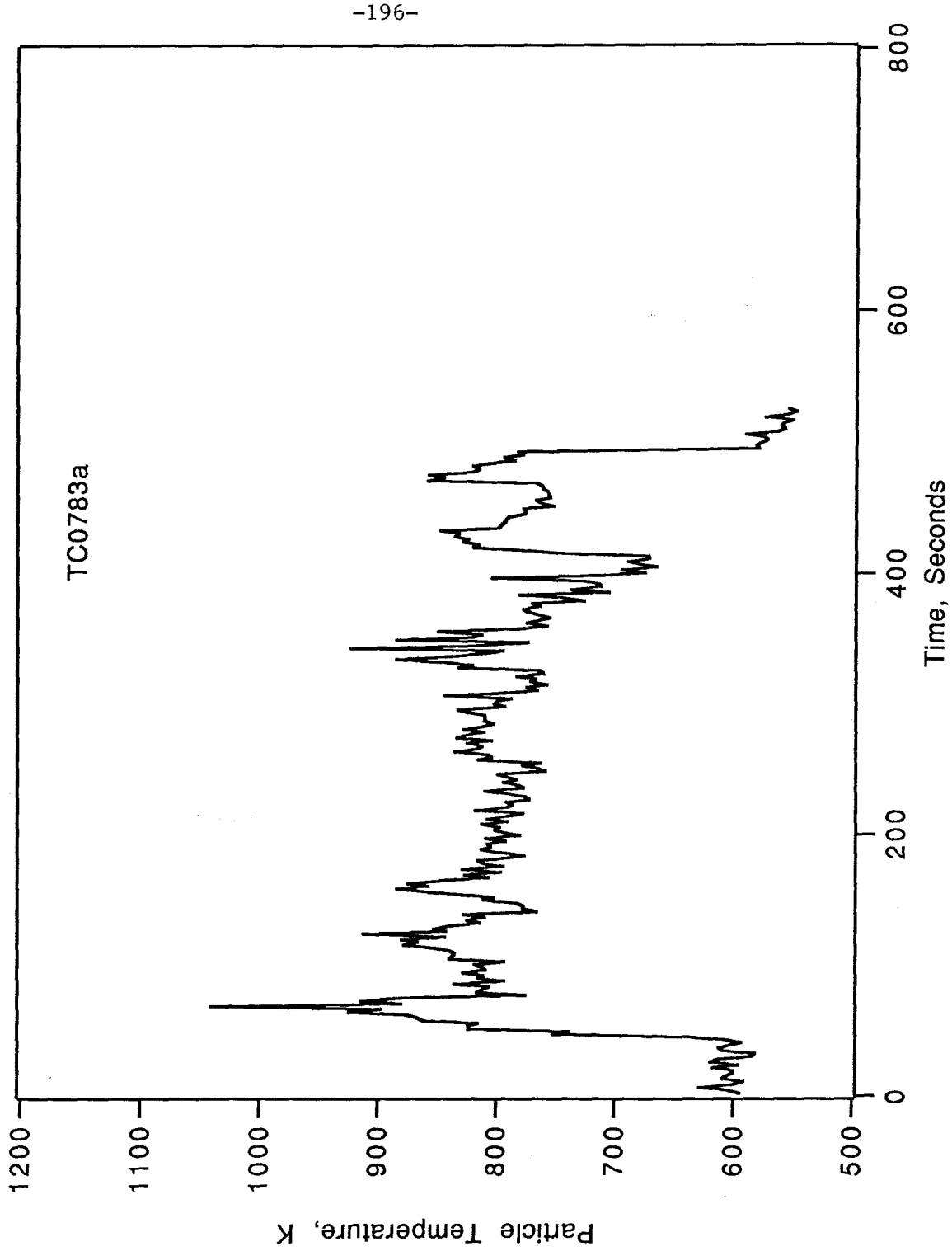
TC0783a
Particle Temperature, K
Time, Seconds
1200
1100
1000
900
800
700
600
500
0
200
400
600
800

Figure 42

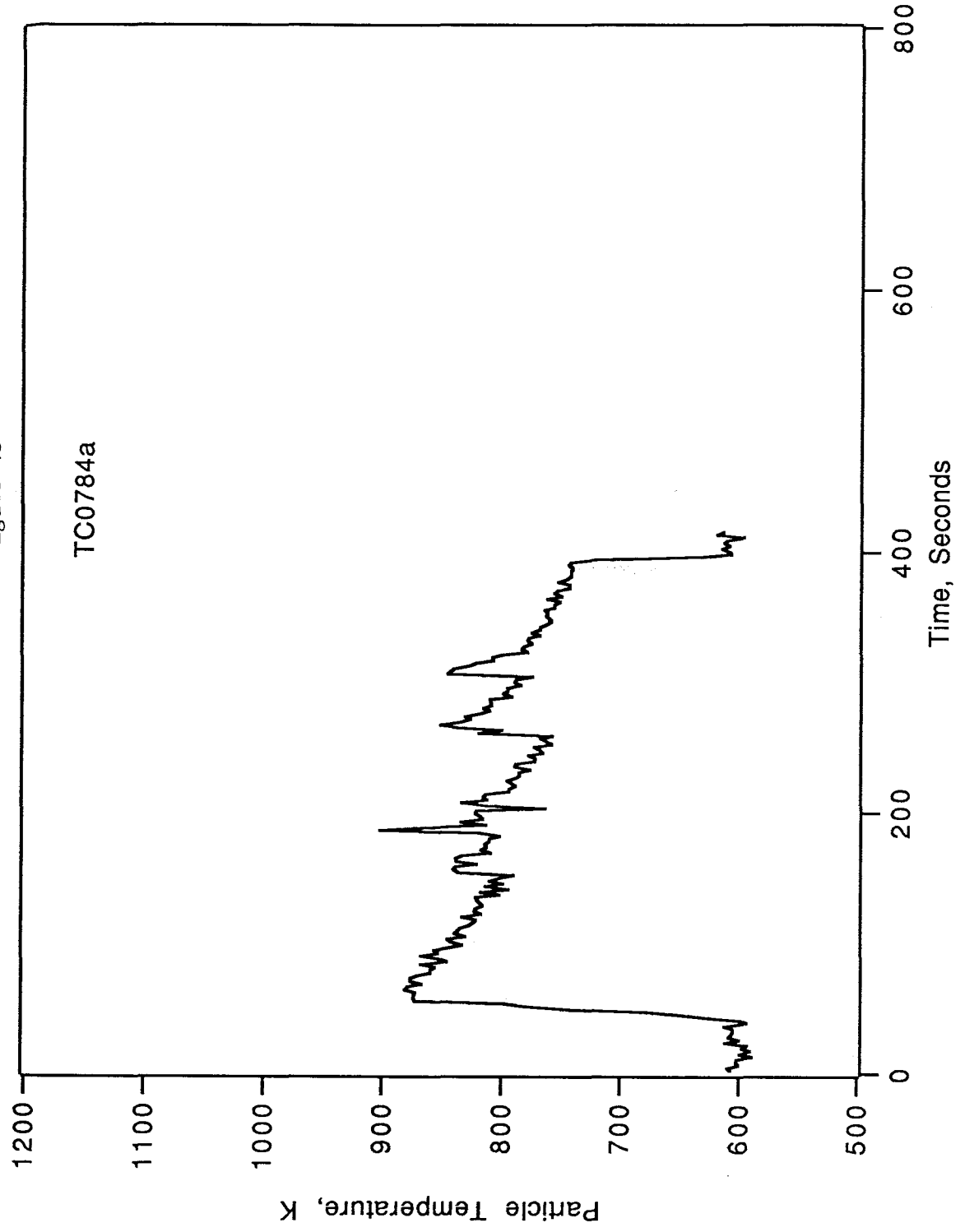
TC0784a
Particle Temperature, K
Time, Seconds
1200
1100
1000
900
800
700
600
500
0
200
400
600
800

Figure 43

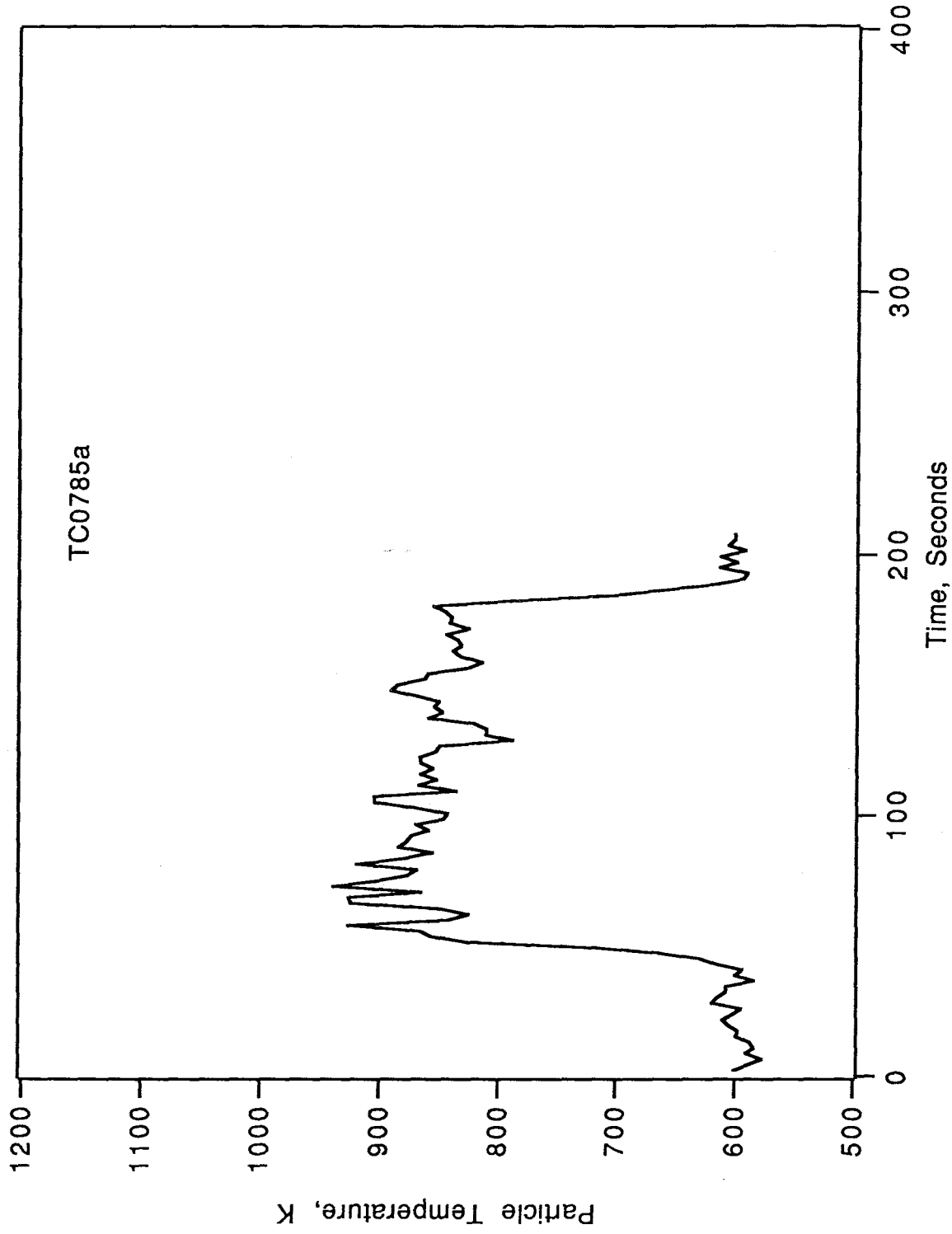
TC0785a
Particle Temperature, K
Time, Seconds
1200
1100
1000
900
800
700
600
500
0
100
200
300
400

Figure 44

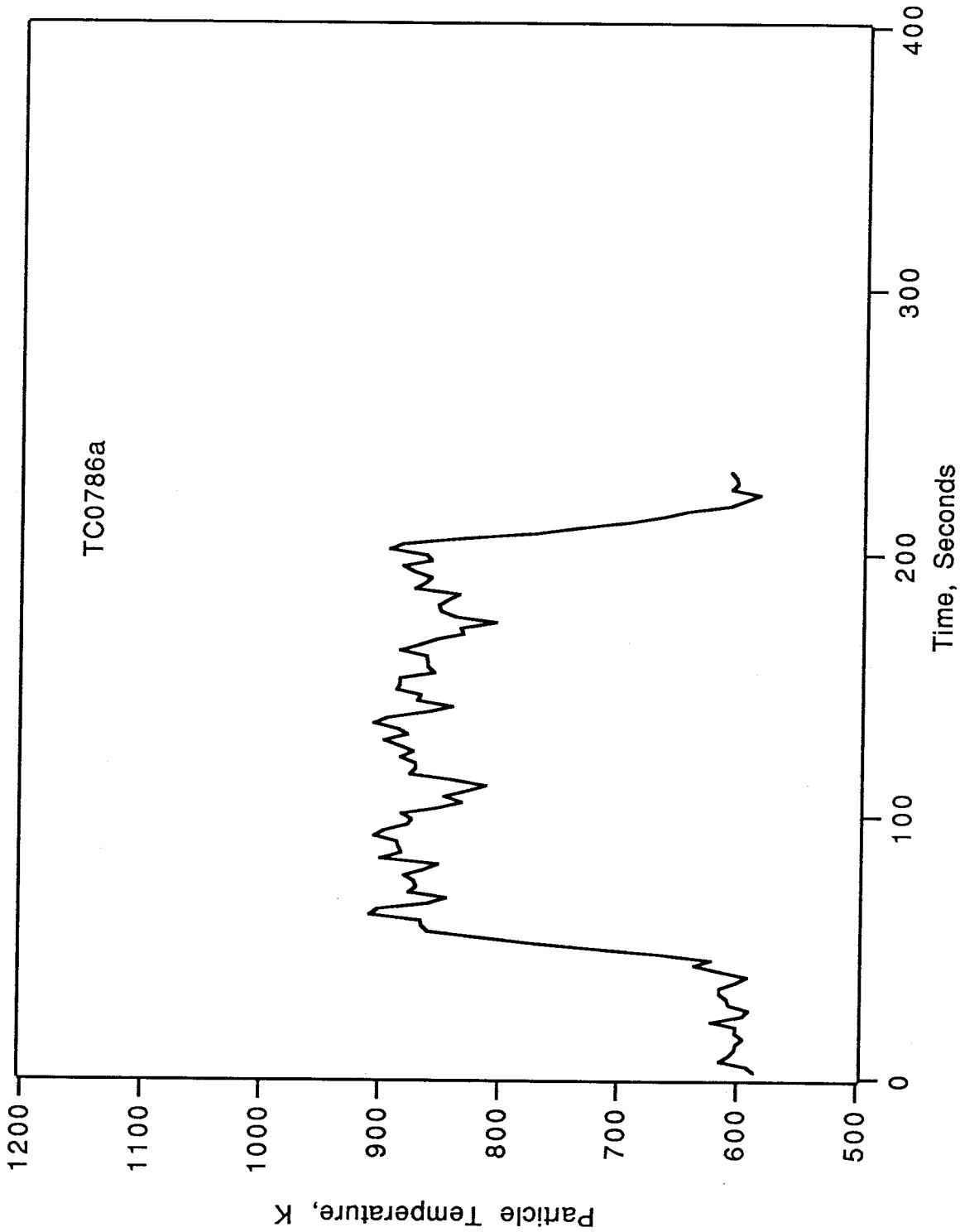
TC0786a
Particle Temperature, K
Time, Seconds
1200
1100
1000
900
800
700
600
500
0
100
200
300
400

Figure 45

Figure 46

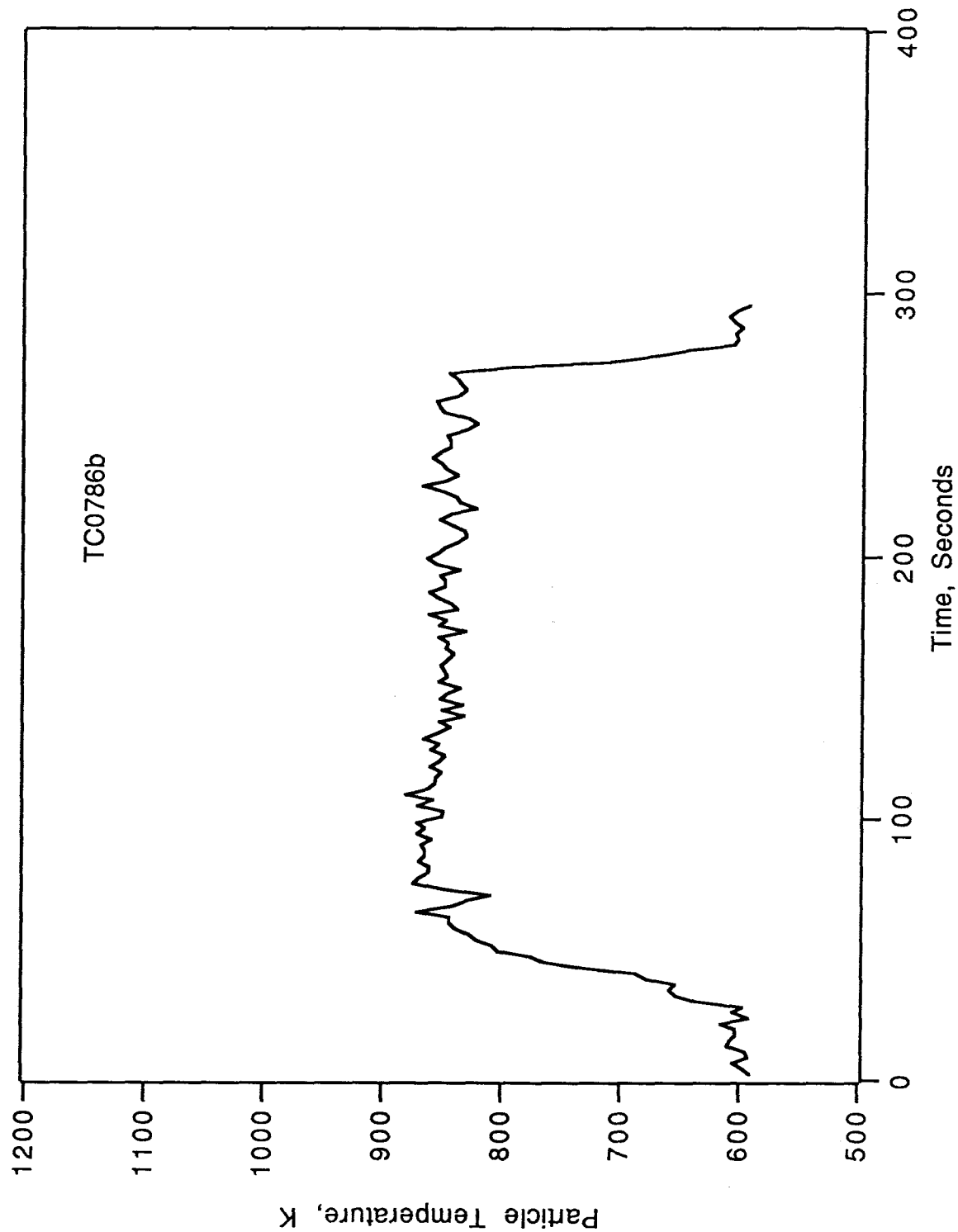
TC0786b
Particle Temperature, K
Time, Seconds
1200
1100
1000
900
800
700
600
500
0
100
200
300
400

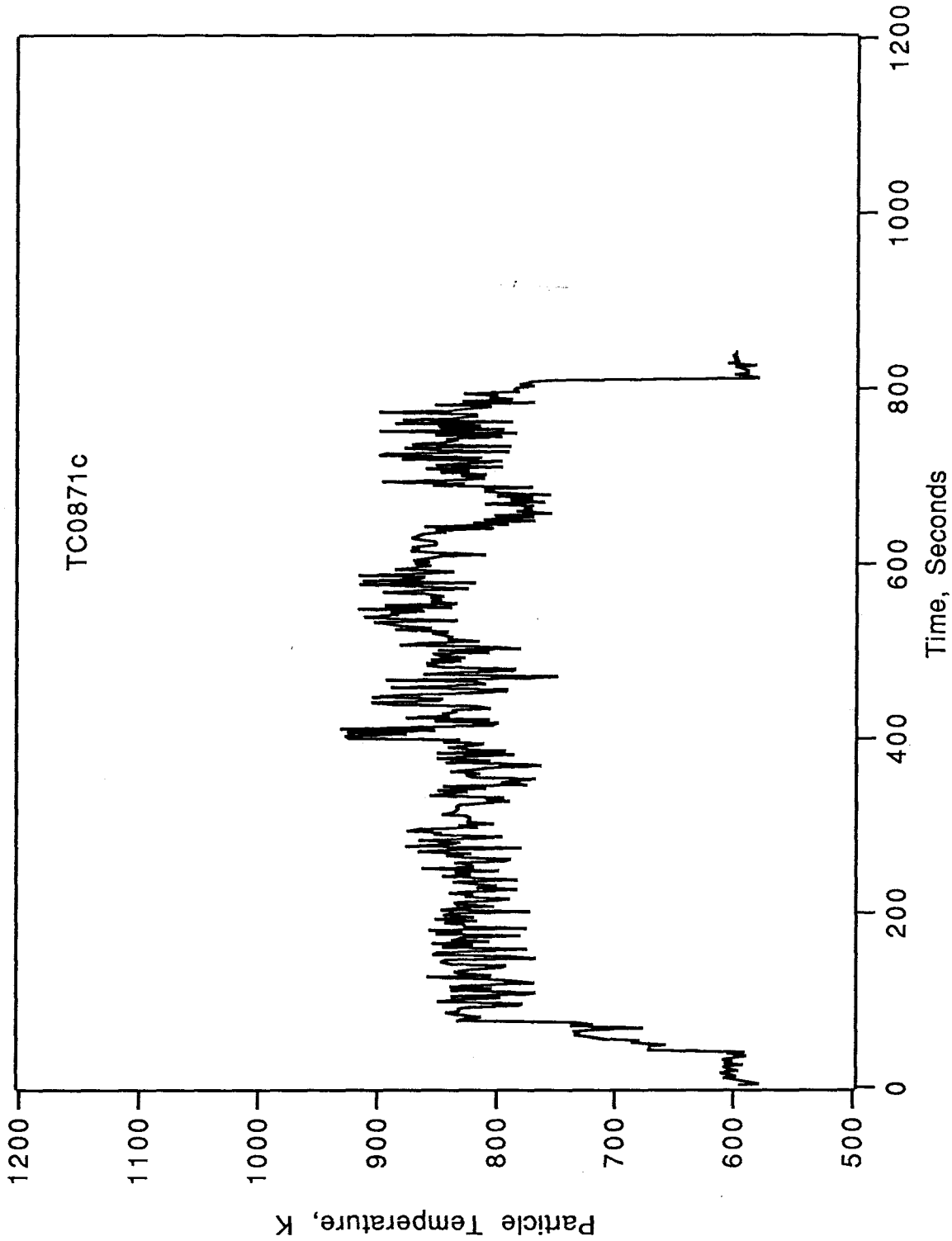
TC0871c
Particle Temperature, K
Time, Seconds
1200
1100
1000
900
800
700
600
500
0
200
400
600
800
1000
1200

Figure 47

Figure 48

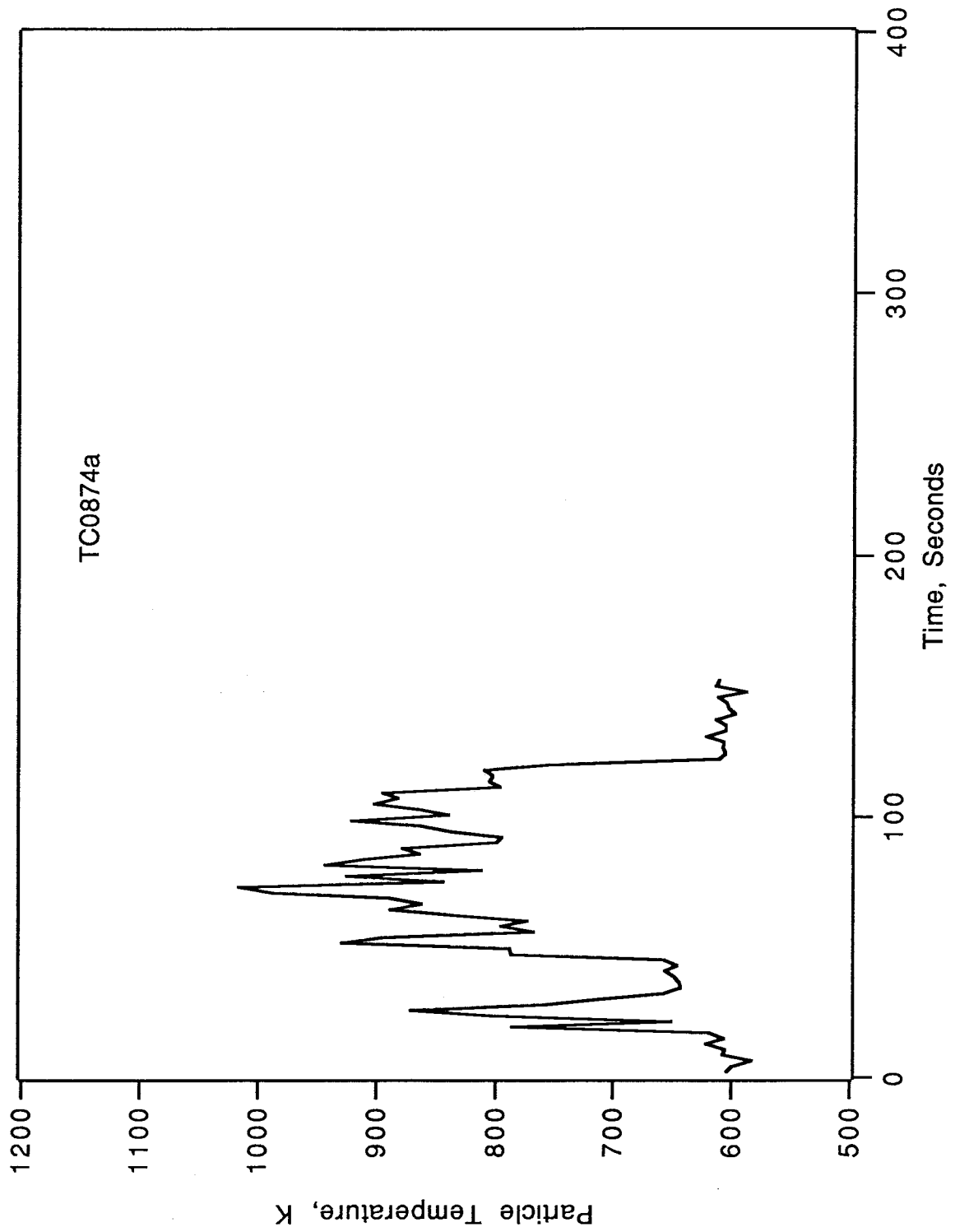
TC0874a
Particle Temperature, K
Time, Seconds
1200
1100
1000
900
800
700
600
500
0
100
200
300
400

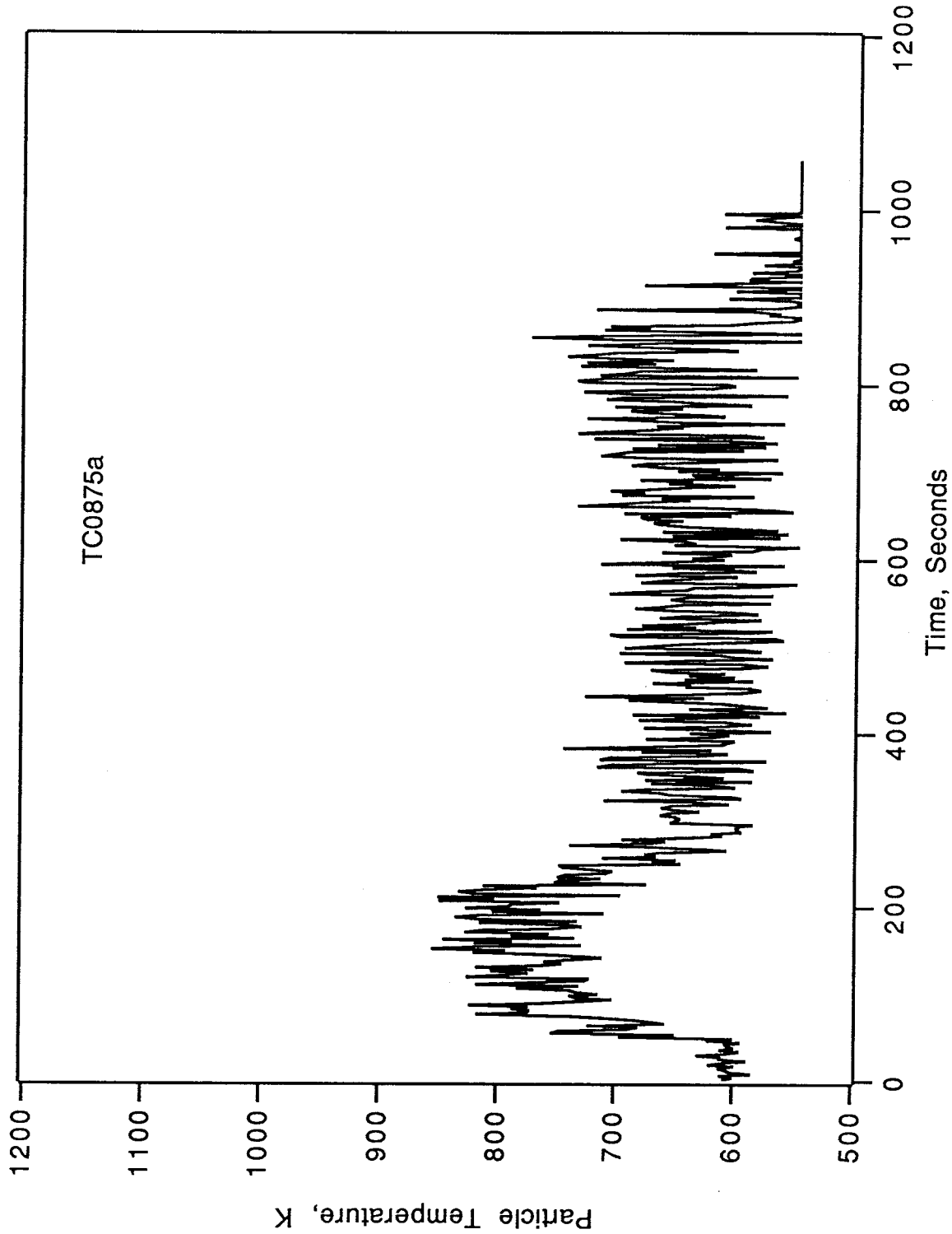
TC0875a
Particle Temperature, K
Time, Seconds
1200
1100
1000
900
800
700
600
500
0
200
400
600
800
1000
1200

Figure 49

Figure 50

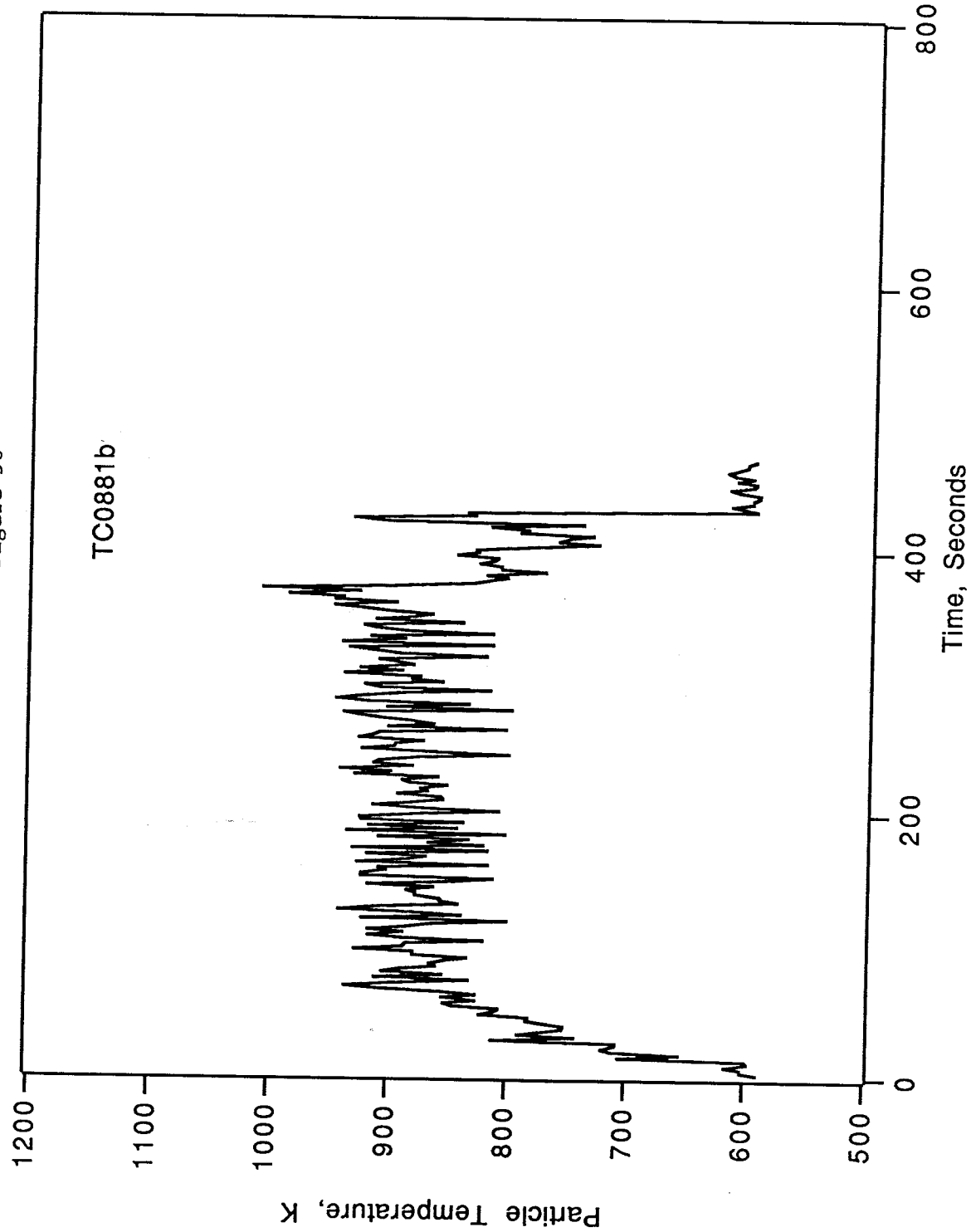
TC0881b
Particle Temperature, K
Time, Seconds
1200
1100
1000
900
800
700
600
500
0
200
400
600
800

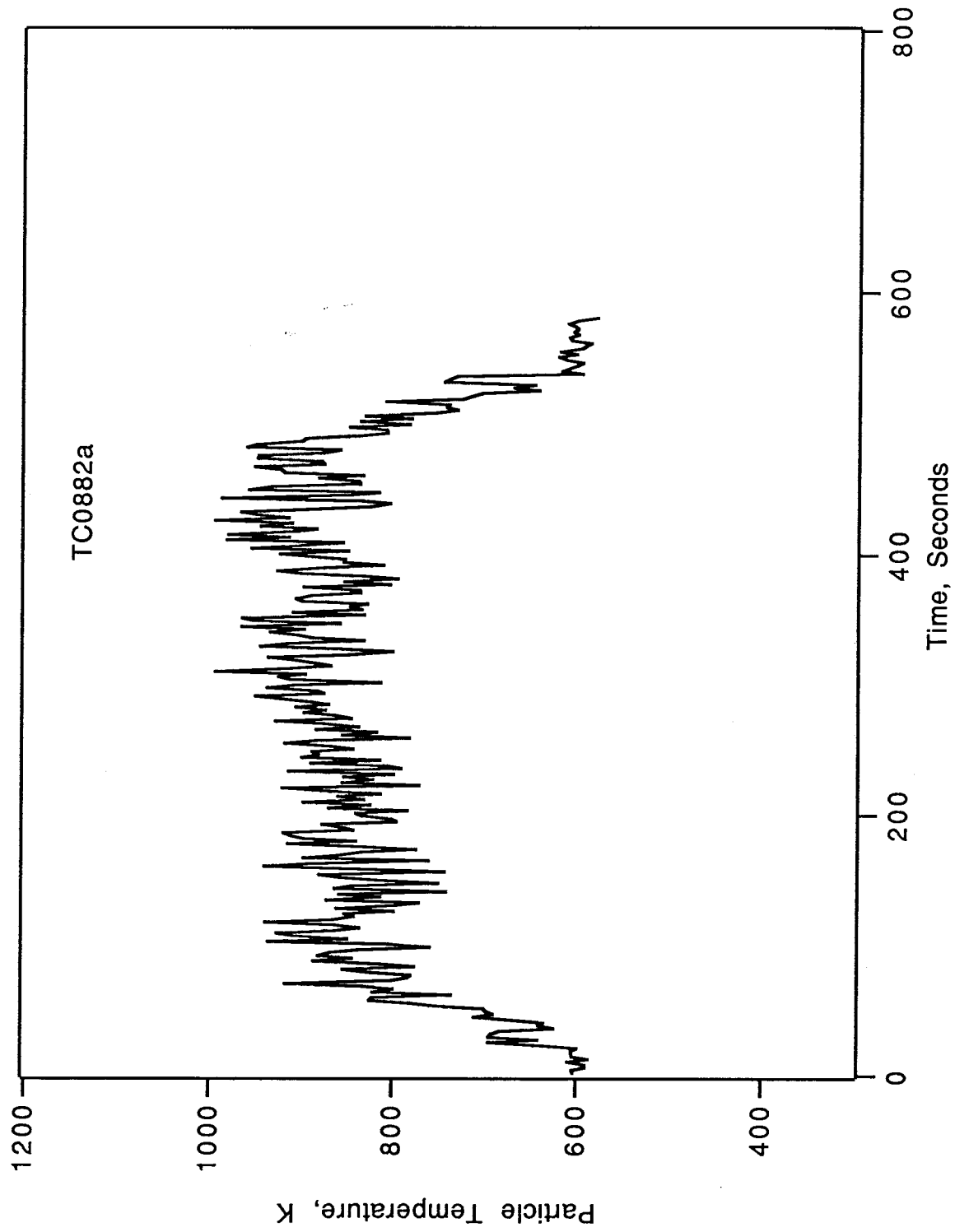
TC0882a
Particle Temperature, K
1200
1000
800
600
400
0
200
400
600
800
Time, Seconds

Figure 51

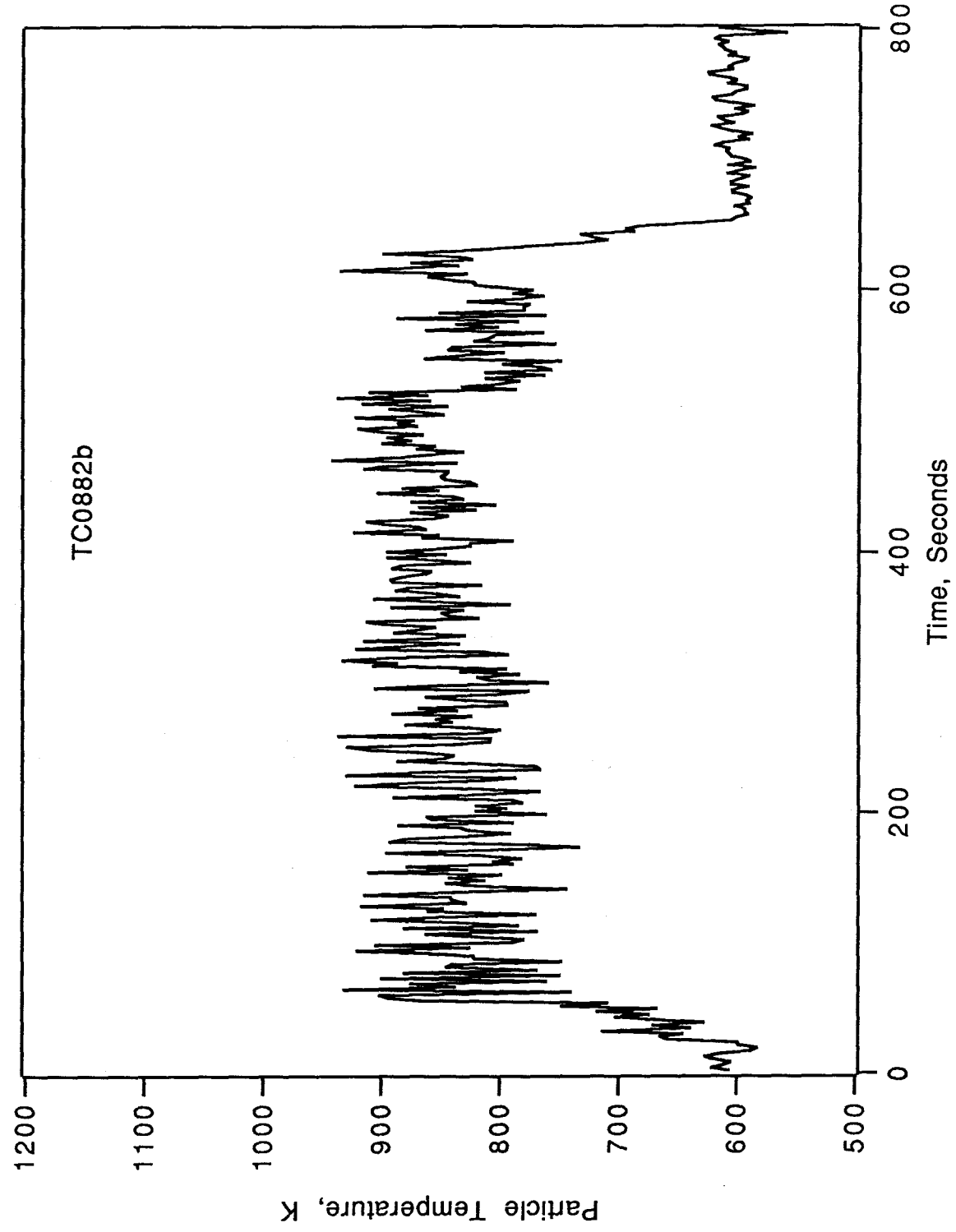
TC0882b
Particle Temperature, K
Time, Seconds
1200
1100
1000
900
800
700
600
500
0
200
400
600
800

Figure 52

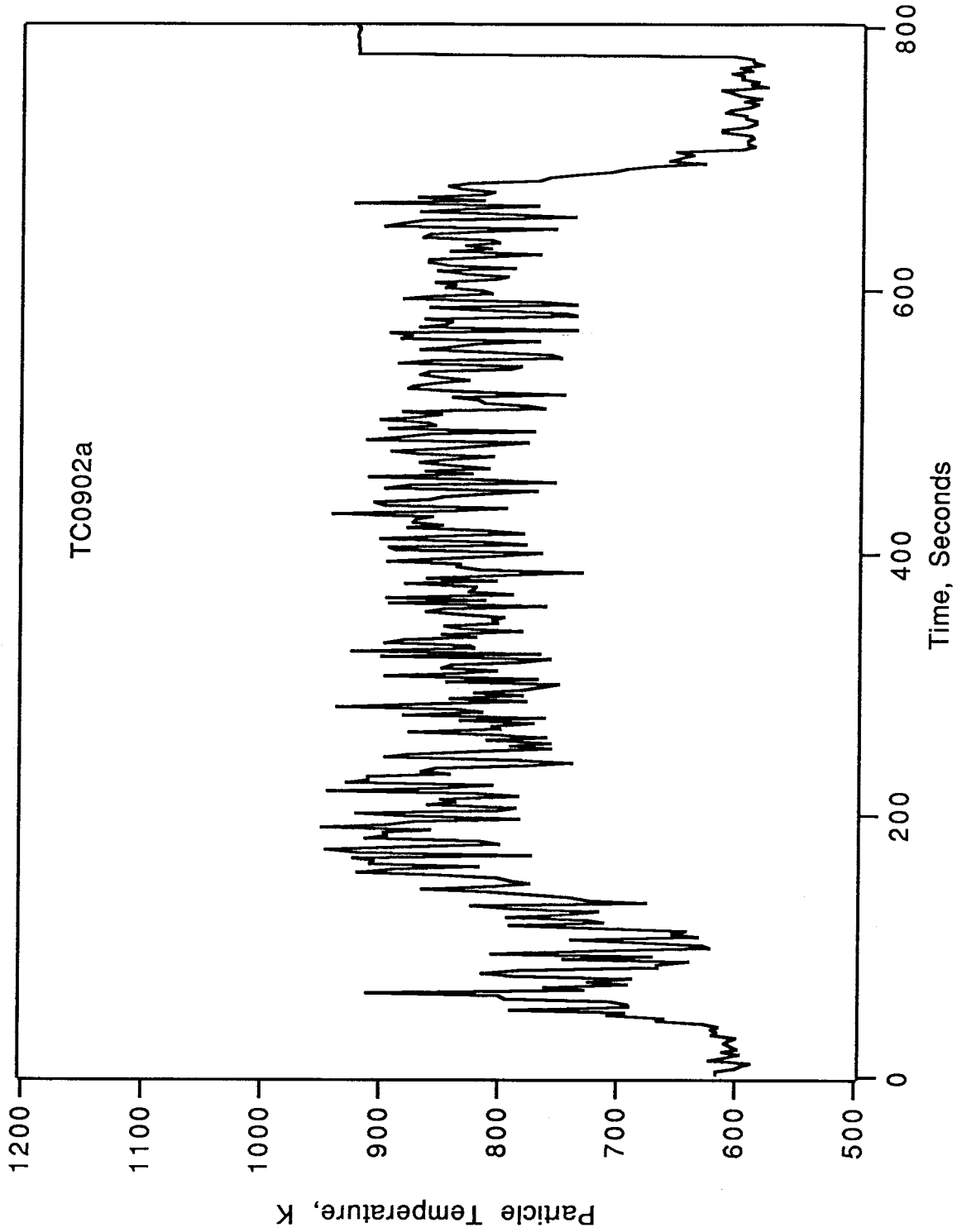
TC0902a
Particle Temperature, K
Time, Seconds
1200
1100
1000
900
800
700
600
500
0
200
400
600
800

Figure 53

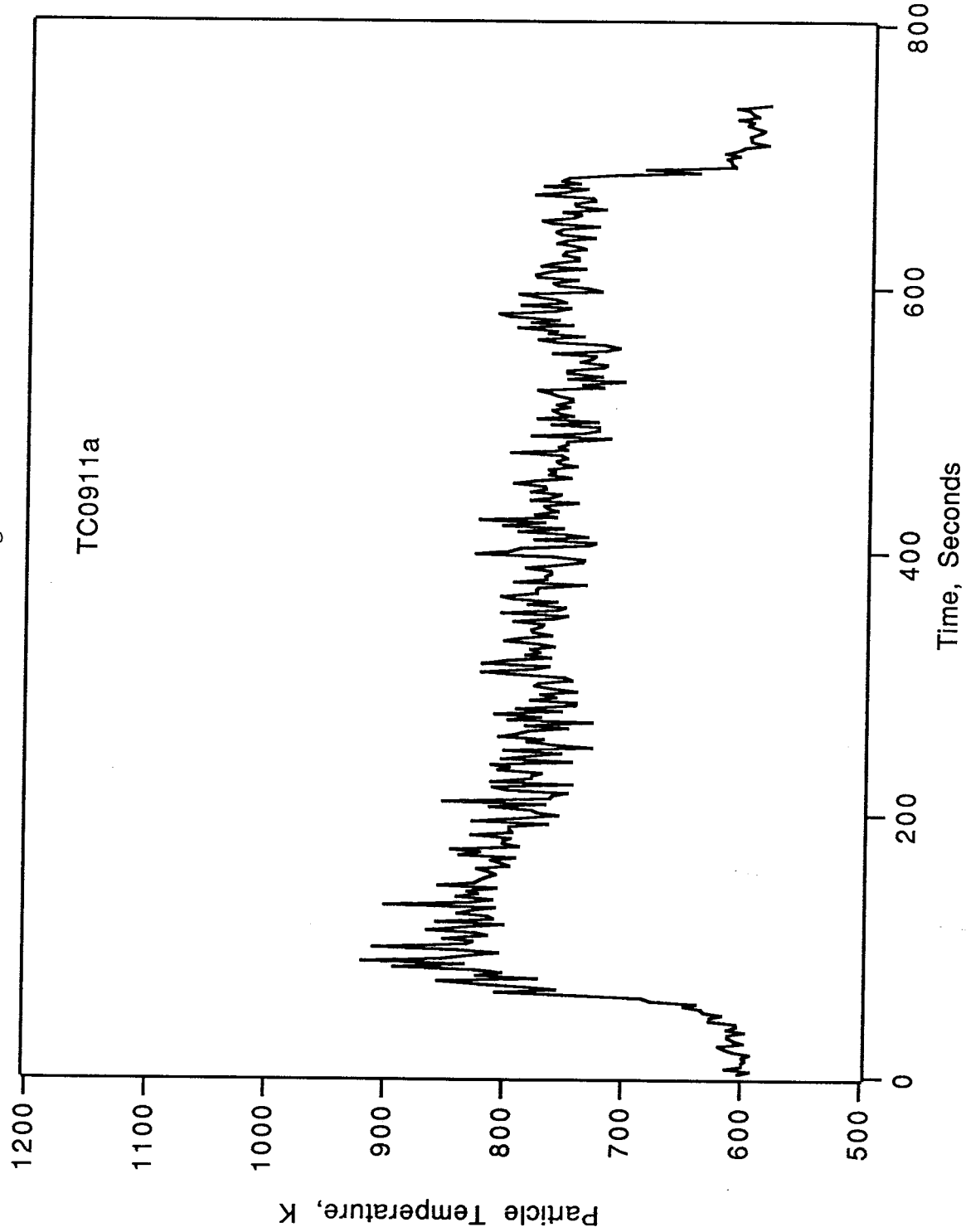
TC0911a
Particle Temperature, K
Time, Seconds
1200
1100
1000
900
800
700
600
500
0
200
400
600
800

Figure 54

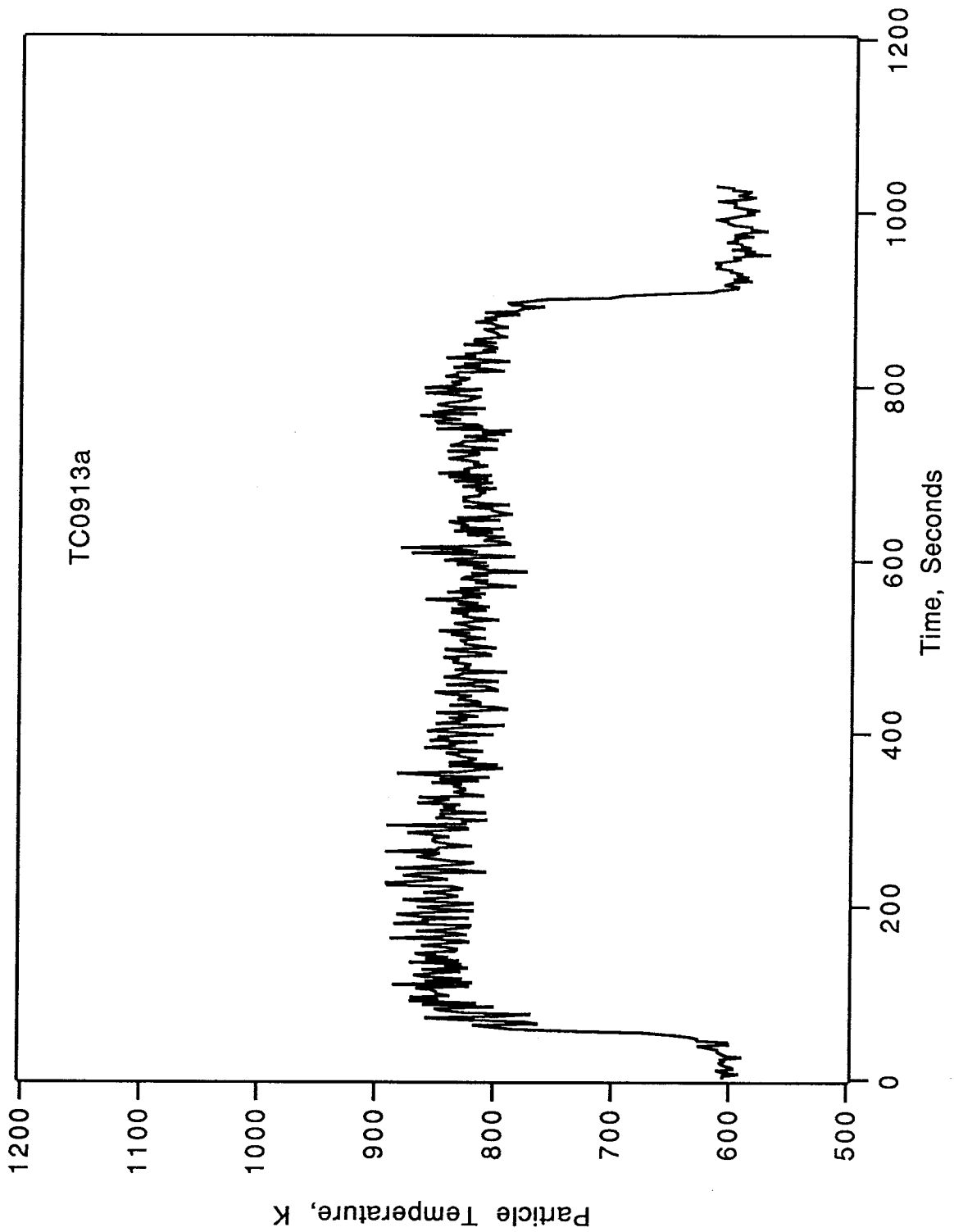
TC0913a
Particle Temperature, K
Time, Seconds
1200
1100
1000
900
800
700
600
500
0
200
400
600
800
1000
1200

Figure 55

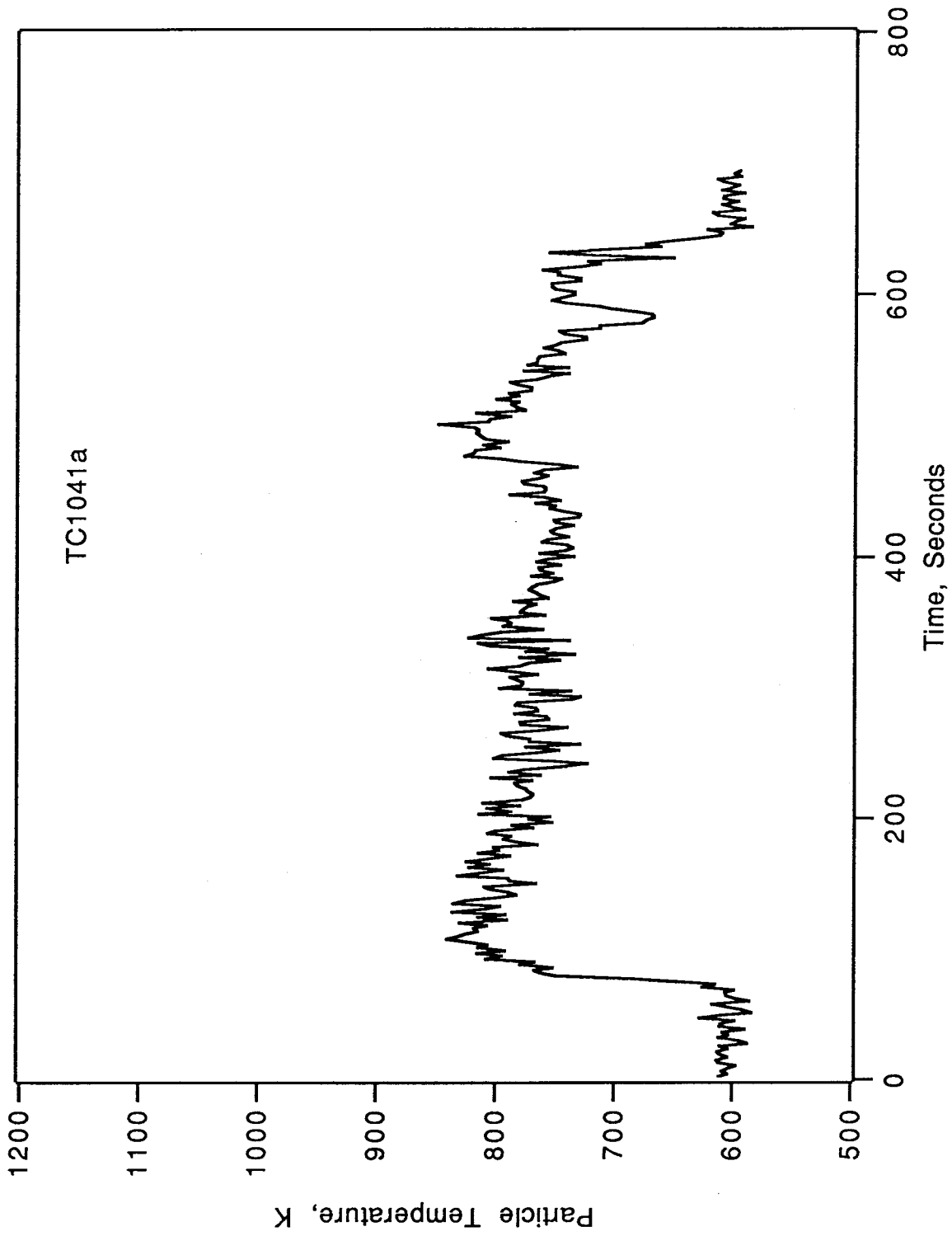
TC1041a
Particle Temperature, K
1200
1100
1000
900
800
700
600
500
0
200
400
600
800
Time, Seconds

Figure 56

Appendix 9

The following paper is being prepared for submission to *Energy and Fuels*

ON FUME FORMATION IN PYRITE REACTIONS BELOW 1420 K

Xiaoming Li, Brian Wong, and Richard C. Flagan*

Department of Environmental Engineering Science
* Department of Chemical Engineering
California Institute of Technology
Pasadena, CA 91125

ABSTRACT

An electrodynamic balance and a drop tube reactor were used to study the fume formation in pyrite reactions below 1420 K. Fume particles were observed directly by electrodynamic balance during reactions of individual pyrite particles. The drop tube reactor experiments allow measurements of the nature of the fume. No evidence was found for the formation of small iron rich particles under our experimental conditions. A large number sulfur particles were collected due to the condensation of sulfur vapor. A theoretical investigation of the possibility of release of iron rich fragments is also described.

INTRODUCTION

Investigations of the submicron fume produced during pulverized coal combustion reveal substantial concentrations of iron in these fine particles (Flagan and Taylor, 1981; Quann et al. 1982). The presence of so much iron in the fume has generally been thought to result from homogeneous nucleation of volatilization iron species. Under combustion conditions, the temperature of coal particles are several hundred degrees higher than the surrounding gas temperature. That some minerals evaporate and then form fine particles due to the rapid temperature drop is well documented (Flagan and Friedlander, 1978; Neville and Sarofim, 1982). The size distributions of the fume closely approximate the so-called *self-preserving* particle size distribution that would be expected for free molecular particles grown by Brownian coagulation from ultrafine sizes generated by homogeneous nucleation to the sizes much larger than original nuclei (Flagan and Taylor, 1981). Detailed mechanisms for iron volatilization have not, however, been presented.

Baxter and Mitchell (1989) recently examined the fate of pyrite iron in coal combustion. Their analysis of the thermochemistry of the iron/sulfur/oxygen system suggested that iron volatilization was probably not the source of the iron rich fume in their

experiments. They reported substantial loss of iron from coal particles just at completion of devolatilization when the char surface is exposed to an oxidizing atmosphere. During devolatilization, pyrite decomposes to form highly porous pyrrhotite (FeS_{1+x}). There is a net mass flux away from the surface when oxygen attacks char particles. They postulate that the iron-rich fume results when iron or pyrrhotite nodules detach from the surface of the char particles due to aerodynamic forces caused by the outflux. No direct measurements of the sizes of the fume particles that penetrated the filters (1.0 μm pore size, polycarbonate nuclepore filters) were made in their experiments. The iron fume produced is thought to consist of particles in the 0.02 to 0.2 μm range. The filtration velocity was about 12-14 cm sec^{-1} (Baxter, 1990; personal communication). Limited insights into the nature of the particles that escape collection can be gained by examining the filtration efficiencies. Liu et al. (1983) have measured the size dependent penetration for the same polycarbonate filters. Their data for a velocity of 13 cm sec^{-1}, shown in Fig. 1, indicates a minimum collection efficiency of 50% at 0.1 μm, with smaller particles being more efficiently captured due to Brownian diffusion. These data suggest that the particles that apparently penetrated the filter in Baxter and Mitchell's experiments were indeed smaller than 1 μm, and probably larger than 0.01 μm. Without more direct measurements, it is impossible to make more definitive statements about the particle sizes.

The present study explores fume formation during pyrite pyrolysis and combustion, with particular emphasis on the supposed formation of iron rich particles in the 20 to 100 nm size range. We report direct observations of fume formation during reactions of individual particles, as well as drop tube reactor experiments that allow measurements of the nature of that fume. A theoretical investigation of the possibility of release of iron rich fragments is also described.

EXPERIMENTS

Electrodynamic Balance

The Electrodynamic Thermogravimetric Analyzer (EDTGA) utilizes a modern version of the Millikan oil-drop experiment known as the electrodynamic balance to levitate a single charged particle within a tightly constrained space for the study of high temperature processes. The traditional electrodynamic balance (EDB) design utilizes a bihyperboloidal electrode system, although a variety of much simple electrode designs have been used

successfully. For the present study, the end caps are hemispherical and the ring is a right cylinder. The system diagram is illustrated in Fig. 2.

The particles to be injected into the EDTGA are charged by applying a high voltage pulse between a small cup containing these powders and the bottom electrode of the EDB. Electrostatic forces then accelerate the charged particles upward into the EDB. An AC potential on the ring electrode traps one or more particles in the electrodynamic balance. The DC potential is then adjusted to bring one particle to the center of the chamber. By reducing the AC strength, all other particles are released from the chamber. The AC is then applied to the ring electrodes so that the selected particle is stably trapped throughout the experiment. An optical servo system is used to adjust the DC potential continuously such that the particle is maintained at the center of the chamber as its mass changes or when it is otherwise disturbed. The control voltage provides a continuous record of the force required to hold the particle at the center of the chamber. It should be noted that during heating, this force does not correspond directly to the charge to mass ratio. The drag forces due to the buoyancy induced flow around a hot particle levitated in a cold gas and photophoretic forces must also be taken into account (Spjut et al., 1985).

The trapped particle is illuminated by a helium neon laser (Melles-Griot Model 05-LPH-151) that is directed down through a hole in the top electrode. The light scattered from the particle is imaged by an f/1 lens. Light scattered at 90° is also focussed onto a 1x3 mm silicon position sensitive detector (Hamamatsu S1543). An interference filter is used to block wavelengths other than that of the HeNe laser (632.8 nm) to reduce spurious signals as the particle is heated. The output of the position sensitive detector is amplified and then transmitted to a proportional-integral-differential (PID) controller. The controller continuously adjusts the output of the high voltage amplifier (TREK Model 603) that controls the DC voltage applied to the end caps of the electrodynamic balance. The particle is also monitored with a video system consisting of a Questar QM1 long range microscope and a Cohu CCD video camera, and recorded on a Panasonic super-VHS AG1830 video recorder. Two modes of particle illumination were employed. Bright field illumination was provided by placing a diffusing screen outside the window opposite the viewing window and illuminating the screen with a white light source. In this case, an interference filter was mounted outside the viewing window to eliminate scattered light from the HeNe laser. The particle appeared as a dark shadow in the bright-field image until ignition raised the temperature sufficiently high for the thermal emission from the particle to become visible.

Dark field images of the laser light scattered from the particle made the clouds formed around reacting particles visible.

The levitated particle was heated by a 20 W Advanced Kinetics flowing gas CO_2 laser. A refractory shutter was installed at the laser output to allow the laser to run until stable operation was achieved before introducing the bean into the EDTGA. The beam from the CO_2 laser was directed through a beam combiner, where it was combined with the HeNe laser beam that facilitated tracking of the invisible CO_2 beam, as well as optical alignment. Laser alignment problems were minimized by directing a single laser beam through the top of the electrodynamic balance. A large bore laser tube was used so that the laser could be operated in TEM 01^* mode (the so-called "donut" mode), simplifying the retention of the particle in the laser beam. For the experiments described in the present study, the laser was operated at constant output with the intensity delivered to the particle being controlled by the degree of focussing of the beam. A Zn-Se lens above the top of the EDTGA was mounted on a motorized translation stage to facilitate rapid heating of the particle. The non-Gaussian laser beam and the incompletely determined optical properties of the pyrite particles precluded quantitative theoretical predictions of the particle temperature. The particle temperature was estimated using a two color pyrometer operating at wavelengths of 1.8 and 3.4 μm, illustrated in Fig. 3a. Radiation emitted by the particle was collimated by a CaF_2 lens. The collimated radiation was divided by a grating-type beam splitter which reflected the infrared radiation through two narrow band pass filters (1.48 μm with bandwidth 70 nm; and 3.42 μm with bandwidth 130 nm). CaF_2 lenses then focused the beams onto separate solid state detector, an InGaAs detector that was active from 1.1 to 1.8 μm, and an InSb detector that was active from 2 to 5 μm. The signals from the two detectors were amplified and then processed with a log-ratio amplifier. The resulting signal was a function of the temperature of the emitting material. Because the pyrite particles were irregularly shaped, and the optical properties of the pyrite were not well known, the optical pyrometer response was determined empirically. A type R (Pt - Pt/13% Rh) thermocouple was coated with silica (Fristrom and Westenberg, 1965) and then with fine pyrite particles ($d_p < 4$ μm). The thermocouple bead was then heated with the CO_2 laser. Monitoring the thermocouple response, an empirical calibration of the optical pyrometer response as a function of temperatures was obtained. Fig. 3b shows the pyrometer response as a function of indicated thermocouple temperature. Note that the pyrometer response changed with repeated heating, indicating a change in the optical properties of the coating material. This is not surprising since the pyrite decomposition to

pyrrhotite is expected at the highest temperatures encountered. Thus, temperatures reported below are subject to an uncertainty of ±40°C.

Several different approaches to particle heating and data acquisition were used over the course of the pyrite EDTGA experiments. (1) *Pulse heating*: The particle was initially heated by the laser at a very low power to a temperature below the threshold of the pyrometer (280°C). The pyrometer signal was sampled at about 2500 Hz. After establishing the pyrometer baseline, the laser power was increased in a pulse. (2) *Ramped pulse heating*: The basic method was the same as (1), except that the initial low level of heating was slowly increased until fume formation was observed. (3) *Ramped heating - laser control*: The laser power was externally controlled by a circuit which slowly increased the laser power. Data acquisition was conducted at the slow rate. (4) *Ramped heating - focus control*: Rather than change intensity of the laser beam at the particle by changing laser power, the intensity was changed by moving the laser focusing lens with respect to the particle.

Drop Tube Reactor

The electrodynamic balance makes it possible to observe some of the transformations of a single particle directly, however uncertainties in the particle temperature, possible effects of nonuniform laser heating, and the inability to make direct measurements of the products of reaction limit our ability to make quantitative measurements with the present system. Hence, parallel experiments were performed using a drop tube reactor to characterize the nature of the fume produced by reactions of pyrite at elevated temperatures.

The experimental system illustrated in Fig. 4 has been described in detail elsewhere (Sahu, 1988) and is only briefly described here. The drop tube furnace is an Applied Test Systems Series 3310 tube furnace with a maximum temperature of 1650°C. The reactor tube is a 99.8% alumina tube of 5 cm ID. and 71 cm length. A large bore (1 cm I.D.) water cooled stainless steel injector was used to inject the reactant particles directly into the hot zone of the reactor. Low density zirconia refractory insulation in the cooled injector reduces the load on the furnace and allows the gas that enters coaxially with the injection stream to be preheated upstream of the particle injection point. The isothermal zone of the reactor is about 30 cm long. In the present experimental conditions, the centerline temperature differs from the wall temperature about 40-50 K. Nitrogen and air gas temperatures agree within

40 K or less. Aerosol samples were extracted with a water-cooled, gas dilution quench probe. The dilution gas was injected into the sample through a number of small holes near the probe entrance. A portion of the aerosol flow was extracted from the sampling probe, through a dilution system, and into the aerosol measurement instruments. The aerosol sample flow was controlled by the critical orifice of Condensation Nucleus Counter (CNC, TSI Model 3760). The sample was diluted by recycling part of the sample through an absolute filter (MSA Ultra Filter, type H cartridge) using a two-stage diaphragm pump to keep particle concentrations within the operating limit of the CNC. The aerosol concentration and size distribution were measured with a Scanning Electrical Mobility Spectrometer (SEMS) (Wang and Flagan, 1990) based on a computer controlled Differential Mobility Analyzer column (DMA) (TSI, Model 3071) with the Condensation Nucleus Counter as a detector. Particles were also collected on silver grids for structure and chemical composition analysis using Transmission Electron Microscope (TEM, Phillips EM 430) equipped with energy dispersive X-ray analysis (EDX). The mass feed rates of the different experiments were adjusted so that the particle number concentrations could be kept below the upper detection limits of the aerosol instruments.

Two types of pyrite were examined, a natural pyrite (85% purity, EM Science) and a synthetic pyrite (99.9% purity, AESAR). Scanning electron microscope pictures of both types of pyrite particles are shown in Fig. 5. The pyrite compositions are summarized in Table 1. Both the supplier's analysis and qualitative analysis obtained using a Kevex EDS X-ray fluorescence spectrometer (XFS) are reported. The predominant impurity species in the natural pyrite are calcium and silicon, with small quantities of copper and zinc. The natural pyrite was first size classified to 53-74 μm. The pyrite particles were reacted in high purity N_2 or in clean dry air at temperatures ranging from 750 to 1220 K. Due to agglomerate nature and the fine particle size of the synthetic pyrite, it was not possible size classify sufficient material for the experiments performed. Hence, polydisperse particles of this material were used for drop-tube furnace experiments. The fine synthetic pyrite particles tended to cake upon exposure to air, so it was necessary to dry the powder in the feed test tube by heating mildly ($\leq 40^{\circ}C$) and evacuating the sample for 5 to 12 hours prior to the experiments. Polydisperse particles of the synthetic pyrite were reacted at 873 to 1420 K in either high purity N_2 or dry clean air.

EXPERIMENTAL RESULTS

Electrodynamic Balance

(1) Fume Formation

When some pyrite particles were heated, a fume or cloud of vary fine particles was formed around the particle as illustrated in Fig. 6. The cloud was observed to start from the particle, expand quickly to several particle diameters, and generally maintained its spherical shape as it rose, due to buoyancy, out of view. The fume formation was affected by the heating rate and oxygen concentrations. The fume was observed occasionally when the particle was heated slowly by a ramping procedure, but was more often seen when the particle was hit by a sudden laser pulse; the temperature of the particle just prior to fume formation in air was in the range of 300 to 400°C, but in a nitrogen atmosphere, some fume formation was observed when particles were heated at temperatures up to 500°C. The mass changes in the particles during fume formation were generally very small. In many cases, mass changes were undetectable to a resolution of 1 part in 10^5. In experiments where particle temperature was maintained at 300 to 350°C, for 30 seconds to 3 minutes, particle mass was reduced by 6 to 8%. The mass loss that would be observed is 23% if pyrite is completely converted to pyrrhotite .

Fig. 6a and 6b show the darkfield images of a pyrite particle of approximately 100 μm size prior to laser heating and the fate of when it was heated to about 320°C by a single laser pulse of approximately 10 ms duration. The cloud formed is approximately 4 particle radii in size. Fig. 6c shows the corresponding temperature trace. The laser was operated at a steady state that maintained the particle at a steady temperature below the threshold of the pyrometer and briefly pulsed to heat the particle. The charge-to-mass ratio change during this initial pulse was less than 1 part in 10^5.

(2) Particle Fragmentation

The fragmentation of pyrite particles was observed at temperatures between 300 and 700°C. The pyrite particle occasionally broke into two or more particles when the particles were hit by a sudden laser pulse. No fragmentation was observed in any of the ramped experiments, when the pyrite particles were subjected to a slow rate of heating. At the temperatures higher than 700°C, ignition was observed. The rapid particle loss due to

charge loss from the burning particle precluded direct observations of fragmentation although in some cases a fragment remained captured in the balance.

(3) Ignition

Ignition was usually the terminal event in a pyrite experiment conducted in air. In general, a denser cloud was formed around the particle than for the lower temperature reactions. Occasionally, a small remnant particle would remain trapped. In some cases, jetting was observed. Smoke remained visible in the chamber for several seconds after the ignition event. Figure 7a shows a typical ignition event, with a cloud forming in streaks both above and below the particle. The corresponding temperature profile is shown in Figure 7b, with maximum temperatures of the particle, reaching nearly 1000 K.

During some of the ramped heating experiments, fume formation and ignition were observed nearly simultaneously. As the pyrite particle was heated, a fume cloud suddenly formed around the pyrite particle and gradually rose out of view which the particle dropped down, due either to charge loss, or to the position control system's attempt to track the rising cloud. The focus of the lens was usually below the initial starting point of the particle, so as it dropped down into a region of higher intensity, it ignited, generating a much larger cloud of smoke.

Drop Tube Reactor

Drop tube studies of pyrite reactions were undertaken to probe the nature of the fume produced during the reactions of pyrite at relatively low temperatures. The particle number concentration and size distribution of produced fume were measured by SEMS under different conditions. Figures 8 and 9 show the typical particle volume distributions obtained in N_2 or in air at different temperatures, using either natural pyrite or synthetic pyrite. The contribution of the original polydisperse synthetic pyrite to particles in the measured size range was examined by measuring the size distribution of the entrained particles in air at room temperature by SEMS. Few small particles were detected under this condition. The detailed experimental conditions and average results are summarized in Table 2.

(1) Natural Pyrite

Initial experiments were performed using natural pyrites in the 53-74 μm sieve fraction at temperatures ranging from 750 to 1220 K. At the temperature of 750 K, most of the fume particles were smaller than a few tens of nanometers in diameter (Fig. 8a), although a small but significant aerosol volume was observed above 50 nm diameter. The minimum detectable particle size of the Differential Mobility Analyzer system used for these measurements was 13 nm. The data suggest that the number concentration increased further at smaller sizes. The total mass of fume produced with sizes ranging from 13 nm to 190 nm at this low temperature in air amounted to about 40 parts per million of the original pyrite mass. Similar experiments done in nitrogen resulted in a somewhat smaller number of fine particles. The total mass of fume produced in N_2 was estimated about one-half of that in air. This difference increased with temperature. The fume yield also increased with temperature as indicated by the volume distribution for the reactions of pyrite. A peak shown around the particles of 70 μm (Fig. 8b) indicated the occurrence of the coagulation due to the presence of large numbers of extremely fine particles. The estimated mass of fume generated in air at 1220 K was about 7% of the original pyrite mass, whereas, that in N_2 was only around 0.3% of the original pyrite mass.

Samples of particles produced during these experiments with the natural pyrite were collected directly on silver TEM grids. They were then characterized by TEM with EDX. Fig. 10 shows small crystalline particles with sizes of 20 to 40 nm typical of the samples collected for reaction of the natural pyrite in air. The primary constituents of these particles were silicon, calcium, copper, and zinc. Neither sulfur nor iron were detected except for one sample shown in Fig. 10. Within the circle in Fig. 10, small amounts of iron and sulfur were found, as indicated by the EDX spectrum. A much smaller iron level was detected in one other such mass.

(2) Synthetic Pyrite

Additional experiments were conducted with synthetic pyrite to reduce the influence of impurities. The particle volume distributions generated in reactions at elevated temperatures in air were broad (Fig. 9a), indicating the presence of great numbers of extremely fine particles that might be expected if homogeneous nucleation were responsible for particle formation, but without the characteristic peak in the particle size distribution that resulted when a fume was allowed to coagulate for a long time. The quantity of fume appeared to increase with temperature and with oxygen level (Figs. 9a and 9b).

The fume particles were analyzed by TEM with EDX. Reaction in air at 1420 K produced particles similar to those seen from the natural pyrite both in morphology and chemical composition (Fig. 10). The particles consisted of the major impurities present in original material (Table 2), such as silicon, calcium, copper and zinc, with a very small amount of sulfur. Although the particles produced in N_2 at 1420 K had similar chemical compositions to those produced in air, the collected particles appeared to be extensively agglomorated and lack the crystalline particles produced in air (Fig. 11). The sulfur content of the fume particles increased with decreasing temperature. Analysis of the fume produced by reaction in air at 873 and 1220 K revealed fume particles consisting of elemental sulfur. Fig. 12 illustrates numerous particles with crystalline shapes. During analysis of the samples, the portion of them were damaged by the electron beam, which could be seen from the formation of bubbles in the crystals (Fig. 12). Some small particles even disappeared completely.

The mass of fume generated from pyrite was very low in our experiments. The fume particles had a very broad size distribution and vary significantly in morphology and chemical composition depending on the experimental conditions. Elemental analysis of the fume particles ($d_p < 50$ nm) revealed the predominance of sulfur and impurities present in the original pyrite. No evidence was found for the formation of small iron rich particles under our experimental conditions. Hence, the cloud observed in EDB experiments (Fig. 6b) is thought to consist mainly of impurities released during pyrite decomposition and condensed due to the dramatic temperature drop from the particle to the surrounding gas. These observations differ from the iron fume formation in coal combustion as reported by Flagan and Taylor (1981) or by Baxter and Mitchell (1989). They both reported that iron rich small particles were generated when burning pulverized coal. Flagan and Taylor measured the composition-size distribution of ash particles generated during combustion and found a pronounced peak in the iron mass distribution below 0.1 μm diameter. The differences between the previous results and our experiments may be caused by the materials and gas temperatures of the various experiments. Gas temperatures in the coal combustion experiments were about 100 to 300 K higher than the highest temperature used in our experiments. The reactions of pyrite within coal particles could differ significantly from those of pure pyrite because of the locally reducing atmosphere at the surface of the burning carbon and because of modified surfaces of the included pyrite. Particle temperatures may also be exceed the surrounding gas temperature during char oxidation.

We have found no direct evidence for the formation of an iron rich fume during pyrolysis or oxidation of isolated pyrite particle. The low temperatures of our experiments makes iron vaporization unlikely. Fragmentation does not appear to generate large numbers of fume particles. Baxter and Mitchell (1989) suggested that gases evolved during coal devolatilization entrain fine iron-rich particles. Reactions of isolated pyrite particles or of coal chars will not generate the same high velocities. The formation of soot or impurity-derived fumes would interfere with our present methods of estimating pyrite derived fume production. For these reasons, we turn to theoretical arguments to examine whether the fragmentation / entrainment mechanism suggested by Baxter and Mitchell (1989) could be expected to generate significant quantities of submicron fume. The key question is whether the aerodynamic forces are sufficient to dislodge small particles from the surface of the burning char.

THEORETICAL CONSIDERATIONS

To dislodge a solid particle from a surface requires a removal force provided by the drag and lift of the gas stream on the particle. Experimental studies of the reentrainment of sand particles by wind (Bagnold, 1960) showed that the velocity must exceed a limiting value for entrainment to occur, and the value varies with particle size. The velocity increases due to particle-to-particle cohesive forces as the particles become smaller. For submicron particles, the intermolecular attraction force is dominant. Electrostatic effects have been observed to be much smaller than intermolecular attraction force (Lipinski et al., 1985). The force needed to separate two spherical particles of radii r_1 and r_2 from one another was given by Bradley (1932),

$$F_{surf} = 4 \pi \sigma \frac{r_1 r_2}{r_1 + r_2} \qquad (1)$$

where σ is the surface free energy of the particles. σ is equal to one-half of the (van der Waals) energy needed to separate two surfaces from contact to infinity, and can be estimated by (Israelachvili, 1985)

$$\sigma = \frac{A}{24 \pi D_0^2} \qquad (2)$$

where D_0 is the distance between two surfaces in contact. The value of D_0= 0.165 nm yields surface energy estimates in close agreement with measured values. A is the Hamaker constant,

$$A = \pi^2 C \rho_1 \rho_2 \qquad (3)$$

where C is the coefficient in the atom-atom pair potential, ρ_1 and ρ_2 are the number of atoms per unit volume in the two bodies. Typical values of A are 7×10^{-13} erg, with values ranging as high as 3×10^{-12} erg. A more rigorous method of calculating the Hamaker constant in terms of the macroscopic properties of the media is based on the Lifshitz theory (Israelachvili, 1985). For two identical phases 1 interacting across medium 2,

$$A \approx \frac{3}{4} kT \left(\frac{\varepsilon_1 - \varepsilon_2}{\varepsilon_1 + \varepsilon_2}\right)^2 + \frac{3h\upsilon_e}{16\sqrt{2}} \frac{(n_1^2 - n_2^2)^2}{(n_1^2 + n_2^2)^{3/2}} \qquad (4)$$

The estimated value A of ferrous oxide in air at the temperature of 1600 K is 3.3×10^{-12} erg. Thus, the surface energy σ calculated from Equation 2 is 160.8 erg cm^{-2}.

The primary forces acting to remove the particles from the surface result from aerodynamic drag. For the small particles of interest here, the drag force acting on a free spherical particle moving at a velocity v relative to the gas in which it is immersed is

$$F_{drag} = \frac{3 \pi \mu d_{p_1} v}{C_c(Kn)} \qquad (5)$$

where the slip correction factor C_c

$$C_c = 1 + Kn\{1.257 + 0.4 \exp(-\frac{1.1}{Kn})\}$$

corrects the Stokes drag for noncontinuum effects when the particle diameter d_{p_1} is small compared to the mean free path of the gas molecules l, i.e. Knudsen number ($Kn = \frac{2l}{d_{p_1}}$) is greater than 1 .

In following calculations, we assume that the drag force exerted by the fluid is the only force acting to remove a particle from a surface, and that the drag can be calculated as through the particle were immersed in the flow. This is illustrated in Fig. 13. The critical velocity required to separate particle 1 from particle 2 is that for which

$$F_{surf} = F_{drag}$$

We find

$$v_{crit} = \frac{2\ C_c\ \sigma\ d_{p_2}}{3\ \mu\ (d_{p_1} + d_{p_2})} \qquad (6)$$

The critical velocities thus depends on fluid and particle properties as well as the sizes of particles to be separated. The calculated results for a 100 μm coal particle are shown in Fig. 14. For the larger Hamaker constants, indicated by the dashed lines in Fig. 14, the velocities required to separate the particle from the surface are too high to be achieved at normal conditions. The critical velocities decrease with the increasing ash particle diameters for submicron particles (d_{p_1}), and are proportional to the surface free energy. The maximum value of v_{crit} corresponds to the removal of a very small particle from a much large one, i.e., $d_{p_1} \ll d_{p_2}$,

$$v_{crit,max} = \frac{2\ C_c\ \sigma}{3\ \mu}$$

The minimum critical velocity is that for which $d_{p_1} = d_{p_2}$, and amounts to

$$v_{crit,min} = \frac{1}{2}\ v_{crit,max}$$

There are few experimental measurements of v_{crit}. Corn and Stein (1965) studied the reentrainment of glass beads by high velocities of air flow. They found that particles with sizes less than 0.5 μm could not be removed from a surface even by a flow with a free stream velocity of 150 m sec^{-1}. The reentrainment velocities of particles in a broad range has been studied by Lipinski et al. (1985). The minimum velocity for particle resuspension from a dry surface is about 1.8 m sec^{-1} for 10 μm particles. Although the drag force we consider is valid for a free particle of spherical shape, it provides an estimate of the force

acting on a spherical particle adhering to a substrata. These results of previous studies are consistent with our estimates.

From Baxter and Mitchell's report (1989), there was a significant fraction of the iron in the coal lost in the 25 ms time period just after the completion of coal devolatilization. During the iron release, the peak measured particle temperatures was 1710 K in the 6% oxygen environment. The carbon consuming rate is 0.006 gm cm^{-2} sec^{-1}, estimated using the particle combustion model of Sahu (1988). Thus, the estimated velocity of releasing gas is 70 cm sec^{-1}. Comparing this value with those in Fig. 14 calculated by Hamaker constant of $3.3x10^{-12}$ erg, we can find that the velocity of the releasing gas is much smaller than the critical velocities required to release the particles with sizes less than 1 μm to the surrounding gases. It is even smaller than the required velocities calculated by the abnormally low value of Hamaker constant (Hamaker, 1937). Therefore, the mechanical mechanism of iron fume formation proposed by Baxter and Mitchell does not appear to be viable.

DISCUSSION

An experimental investigation of the reactions of pyrite has been undertaken to seek the sources of iron-rich fume in coal combustion. A fume was formed in low temperature reactions, but it contained virtually no iron. The primary constituents of the fume were impurities derived from the starting mineral and sulfur. When pyrite was oxidized in air at temperature below 1220 K, or pyrolyzed in nitrogen at temperatures up to 1420 K, a sulfur rich fume was generated. Some of the particles were crystalline. During electron microscope analysis, the beam damaged some of the crystallites. The sulfur-rich particles are thought to be elemental sulfur. Due to the low vapor pressure of sulfur at room temperature, it probably condensed in the cooled sampling probe in the drop tube reactor experiments. The observed fume particle size distribution is, therefore, determined by the sample extraction system and is not directly related to the pyrite reaction. Similarly, a cloud is formed around the laser heated particles where the temperature drops to near ambient levels. The persistence of elemental sulfur to temperatures as high as 1220 K suggests relatively slow reaction of the predominant S_2 species. Sulfur was not found in the higher temperature oxidation experiments, presumably due to SO_2 formation.

Baxter and Mitchell (1989) have observed significant iron loss in the early phases of coal combustion when temperatures are too low for volatilization to be significant. They

provide no data on the size, structure, or composition of the iron containing particles that escaped their collection system. Examination of the filters used in their measurements reveals that a broad range of particle sizes might penetrate. The large fractional loss they report suggests that the particles are near the minimum of the collection efficiency curve, i.e., between 0.04 and 0.2 μm. They hypothesize that pyrrhotite nodules, which are observed to be of order 0.1 μm diameter, are entrained by the gases released during devolatilization or the early phases of oxidation. Our experiments show no evidence for such release during reactions of pyrite alone.

We have examined the ability for aerodynamic force to remove particles held on a surface by van der Waals force. The velocities required to entrain submicron particles are too large for this mechanism to produce significant quantities of fine particles directly. Fragments of order 10 μm in size or larger might be released, however. Two mechanisms might allow fine iron particles to be formed by fragmentation. If a carbonaceous bridge holding a mineral inclusion on the parent particle were consumed by oxidation, the separation distance might be large enough to allow even a very small particle to be removed aerodynamically. On the other hand, oxidation of a large carbonaceous fragment could have behind relatively small residual ash particles. The former mechanism could generate a large number of fine fragments since the apparent surface free energy scales inversely as the square of the separation distance. It would likely appear early in the oxidative phase of coal combustion when temperatures are low enough for the pyrrhotite to be solid and when sufficient oxygen reaches the coal surface to consume carbon bridges. These conditions are consistent with the observations of Baxter and Mitchell (1989), as well as with the lack of fine fragment in the present study. The latter mechanism would required that a significant amount of carbon be associated with each fine particle and would, therefore, limit the number of fine fragments generated. Moreover, it would likely occur late in the combustion process when pore enlargement cause the entire char particle to disintegrate.

Previous coal combustion studies have shown substantial evidence for iron volatilization (Taylor and Flagan, 1981; Flagan and Taylor, 1981; Quann et al, 1982; and Neville and Sarofim, 1982). The evidence from these pyrite studies suggest that more than one mechanism may be responsible for the production of fine ash particles of all types in coal combustion. The distribution of a mineral in the parent coal and the transformation that the mineral experiences will influence the extent of fine particle formation by fragmentation. Carefully designed experimental investigations of mechanical generation of fine particle

from pyrite in coal combustion may shed light on the origins of other combustion-derived fine particles.

ACKNOWLEDGEMENTS:

This work was supported by the United States Department of Energy under grant number DE-ACC22-86PC90751.

Table 1. Impurities in Pyrite Samples

Element	Natural Pyrite		Synthetic Pyrite	
	Supplier	XFS	Supplier	XFS
B			10ppm	
Ca		~10%	<10ppm	trace
Cu	0.5%	~ 1%	100ppm	
Cr		trace		≤0.1%
K		< 1%		
Mg		trace	<10ppm	trace
Mn		< 5%	<10ppm	
Mo			10ppm	
Ni			10ppm	
Pb	0.04%			
Si			700ppm	
Ti			10ppm	
Zn	0.03%	~5-10%		
Zr			100ppm	

Table 2. Experimental Conditions and Average Results

Natural Pyrite:

T_{wall} (K)	750		873		1220	
Gas	N_2	air	N_2	air	N_2	air
Q_{mass} (gm hr^{-1})	1.08	0.94	0.22	0.022	0.87	0.016
$Q_{in,total}$ (lpm)	4.0	4.0	4.0	4.0	4.0	4.0
Q_{probe} (lpm)	5.0	5.0	5.0	5.0	5.0	5.0
$Q_{dilutor}$ (lpm)	0.0	0.0	28.0	28.0	28.0	28.0
V_{tot} ($\mu m^3\ cm^{-3}$)	3.4	6.9	7.7	8.8	96	39
N_{tot} (cm^{-3})	$1.9x10^6$	$4.1x10^6$	$2.0x10^6$	$1.3x10^6$	$3.2x10^6$	$7.2x10^6$
$C_{FeS_2,reacted}$ (ppm) (based on ρ_{FeS_2})	16ppm	38ppm	0.1%	1%	0.3%	7%

Synthetic Pyrite:

T_{wall} (K)	873		1220		1420	
Gas	N_2	air	N_2	air	N_2	air
Q_{mass} (gm hr^{-1})	0.23	0.072	0.46	0.034	0.43	0.048
$Q_{in,total}$ (lpm)	4.0	4.0	4.0	4.0	4.0	4.0
Q_{probe} (lpm)	4.5	4.5	4.5	4.5	4.5	4.5
$Q_{dilutor}$ (lpm)	20.0	20.0	20.0	20.0	20.0	20.0

NOMENCLATURE

A	Hamaker constant (erg)
d_p	particle diameter (μ)
h	Planck's constant = 6.626×10^{-27} erg sec
k	Boltzmann's constant = 1.381×10^{-16} erg K^{-1}
l	mean free path of the gas
n_i	refractive index of the medium i in the visible
r	particle radius (μm)
T	absolute temperature (K)
v	fluid velocity
ε_i	static dielectric constants of the medium
υ_e	plasma frequency of the free electron gas, typically in the range 3 to 5×10^{15} sec^{-1}
σ	free surface energy (erg cm^{-2})
μ	fluid viscosity (gm cm^{-1} sec^{-1})

REFERENCES

Bagnold, R. A. (1960), "The Re-entrainment of Settled Dusts", *Int. J. of Air Pollution*, 2, p.357.

Baxter, L. L., and Mitchell, R. E. (1989), "The Release of Iron during the Combustion of Illinois #6 Coal", *presented at the Pittsburgh Coal Conference.*

Bradley, R. (1932), "The Cohesive Force between Solid Surface and the Surface Energy of Solids", *Phil. Mag.* 13, pp. 853-862.

Corn, M and Stein, F. (1965), "Re-entrainment of Particles from a Plane Surface", *Amer. Ind. Hyg. Assoc. J.*, 26, pp. 325-336.

Flagan, R. C., and Friedlander, S. K. (1978), "Particle Formation in Pulverized Coal Combustion: A Review, " *Recent Developments in Aerosol Science* (Shaw, D. T. Ed.), Wiley-Interscience, New York, pp. 25-59.

Flagan, R. C., and Taylor, D. D. (1981), "Laboratory Studies of Submicron Particles from Coal Combustion", *18th Symp. (Int.) on Combustion*, The Combustion Institute, Pittsburgh, PA, pp. 1227-1237.

Fristrom, R. M., and Westenberg, A. A. (1965), *Flame Structure*, McGraw-Hill, New York, New York.

Hamaker, H. C. (1937), "The London-van der Waals Attraction between Spherical Particles", *Physics*, 4(10), pp. 1058-1072.

Israelachvili, J. N. (1985), *Intermolecular and Surface Force with Applications to Colloidal and Biological Systems*, ed., Academic Press Inc. (London) LTD.

Lipinski, R. J., Bradley, D. R., et al. (1985), "Uncertainty in Radionuclide Release under Specific LWR Accident Conditions", Appendix G on Resuspension & Reentrainment, SAND84-0410, 2, R5.

Liu, B. Y. H., Pui, D. Y. H., and Rubow, K. L. (1983), "Characteristics of Air Sapling Filter Media", *Aerosols in the Mining and Industrial Work Environments, Vol. 3 Instrumentation and Arbor Science*, (Marple, V. A. and Liu, B. Y. H., Ed.),

Neville, M. and Sarofim, A. F. (1982), "The Stratified Composition of Inorganic Submicron Particles Produced during Coal Combustion", *19th Symp. (Int.) on Combustion,* The Combustion Institute, Pittsburgh, PA, pp. 1441-1449.

Quann, R. J., Neville, M., et al. (1982), "Mineral Matter and Trace-Element Vaporization in a Laboratory-Pulverized Coal Combustion System", *Environ. Sci. Technol.*, 16, pp. 776-781.

Sahu, R. (1988), *On the Combustion of Bituminous Coal Chars*, Ph. D. Thesis, California Institute of Technology.

Spjut, R. E., Sarofim, A. F. (1985) and Longwell, J. P., "Laser Heating and Particle Temperature measurement on an Electrodynamic Balance", *Langmuir*, 1, pp. 355-360.

Taylor, D. D. and Flagan, R. C.(1981), "Aerosols from a Laboratory Pulverized Coal Combustior", *Atmospheric Aerosols - Source / Air Quality Relationships*, E.S. Macias and P.K. Hopke, Eds., ACS Symposium Series No. 167.

Wang, S. C., and Flagan, R. C. (1990), "Scanning Electrical Mobility Spectrometer", *Aerosol Sci. Tech.*, 13(2), pp. 230-240.

Wiltowski et al. (1987), "Kinetics and Mechanisms of Iron Sulfide Reductions in Hydrogen and in Carbon Monoxide", *J. Solid State Chem.*, 71, pp. 95-102.

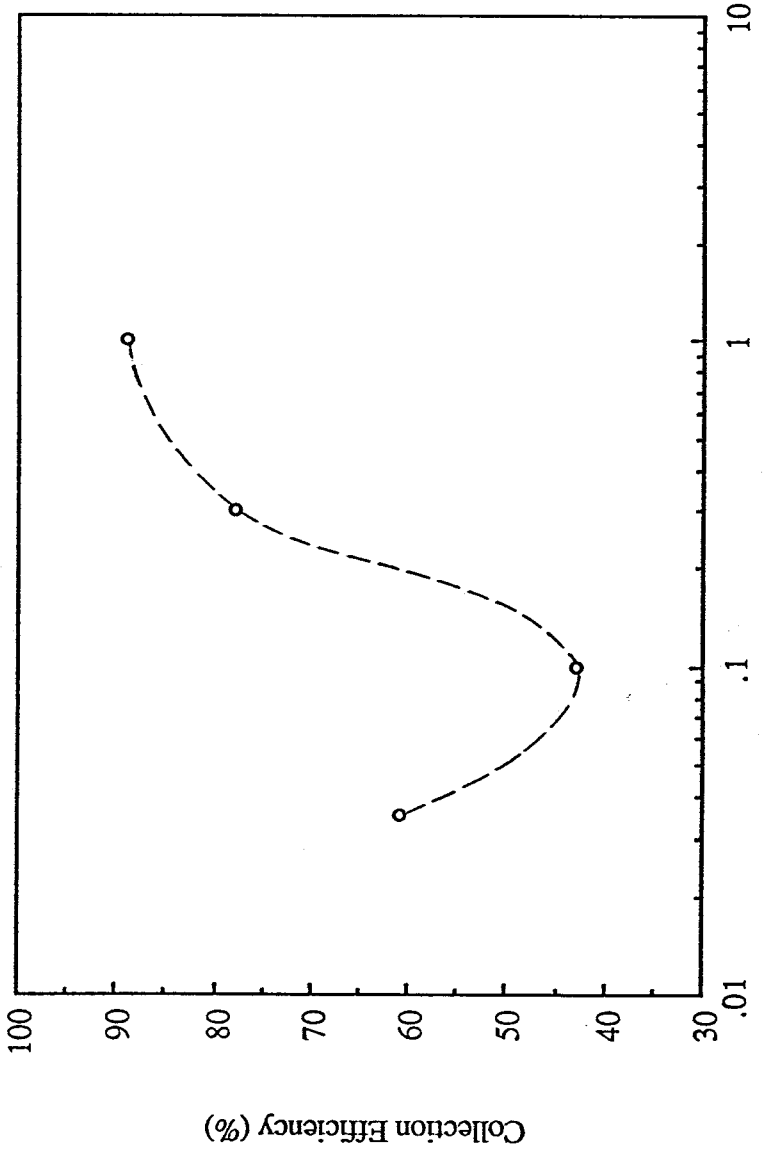

Fig. 1 Particle collection efficiency of nuclepore N100, polycarbonate membrane, 1.0 μm pore with the velocity of 13 cm/sec (Lui, et al., 1983)

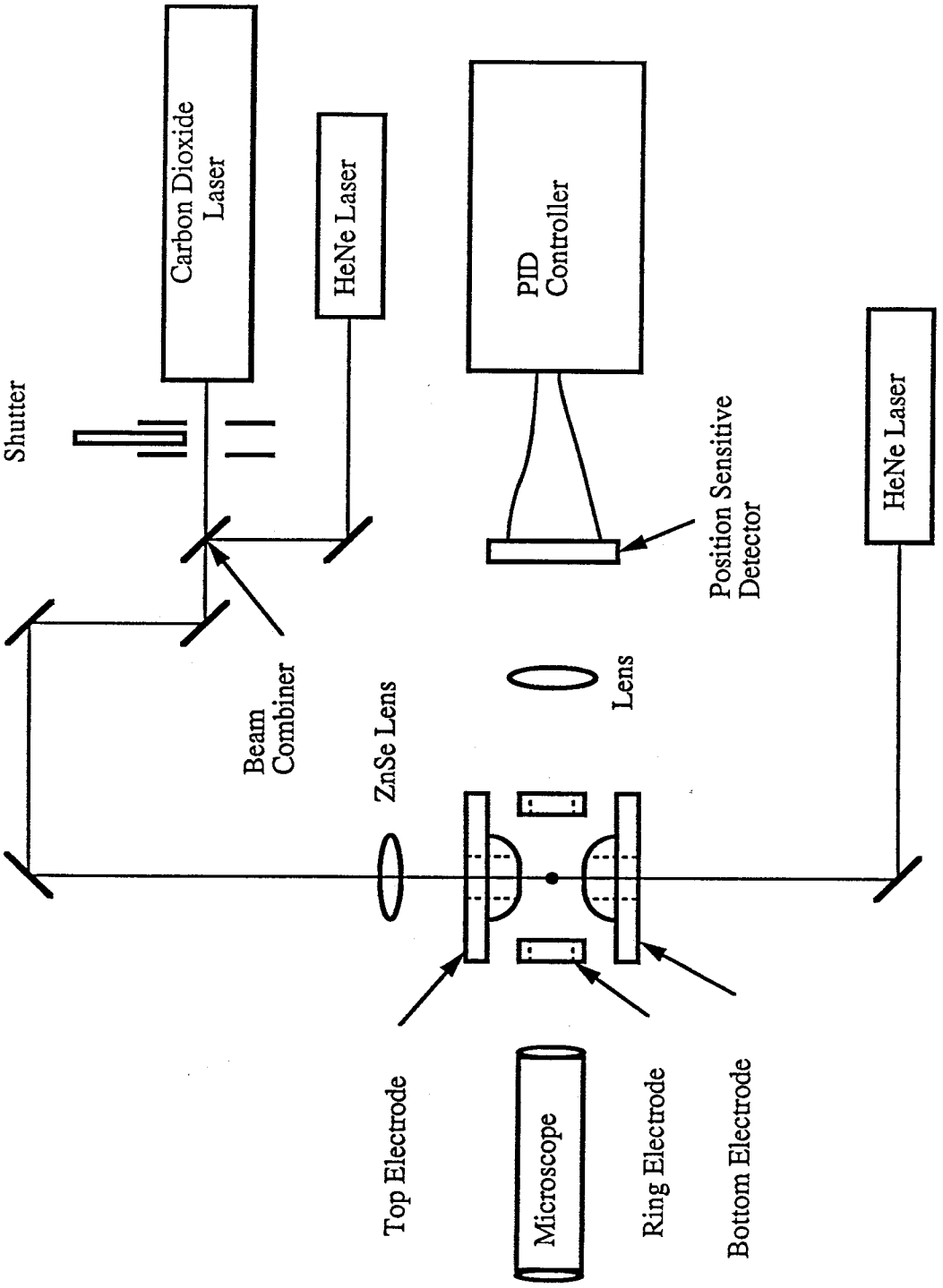

Fig. 2 Schematic of the EDTGA

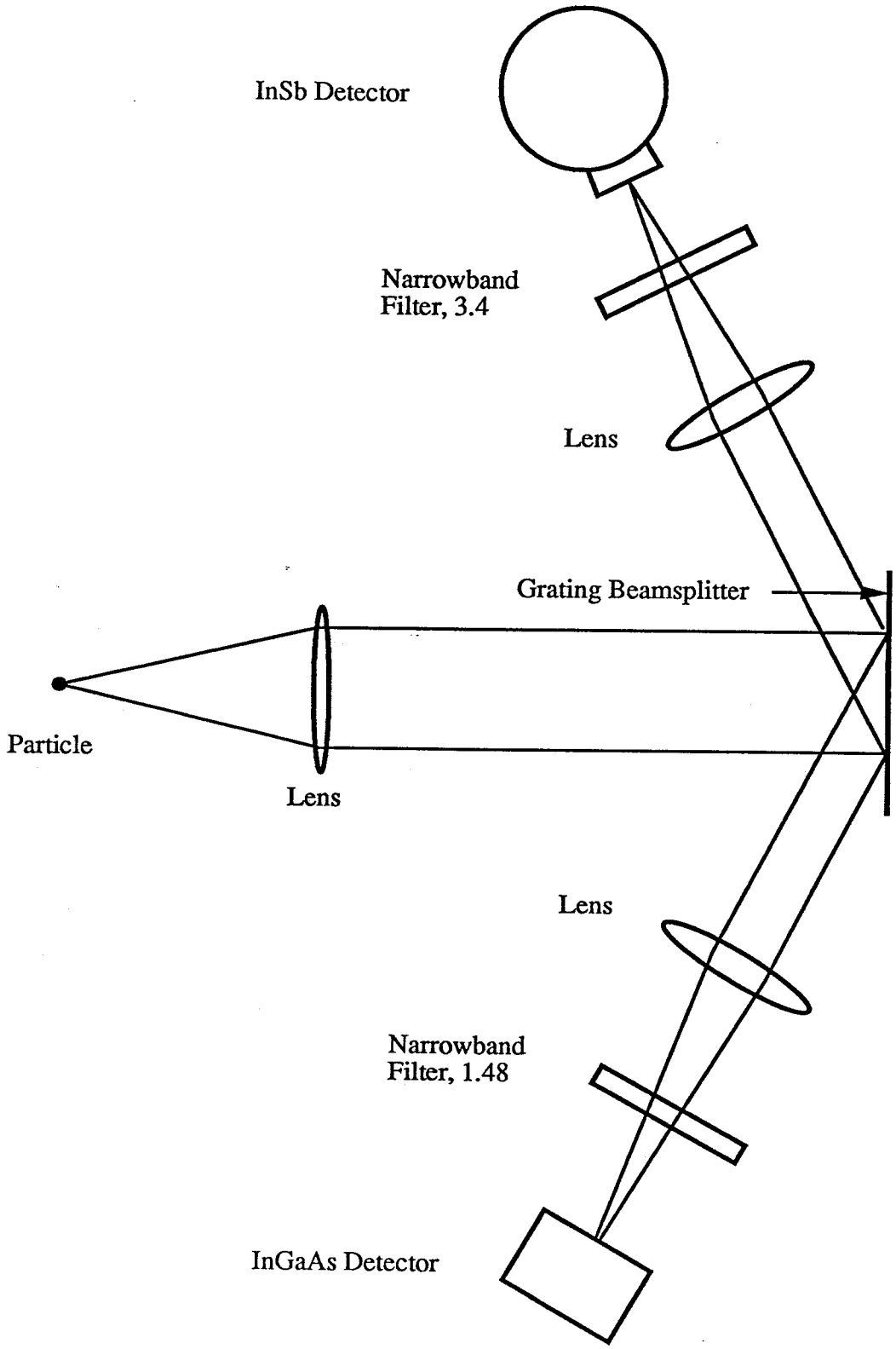

Fig. 3a Pyrometer Schematic

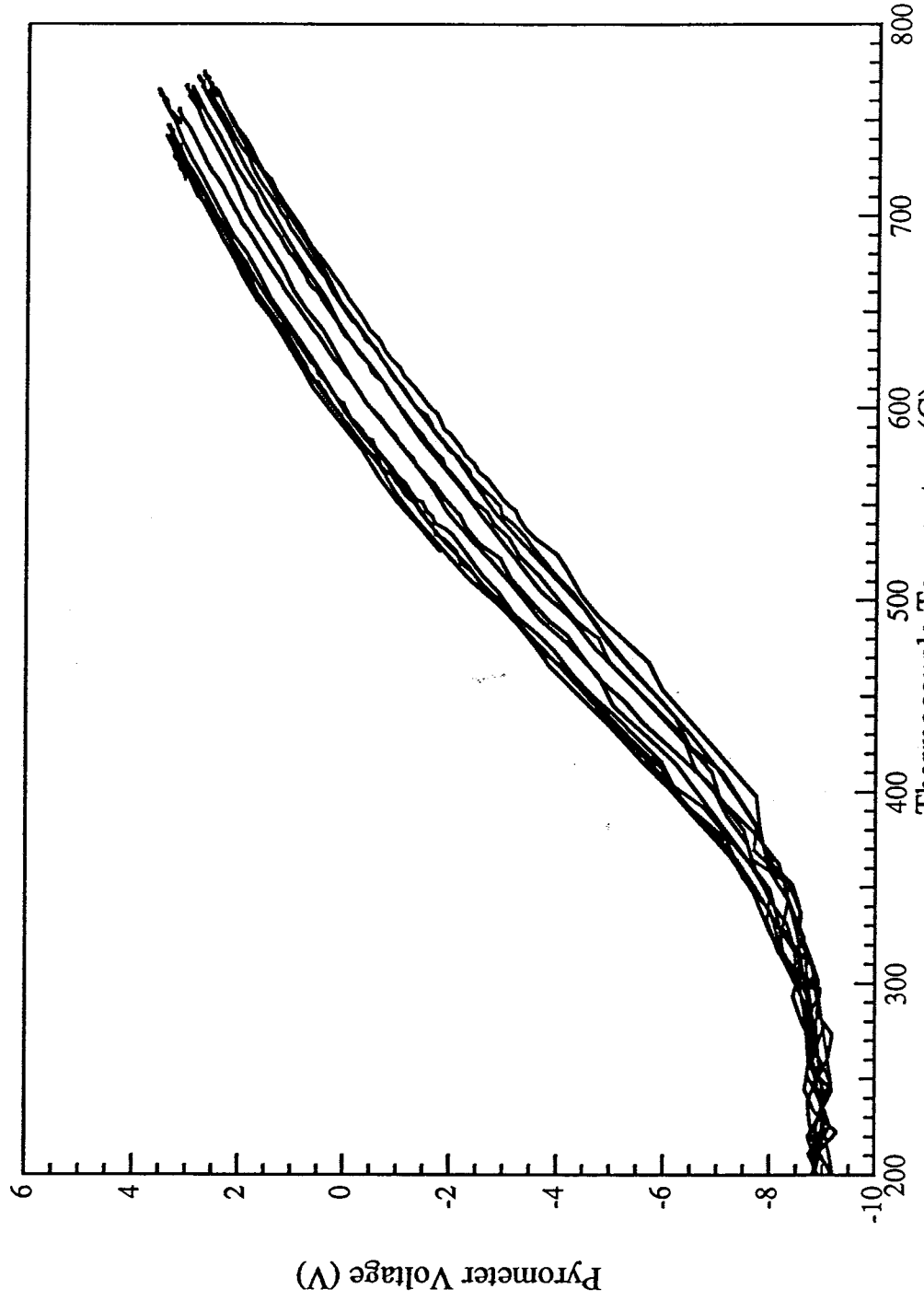

Fig. 3b Optical pyrometer calibration data obtained using a pyrite coated thermocouple bead

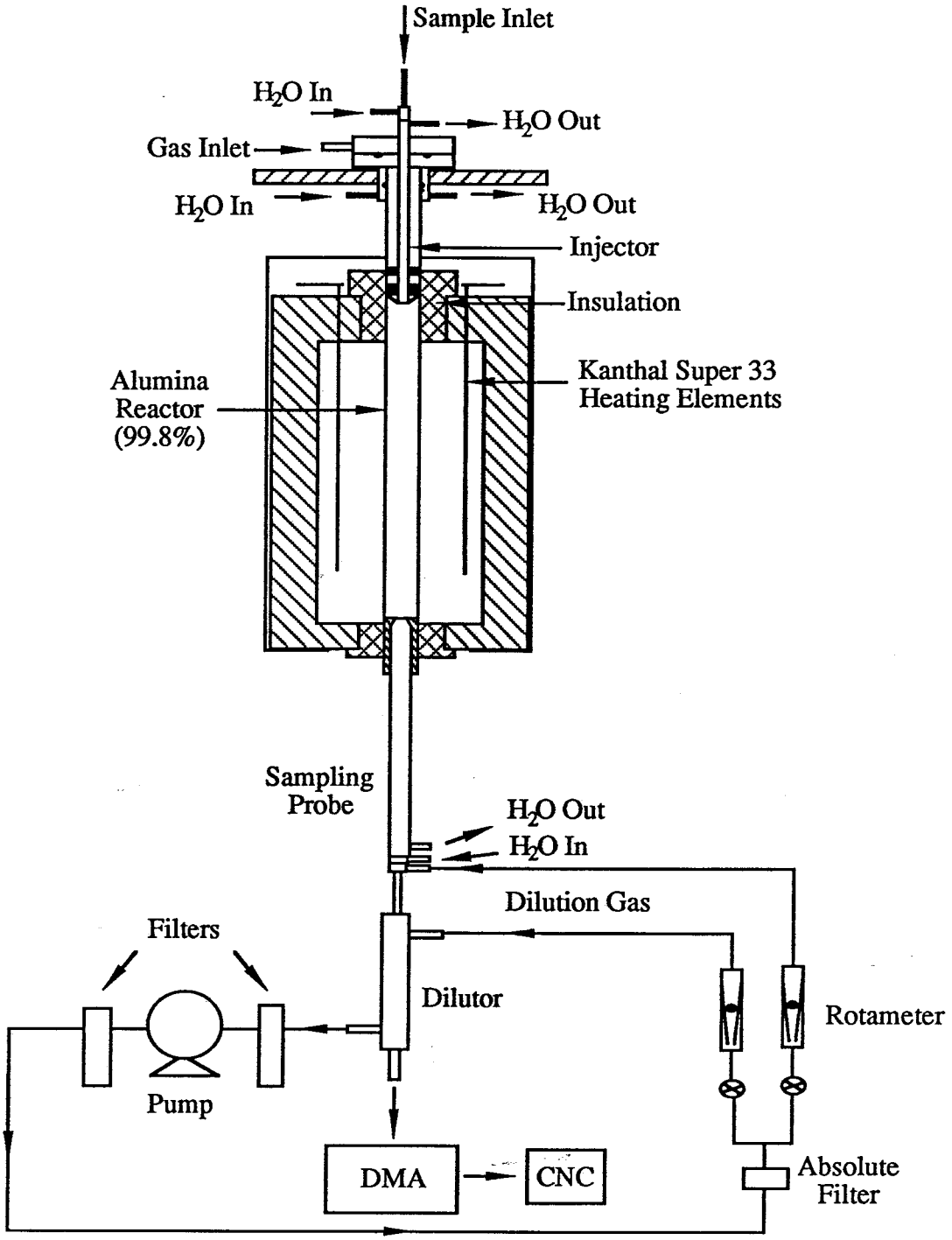

Fig. 4 Schematic of experimental system

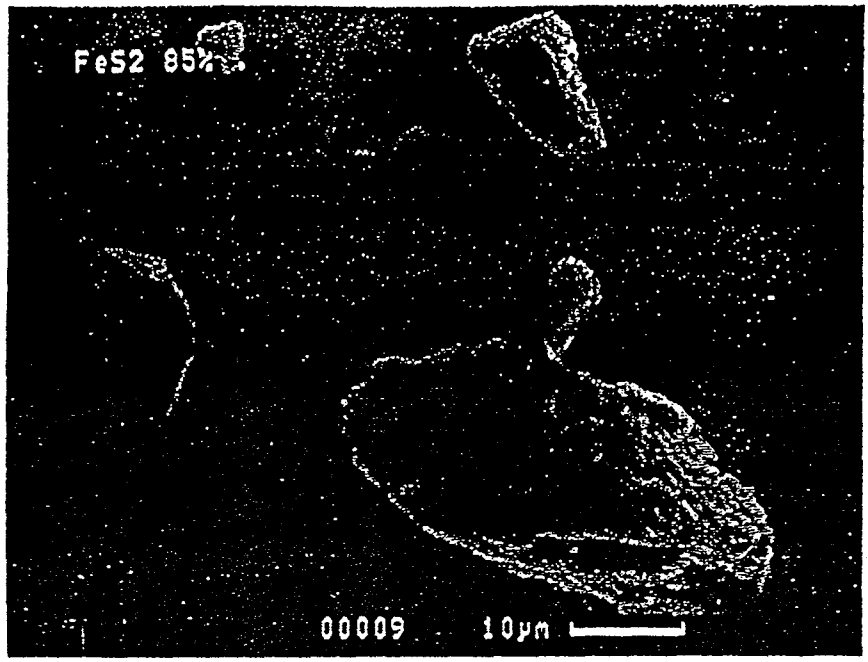

(a)

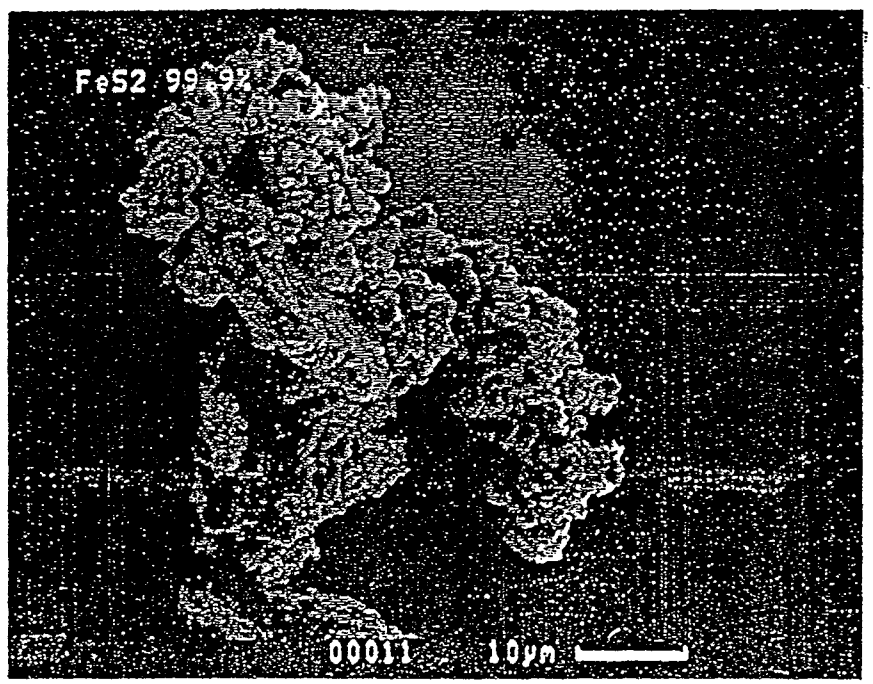

(b)

Figure 5. SEM pictures of pyrite particles (a) natural pyrite; (b) synthetic pyrite.

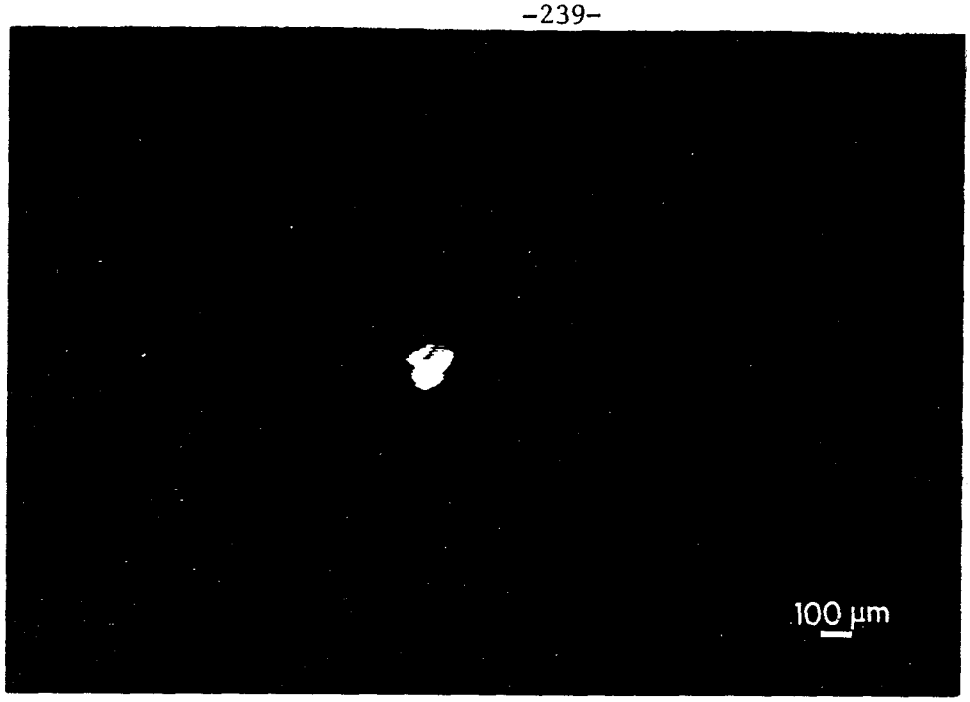

(a)

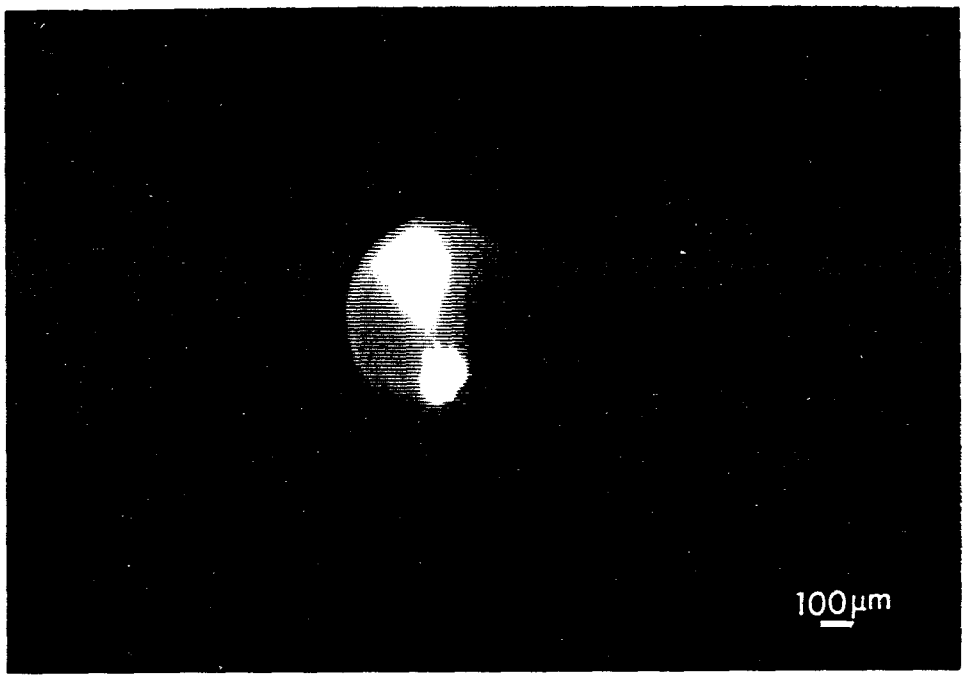

(b)

Fig. 6 (a) Image of pyrite particle trapped in the electrodynamic balance
(b) Cloud formation around the particle after a single laser pulse

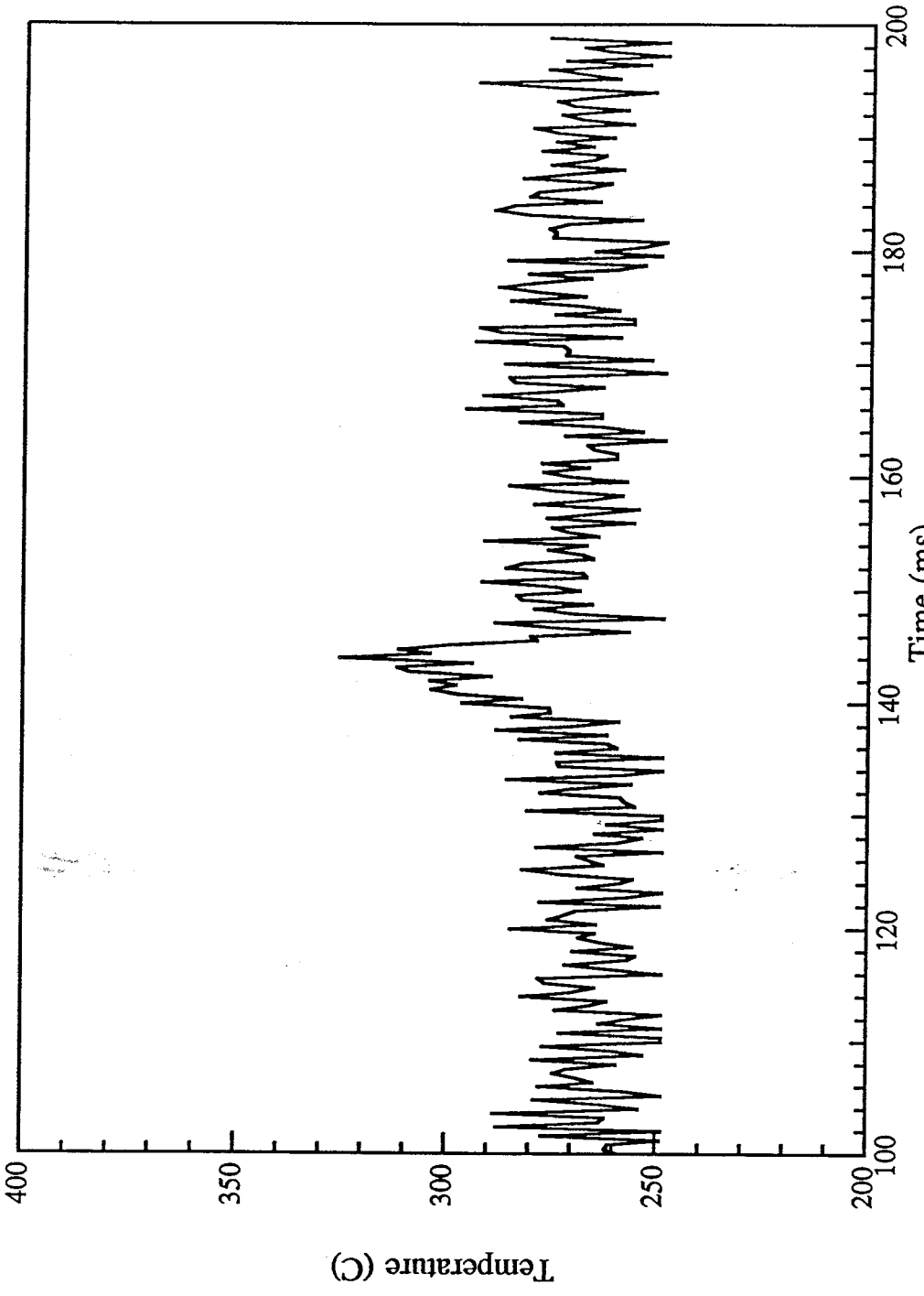

Fig. 6c Optically measured temperature profile for the laser pulse

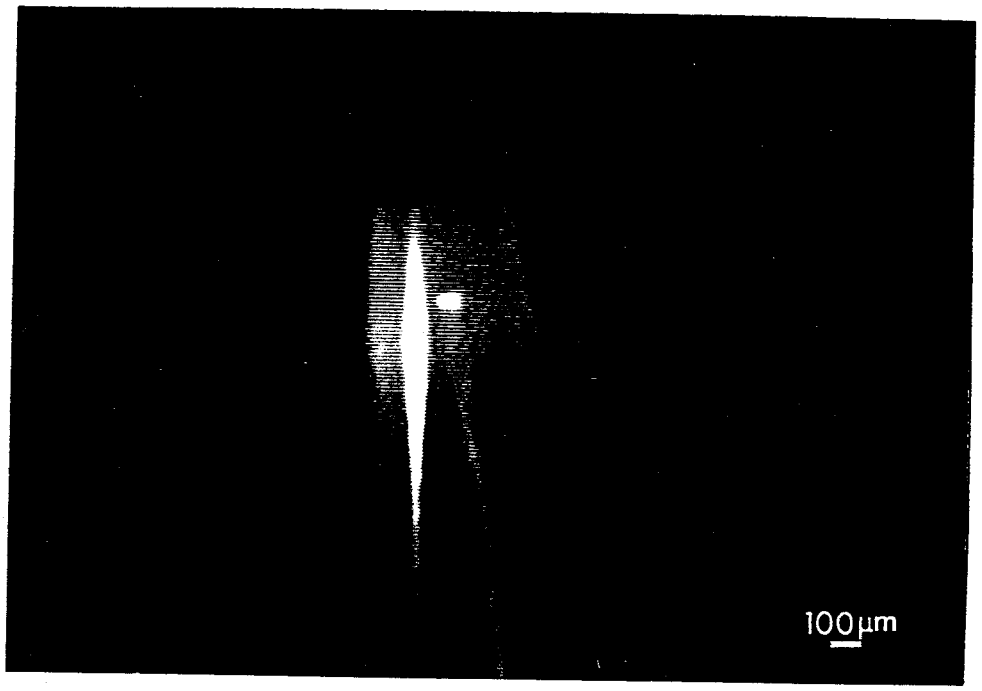

Fig. 7a Ignition of the pyrite particle by a single laser pulse

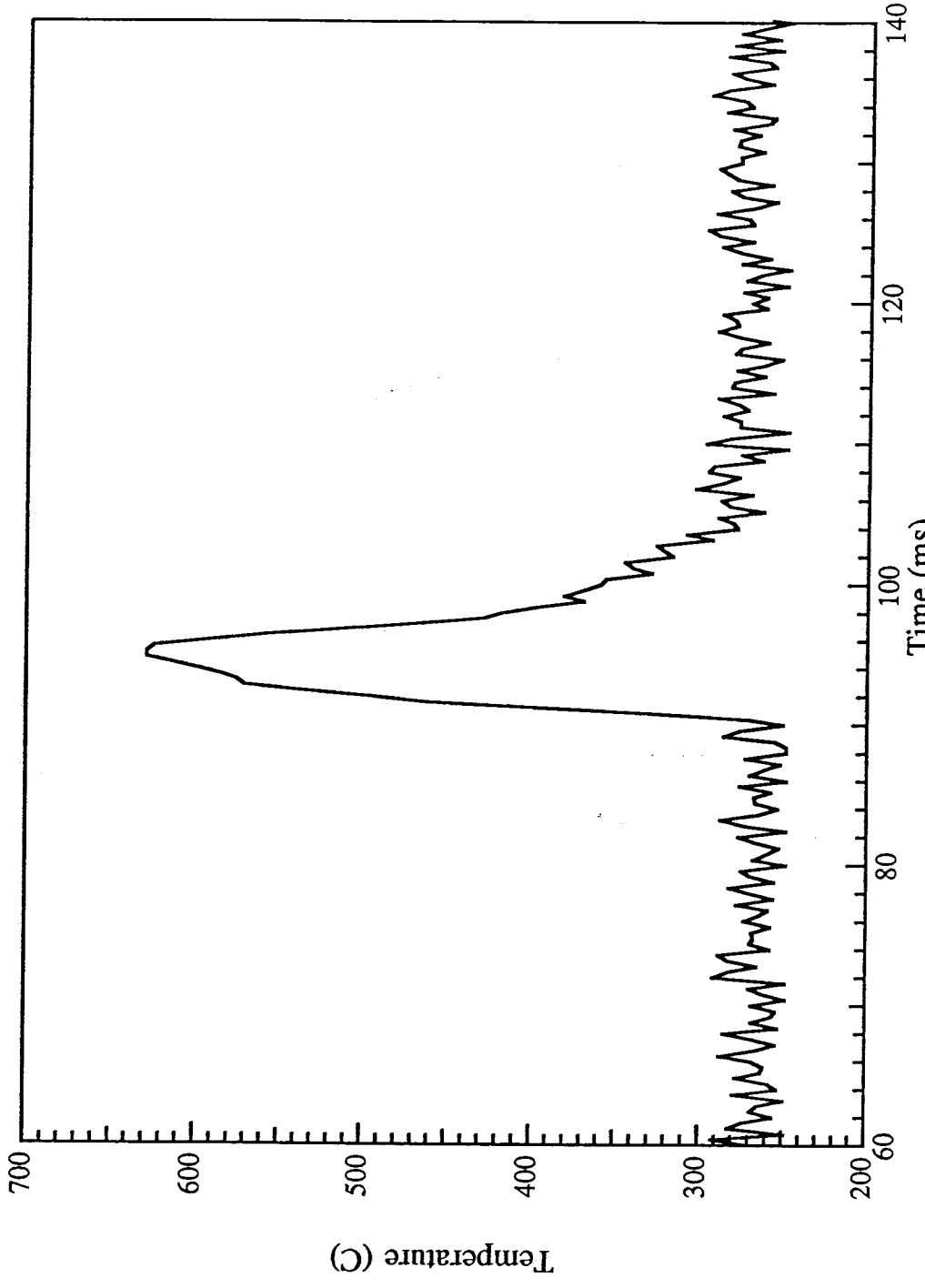

Fig. 7b Temperature history of the pyrite particle during the laser pulse

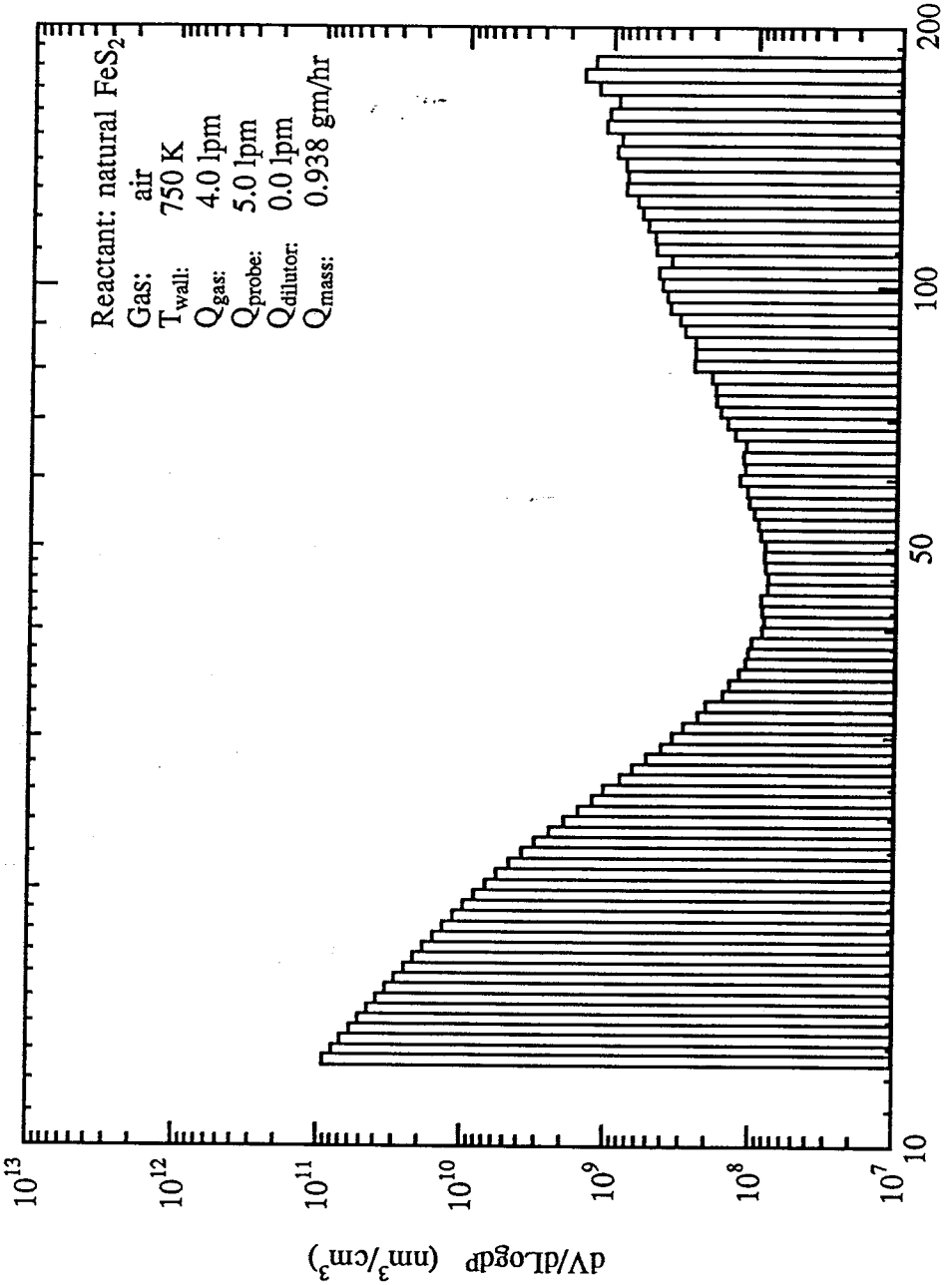

Fig. 8a Particle volume distribution of the fume generated by reaction of natural pyrite in air at 750 K

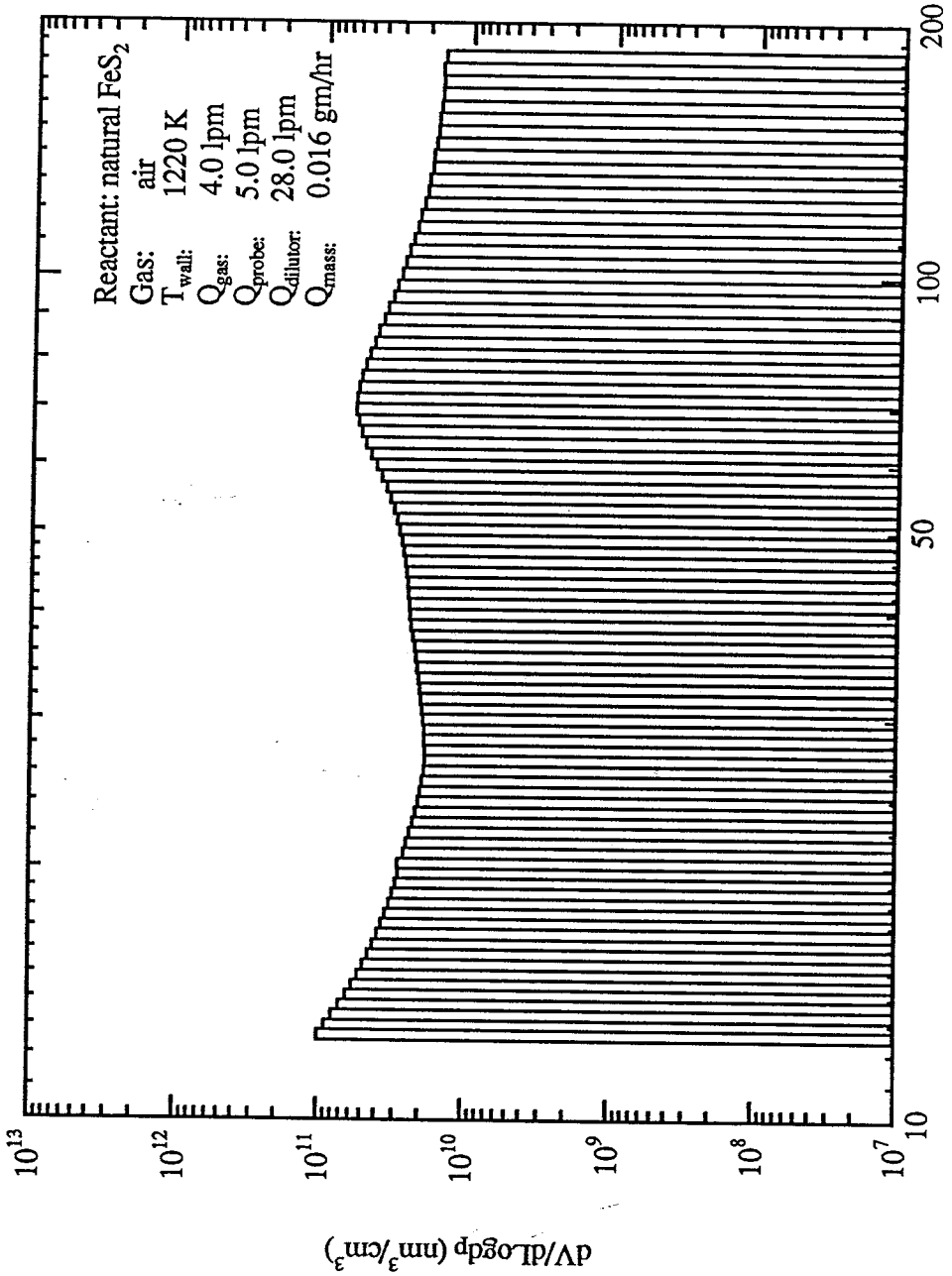

Fig. 8b Particle volume distribution of the fume generated by reaction of natural pyrite in air at 1220 K

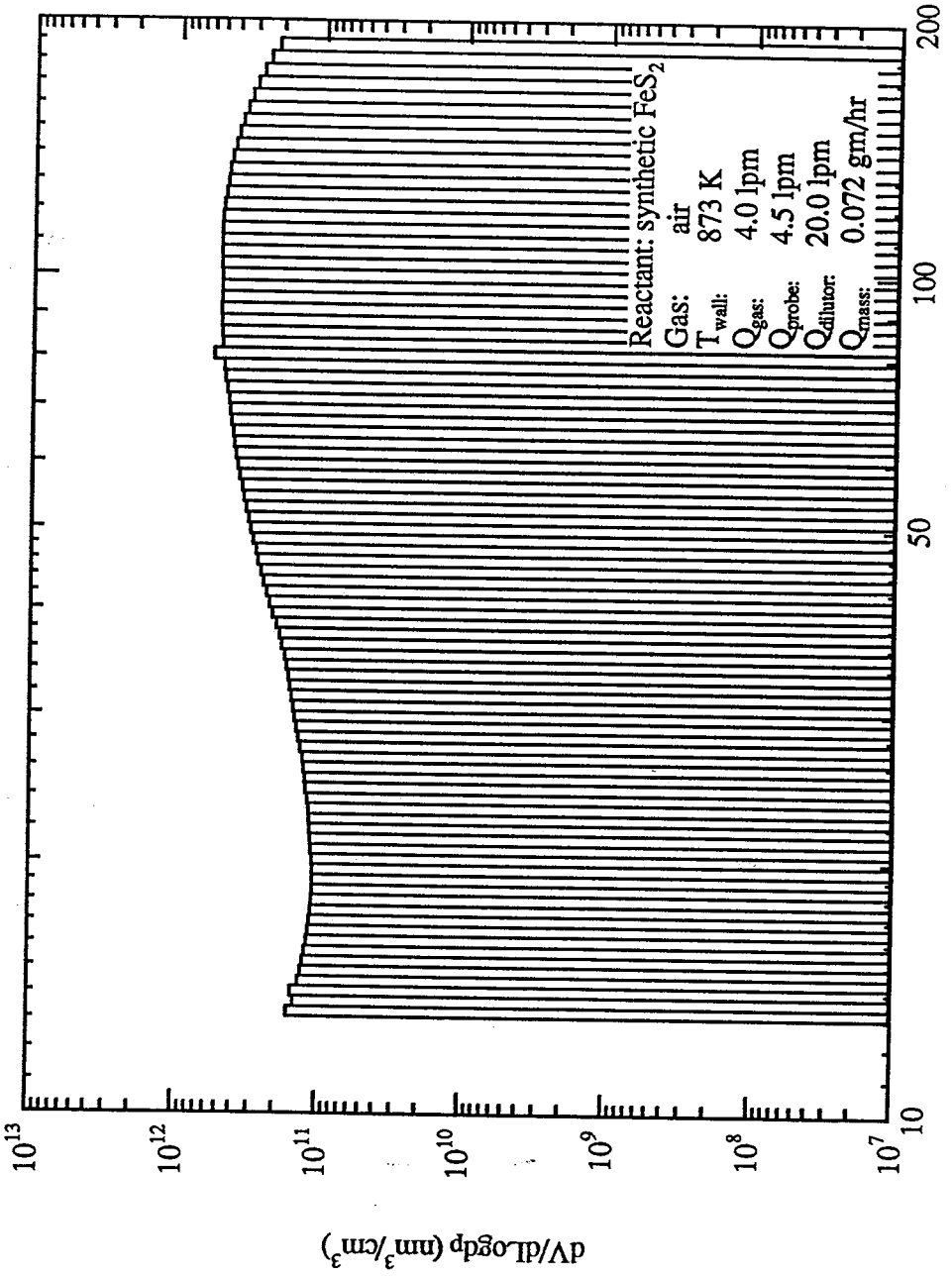

Fig. 9a Particle volume distribution of the fume generated by reaction of synthetic pyrite in air at 873 K

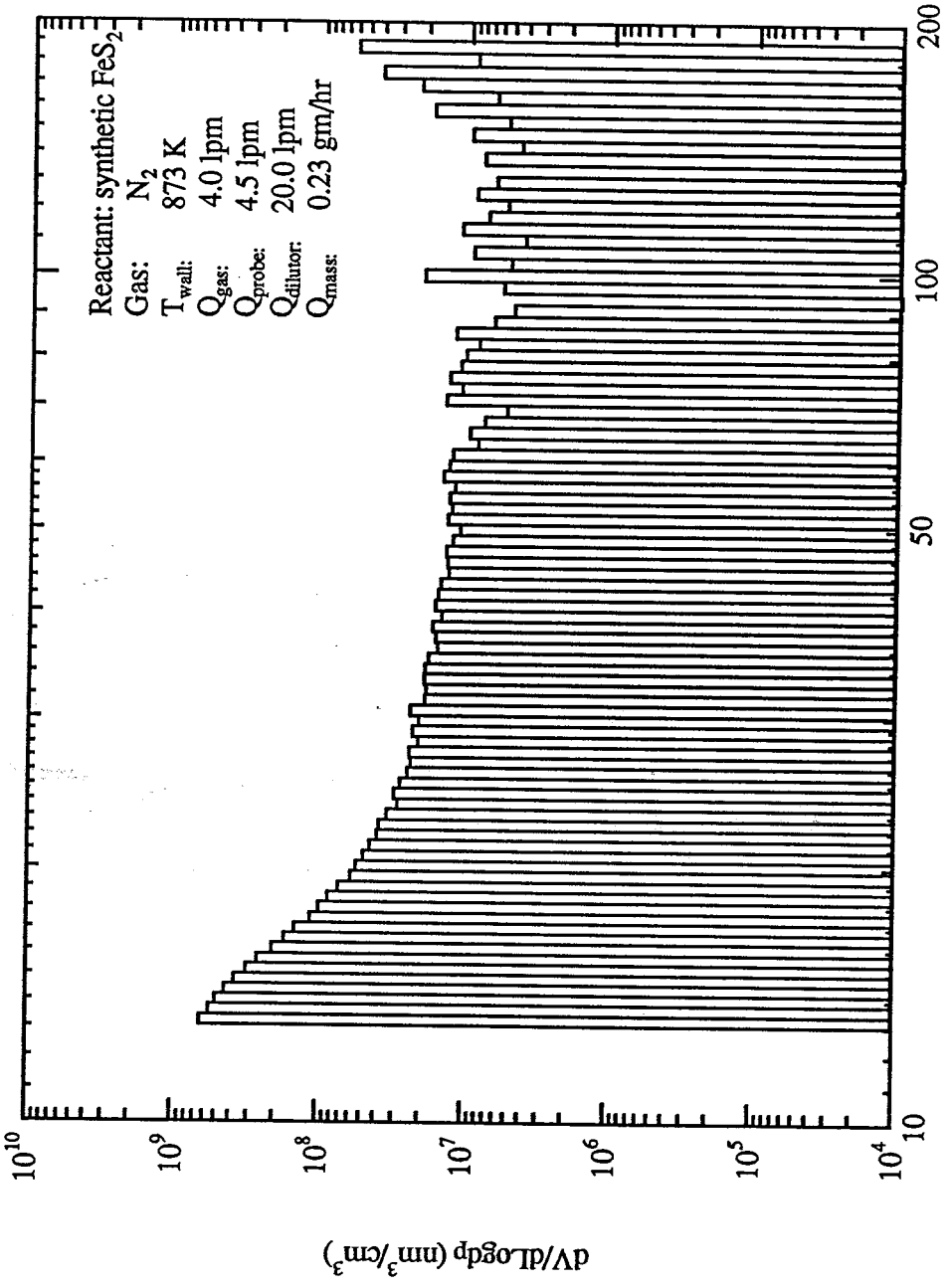

Fig. 9b Particle volume distribution of the fume generated by reaction of synthetic pyrite in N_2 at 873 K

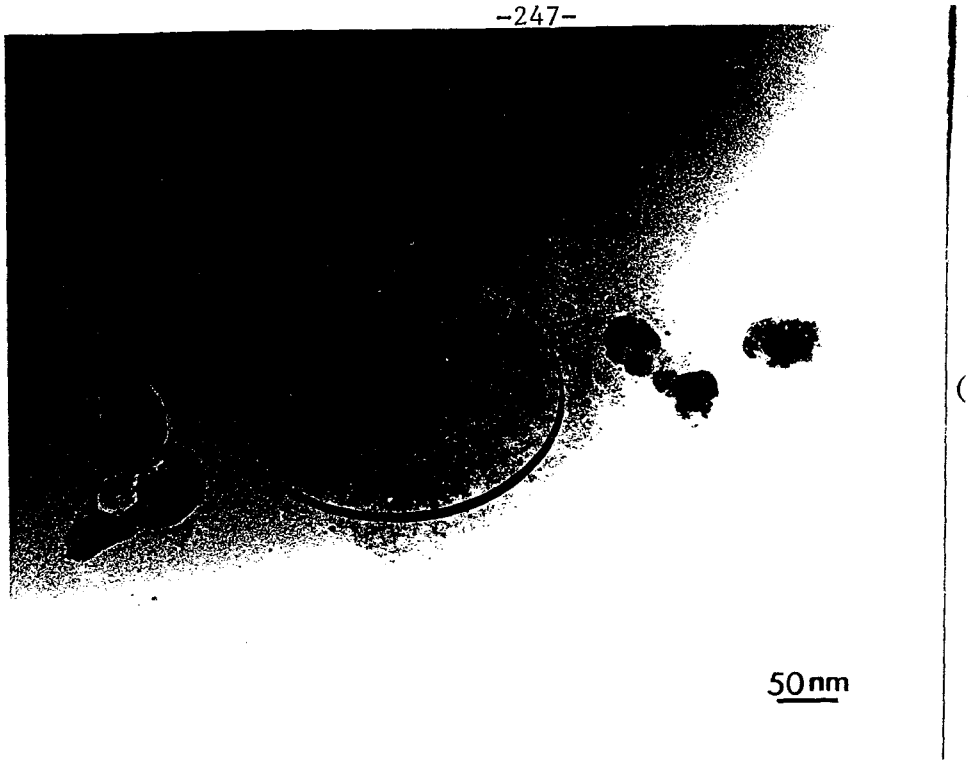

(a)

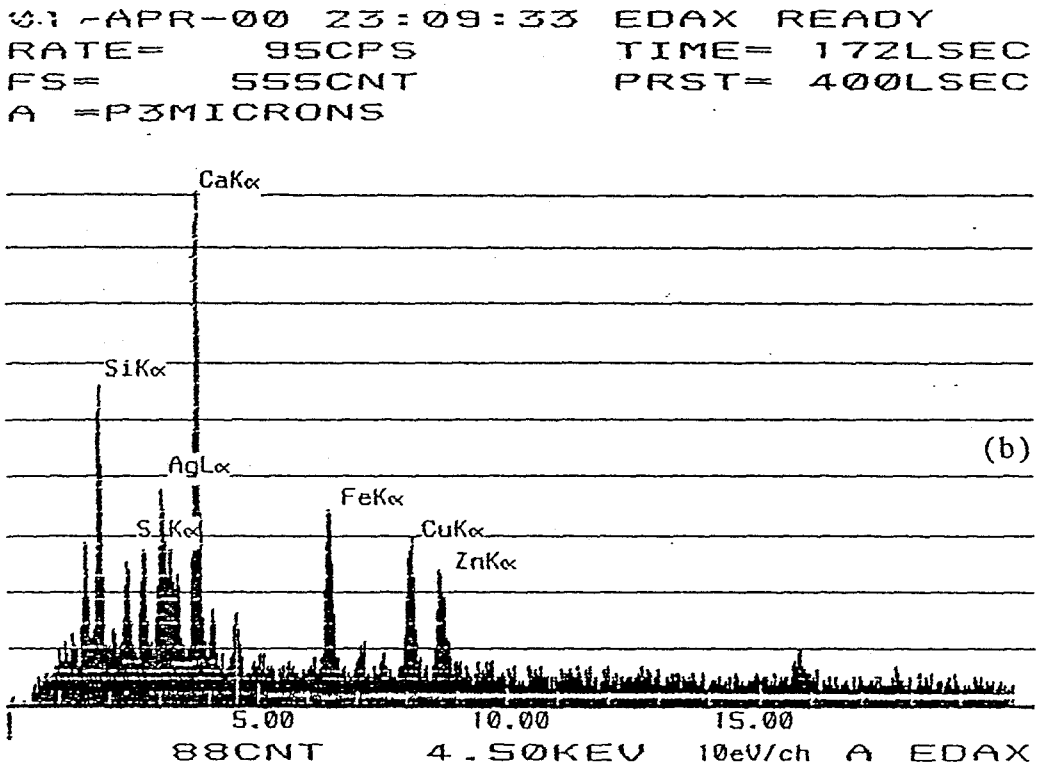

(b)

Fig. 10 Fume produced during reaction of natural pyrite in air at 1220 K (a) Micrograph; (b) EDAX spectrum of the low density material within the circle

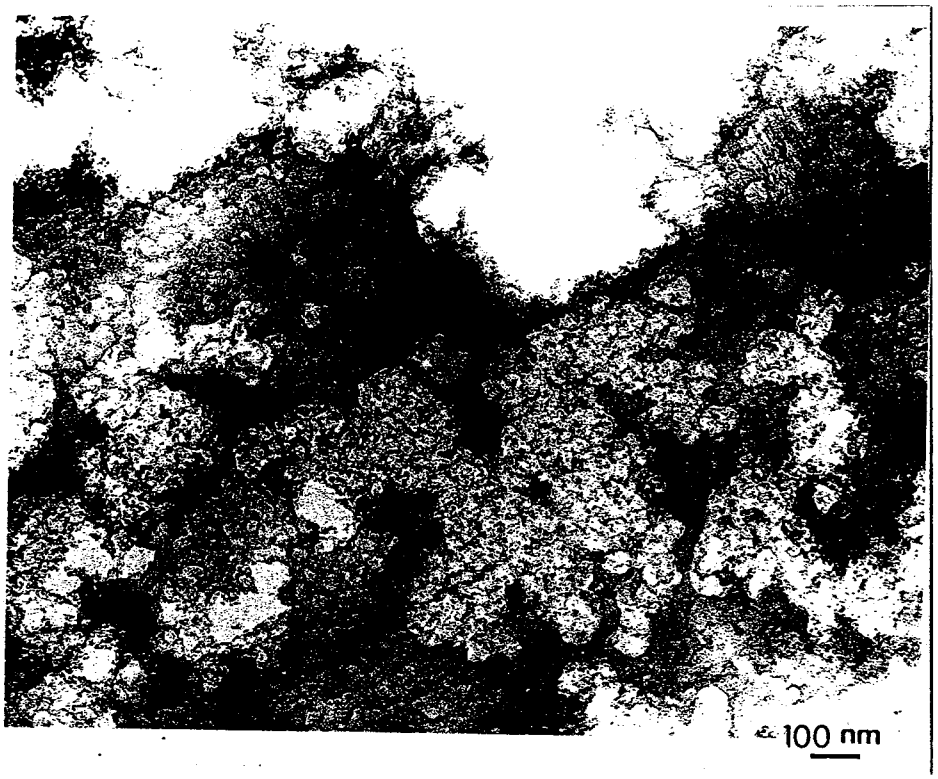

Fig. 11 Agglomerate particles produced during reaction of synthetic pyrite in nitrogen at 1420 K.

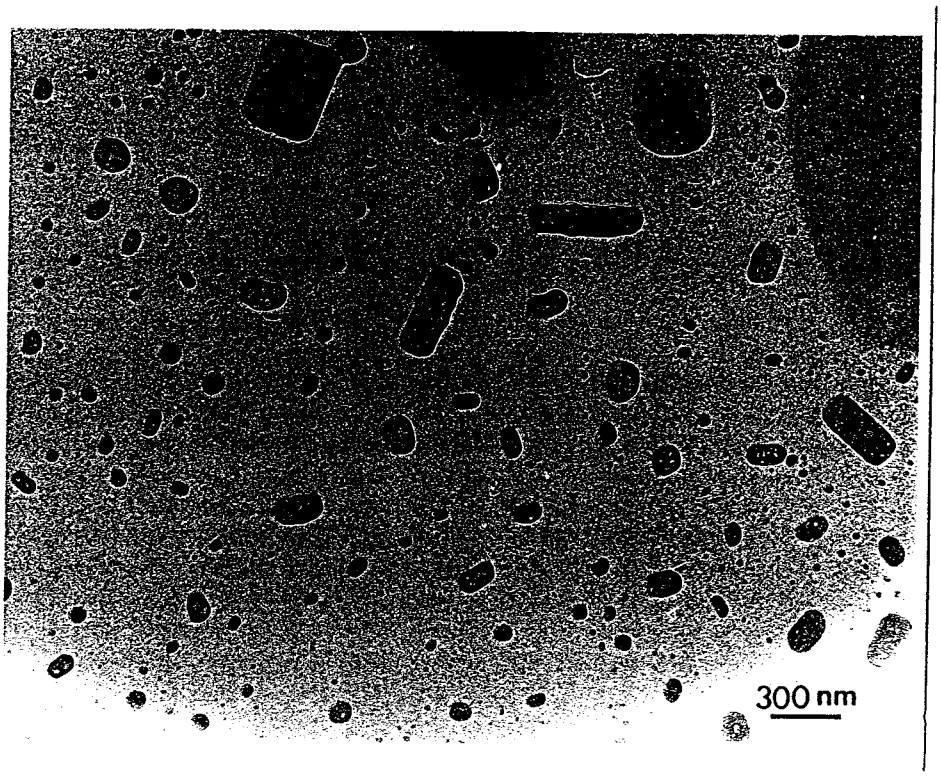

Fig. 12 Sulfur crystals produced by reaction of synthetic pyrite in air at 873 K.

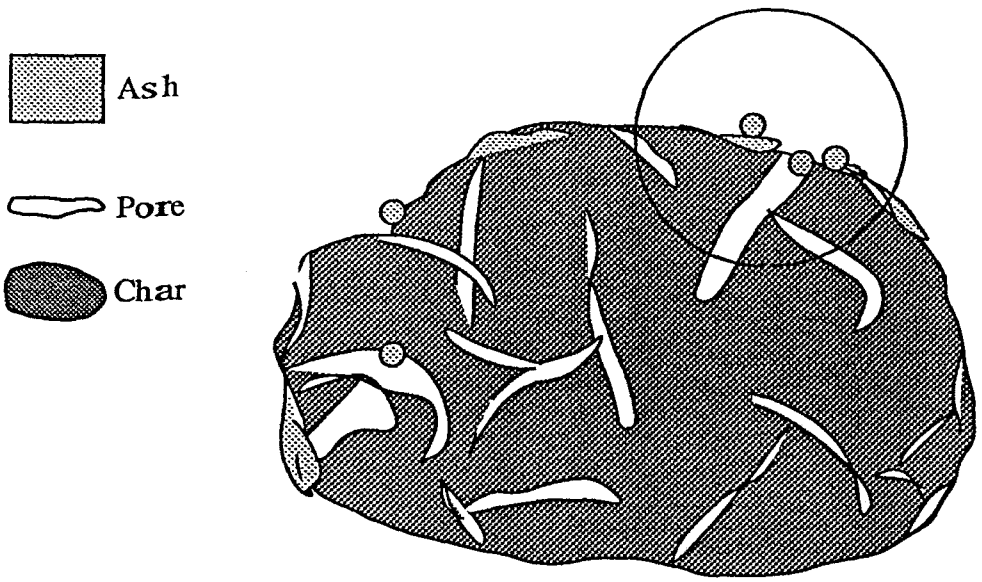

Enlarge View :

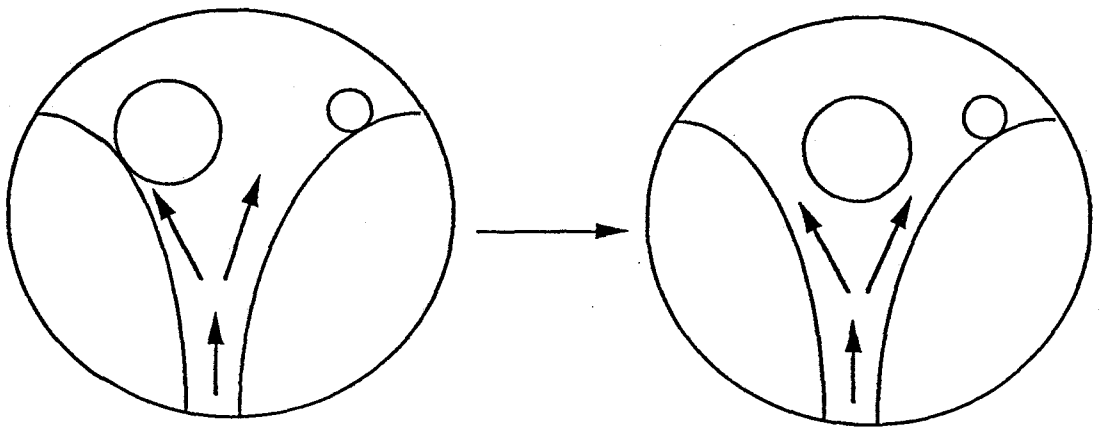

Fig. 13 Schematic of the adhesive force and drag force acting on a removal particle

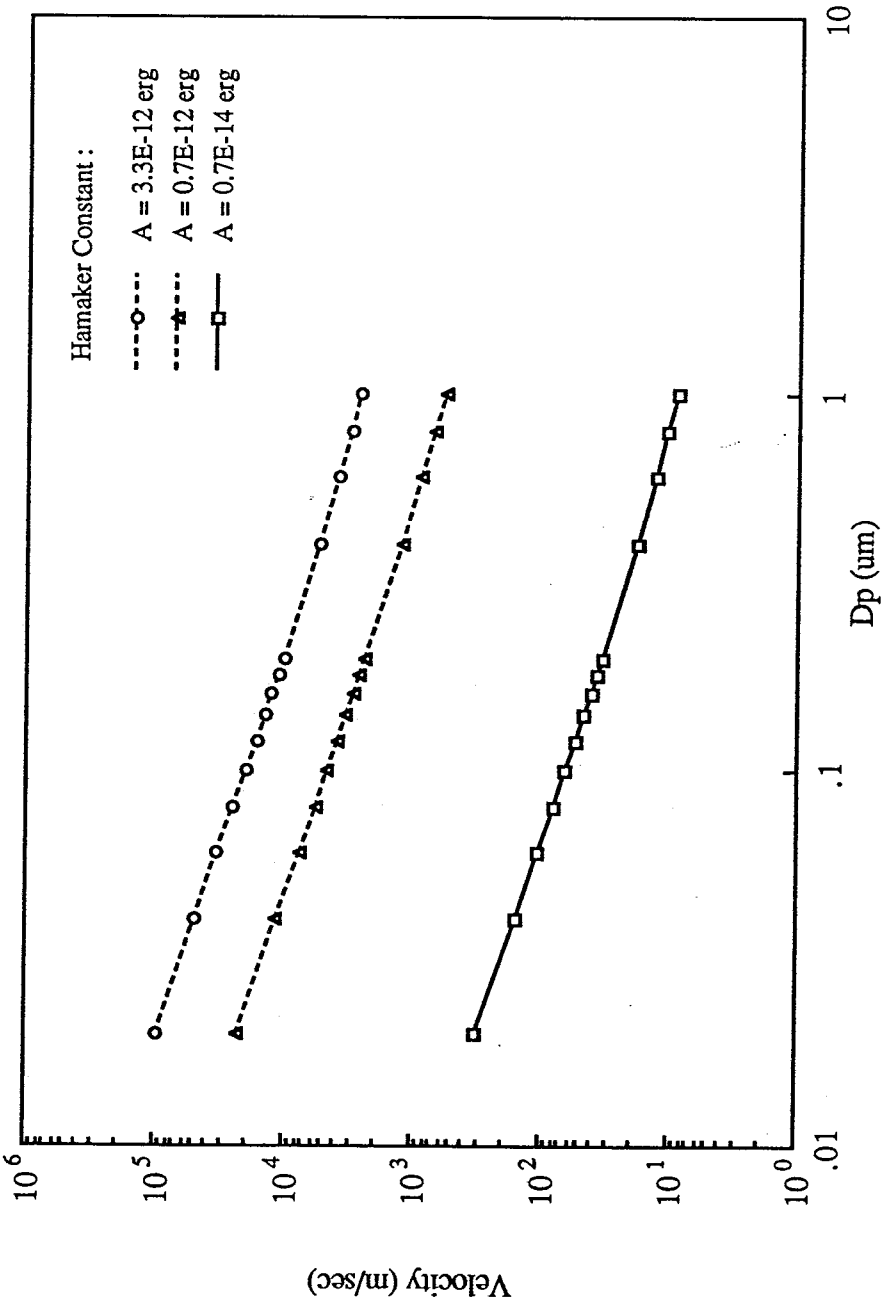

Fig. 14 Velocity calculated by drag force and surface energy (dp = 100 μm)